Formulation Strategies to Enhance Nose-to-Brain Delivery of Drugs

Sasi Bhushan Yarragudi

A thesis submitted for the degree of

Doctor of Philosophy

at the University of Otago

Dunedin, New Zealand

June 2018

Abstract

Delivery of drugs via the intranasal olfactory route is a non-invasive and practical method of bypassing the blood-brain barrier (BBB). However, targeted delivery and retention of drugs to the olfactory region is a significant challenge due to the geometrical complexity of the nasal cavity and mucociliary clearance. Formulating drugs into particulate-carriers, specifically, carriers with mucoadhesive properties can potentially overcome this challenge by enabling targeted deposition and retention of the drug onto the olfactory epithelium for subsequent nose-to-brain transport. Recent modeling data indicates that particles around 10 μm in size show maximum deposition in the olfactory region, the target site for nose-to-brain drug absorption. Therefore, the primary objectives of this thesis was to develop and characterize 10 μm-sized mucoadhesive microparticles for selective drug deposition in the olfactory region and enhanced nose-to-brain delivery. Furthermore, recently several drug delivery devices that aim to target drug formulations to the olfactory region in the nasal cavity are making their way to the market. Therefore, the second objective of this thesis was to explore if the formulative approach of making particles to a specific size and combining it with a targeting device could augment olfactory targeting and further enhance nose-to-brain delivery of therapeutic molecules. Consequently, the effect of particle size combined with a bi-directional delivery technique on the olfactory deposition of microparticles in the human nasal cavity was investigated.

A naturally occurring mucoadhesive polymer, tamarind seed polysaccharide (TSP), was spray-dried with model drugs, FITC-Dextrans of molecular weight (MW) 3 to 40 kDa. The spray-drying process was optimized by the Box-Behnken experimental design to produce particles with 10 μm size. *In-vitro* and *ex-vivo* characterization demonstrated mucoadhesive potential and successful drug loading of TSP-microparticles. Particles of 10 μm in size demonstrated higher olfactory deposition compared to 2 μm sized particles in a 3D-human nasal replica, at standard inhalation airflow rate. The nose-to-brain delivery efficiency of the mucoadhesive TSP-microparticles was tested *in-vivo* in a rodent model. An anti-epileptic drug (AED) phenytoin was loaded into TSP-microparticles and administered intranasally to rats with an insufflator. The analysis of phenytoin concentrations in the rat brain revealed a

three-fold greater direct transport of phenytoin with the TSP-microparticles compared to the intranasal solution at the end of 60 min. The results from this study demonstrated the potential of TSP-microparticles to improve direct transport of drugs to the brain by enhancing the nasal residence time of phenytoin due to mucoadhesion.

In-silico computational fluid and particle dynamics (CFPD) techniques were utilized to identify the variability in olfactory deposition of microparticles between three human subjects with the inhalational delivery technique. Three normal human nasal cavities reconstructed using computerized tomography (CT)-scans were used to study the deposition of particles. The results identified that particles around 10 µm have consistently high deposition in the olfactory regions of three human subjects without any significant inter-subject variability. CFPD techniques were also used to study the effect of particle size in combination with a novel bi-directional delivery technique (used in the 'OPTINOSE®' targeting device) on the deposition of particles in the human nasal cavities. The deposition of particles in the olfactory region was found to be a function of particle size. The bi-directional delivery technique demonstrated significantly higher deposition of particles in the olfactory region compared to standard inhalation. The results identified a particle size range of 14 to 18 µm can significantly enhance the olfactory deposition of particles when administered with bi-directional delivery technique without any inter-subject variability.

In summary, this thesis demonstrated that formulation strategies can augment olfactory deposition and enhance nose-to-brain delivery of therapeutic molecules. This thesis integrated data from *in-vitro*, *in-vivo* and *in-silico* studies to refine and optimize a size tailored mucoadhesive microparticle delivery system that has promising potential in the nose-to-brain drug delivery.

అంకితం

అమ్మానాన్నలకు, అనుబంధాలకు, ఆచార్యులకు

అమ్మ భాషకు

To

Parents, teachers & Telugu language

Acknowledgments

Ph.D. has been a life-changing experience. The journey has been incredible, and the memories from New Zealand stay with me forever. First and foremost I am grateful to my supervisors Shakila, Hari, Greg, and Andrew. Shakila, I would not be what I am today without you. Thanks for trusting me and providing me an opportunity to be a Ph.D. student. I am forever grateful for the support and opportunities you gave me during this journey. You have taught me the importance of work-life balance and inspired me to become a responsible researcher and person. I cannot thank you enough. Hari, you have been an excellent teacher and a nice person. I am highly indebted for your support and patience during my learning phase of the engineering topics. Thanks for all those late night meetings and weekend corrections. You inspired me to work harder and smile no matter what the situation is. Greg, I am grateful for your support and ideas during my Ph.D. My journey wouldn't be same without your inputs and suggestions. Andrew, thanks for the corrections and suggestions during my Ph.D. I would like to thank Dr Ravi Jain and Dr Richard Douglas from Department of surgery at University of Auckland, for sharing CT images of healthy normal human subjects used in this study.

My gratitude also extends to our technical and administration team at the school of pharmacy. Kevin, you are a genius and a problem solver. Pummy, your dedication, and experience are impeccable, and you are an inspiration. Blake, Jo, and Kathy, you guys, are sunshine to the school of pharmacy, you inspired me with your smile and time management skills. Denise, thanks for helping me out in all the administration process. My sincere thanks to Tim for his support with always troubling computers and software. Special thanks to Dot for feeding me on most of my late night experiment days.

I would like to thank my friends in Dunedin who made this journey memorable. Sid, you are the best happened to me in this journey. You aren't just a friend, you and Mona are family. Younus, you are a menace, you are like a bad habit that I cannot get rid of. I enjoyed and hated the conversations and time we spent together. Jackmil, you are my partner in crime thanks for the support and time. You are a strong woman and an inspiration. Words aren't

enough to express my love towards you three guys. The memories we made together will rule my heart forever, Thanks.

I am thankful for the fantastic friend gang I have had here. Basanth & Raji, Vijayanna & Swarna, Shivaji, Manoj the traveling and potlucks we have had together will be the memories that I cherish all my life. Siri, my little angel, I can never forget you, and I am proud that the first name you spoke was mine. Special thanks to my 17 grange buddies, Dinesh & Anurag who weren't just flatmates but brothers in crisis. Raadha and Priya you are amazing women, I am grateful for the conversations we have had. Thanks to Anita for helping me with animal experiments. Thanks to Helen lee, Katrin voos, Sumith, Sameek, Sujitha, Deji, Harry, Rinky, Swethakka, Lohitha, Vijaybhaskar, Hanisah, Kristina, Hendrick, Nirmal and Martin for being part of my journey, it has been amazing to know you guys. Special thanks to Richard for his valuable suggestions, help and corrections in my thesis. To Robert, who taught me the essence of traveling and joy of being honest, and Arnold, an engineering soul trapped in pharmacist who helped me with his incredible 3D printing skills, you both deserve credit in the success of my experiments, Thank you guys. I would like to thank my teachers and friends back in India, especially, Kranthi and Deepika who always encouraged me to pursue my career and been there in my low times. I am thankful to university of Otago doctoral scholarship for supporting my studies in Dunedin, also I am thankful to School of pharmacy for six months scholarship and fourth year tuition fees.

I am highly indebted to my parents, who sacrificed everything for me. Amma, I love you, and this thesis is dedicated to you. I haven't seen a beautiful and stronger woman, you are my strength. Daddy, I miss you. I wish you are here to see my success. It is the patience, smile, and love for the Telugu language I inherited from you made me who I am. Thanks for providing me the opportunities to pursue my goals. I hope I made you both happy. Last but not least, the Almighty, force beyond imagination. Thank you.

Publications arising from this thesis

Refereed journal articles

Sasi B. Yarragudi, Robert Richter, Helen Lee, Greg F. Walker, Andrew N. Clarkson, Haribalan Kumar, Shakila B. Rizwan, Formulation of olfactory-targeted microparticles with tamarind seed polysaccharide to improve nose-to-brain transport of drug, *Carbohydrate Polymers*, 2017, 163: 216–226.

Sasi B Yarragudi, Richard F Prentice, and Shakila B Rizwan, *In-vivo* brain uptake of phenytoin following the intranasal administration of the size tailored microparticles, *Journal of controlled release.* (Manuscript in preparation)

Sasi B Yarragudi, and Shakila B Rizwan, Solubility enhancement of phenytoin by formulating into mucoadhesive microparticles, *International journal of pharmaceutics.* (Manuscript in preparation)

Sasi B Yarragudi, and Shakila B Rizwan, A review on role of microparticles in nose-to-brain delivery of drugs so far, *European journal of pharmaceutics and biopharmaceutics.* (Manuscript in preparation)

Sasi B Yarragudi, Haribalan Kumar, and Shakila B Rizwan, Predicting fate of mucoadhesive microparticles after deposition in the human nasal cavities: An *in-silico* model development, *Journal of aerosol medicine and pulmonary drug delivery.* (Manuscript in preparation)

Conference contributions

Oral presentation

Biodegradable, mucoadhesive microparticles of tamarind seed polysaccharide for enhanced olfactory deposition" at 'The globalization of pharmaceutics education network' (GPEN), 2016, Kansas, USA.

Poster presentations

"Direct nose-to-brain-delivery of drugs: size matters" at BHRC annual meeting, Dunedin, NZ.

"Olfactory targeted mucoadhesive microparticles for enhanced brain uptake of phenytoin" at APSA-ASCEPT meeting, 2017, Brisbane, Australia.

"Modelling of inhalation and bi-directional airflow effects on olfactory targeted micro-particle deposition in human nasal cavities" at BMES annual meeting, 2017, Phoenix, USA.

"Battle to bypass the blood-brain–barrier: mucoadhesive microparticles with enhanced olfactory deposition for nose-to-brain drug delivery" at AAPS annual meeting, 2016, Denver, USA.

"Formulation of olfactory-targeted microparticles of tamarind seed polysaccharide for nose-to-brain delivery of drug" at DDA meeting, 2016, Sydney, Australia.

"Scanning electron microscopy as a tool to understand the effects of process variables on microparticle formulation" at Microscopy New Zealand, 2015, Dunedin, NZ.

"Olfactory-targeted microparticles: a novel approach to bypass the blood-brain barrier" at AWCBR, 2015, Queenstown, NZ.

Awards

Winner of the best poster presentation at APSA-ASCEPT meeting (2017), Brisbane, Australia.

Silver medal in three-minute thesis competition (2016), University of Otago, Dunedin, NZ.

Awardee of Dean's Fund (2014), School of Pharmacy, University of Otago, Dundein, NZ.

Table of contents

List of figures

List of tables

List of abbreviations

AED	anti-epileptic drug
ANOVA	analysis of variance
AUC	area under curve
BBB	blood-brain barrier
CFPD	computational fluid and particle dynamics
CNS	central nervous system
CSF	cerebrospinal fluid
CT	computerized tomography
Da	dalton
DE	deposition efficiency
DL	drug loading
DOE	design of experiments
DSC	differential scanning calorimetry
DTP	direct transport percentage
EE	encapsulation efficiency
FDA	food and drug administration
FESEM	field emission scanning electron microscopy
FITC	fluorescein isothiocyanate
GRAS	generally recognized as safe
HPLC	high performance liquid chromatography
HPMC	hydroxypropyl methyl cellulose
ICH	international conference on harmonization
IM	intramuscular
IV	intravenous

J_{ss}	steady state flux
kDa	kilo dalton
LOD	limit of detection
LOQ	limit of quantification
MW	molecular weight
NBF	neutral buffered formalin
NP	nanoparticle
PBS	phosphate buffer
PEG	polyethylene glycol
PG	propylene glycol
phenytoin	phenytoin sodium
PLA	poly (lactic acid)
PLGA	poly(lactide-co-glycolide)
SEM	scanning electron microscopy
TBME	tert-butyl methyl ether
TKP	tamarind kernel powder
TSP	tamarind seed polysaccharide
XRPD	x-ray powder diffraction

Chapter 1

Introduction

1 Introduction

1.1 Rationale

The blood-brain barrier (BBB) serves as a barrier to restrict the entry of potential drugs from the systemic circulation into the central nervous system (CNS). The discovery of direct drug transport pathways found in the olfactory region of the nasal cavity that can bypass the BBB has provided a non-invasive approach to treat complex CNS disorders. However, exploiting these direct nose-to-brain pathways and translating them into effective treatment strategies for CNS disorders has been challenging. In last 20 years, the vast amount of literature published on direct nose-to-brain delivery has led to approximately 165 clinical trials, and from this, only five drugs have been approved by the US food and drug administration (FDA) for use in the clinic (**Appendix A**). One of the main reasons behind the failure to translate the preclinical research to the clinical stage has been the subtherapeutic concentration of drugs reaching the brain following intranasal administration.

There has been intensive research and development in innovative drug formulation technologies to address the inadequate therapeutic drug levels in the brain. Much of this research has resulted in the evolution of polymer-based, mucoadhesive, microparticle and nanocarrier drug delivery systems. Each of these systems has been shown to deliver higher drug concentrations to the brain by sustained release and improved residence time of drugs in the nasal cavity. However, to obtain sufficient therapeutic drug levels in the brain, it is necessary for a delivery system to target the site of nose-to-brain transport (the olfactory region) in the nasal cavity.

The complex geometry and narrow airways (**Figure 1.1**) of the nasal cavity makes targeted delivery of drug formulations to the olfactory mucosa a significant challenge[1]. Drugs administered as solutions often cannot be retained by the upper, neuron-containing, region of the nasal passage and are instead cleared by nasal mucociliary clearance or swallowed or lost to dripping[2]. Drugs formulated as mucoadhesive microparticles might have advantages in targeting and retaining the drugs in the olfactory region due to their size

and mucoadhesive properties. Therefore, the overall focus and aim of this thesis is the development of an olfactory-targeted mucoadhesive microparticulate delivery system, with the idea that this will offer an improved nose-to-brain delivery of drugs.

1.2 Nose-to-brain drug delivery

Considering the potential advantages microparticles can offer in nose-to-brain drug delivery, it may be hard to understand their poor representation in the pharmaceutical market. Nasal formulations intended for nose-to-brain delivery are predominantly available as liquid formulations, for example, Fentanyl citrate nasal spray (Lazanda®), Ketorolac tromethamine (Sprix®), Zolmitriptan (Zomig®) and Sumatriptan nasal spray (Imitrex®) to treat pain and/or a migraine[3]. To facilitate the discussion on the application of microparticles to overcome the challenges of nose-to-brain delivery, some fundamental concepts will be introduced first.

1.2.1 Anatomical and physiological aspects

The physiology of the human nose is intended for warming and moistening of inspired air and olfaction. The nasal cavity is divided into two separate passages by the nasal septum. Each nasal passage ends anteriorly in a nostril and posteriorly at the nasopharynx. The nasal passage contains comma-shaped, bony turbinates protruding into the cavity allowing only a narrow pathway for the inspired air[4,5] as shown in **Figure 1.1 B**. These geometrically complex airways act as a filter for inhaled particles at the same time and help in conditioning the inhaled air so that air reaching the lungs is warm and moist[6].

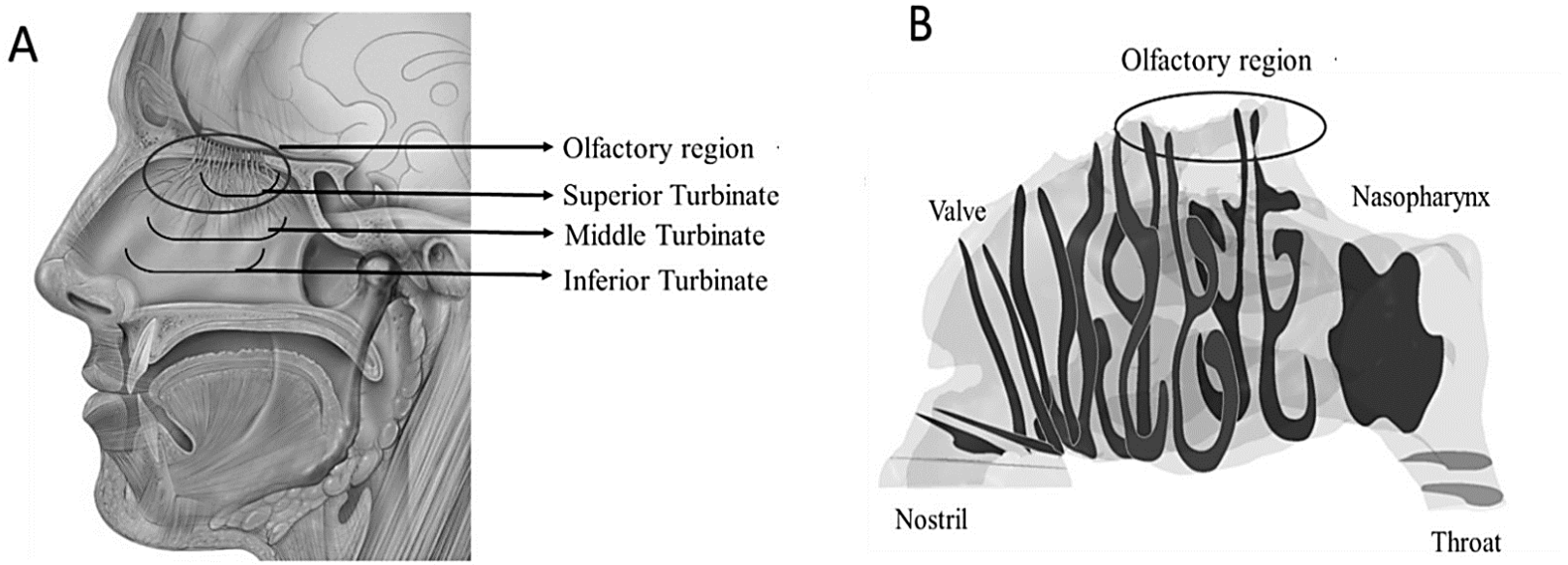

Figure 1.1 A. A sagittal view of human nasal cavity displaying the location of the olfactory region and turbinates. B. Transparent view of human nasal cavity revealing the narrow airways for the inhaled air. Figure modified with permissions from Fasiolo et al.[7]

The nose is a direct entry point to our internal body. To help protect our body from the inhaled material, the nasal cavity is lined with mucosa along the nasal passage. Depending on where we look in the nasal cavity, three different mucosae are present, which serve different purposes. Near to the nostrils, stratified squamous epithelium is found and gradually transforms into a pseudostratified columnar epithelium (respiratory mucosa). The respiratory mucosa is innervated by the trigeminal nerve and covers most of the nasal cavity. The pseudostratified columnar epithelium in the olfactory region (olfactory mucosa) contains olfactory neurons responsible for the detection of smell[4,8]. The intranasal administration of drugs provides access to the olfactory neurons in the olfactory mucosa and trigeminal nerves in the respiratory mucosa.

The olfactory region is situated in the upper deep posterior region of the nasal passage as shown in **Figure 1.1**. The surface area of the olfactory region is small and covers approximately 10 cm^2 of the total nasal cavity[8]. Due to curved, narrow airways and the location of the olfactory region situated deep in the nasal cavity, it is difficult for inhaled particles to reach this region. The CNS opens into the nasal cavity through the olfactory neurons in the olfactory mucosa as shown in **Figure 1.2 A**. The olfactory neurons contain several non-motile cilia with odorant receptors that extend into the overlying mucus. The unmyelinated axons from olfactory neurons extend through the basal lamina and converge with axons from other olfactory neurons to form nerve bundles called *fila olfactoria*. Olfactory ensheathing cells and fibroblasts enclose fila olfactoria to form a perineural like a sheath. These ensheathed fila olfactoria form the olfactory nerve and travel through the cribriform plate into the mitral, periglomerular, and tufted cells in glomeruli of the olfactory bulb. Axons from the olfactory bulb project to a number of rostral areas in the brain including piriform cortex, amygdala, and entorhinal cortex, forming a channel from the olfactory region within the nasal cavity to the brain[9–11]. The olfactory mucosa also contains supporting cells, microvillar cells secured in the basement membrane. The submucosa under the basement membrane is highly vascularized, it contains Bowman glands and a variety of other cells including progenitor cells such as globose and horizontal basal cells[12–15].

In addition to the olfactory neurons, the CNS opens into the nasal cavity through trigeminal nerve endings in the respiratory mucosa. The free trigeminal nerve endings are extended into the respiratory region as shown in **Figure 1.2 B**. The axons of the trigeminal nerve project into the brainstem through the pons and enter into the forebrain through the cribriform plate[16]. Therefore the trigeminal nerve connects to both the caudal and rostral parts of the brain, consequently, forming a channel from the respiratory mucosa in the nasal cavity to the CNS[16,17]. The respiratory region contains ciliated and non-ciliated columnar cells, mucus-producing goblet cells with tight junctions. The movements of cilia in the respiratory region are responsible for the mucociliary clearance in the nasal cavity. The submucosa is highly vascularized[9].

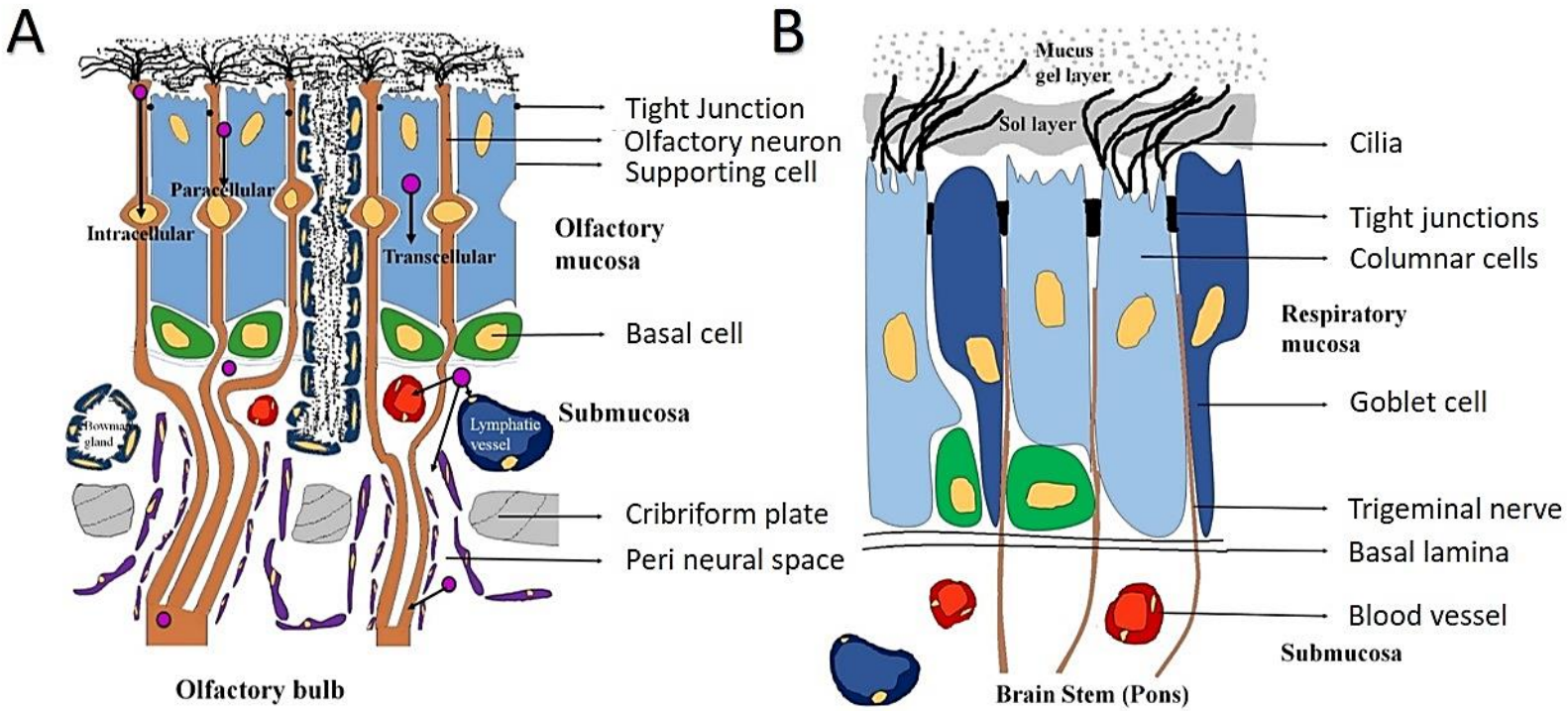

Figure 1.2 A. Drug transport pathways and organization of the olfactory mucosa B. Trigeminal innervation and the organization of the respiratory mucosa. Figure modified with permissions from Thorne et al[9]

The trigeminal nerve and olfactory bulb were reported to be connected by the sensory endings of the trigeminal ganglion cells located in the nasal epithelium. The sensory endings were found to send collaterals directly into the olfactory bulb[18]. Along with trigeminal and olfactory nerves, the nasal passage also contains the nervus terminalus and the vomeronasal nerve. However, their role in drug transport to CNS has not been established[9].

1.2.2 Pathways and mechanisms for nose-to-brain transport of drugs

The exact pathways and mechanisms of direct drug transport into the brain following intranasal administration have not been fully characterized. However, specific pathways through olfactory, trigeminal nerves, and nasal mucosa have been proposed by experimental evidence obtained from published literature.

1.2.2.1 Neuronal pathways

Intracellular uptake of molecules into olfactory neurons and trigeminal nerves leads to axonal transport of the molecules that have been taken up into the brain. Large protein molecules such as horseradish peroxidase and wheat germ agglutinin-horseradish peroxidase have been previously reported to be taken up into olfactory neurons via pinocytosis and adsorptive endocytosis[19]. Wheat germ agglutinin-horseradish peroxidase is also reported to be endocytosed into the trigeminal nerves and transported to the brain stem by axonal transport[20,21]. Endocytosis of proteins, viruses, and bacteria by the olfactory and trigeminal nerves and their subsequent intracellular transport to the brain has been previously reported[22–26].

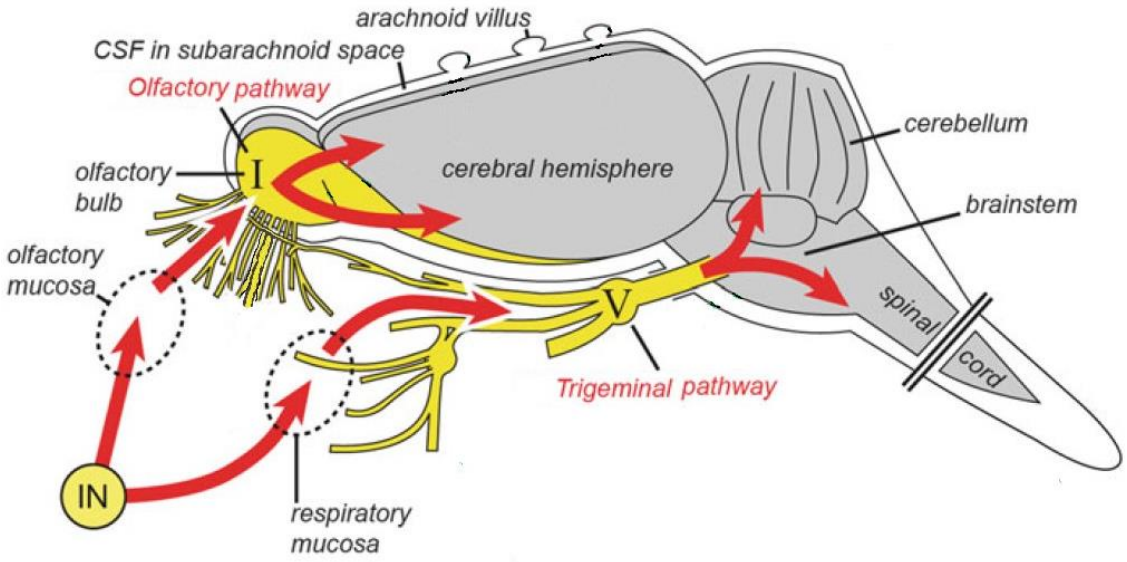

Figure 1.3 Nose-to-brain direct pathways from olfactory and respiratory mucosa via olfactory nerve and trigeminal nerves. Figure adapted with permissions from Thorne et al[9]

The olfactory and trigeminal pathways potentially occur in the olfactory and respiratory regions of the nasal cavity. The olfactory neuronal transport target the rostral area of the brain and the trigeminal transport target both the rostral and caudal areas of the brain[27] as shown in **Figure 1.3**. Specifically, olfactory pathway contributes a vital role in direct nose-to-brain transport, hence targeting drugs to olfactory mucosa/region can aid nose-to-brain delivery[28].

1.2.2.2 Mucosal pathways

In addition to neuronal pathways, drugs can also cross nasal mucosa in the olfactory region to access the perineural space and thereby reach the brain via extracellular pathways (**Figure 1.2 B**). Transcytosis and paracellular diffusion across the nasal mucosa have been proposed as the extracellular pathways[29–32].

Receptor-mediated endocytosis is involved in the transcytosis pathway. Size of the molecule determines the mechanism of endocytosis, for example, molecules less than 200 nm follow clathrin-dependent endocytosis and molecules with 100-200 nm are

transported by caveolae-mediated endocytosis[33,34]. Cell type, surface charge, and concentration are the other important factors that influence the mechanism of endocytosis in transcytosis[35].

Paracellular transport involves opening of tight junctions between the cells in the olfactory and respiratory mucosa. The continuous turnover of basal cells as a part of the life cycle of biological membranes causes loosening and the opening of tight junctions and promotes paracellular transport[36,37]. Drugs crossing nasal mucosa via extracellular pathways may enter the systemic circulation or lymphatic system or can access the perineural spaces. Perineural distribution of potassium ferrocyanide, ammonium citrate and fluorescein-Dextran (3 kDa) in olfactory nerve bundles and their subsequent entry into the brain following the intranasal administration was reported[38,39].

Distribution of drugs to the different areas of the brain from the site of entry occurs by bulk flow within perivascular spaces of cerebral blood vessels[27,40]. Wider distribution of fluorescent liposomes in the brain parenchyma with increased blood pressure after intrastriatal injection demonstrated the role of bulk flow in the distribution of the drug molecules[41]. Cerebrospinal fluid (CSF) flow also plays a role in distributing the drug into widespread areas of the brain. Rapid distribution following tracer application into the CSF was reported[42,43]. Drugs reaching the perineural spaces are distributed to the CSF, and the flow of CSF can further transport the drug to more distant sites of the brain. However, the barrier between the perineural space and CSF is shown to be selective[27], and the physiological aspects of this distribution are yet to be completely understood.

1.2.3 Mucociliary clearance of drugs in nasal passages

The nasal passage is covered with mucus produced by submucosal glands and goblet cells in the respiratory mucosa. The mucus in nasal passages are composed of >90 % water, 0.5-5 % mucus glycoproteins, 1-2 % salts and 0.5-1 % free proteins and is slightly acidic with a pH of 5.5-6.5[6,44]. The overlying mucus is between 10-20 µm in depth and consists of two distinct layers, a lower less viscous (sol) and an upper high viscous (gel) layer[45,46]. Mucus glycoproteins are responsible for the gel-like structure of the mucus; they are formed

from a protein core surrounded by carbohydrate chains[47]. Many columnar cells in the respiratory mucosa possess hair-like protrusions called cilia that are around 5-10 µm long and width from 0.1-0.3 µm extending into the sol layer. The number of cilia per cell is approximately 300[48,49]. The synchronized movement of cilia in the sol layer causes the transport of the upper gel layer towards the nasopharynx where it is swallowed[50,51]. The human nasal cilia beat with a frequency of 10 Hz, and the average velocity of the mucus transport is around 8 mm/min and can vary between 3-25 mm/min[52,53]. Airborne particles entering the nasal passages are entrapped in the mucus layer and get transported along with it to the nasopharynx and are eventually cleared from the nasal cavity. The combined action of the cilia and mucus layers is called mucociliary clearance.

Mucociliary clearance is an essential physiological defense mechanism to protect the nasal cavity against noxious inhaled particles. On the other hand, it is responsible for the rapid clearance of the drugs and formulations after intranasal administration. The average nasal clearance half-life for drugs is about 12-15 mm/min. Mucociliary clearance decreases the contact time with the nasal mucosa, ultimately leading to decreased drug delivery to the brain[54,48].

1.2.4 Current status of nose-to-brain drug delivery

Conventionally, the nasal route has been used for the systemic delivery of drugs, but now it has become an increasingly popular method to bypass the BBB and blood circulation to deliver neurotherapeutics to the brain/CNS[24,55]. The published literature now includes substantial evidence for the advantages of nose-to-brain delivery over the other routes of administration. Most importantly, a wide range of therapeutic agents including proteins, plasmids, gene vectors and stem cells have been shown to reach the brain following intranasal administration via olfactory and trigeminal pathways[32,56–58].

1.2.4.1 Small molecular drugs

Over the decades, intranasal administration of small molecular drugs has been explored for enhancing systemic bioavailability. However, small molecules have relatively easy access to the paracellular pathways compared with macromolecules due to their size and can directly reach the brain via perineural spaces of olfactory and trigeminal nerves[59]. All of the currently marketed drugs for nose-to-brain delivery are small molecules and are used for the management of migraine and/or pain as shown in **Table 1**[60].

Table 1. Currently marketed drugs intended for nose-to-brain drug delivery.

Drug	Molecular weight (Da)	Indication
ketorolac tromethamine (Sprix®)	255	Moderate to severe pain
Zolmitriptan (Zomig®)	287	Migraine
sumatriptan nasal spray (Imitrex®)	295	Migraine
fentanyl citrate (Lazanda®)	336	Cancer pain
sumatriptan powder (Onzetra Xsail®)	295	Migraine

Several other small molecules have been reported to be promising in animal CNS disease models. For example, deferoxamine (MW = 561 Da) exhibits neuroprotection in Parkinson's disease[61], Alzheimer's disease[62] and ischemic stroke[63]. Losartan (MW = 423 Da) decreased inflammation and amyloid β plaques in Alzheimer's disease[64]. Other small molecules such as Remoxipride (MW = 371 Da), which are glycine receptor antagonists (MW = 369-611 Da) were shown to have high brain concentrations following intranasal administration[65,66]. Small molecules such as Sumatriptan (with permeation enhancer)[67,68], lidocaine[69], Zolmitriptan[70], glutathione[71], are at the clinical trial stage and are expected pipeline drugs.

1.2.4.2 Macromolecular drugs

Macromolecular drugs like proteins and peptides have limited permeation across biological membranes and are prone to metabolic degradation in the blood and tissues. Intranasal administration provides a promising route for such molecules. Melanocortin, arginine-vasopressin and insulin were among the first peptides determined in CSF following intranasal administration, all these peptides were detected within 30 min in CSF of human volunteers[72]. Detectable brain concentrations of growth factors[73–76], neuropeptides[77,78], neurotrophic factors[79,80,81] and other macromolecules[82] have been reported following intranasal administration in animal models. Higher CNS levels of intranasal insulin compared to subcutaneous injection were reported in mice. Highest levels were found in the trigeminal nerve and olfactory bulbs suggesting the transport to the CNS through neuronal pathways[83]. Clinical trials in Alzheimer's disease patients showed intranasal insulin improved memory and preserved general cognition[84,85] and had rapid action[86]. Efficacy of intranasal insulin in treating obesity in humans and mice has been reported[87]. Intranasal administration of sleep-related peptide orexin-A has shown improved brain metabolic activity in rhesus monkeys and stabilized REM sleep in humans[88–90].

An increasing number of protein drugs for the treatment of CNS diseases and recent discoveries of essential brain functions have stimulated this area of research. Analysis of the literature shows a doubling of the number of publications on nose-to-brain peptide delivery reporting *in-vivo* studies in the last seven years (55 versus 120 reports [pubmed database]).

Currently, many intranasal peptide and protein drugs are undergoing clinical trials and represent the most promising group of pipeline drugs to treat complex CNS diseases. Insulin is under clinical trials for the treatment of Schizophrenia (Phase I)[91], Alzheimer's disease (Phase I and Phase III)[92–95], obesity (Phase II)[96] and major depressive disorder (Phase II)[97]. Oxytocin is being examined for the treatment of schizophrenia (Phase I)[98–100], autism spectrum disorder (Phase I and Phase III)[101–103] and post-traumatic stress disorder (Phase I, II and Phase III)[104–106]. The efficacy of Arginine-vasopressin in the treatment of cognitive and behavior disorders (Phase I)[107,108], Neuropeptide Y in the treatment of obesity (Phase I)[96], insulin-like growth factor-I in the treatment of obesity and diabetes (Phase I)[109]

are also being investigated. Other potential peptide drugs such as melanocortin, cholecystokinin, NAP neuropeptide and hexarelin are also under clinical trials for nose-to-brain delivery[82]. Although intranasal administration is a potential route for peptide drugs, many reported studies use simple drug solutions and the drugs are failing to reach the brain/CNS in therapeutic concentrations. Nevertheless, the trend is now changing to the carrier-based formulation of peptide drugs to improve the efficacy of such drugs.

1.2.4.3 Cell-based therapies

Targeting of stem cells to the brain via intranasal endocytic neuronal pathways represents the most recent group of intranasal drugs. Mesenchymal cells administered intranasally in mice have shown therapeutic potential in Parkinson's disease and several models of stroke[110–113]. Fluorescently labeled mesenchymal stem cells has been transported to the brain via neuronal pathways 1 h after intranasal delivery in mice[64]. The therapeutic potential of intranasal neural stem/progenitor cells has been recently identified; with intranasal delivery providing direct transport of neural stem/progenitor cells to intracerebral gliomas in six h[58]. Finally, intranasal administration of genetically engineered T-cells has been successful in suppressing the inflammation in mouse models of multiple sclerosis[114]. The potential of such cell-based therapies has only recently been identified and is yet to be fully explored.

1.2.5 Challenges and strategies for efficient nose-to-brain drug delivery

As discussed in the previous sections, nose-to-brain administration has excellent potential for delivery of novel therapies for brain diseases. However, achieving sufficient therapeutic drug levels in the brain is still a challenge. In addition to the fast mucociliary clearance and loss of drug to the systemic and lymphatic circulation, targeting drugs to neuronal rich regions like the olfactory region in the nasal cavity and facilitating the transport across mucosal membrane are the significant challenges for attaining therapeutic drug levels in the brain via nose-to-brain delivery. Hydrophilic small molecular drugs have a bioavailability of 10 %, and peptide and protein drugs have a bioavailability of about 1 % following intranasal administration[115]. Therefore, to achieve efficient absorption and

therapeutic efficacy, approaches to target the olfactory region in the nasal cavity, increase the contact time of drugs with nasal mucosa, and facilitate the transport of drugs across the mucosa are required.

Many strategies such as, use of permeation enhancers to facilitate the drug transport across the nasal mucosa, use of vasoactive agents (bradykinin) to chemically disturb the BBB[116,117], use of microbubble facilitated focus ultrasound waves to open the BBB[118], implanting polymeric wafers[119,120] & programmable microchips[121], and chemically modifying the drug to increase the permeability and water solubility[122,123], to improve the drug delivery to the brain are being researched upon. As stated in **Section 1.1,** much of the research has led to development of nano/microparticle delivery systems. The objective of this thesis is not, however, to review the many exciting aspects of these strategies as many of them are either invasive[28] or associated with side effects[124]. Nevertheless, a brief comparison of the strengths and weaknesses of non-particle approaches to nano/microparticle delivery systems to increase drug transport across the nasal mucosa is presented here.

Administration of drug solutions with permeation enhancers to open the tight junctions in the epithelial cells and enhance the transport across the nasal mucosa has been reported[115]. However, the permeation enhancers used in the studies such as surfactants, phospholipids, bile acids, etc. are reported to produce toxic effects on the nasal mucosa including decreased ciliary beat frequency, tissue damage, and irreversible ciliotoxicity[125]. On the contrary, nanoparticles can provide enhanced transport across the nasal mucosa without the use of an enhancer due to their size. Nanoparticles less than 20 nm can pass the epithelial tight junctions, while larger nanoparticles can cross the mucosal barrier transcellularly, by entering into the cell by the process of endocytosis or phagocytosis[115].

Another strategy, is to chemically modify the drug to improve solubility and permeability which has been reported for nose-to-brain delivery[126]. Producing prodrugs by chemical modification of a drug to change its lipophilicity to increase permeability and water solubility has been reported[127–129]. However, prodrug synthesis requires challenging skills involving reduction of polar groups or linking a lipophilic moiety to the drugs and in general is not fruitful[28]. On the contrast, nano/microparticles can be produced by single step processes like

spray-drying and have given promising results in pre-clinical studies to improve the brain delivery of a variety of drugs such as brimocriptine[130], rokitamycin[131], rivastigimin[132], venlafaxine[133,134], tizanidine[135].

Formulating drugs as nano/microparticle delivery systems, in general, has numerous advantages for nose-to-brain delivery of drugs. These delivery systems can control the release of drugs at a predetermined rate and desired drug levels can be maintained[136]. Nano\microparticles can prevent drug loss and degradation and improve drug solubility[137] in the nasal cavity[28]. Nano/microparticle delivery systems can reduce the mucociliary clearance, increase residency time, enhance the permeation of drug through nasal mucosa, and promote large molecular[138]/phytochemical[139] drug delivery across the nasal cavity[28]. Due to their advantages, these delivery systems are being extensively researched and are delivering promising results in pre-clinical studies[28,140].

Although nano\microparticle delivery systems have several advantages, a few limitations of these delivery systems exist in nose-to-brain delivery. Mucosal damage, nasal irritation, the effect of patients position during administration on brain uptake, low entrapment efficiency and storage related problems need to be addressed by further investigations to exploit the full potential of these delivery systems[28,115].

1.3 Delivery systems for nose-to-brain drug delivery

Drug delivery systems intended for nose-to-brain delivery are designed to transport the drug to the brain, attain a desired therapeutic level and maintain the drug concentration within the therapeutic window. Furthermore, the desired characteristics of an ideal drug delivery system are to reduce the dose of the drug, have minimal side effects and ease of administration. Based on the size, drug delivery systems for nose-to-brain can be divided into nanocarriers and microparticles. Nanocarriers and microparticles have a potential to achieve the desired therapeutic level of drug in the brain by controlling and/or sustaining the release rate of encapsulated drug and nasal residence time[141].

Nanocarrier drug delivery system include polymeric nanoparticles, nanoemulsions, micelles, liposomes and nanogels. These delivery systems provide a versatile platform with great potential in overcoming the challenges associated with nose-to-brain delivery. However, the focus of this thesis is microparticles and not the nanocarriers; nonetheless, a short introduction on the impact of the nanocarrier drug delivery system will be provided to facilitate further discussions.

1.3.1 Nanocarrier drug delivery systems

The rapid increase in the number of publications reporting nanocarrier systems for nose-to-brain delivery demonstrates the enormous potential of such delivery systems in recent times[142]. Polymeric nanoparticles (NPs) have been successful in the delivery of small molecules to the brain. For example, chitosan NPs were shown to increase the concentration of two small MW drugs rasagiline and bromocriptine significantly in the brain after intranasal administration compared to intravenous (IV) adminsitation[143,130]. Use of other polymers such as polyethylene glycol (PEG), PLGA, poly (lactic acid) (PLA) and gelatin to formulate the NPs has also been reported[28,82,144].

Polymeric NPs have also been reported for their success in encapsulating and delivering macromolecular protein and peptide drugs such as a thyrotropin-releasing hormone, which when encapsulated in PLA NPs successfully suppressed seizures in epileptic rats[145,146]. Other peptides and protein drugs such as leucine–encephalin[147], osteopontin[148], and vasoactive intestinal peptide[149] were reported to show higher brain concentrations with polymeric NPs[82]. Similarly, the ability of other nanocarrier systems such as nanoemulsions[150], micelles[151,152], liposomes[153,154], and nanogels[155] to enhance nose-to-brain delivery has been reported. Polymers employed in the preparation of nanoparticles and their size are found to be two critical factors that influence drug targeting to the brain after intranasal administration[156].

As implied above, nanocarrier systems could be an excellent platform for drug delivery to treat CNS diseases. However, still, no nanocarrier delivery system has reached the clinical

development phase. More conclusive studies, pharmacokinetic and pharmacodynamic data are required to unveil the full potential of such nanocarrier delivery systems.

1.3.2 Microparticle drug delivery system

As the name suggests, microparticles are tiny particles with size ranging from 1 to 1000 µm. In the drug delivery field, microparticles are vesicles made up of a polymer into which drugs can be loaded for protection, transport, targeting, and release. Due to their size, microparticles provide an increased surface area which is advantageous for drug delivery. The high surface area of microparticles can aid faster drug diffusion into the external environment. Also, by changing the characteristics of the polymer drug release from the microparticles can be tuned to meet therapeutic requirements[157].

Microparticles can encapsulate many types of drugs including small molecules and peptide and protein drugs. They are biocompatible and can provide sustained release of the drug over long periods of time. For example, the commercially available PLGA microparticle products Nutropin Depot® and Lupron Depot® can sustain the release of macromolecular drugs somatropin and leuprolide respectively, for over a month replacing the need for daily injections[158].

Microparticle formulations can be administered as suspensions or solids (powders), and are administered via oral[159], pulmonary[160] and parenteral (intramuscular (IM)[161], Subcutaneous[159]) routes. However, for nasal administration, solid particles can have good patient compliance, deposition in the nasal cavity and provide high dose without the necessity of a liquid vehicle[162,163]. Also, solid particles can enhance drug diffusion and absorption across the mucosa[164]. Many studies have reported *in-vivo* the advantage of administering drugs formulated as solid microparticles for intranasal administration, a few examples are reported in **Table 2**.

Table 2 In-vivo studies reporting the advantages of intranasal solid microparticles.

Drug	Animal model	Particle size (µm)	Polymer	Observation	Ref
Carvedilol	Rabbits	20 to 50	Chitosan	Microparticles enhanced bioavailability (72.29 %) after intranasal administration vs IV (67.87 %)	165
Repaglinide	Rats	1 to 5	Pectin Gellan gum Dextran sulfate	Intranasal administration of microparticles produced a prolonged hypoglycemic effect (2-6 h) vs. IV (1 h)	166
Gentamicin	Rabbits	19 to 46	Chitosan Hyaluronic acid	Intranasal microparticles enhanced the bioavailability of gentamicin by two-fold compared to the intranasal solution	167
Insulin	Rats	1 to 80	Thiolated chitosan	Intranasal microparticles produced 4-5 fold higher bioavailability compared to the control (mannitol), and the hypoglycemic effect lasted for more than 2 h vs. IV (15 min)	168
Verapamil	Rabbits	21 to 53	Chitosan	Intranasal microparticles produced higher bioavailability (58.6 %) than the intranasal solution (47.8 %)	169

1.3.3 Nanocarrier versus microparticles for nose-to-brain drug delivery

It is an important question to reflect on as to why microparticles but not nanocarriers are used in this thesis for nose-to-brain delivery, especially, after having presented the success of nanocarrier delivery systems. In this case, it's a matter of size perhaps literally, as will be discussed in **Section 1.3.5.1.1.** This section compares microparticles and nanocarrier delivery systems for nose-to-brain delivery of drugs.

Estimation of drug transported through direct neuronal pathways as a function of the formulation can represent the efficiency of the formulation. Nose-to-brain *direct transport percentage* (%DTP) is the amount of the drug dose that is estimated to reach the brain via direct routes. The %DTP offers an interpretation of drug fraction transported through the neuronal pathways and has been used to represent the efficiency of formulations and delivery systems[142,170,171]. The values of %DTP can range from -∞ to 100, values between -∞ to 0 indicate the drug transport is only through IV route, higher than 0 indicates drug transport through direct nose-to-brain neuronal pathways[171].

The %DTP is calculated using Equation 1

$$\%\mathrm{DTP} = \frac{\mathrm{AUC}_{\mathrm{brainintranasal}} - \mathrm{F}}{\mathrm{AUC}_{\mathrm{brainintranasal}}} * 100 \qquad |Equation\ 1$$

Where AUC is the area under the curve representing drug concentration variation over time in the brain and F is given by Equation 2 below:

$$\mathrm{F} = \frac{\mathrm{AUC}_{\mathrm{brainIV}}}{\mathrm{AUC}_{\mathrm{bloodIV}}} * \mathrm{AUC}_{\mathrm{blood\ intranasal}} \qquad |Equation\ 2$$

With an aim to compare the efficiencies of nanoparticle systems and microparticles, %DTP values from the reported literature of the respective delivery systems were calculated. Initially, scientific publications reporting quantitative data on drugs by nose-to-brain delivery of microparticle delivery systems were identified. Specific keywords were used to search the PubMed database, and the search resulted in 303 articles. Further screening was performed based on their title, abstract and subsequently full text to identify publications reporting *in-vivo* brain or CSF concentrations of the drug. A total of 45 publications were identified reporting the formulation of drugs into microparticles for nose-to-brain delivery, out of which only seven had quantitative brain/CSF drug concentrations. The %DTP values were calculated using the Equation 1 and Equation 2. The %DTP values for nanocarrier systems were obtained from a recently published scientific article by Pires C.P and Santos O.A.[142].

Microparticles containing hydrophobic drugs had relatively low %DTP values as their efficiency to reach the brain after IV administration was higher which decreased the "F" value and thereby the %DTP[131,172]. Higher %DTP were observed for microparticles loaded with hydrophilic drugs indicating their difficulty in permeating the BBB[173–175].

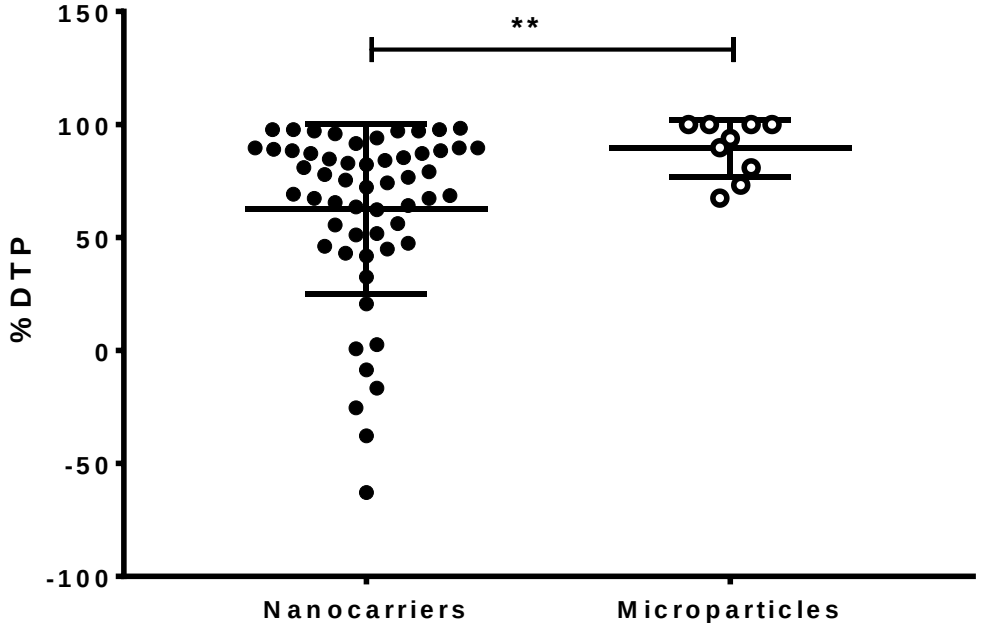

Figure 1.4 Comparison of drug delivery efficacy via neuronal pathways of nanocarriers and microparticles. Lines represent the arithmetic mean for the individual delivery systems. Statistical analysis was done by applying Mann-Whitney U test, **P *=0.0037. Data for individual studies are reported in* ***Appendix B***.

The %DTP of the microparticles calculated from the identified publications and the %DTP of nanocarriers obtained are grouped according to the delivery system and presented in **Figure 1.4**. The statistical analysis resulted in a significant difference between the delivery systems. The %DTP of microparticles was significantly higher than the nanocarrier systems (P = 0.0037) indicating direct transport of drugs to the brain from the microparticle delivery system is higher than the nanocarrier delivery system. Although the %DTP is a good indicator of nose-to-brain drug delivery, this comparison alone may not provide conclusive evidence to confirm microparticles are more advantageous than nanocarriers. This is due to the fact that this study compares only one parameter, but critical factors such as

pharmacological efficacy, toxicity, and therapeutic outcomes must be compared to prove the advantage of microparticles over nanocarrier systems.

This comparison of %DTP values also has its own limitations. For instance, the difference in number of reports being compared between microparticles and nanocarriers (7 vs. 56) and the presence of outliers with very low %DTP values for certain nanocarrier systems[176–178] are two major downsides of the study. In addition, formulation and delivery factors such as differences among administered formulations (suspension, powder etc.), difference among the size of nanoparticles (100 nm-1 µm), variety of drug delivery methods and apparatus employed for drug delivery to animals and site of drug delivery (tip of the nostril/inside the nasal cavity) might have affected the %DTP values. Also, a variety of animal models employed, variable factors among the animals that can affect the drug kinetics such as age, body weight, breed, etc. might have contributed to the %DTP values. In summary, consideration of more factors and data from extensive studies are required to identify the ideal delivery system for nose-to-brain delivery of drugs. However, in this thesis, a microparticle delivery system is studied due to its size as will be discussed in **Section 1.3.5.1.1**

Interestingly, this study revealed a very low number of preclinical studies utilizing the microparticle delivery system for the nose-to-brain delivery of drugs, identifying shortage in critical pharmacokinetic and pharmacodynamic data required for clinical translation of microparticle systems. Though many scientific articles reported formulation and in-vitro characterization of drugs for nose-to-brain delivery of drugs, only a few reported results from in-vivo studies. This study could not identify the exact reason for this poor translation of microparticles compared to nanocarriers in nose-to-brain drug delivery. However, based on the literature, a few assumptions can be made. The advantageous characteristics of nanocarriers in nose-to-brain delivery such as the high surface area to volume, ability to bypass biological barriers (enhanced drug absorption) due to size and ability to enter cells by pinocytosis (enhances drug absorption)[179] might have contributed to their comparatively better translation into preclinical studies.

Despite the advantages of microparticle delivery systems as stated in previous sections, the absence of well-distributed data indicates that this is an area where more research is needed to fully characterize and exploit its potential in nose-to-brain delivery of drugs.

1.3.4 Microparticles for nose-to-brain delivery

As stated in the previous section, few scientific articles are identified in the published literature reporting microparticles intended for nose-to-brain delivery. Among these, 51 % reported only *in-vitro* data and only one article reported the extent of pharmacological effects[180], which represents the significant lack of critical data in this field.

Among the studies reporting *in-vivo* pharmacokinetic data, only seven studies quantified the drug concentrations in the brain/CSF. However, these studies reported encouraging results, for example, the antiviral prodrug zidovudine formulated into chitosan and stearic acid microparticles had a six-fold increase in CSF uptake through the neuronal pathways[181,174]. Faster CSF uptake of the antimigraine drug zolmitriptan and reduction in the peripheral drug levels have been reported from chitosan and hydroxypropyl methylcellulose (HPMC) microparticles[182]. Enhanced CSF uptake of deferoxamine mesylate from methyl-β-cyclodextrin microparticles has been reported as the first formulative approach to increase the nose-to-brain transport of deferoxamine mesylate[175]. Also, increased CSF uptake of N^6-cyclopentyladenosine, rokitamycin from mannitol-lecithin, chitosan and chitosan glutamate microparticles has been reported[131,173]. Most of these studies report that the presence of mucoadhesive polymers like chitosan and HPMC increase the residence time of the formulations in the nasal cavity and lead to enhanced brain/CSF drug transport. The mechanism of mucoadhesion and its effect on the bioavailability of drugs will be described in detail in **Section 1.3.5.2**.

Mucoadhesive microparticles have been studied in three *in-vivo* studies in humans[183] and rabbits[184,185]. These studies reported increased residence time of microparticle formulations in the nasal cavity due to the mucoadhesive nature of the polymers used. One study reported increased accumulation of the analgesic tramadol in the brain by HPMC microparticles. The mucoadhesive strength of HPMC microparticles retained tramadol in the rabbit nasal cavity

for extended time periods consequently increasing tramadol accumulation in the brain as observed by gamma scintigraphy studies[186]. Sustained drug release resulting in constant plasma profiles of the antiemetic drug ondansetron was also reported with chitosan, PLA, and PLGA microparticles[187,188]. Rapid absorption of the drug and high bioavailability was reported with carbamazepine loaded chitosan glutamate microparticles[189] and lorazepam[95]. Only one study reported no difference in the bioavailability of drug between starch microparticles and control in a rabbit model[190]. Moreover, one study has emphasized the importance of drugs reaching the olfactory region for obtaining therapeutically sufficient brain concentration. Sun *et al.* reported that methotrexate loaded chitosan microparticles enhanced brain tissue uptake of the drug. However, the levels were still not therapeutic due to low amounts of drug reaching the olfactory region[172]. A substantial fraction of the reported *in-vivo* studies focused on the formulation of small MW drugs (232-827 Da), with insulin[191,192] and α-corobotoxin[180] being the only two macromolecules reported.

Drug and characteristics of polymers have been shown to have a significant impact on nose-to-brain delivery of microparticles. Although particle size and method of manufacturing can impact drug loading and delivery efficiencies, their effect has not been discussed extensively in the reported literature. Spray-drying is the most popular method of microparticle preparation, and chitosan is the most used polymer for the formulation of microparticles intended for nose-to-brain delivery. Almost half of the reported studies used chitosan and/or chitosan derivatives and this can be attributed to mucoadhesive nature. A summary of formulation properties is given in **Table 3.**

Table 3: Summary of microparticle formulation properties from the literature intended for the nose-to-brain delivery.

Drug	Polymer	Particle Size (µm)	Method	Ref
Levodopa	Gelatin	16	water-in-oil (w/o) emulsification solvent extraction	193
Promethazine	Ethyl Cellulose and chitosan	2-3	Spray-drying	194
Metoclopramide	Methylpyrrolidinone chitosan	5-8	Spray-drying	195
Lorazepam	HPMC and Carbomer	2-3	Spray-drying	196
Rokitamycin	Chitosan	2-5	Spray-drying	197
Zolmitriptan	Chitosan	1-4	Spray-drying	198
Rokitamycin	Chitosan derivatives	1-6	Spray-drying	199
Sumatriptan	HPMC	20-35	Spray-drying	200
Ondansetron	Gellan gum	9-11	Spray-drying	201
β-cyclodextrin or hydroxypropyl-βcyclodextrin	Chitosan and Alginate	1-3	Spray-drying	202
Methotrexate	Chitosan	2-5	Spray-drying	203
Ketorolac	Carbopol, Polycarbophil, and Chitosan	14-46	w/o emulsification solvent extraction	204
Phosphorothioate antisense oligonucleotides	Polycarbophil-cysteine reduced glutathione	30	w/o emulsification solvent evaporation	205
Granisetron	Sodium CMC	7-15	Freeze drying	206
Lysozyme as model protein	HPMC and water-soluble chitosan	7-12	Freeze drying	207
No drug	Chitosan	28-46	emulsification-crosslinking	208
Lorazepam	Chitosan microparticles in pluronic gel	NA	emulsion crosslinking	137
Metoclopramide	Sodium alginate and Chitosan	3-10	Spray-drying	209
Ropinirole hydrochloride	PLGA/DPPC/ trimethyl chitosan	2	Spray-drying	210
Metoclopramide	Gellan gum	9-10	Spray-drying	211
Tacrine hydrochloride	Chitosan/pectin	1-19	Spray-drying	212

1.3.5 Application of microparticles to overcome the challenges of nose-to-brain delivery

As described in **Section 1.2.5**, targeting drug to the olfactory region, overcoming mucociliary clearance and facilitating drug transport across the mucosal membrane remain significant challenges for nose-to-brain drug delivery. In this thesis, formulating drugs into microparticles is investigated as a strategy to address these delivery challenges.

1.3.5.1 Targeting the olfactory region

1.3.5.1.1 Effect of particle size

It has been reported that the size of a particle defines its aerodynamics and deposition in the geometrically complex human nasal cavity. Particles larger than 20 µm show preferential deposition in the anterior part of the nasal cavity due to high inertial impaction, while the majority of particles less than 5 µm escape the nasal cavity, following the air streamlines, and deposit in the lungs as shown by low deposition fraction in the nasal cavity[213].

With the advancements in computational power, recently, *in-silico* modeling has become a critical tool in characterizing various factors affecting deposition of particles in the nasal cavity. Recent modeling data from two reports suggested that particles around 10 µm in size show high deposition in the olfactory region when administered intranasally at normal inhalation rates of around 20 L/min[214,215]. **Figure 1.5** shows the deposition of particles in the olfactory region as a function of size in one human subject from a modeling study**.** These studies have triggered the idea of controlling particle size to target specific sites in the nasal cavity. Therefore, this thesis postulates that formulating microparticles which are around 10 µm in size and loaded with drugs can potentially target the drug to the olfactory mucosa after inhalation.

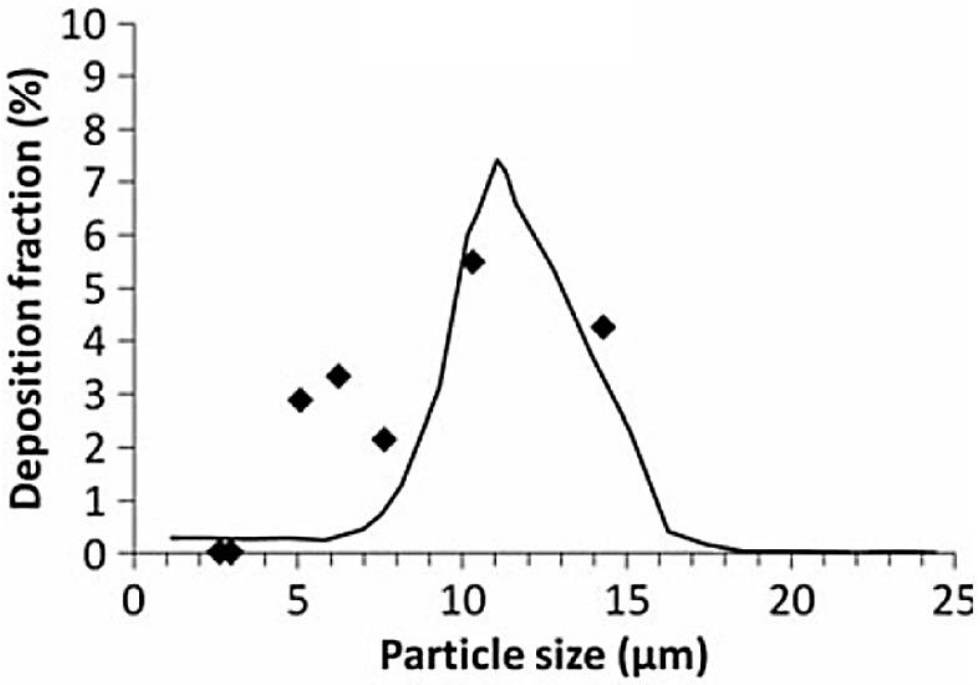

Figure 1.5 Deposition of microparticles in the olfactory region as a function of particle size. The particles with size around 10 µm are shown to enhance the particle deposition in the olfactory region. Solid line represents computational simulation modeling studies and diamond symbols represent the study in a 3D human nasal cast. Figure adapted with permissions from Schroeter et al[214]

1.3.5.1.2 Targeting devices

Use of novel and effective drug delivery device technologies for targeting drug formulations to the olfactory region are reported in the literature. Among such systems, pressurized olfactory delivery technology (POD, Impel neuropharma), controlled particle dispersion technology (Kurve) and breath powered bi-directional technology (OPTINOSE) have shown potential for nose-to-brain drug delivery[216–218].

Figure 1.6 Delivery devices to target drug to the olfactory region in the human nasal cavity. Images are taken from http://impelnp.com/, http://www.kurvetech.com/devices.asp, and https://www.optinose.com

Preclinical studies in rats with POD technology show high deposition of drug in the olfactory region. Studies have reported pain relief by morphine[216], the prolonged anti-depressant effect by a peptide drug[219] and a 13.6 fold increase of nelfinavir brain-to-blood ratio[220]. Kurve technology has shown increased olfactory deposition in five human subjects[217] and promising results in Phase II clinical trials with insulin for the treatment of Alzheimer's disease and Amnestic Mild Cognitive Impairment[84]. Finally, due to the ability to deposit high amounts of drug in the olfactory region, OPTINOSE technology was shown to decrease the dose of oxytocin required to produce the cognitive responses in trials with healthy humans[218]. Recently, the FDA approved sumatriptan powder (Onzetra Xsail®), which utilizes this technology for delivery of sumatriptan into the anterior part of the nasal cavity, for treatment of migraine.

All these delivery devices target the olfactory region by dispersing the drug into micron size particles. Because particle deposition in the nasal cavity is known to be affected by particle size, it would be interesting to explore if the combination of controlled particle size with a targeting device can further enhance the olfactory targeting of the drugs.

1.3.5.2 Mucoadhesion

In addition to targeting the olfactory region, it is helpful if the drug formulation is retained in the olfactory region long enough for absorption to take place. Many polymers used in microparticle formulations can adhere to mucus, therefore, prolonging the residence time of drug in the olfactory region.

Two critical steps in the mucoadhesion process are the initial *contact stage* and then the *consolidation stage*. For solid microparticles, the contact stage is most likely achieved by water movement from the mucosa into the formulation and hydration of polymer chains[221]. Consequently, the nasal mucosa de-hydrates causing the mucus viscosity to increase. In the second stage, consolidation between polymer and mucin happens by interpenetration of polymer chains into mucin to form entanglements, the formation of van der Waals, hydrogen and/or electrostatic bonds such as disulfide bonds[222]. These chemical bonds and molecular entanglements create regions where mucus viscosity is further increased leading to high resistance to the ciliary movement, resulting in decreased mucociliary clearance[223–225] and providing a prolonged contact time for the drug in the nasal cavity. As solid microparticles can de-hydrate the nasal mucosa leading to an increase in mucous viscosity, they would lower the usual requirements for the formation of secondary chemical bonds compared to the pre-hydrated suspensions[54,226]. Hence, solid microparticles engineered with mucoadhesive polymers are exceptionally well suited for nose-to-brain drug delivery.

1.3.5.3 Facilitating transport across the mucosa

Solid microparticles are shown to increase the paracellular absorption of drugs loaded into them by opening tight junctions. For example, dry starch microparticles containing insulin temporarily opened tight junctions between epithelial cells and enhanced the absorption of insulin compared to pre-hydrated microparticles[227–229]. The opening of tight junctions by dry starch microparticles was thought to be caused by the initial dehydration of the mucosa which was not required in the case of the pre-hydrated microparticles[230]. Also, polymers such as chitosan and polycarbophil used for microparticle preparation were shown to open the tight junctions reversibly by inducing changes in transmembrane proteins and

chelation of calcium ions respectively and may have potential to increase extracellular transport along neurological pathways into the brain[231,232]. Finally, solid microparticles can increase absorption due to the higher concentration gradient of the drugs released to external environments as a virtue of their high surface area. Considering the advantages of solid particles in nasal delivery and the ability of 10 µm sized particles to target the olfactory region, formulating drugs as solid microparticles for nose-to-brain delivery can be beneficial.

1.4 Size tailored, mucoadhesive microparticles for nose-to-brain drug delivery

The introduction highlighted the potential of microparticles as one promising strategy to provide enhanced drug delivery to the brain, with the potential to treat complex CNS disorders. The versatility of microparticle delivery systems, i.e., the ability to tailor their size and choice of mucoadhesive polymers, therefore poses the research question of whether such microparticles can be optimized to deliver drugs efficiently to the brain through the intranasal route.

1.5 Hypothesis

This thesis will explore the following hypotheses

1. That a combined formulative approach of packaging drugs into solid mucoadhesive microparticles and size tailoring them to 10 µm can enhance deposition and retention in the olfactory region and increase brain uptake of the encapsulated drug.
2. That inter-subject variability does not affect the preferential deposition of 10 µm particles in the human nasal cavity.
3. Combination of controlled particle size with an intranasal device can further enhance the olfactory targeting of microparticles.

1.5.1 Aims

In order to investigate the above hypotheses, the aims of this thesis are

1. To develop mucoadhesive 10 µm sized microparticles and characterize their olfactory deposition *in-vitro*.
2. To develop a model drug-loaded mucoadhesive 10 µm sized microparticles and investigate its brain uptake of the drug in a rat model.
3. To evaluate inter-subject variability in olfactory deposition of particles *in-silico*.
4. To identify the effect of particle size on olfactory deposition in the human nasal cavity combined with a delivery device *in-silico*.

Chapter 2

General Materials & Methods

2 General Materials and Methods

2.1 Materials

Mucin (bovine submaxillary glands Type I-S, M3895), cellulose acetate membrane (MW cut off 50,000 Da), propylene glycol (PG), three-way stopcock, phenytoin sodium, 5-(4-methyl phenyl)-5-phenyl-hydantoin, 5-(4-hydroxyphenyl)-5-phenyl-hydantoin and fluorescein isothiocyanate (FITC)-labelled dextrans with MW of 3-5, 10, 20 and 40 kDa were purchased from Sigma-Aldrich (New Zealand). Tamarind gum powder was purchased from Xi'an Jiatian Biotechnology (China). HPLC-grade acetonitrile, ethanol, and methanol were purchased from Merck KGaA (Darmstadt, Germany). A manual anemometer (N1287) was purchased from Digitech (Australia). Water was ion-exchanged distilled and passed through a Milli-Q water purification system (Millipore, Bedford, MA, USA) and was used for all the studies, sample preparation and HPLC analysis.

2.2 Isolation of Tamarind seed polysaccharide

A naturally mucoadhesive Tamarind seed polysaccharide (TSP) was used as the polymer in this thesis. A detailed discussion on the purpose and advantages of TSP as a polymer in drug delivery is provided in **Chapter 3, Section 3.1.1**. TSP was isolated from tamarind gum powder using methods described by Rao *et al*[233]. Tamarind gum powder (20 g) was dispersed in 200 mL of Milli-Q water to obtain a slurry, which was then mixed with a further 800 mL of Milli-Q water and boiled for 20 min under constant stirring (800 rpm). This dispersion was kept overnight to allow proteins and fibers to sediment and subsequently centrifuged at 5000 rpm for 20 min. The supernatant was separated and mixed with twice the volume of absolute ethanol under constant stirring. Since the TSP is soluble in water and insoluble in most of the organic solvents[234,235] this led to a precipitate of TSP, which was washed with Milli-Q water and dried at 60 °C for 12 h to obtain a film of TSP. The film was crushed using a mortar and pestle to a fine powder and stored in a desiccator at room temperature until required.

2.3 *In-vitro* and *ex-vivo* studies

2.3.1 Preparation of TSP-FITC-Dextran microparticles

All microparticle formulations in the study were prepared by spray-drying methods based on literature[203,236,237] using a laboratory-scale mini Spray Dryer (Büchi B-290, Büchi Labortechnik AG, Switzerland).

The effect of the spray-drying process variables; atomizing air flow, aspiration air flow rate, FITC-Dextran concentration and inlet temperature (independent factors) on the mode size of microparticles (response) was determined using a 4 factor (independent factors), 3 level (low (-1), base (0) and high (+1)) Box-Behnken design[238,239] (**Table 4**). A total of 29 experiments were designed and analyzed using Design-Expert® Software Version 9 (Stat-Ease Inc., MN, USA). The effect of independent variables upon the responses was modeled using a linear mathematical model. One-way Analysis of Variance (ANOVA) was applied to determine the significance of the model ($P < 0.05$). The optimized spray-drying conditions for producing 10 µm sized particles was determined by applying the numerical optimization methodology using Design-Expert® Software. The microparticles were prepared, and their size was measured to validate the optimized spray-drying conditions obtained from Design Expert®.

Table 4. Actual and coded values of independent factors used in the Box-Behnken design.

Independent factor	Coded level		
	Low (-1)	Base (0)	High (+1)
Atomizing air flow (L/h)	246	494	742
Aspiration air flow rate (%)	50	60	70
Amount of FITC-Dextran (%w/w)	0.10	0.25	0.50
Inlet temperature (°C)	100	110	120

Feed solutions for spray-drying were prepared as follows. TSP was dissolved in water under constant stirring at 60 °C for 2 h and cooled to room temperature. To this solution different amounts of FITC-Dextrans were added and mixed for a further 1 h. The total

amount of solids in the feed solution was 2 % w/w. The solutions were spray-dried with a standard nozzle cap with an orifice diameter of 0.7 mm and feed solution flow rate of 2 mL/min. The dried microparticles were collected and stored in a desiccator until required.

2.3.2 Preparation of TSP-phenytoin sodium microparticles

The feed solutions were obtained as follows; Phenytoin sodium was dissolved in the water and different amounts of propylene glycol (PG) mixture by sonicating for 8 min. Different amounts of this solution was added to the TSP solution (prepared as described above) under stirring at room temperature and allowed to mix for 1 h. The total amount of solids in the feed solution was 1.5 % w/w. These solutions were spray-dried, and the microparticles were collected and stored in a desiccator at room temperature until further analysis.

2.3.3 Particle size analysis

The sizes of all microparticle formulations were determined using laser diffraction (Horiba™ Particle LA-950V2, HORIBA, Ltd. Kyoto, Japan). A 5 mg sample of microparticles was dispersed in ethanol (5 mL), from which a 200 µL aliquot was diluted with 10 mL of ethanol prior to analysis. Mode size (most common size in the particle population) of each formulation was determined and reported. All measurements were performed at 25 °C and results are presented as the mean ± standard deviation (SD) of at least three independent experiments.

2.3.4 Morphology of microparticles

Microparticles were adhered to double-sided adhesive carbon tape on metallic stubs, coated with a thin layer of platinum-palladium (Emtech K575X, Quorum Technologies Ltd, UK) and viewed under a scanning electron microscope (Zeiss Sigma VP variable-pressure scanning electron microscope (Carl Zeiss Inc, Oberkocken, Germany) fitted with a HKL

INCA Premium Synergy Integrated ED/EBSD system (Oxford Instruments, Oxfordshire, UK)) with an electron beam at an acceleration voltage of 1 kV.

2.3.5 Determination of FITC-Dextran content

To determine the amount of FITC-Dextran incorporated into TSP-microparticles, 5 mg of microparticles were dissolved in 10 mL of Milli-Q water under constant stirring at 60°C for 2 h. A 1 mL sample was collected and filtered through a membrane filter (0.45 μm). The filtrates were diluted to 10 mL with Milli-Q water, and the amount of FITC-Dextran quantified by spectrofluorometry (Hitachi F-7000 Spectrophotometer, High-Technologies Corporation, Japan) using an excitation and emission wavelength of 498 nm and 520 nm, respectively. Samples were quantified against calibration curves constructed of standard FITC-Dextran solutions in the range of 0.5−100 μg ($n = 3$, $r^2 > 0.999$). The standards were made by processing the blank TSP-microparticles, which do not contain FITC-Dextran, and spiking with a known amount of FITC-Dextran to normalize the interference of TSP on fluorescence. FITC-Dextrans were reported to be stable at the temperatures employed in the study[240,241].

2.3.6 Determination of phenytoin sodium content

For the TSP-Phenytoin sodium (referred to as phenytoin from this point onwards) microparticles, 25 mg of microparticles were dissolved in 3 mL of Milli-Q water under constant stirring at 60 °C for 2 h. The solution was allowed to cool down to room temperature while stirring, then sufficient amount of methanol was added to make it a 70 % methanol solution with a total volume of 10 mL. A 3 mL aliquot of the solution was collected and centrifuged at 13000 rpm for 5 min. A 1 mL sample was collected and filtered through a 0.22 μm syringe filter, and the amount of phenytoin was quantified by high-performance liquid chromatography (HPLC), according to a validated method (Younus et al, unpublished data) developed from modification of published method[242] as described below.

A reverse phase HPLC-system (Agilent 1200 series) with UV detector coupled with EZChrom Elite software, version 3.2.0 (Agilent Technologies, California, USA), a C-18 (150 X 4.6 mm) column (5 µm particle size) with a C-18 guard cartridge (5 X 4.6 mm) (Phenomenex, California, USA) kept at 25 ºC were used for the analysis. An isocratic method was used to quantify the phenytoin. The mobile phase consisted of 70 % (v/v) methanol and 25 % (v/v) HPLC-grade water with a flow rate of 1 mL/min. A mixture of methanol and water (90:10, v/v) was used to perform needle wash. The injection volume was 20 µL and detection was at 254 nm resulting in a retention time of 4.3 min for phenytoin. The standard curve range was 5 to 100 µg/ml ($r^2 = 1$) and a new standard curve was prepared each day.

2.3.7 Drug loading and Encapsulation efficiency

Drug loading (DL) and encapsulation efficiency (EE) of microparticles were calculated by using Equation 3 and 4, respectively.

$$\mathrm{DL}\ (\%) = \frac{\mathrm{D\ (actual)}}{\mathrm{Weight\ of\ TSP-microparticles}} \times 100 \qquad |Equation\ 3$$

$$\mathrm{EE}\ (\%) = \frac{\mathrm{D\ (actual)}}{\mathrm{D\ (theoretical)}} \times 100 \qquad |Equaiton\ 4$$

Where D (actual) and D (theoretical) are the actual and theoretical amounts of FITC-Dextran/phenytoin in microparticles, respectively.

2.3.8 Fluorescence microscopy

Fluorescence microscopy was used to confirm the incorporation of the FITC-Dextran in the microparticle formulations. Samples were prepared by dispersing microparticles (5 mg) in ethanol (2 mL). A sample of dispersed microparticles was added on to a glass slide and examined under an inverted microscope with a fluorescence illuminator with a U-FBN filter block (bandpass = 470-495, barrier filter = 510 (IF) and dichroic mirror = 505) (Olympus IX53, Olympus Corporation, Japan). Images were captured with cellSens™ software.

2.3.9 *In-vitro* mucoadhesion under breathing conditions

Mucoadhesion of TSP-microparticles under simulated breathing conditions was determined *in-vitro* using a method modified from Gavini *et al*[209]. The amount of FITC-Dextran/phenytoin containing TSP-microparticles adhering to a piece of filter paper saturated with mucin after application of an air load was quantified. The mucin from bovine submaxillary glands was compared to human airway mucus in the literature due to its similarities and is used in this thesis[243,244]. The schematic representation of the experimental set-up is shown in **Figure 2.1.** A 3D printed mucoadhesion apparatus as shown in **Figure** 2.2 was designed to emulate the human nasal cavity.

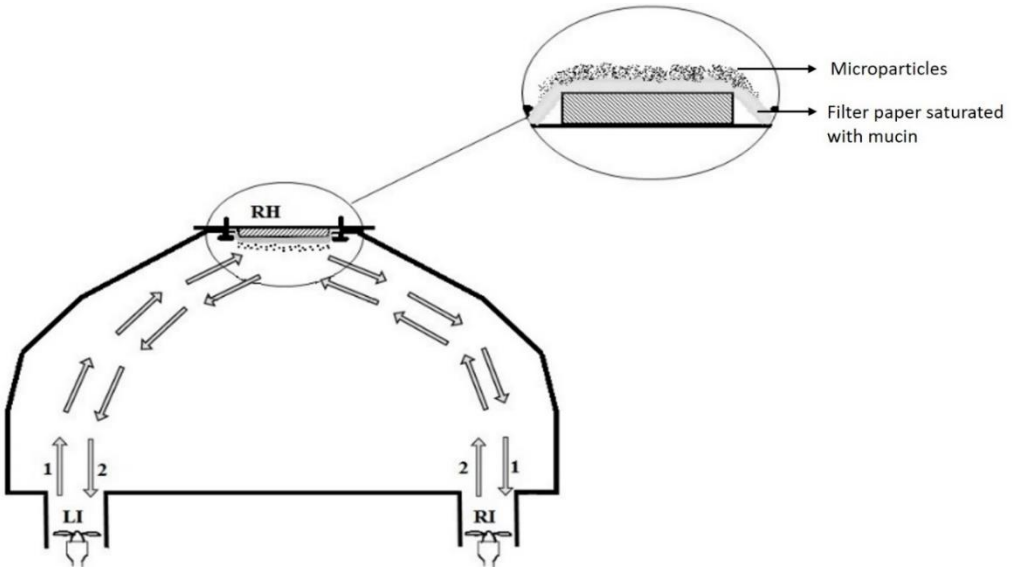

Figure 2.1 Schematic representation of the apparatus used for the evaluation of in-vitro mucoadhesion. LI, Left inlet; RI, Right inlet, RH, removable hatch. Arrows indicate the direction of airflow. Filter paper saturated with mucin and adhered microparticles is shown in the inset.

The filter paper (d = 1.5 cm, A = 1.78 cm^2) was soaked in a solution of mucin (2 % w/v in distilled water) for 20 min to saturate the filter paper with mucin solution. A 5 mg sample of microparticles containing FITC-Dextran or phenytoin was placed on the filter paper saturated with mucin as shown in the inset of **Figure 2.1**. The filter paper was fixed to the roof of the apparatus with the help of a removable hatch, and the hatch was sealed as shown in **Figure 2.1.** A stream of air with a flux of 6.37 ms^{-1} was applied over the microparticles

for 5 sec from the left inlet and then repeated from the right inlet. Since the microparticles contained FITC-Dextran or phenytoin, the amount of microparticles that remained adhered to the filter paper after the applied air load was quantified by spectrofluorometry or HPLC respectively. Mucoadhesion of microparticles was expressed as the percentage of FITC-Dextran or phenytoin remaining on the filter paper after exposure to the air stream as a function of the FITC-Dextran or phenytoin deposited. Mucoadhesion of unformulated FITC-Dextran or phenytoin powders was used as a control.

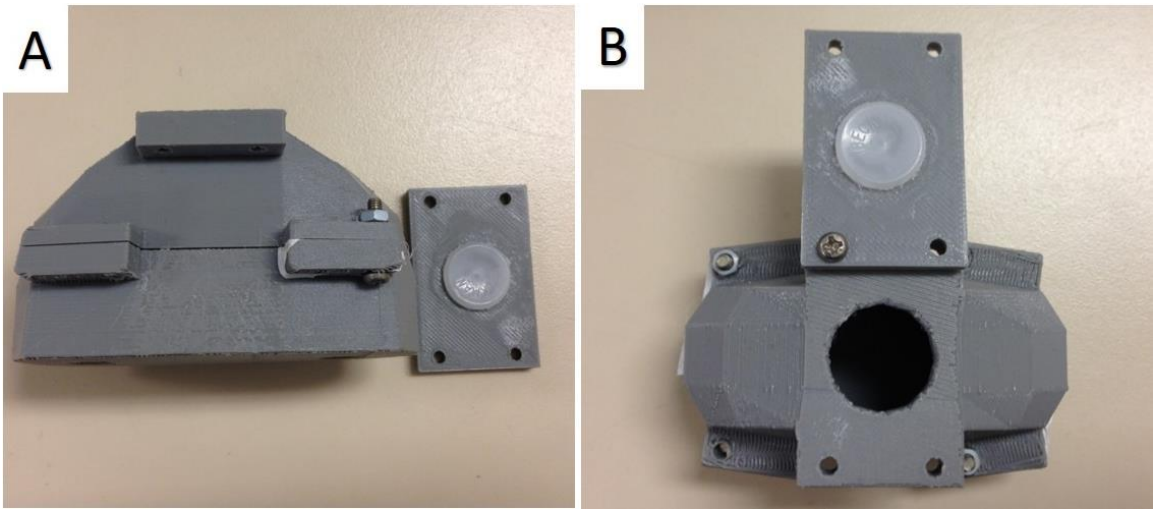

Figure 2.2 Cast used for in-vitro mucoadhesion experiments (A) side view showing the cast and removable hatch (B) top view showing the setup of the removable hatch.

2.3.10 *Ex-vivo* mucoadhesion

2.3.10.1 Isolation of porcine nasal mucosa

Nasal mucosa was isolated from porcine snouts obtained from a local slaughterhouse. The snouts were opened by a longitudinal incision to expose the septum and conchae, and the nasal mucosa was carefully removed from the underlying bone, transferred to ice-cold PBS (pH 7.4) and immediately frozen in liquid nitrogen and stored at – 81 ºC until use.

2.3.10.2 Mucoadhesion strength

Measurement of tensile strength to assess mucoadhesion of powders has been previously reported by Kockish *et al.*[245] and was used in the current study to measure mucoadhesion of TSP-microparticles. Briefly, microparticles were attached to the moving cylindrical probe (Stable Microsystems, United Kingdom) of a texture analyzer (TA HD plus) with a mucoadhesion rig using industrial grade adhesive epoxy. A section of the porcine nasal mucosa was fixed onto the stationary mucoadhesion rig. TSP-microparticles or unformulated FITC-Dextran/phenytoin powders (control) were brought into contact with the mucosa for 30 sec and retracted at a constant speed of 1 cm/min. The force required to disrupt the adhesive bond between microparticles and the mucosa was measured and is reported as mucoadhesion strength in the present study. The tensile strength apparatus and mucoadhesion rig used for these studies are shown in **Appendix C.**

2.3.11 Cryogenic field emission scanning electron microscopy (cryo-FESEM).

The interaction of TSP-microparticles with mucin over time was investigated using cryo-FESEM. Approximately 30 µL of mucin solution (2 % w/v) was spread on the flat surface of metallic stubs to create an artificial mucus layer. TSP-microparticles were distributed over the mucus layers of the stubs, which were subsequently plunge-frozen in liquid nitrogen at time 0, 15, 30 and 60 min, respectively. The samples were then transferred into the cryo-chamber (Gatan, Alto 2500, UK) of the microscope (JEOL, JSM-6700F, Japan), which was maintained at −140 °C. The samples were sublimed at −90 °C for 2–5 min to remove any surface frost and viewed at −140 °C at an acceleration voltage of 3 kV and a working distance of 6 mm.

2.3.12 Crystallinity of microparticles

Crystallinity of the TSP, FITC-Dextrans, and phenytoin and microparticle formulations was examined using an X-ray diffractometer (PANalytical X'Pert PRO MPD PW3040/60 XRD) equipped with a rapid real-time multistrip X'Celerator detector. Approximately

5-10 mg of the powder sample was loaded into the sample holder as a thin layer, and x-ray powder diffraction (XRPD) patterns were recorded over an angular range of 5−35° (2θ) using Cu Kα radiation operating at a generator power of 40 kV and current of 40 mA at ambient room conditions. The results were analyzed using the PANalytical High Score software.

2.3.13 Thermal behavior of microparticles

Thermal behavior of TSP, FITC-Dextrans, phenytoin and microparticle formulations was analyzed using Differential scanning calorimetry (DSC) Q1000 (TA Instruments, USA) calibrated with indium (calibration standard, purity > 99.9 %). Approximately 5 mg of the powder sample was weighed into a standard aluminum pan (TA instruments) and press sealed with the standard aluminum lid. All the samples were scanned at 1°C/min from 30°C to 500°C under a nitrogen gas flow (50 mL/min). An empty aluminum pan with lid served as a control.

2.3.14 Moisture content of microparticles

Moisture content of the microparticles was determined by the oven dry method[246,247]. 250 mg of freshly prepared TSP-microparticles containing phenytoin were accurately weighed (W_1). Microparticles were placed in a glass petri dish and kept in a hot air oven at 110 ºC overnight to dry. The dried microparticles were accurately weighed (W_2). The % moisture content was determined by the following formula.

$$\text{Moisture content (\%)} = \frac{W_1 - W_2}{W_1} \times 100 \qquad |Equation\ 5$$

2.3.15 Stability studies

Stability studies for the TSP-microparticles containing phenytoin were performed according to the international conference on harmonization (ICH) guidelines for stability testing of finished pharmaceutical products[248].

Freshly spray-dried TSP-microparticles containing phenytoin were placed in two glass Petri dishes (2 g each) and stored at 25 °C ± 2 °C and 60 % ± 5 % relative humidity (RH) and 40 °C ± 2 °C and 75 % ± 5 % RH in two separate incubators for six months. A sample of 250 mg of TSP-microparticles was collected on day 1, 30, 60, 90 and 180 from each incubator. The samples were analyzed for the encapsulation efficiency, moisture content, and crystallinity as described before. The storage conditions were monitored during the six month storage time, and any deviations were recorded. Phenytoin has been reported to be stable at temperatures employed in stability studies[249].

2.3.16 *In-vitro* release studies

Release studies were conducted across a cellulose acetate membrane (MW cut-off 50 kDa) using vertical static diffusion cells with an effective diffusion area of 1.77 cm^2 and a receptor chamber volume of 7 mL. The cellulose acetate membrane was saturated with phosphate buffer (PBS) (pH7.4) for 30 min and then mounted onto a vertical diffusion cell. Microparticles containing the equivalent of 1 mg of FITC-Dextran or phenytoin were spread over the membrane as evenly as possible. The receptor compartment was filled with PBS (pH 7.4), and the temperature was maintained at 37 °C using a thermostatic water bath. The PBS in the receptor compartment was magnetically stirred to maintain sample homogeneity. A 1 mL sample was withdrawn at predetermined time intervals from the receptor compartment and replaced with the same quantity of fresh PBS. The samples were diluted with 9 mL of PBS, and the content of FITC-Dextran or phenytoin were quantified using methods described in **Sections 2.3.5** and **2.3.6** and plotted against time. The samples obtained from blank TSP microparticles were used as a reference to normalize any interference caused by TSP. The first 60 min of the drug release data were analyzed against zero-order, first-order, and Higuchi and Korsymeyers-Peppas models to determine the mechanism of drug release from TSP-microparticles.

2.3.17 *Ex-vivo* permeation studies

The porcine nasal mucosa was isolated as described in **Section 2.3.10.1**, and permeability to FITC-Dextrans or phenytoin were quantified using methods described in **Sections 2.3.5** and **2.3.6**. The cumulative amount of FITC-Dextrans or phenytoin permeating through the nasal mucosa per cm^2 over time was plotted, and the steady-state flux (J_{ss}) was calculated from the slope of the linear portion of the curve using Equation 6 as described below.

$$J_{ss} = \frac{\frac{dQ}{dt}}{A} \qquad |Equation\ 6$$

Where J_{ss} is the steady-state flux, dQ/dt is the slope of the cumulative amount of FITC-Dextran permeated versus time curve, and A is the diffusional cross-sectional area of the mucosa. Unless otherwise stated, data presented are the mean ± SD of at least three independent experiments.

2.3.18 Histopathological examination of toxicity to the nasal mucosa

All porcine nasal mucosa specimens were fixed in neutral buffered formalin for 12 h then dehydrated by incubating sequentially for 1 h in 70 %, 80 %, 96 % and 100 % alcohol. The tissue samples were subsequently incubated in methyl benzoate for 24 h then embedded in paraffin. 4 µm sections were cut using a rotary microtome (Leica Jung RM 2025). The sections were stained with hematoxylin and eosin and examined under the light microscope (Olympus Corporation, Tokyo, Japan). The freshly cut porcine nasal mucosa was used as negative control while nasal mucosa treated with 100 µL of 37 % v/v nitric acid served as positive control[250] for the porcine nasal mucosa studies. Sections were analyzed for any pathological changes in cell morphology and tissue organization by personnel blinded to the experimental conditions.

2.3.19 Olfactory deposition of TSP-microparticles in 3D printed human nasal cast

A human nasal replica cast designed from data obtained by magnetic resonance imaging scans (80 cross sections spaced 1 mm apart) of a healthy, non-smoking, adult male constructed using a 3D printer (Dimension Elite 3D printer, Stratasys, USA) with a resolution of 0.178 mm was provided by Auckland Institute of Bioengineering. The airway model encompassed the complete nasal passages from the nostrils to the posterior nasopharynx. The approximate location of the olfactory region where microparticle deposition was quantified is located in the dorsal posterior region of the nasal cavity, starting at the anterior middle turbinate and extending along the septal walls towards the back of the nose as shown in **Figure 2.3**[251].

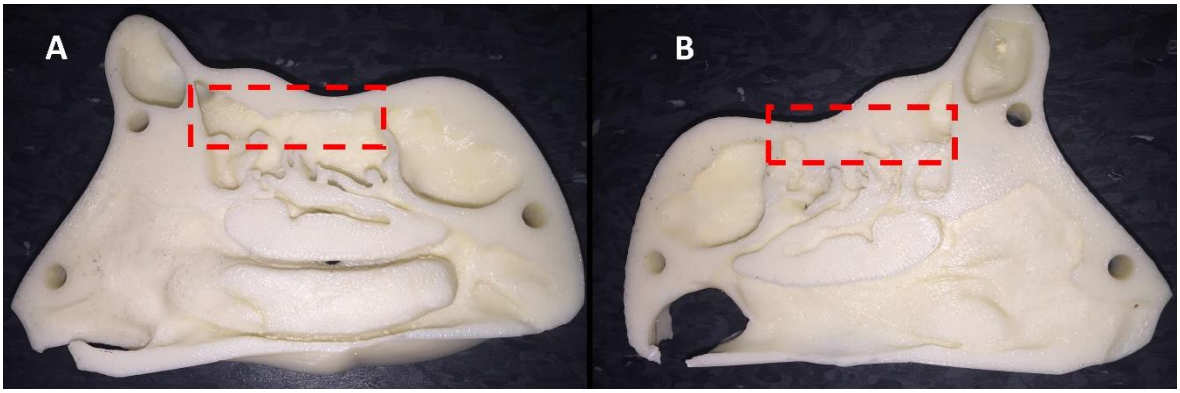

Figure 2.3 A 3D printed cast of the human nasal cavity showing the left (A) and right nasal passage (B). The approximate location of the olfactory region where deposition of microparticles was determined is shown in the dotted region.

A schematic of the experimental setup used for particle deposition experiments is shown in **Figure 2.4**. The sectioned nasal replica was coated with a layer of mucin solution (2 % w/v), assembled, and placed on a metal clamp. The throat side of the nasal cast was connected to a vacuum pump, and the inhalation flow rate was adjusted to ~20 L/min, measured with an anemometer. An air compressor system loaded with microparticles was brought to the right nostril. The microparticles were nebulized into the nasal cast using the air compressor system for 2 sec. Then the air compressor system was removed from the

nostril. Subsequently, the nasal replica cast was disassembled, and microparticles deposited in the olfactory region were carefully collected and analyzed for FITC-Dextrans or phenytoin content. TSP-microparticles of diameter 2 ± 1 µm prepared with spray-drying technique were used as a control in these experiments. The data is expressed as deposition efficiency (DE). Only deposition of microparticles in the olfactory region was considered in this study and is given by Equation 7 as below.

$$DE(\%) = \frac{Amount\ of\ drug\ deposited\ in\ the\ olfactory\ region\ (mg)}{Total\ amount\ of\ drug\ released\ into\ the\ nasal\ cavity\ (mg)} \quad |Equation\ 7$$

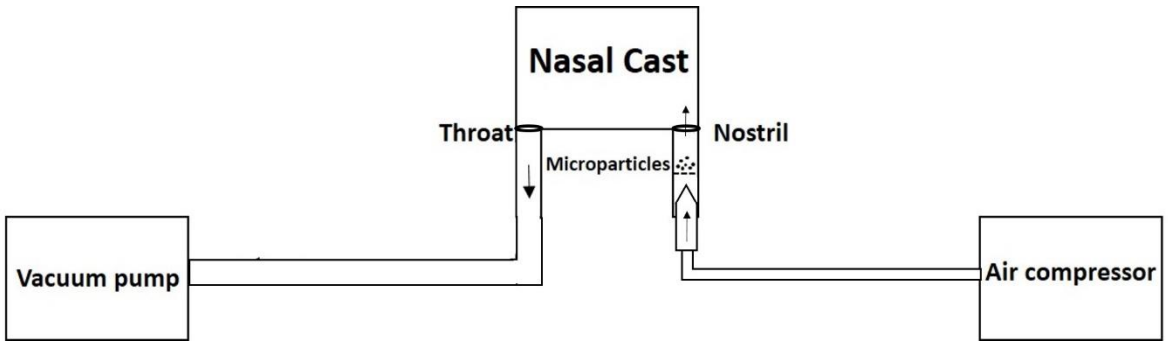

Figure 2.4 Schematic of the experimental setup used for particle deposition experiments. The microparticles were nebulized into the nasal cast using an air compressor for 2 sec. Arrows indicate the direction of air flow.

2.4 *In-vivo* studies

Six to eight week old male Wistar rats were used for all *in-vivo* studies. All *in-vivo* experiments were performed in accordance with an approved protocol by the Animal Ethics Committee (AEC 72/16), University of Otago, New Zealand.

2.4.1 Construction of insufflator for the intranasal delivery of microparticles

An in-house custom insufflator was built for the purposes of administering solid microparticles to the rats as shown in **Figure 2.5**. The design of insufflator was inspired from Penncentury^{TM} dry powder insufflator reported for powder deposition in rat lungs[252,253]. An air syringe, three-way stopcock leur and a 21 gauge needle were used to build the insufflator. Microparticles were loaded into the chamber. Rotation of the handle to different positions in the three-way stopcock enabled the filling and compression of air in the syringe. Depressing the syringe plunger pushed air through the microparticle chamber and "insufflated" the microparticle dose, sending it out the needle to the target region. The needle was blunted and bent 1 cm from the tip at 45^{o} to facilitate its reach to the olfactory region through the rat nostril. The average weight of microparticles loaded and expelled from the insufflator was determined to establish the efficacy of the device (**Appendix D**). In addition, quantity of microparticles expelled during each administration was obtained by measuring the difference in the insufflator weight before and after each insufflation.

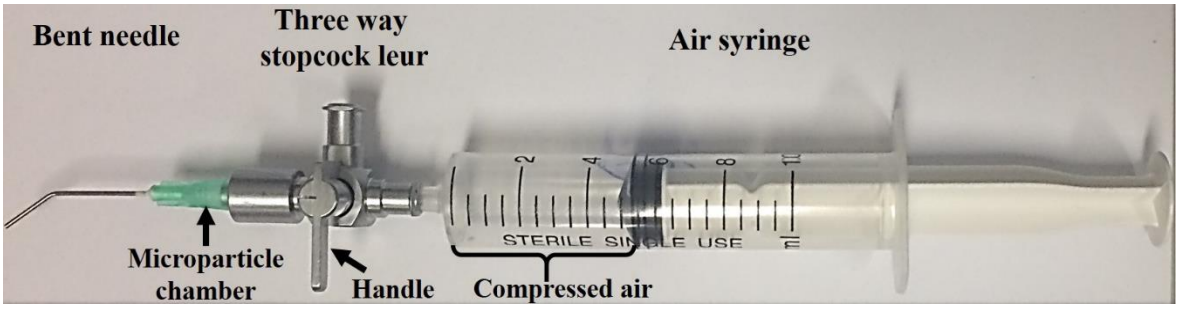

Figure 2.5 Custom built insufflator used for intranasal administration of solid microparticles to rats. Microparticles were filled at the base of the needle and were insufflated by compressed air released by turning the handle to the open position.

2.4.2 Evaluation of nasal toxicity and drug-related behavioral adverse effects of phenytoin loaded TSP-microparticles.

Rats were exposed to 5 % isoflurane for 3 min to induce short-term anesthesia. Once unconscious, the rats were held in the supine position with their head horizontal to the bench. Microparticles were administered into the nostril by the in-house built dry powder insufflator

described above. Rats were held in position for 15 sec after administration. Rats were monitored for any potential signs of nasal irritation such as frequent sneezing, noisy breathing, nose-rubbing, porphyrin (red) discharge, and general signs of pain/discomfort for 60 min.

Rats were euthanized 60 min after intranasal administration by guillotine decapitation. Following this, skin and excess tissue around the nasal passage were removed from the head. A blunt needle was inserted 0.5 cm into the posterior of the nasopharyngeal duct and used to flush the nasal passage with 10 mL of 10 % neutral buffered formalin (NBF) or sodium deoxycholate (positive control). The nasal passage was fixed in 50 mL of NBF for 48-72 h. The fixed nasal passage was subsequently decalcified in 10 % EDTA (pH 7.2) for 2-3 weeks, sliced coronally into blocks and embedded in paraffin. A microtome was used to cut 5 µm sections which were subsequently de-paraffinized, stained with hematoxylin and eosin, and cover-slipped with DPX mounting medium. Sections were imaged on an Aperio ScanScope. Images were analyzed by personnel blinded to the treatments using Aperio ImageScope v12.2.2.5015 software. A rat treated with saline was used as a negative control, and a rat nasal cavity flushed with sodium deoxycholate served as positive control.

2.4.3 *In-vivo* drug administration

Rats were divided into three treatment groups receiving intranasal phenytoin microparticles, intranasal phenytoin solution or IV phenytoin sodium injection under short-term inhaled general anesthesia. The intranasal phenytoin microparticles were administered by the in-house custom built insufflator as described in **Section 2.4.1**. The dose of the drug was determined by weighing the microparticles emitted from an insufflator, an average dose of 1.5 mg phenytoin was administered as shown in **Figure 2.6**. Animals to whom administration was incomplete due to clogging of the microparticles in the needle were temporarily excluded. Considering the half-life of model drugs[254–256] and logistics, animals were experimented with at a later date, at least 4 days later.

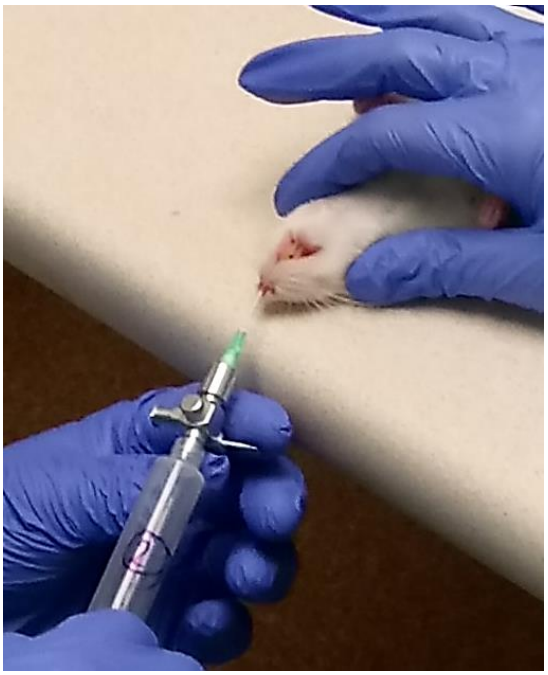

Figure 2.6. Administration of phenytoin microparticles to the rat nasal cavity using the custom-built insufflator.

The intranasal phenytoin solution was administered using a 'rat intranasal catheter device' (Impel Neuro Pharma, USA). The drug solution was administered to anesthetized animals in a similar to the procedure described in **Section 2.4.2**. Drug solution was loaded into a syringe with a piece of plastic tubing attached. The tubing was inserted about 1 cm into the rat nasal cavity to reach the olfactory region and depressing the plunger of the syringe delivered the drug solution through the tubing directly to the olfactory region. Phenytoin sodium solution was prepared by dissolving 100 mg of phenytoin sodium in 1 mL of 50 % ethanol-water mixture containing 10 µL of propylene glycol. Considering the limitation of solution volumes that the nasal cavity can accommodate, a volume of 15 µL solution, equivalent to 1.5 mg of phenytoin was administered to each rat.

DBL^{TM} Phenytoin injection (Hospira, Australia) was used for IV administration. The marketed formulation has a 50 mg/mL concentration of phenytoin sodium. A solution volume of 30 µL, equivalent to 1.5 mg of phenytoin sodium was administered IV by tail-vein injection.

After administration, the rats were sacrificed at 15, 30, 45 and 60 min time points (n = 5 for each time point) by decapitation as described in **Section 2.4.2**. Immediately after decapitation, trunk blood was collected into heparin tubes. The blood was centrifuged at 2000 G for 5 min to collect the plasma. The brain was collected immediately and washed with fresh saline three times to remove any blood. The liver, spleen, kidneys, lungs, and heart were also collected and washed with saline. All the tissues and plasma were stored in a – 81 ºC freezer until further analysis.

2.4.4 Analysis of phenytoin content in rat plasma and tissues by HPLC

2.4.4.1 Equipment and chromatographic conditions

An HPLC (Agilent technologies 1260 infinity) with UV detector, a C 18 column (150 X 4.6 mm) with 5 µm particle size and a C-18 guard cartridge (5 X 4.6 mm) (Phenomenex, California, USA) kept at 40 ºC were used for the analysis. The mobile phase consisted of a mixture of pH 5.8 phosphate buffer (10 mM) and acetonitrile that was regulated by a gradient profile programmed as follows: a linear gradient from 10 % acetonitrile to 50 % over 10 min; maintenance at 50 % for 2 min, a linear gradient from 50 % acetonitrile to 40 % over 1 min; maintenance of acetonitrile at 60 % for 3 min, then a linear gradient from 40 % acetonitrile to 10 % over 1 min. After each cycle, the column was conditioned with 10 % acetonitrile and 90 % phosphate buffer for 3 min. The flow rate was 0.2 mL/min. The phenytoin derivative 5-(4-methylphenyl)-5-phenyl-hydantoin was used as the internal standard for the analysis of blood and tissues (referred to as 'internal standard' from now on in this thesis). The major metabolite of phenytoin in blood and tissues is '5- (4-Hydroxyphenyl)-5-phenyl-hydantoin' (referred to as 'metabolite' from here onwards in this thesis) was also quantified along with the phenytoin. The injection volume was 10 µL, and the UV detection wavelength was 210 nm. The chromatographic data analysis was performed using the OpenLAB software (Agilent Technologies, California, USA). The method was validated for its accuracy, selectivity, precision, and repeatability in plasma, brain, liver, spleen, kidneys, lung, and heart. Chromatographic conditions and the procedure

to extract phenytoin from plasma and tissue samples were optimized by modifying the reported methods[257–259].

2.4.4.2 Stock solutions

Stock solutions of phenytoin, internal standard and metabolite were prepared in methanol at a concentration of 1 mg/mL. Working solutions (100 µg/mL and 10 µg/mL) were prepared by serial dilution of stock solutions with methanol.

2.4.4.3 Plasma sample preparation

For the construction of calibration curves, 200 µL aliquots of plasma were added to 1.7 mL Eppendorf tubes. The samples were spiked with varying concentrations of phenytoin (0.1, 0.5, 1, 2.5, 5, 7.5, and 10 µg/mL) and metabolite (0.5, 1, 2.5, 5, 7.5, 10 and µg/mL) and a fixed concentration of the internal standard (10 µg/mL) using the working solutions and vortexed for 30 sec. Following that, 300 µL of chilled acetonitrile and 300 µL of tert-Butyl methyl ether were added to the spiked plasma samples to precipitate the proteins and extract the phenytoin from plasma. The samples were centrifuged at 13000 rpm at 4 ºC for 20 min. The supernatant was then separated and concentrated overnight by evaporation to dryness in a centrifugal evaporator. The concentrated samples were reconstituted in 200 µL of a mixture of pH 5.8 phosphate buffer and acetonitrile (60:40) and loaded into the auto sampler for HPLC analysis.

For quantification of phenytoin from *in-vivo* studies: the 200 µL plasma samples were spiked with 10 µL internal standard (1 mg/mL) in Eppendorf tubes and vortexed for 30 sec. Following that, the same steps for sample preparation as for the calibration curves were followed and the samples were analyzed for phenytoin content.

2.4.4.4 Tissue sample preparation

All tissues were homogenized in 80 % ethanol solution in water to precipitate proteins and lipids. A volume of 6 mL of 80 % ethanol solution was used for every 1 g of tissue.

Tissue samples were spiked with varying concentrations of phenytoin (0.1, 0.5, 1, 2.5, 5, 7.5, 10 µg/g) and metabolite (0.5, 1, 2.5, 5, 7.5, 10 µg/g) and a fixed concentration of the internal standard (10 µg/g) using the working solutions and vortexed for 30 sec. Tissue samples for constructing calibration curves were then prepared in the same way as the plasma sample preparations using of tissue homogenates equivalent to 200 µg tissue weight. However, multiple tissue aliquots were concentrated then pooled together and reconstituted with 200 µL of a mixture of pH 5.8 phosphate buffer and acetonitrile (60:40) for analysis.

For quantification of phenytoin from *in-vivo* studies: 1 g of tissue homogenates were spiked with 10 µL internal standard (1 mg/mL) in Falcon tubes and vortexed for 30 sec. The same steps for sample preparation as for the calibration curves were followed and the samples were analyzed for phenytoin content.

2.4.4.5 Method validation

The calibration curves were plotted using peak area ratio values obtained from the ratio of phenytoin to the internal standard. The unknown concentrations of phenytoin were determined from the calibration curves. Quality control (QC) samples consisted of low (1 µg/mL) medium (5 µg/mL) and high (10 µg/mL) concentrations of the phenytoin.

2.4.4.5.1 Specificity

The specificity of the method was determined by identifying and separating the phenytoin, the internal standard and the metabolite chromatographic peaks from each other, and from the endogenous materials in plasma, brain, and other tissues. The specificity of the HPLC method is demonstrated by comparing the chromatograms of plasma/tissue samples with no phenytoin, and plasma/tissue samples spiked with known amounts of phenytoin, internal standard, and metabolite.

2.4.4.5.2 Linearity

The linearity of the HPLC method was determined using standard solutions spiked with phenytoin and metabolite with final concentrations in the range of 0.1 to 10 µg/mL and an internal standard of 10 µg/mL. The calibration curves were plotted with peak area ratio values obtained from the ratio of phenytoin and metabolite to the internal standard. The linear regression coefficient (r^2) values were calculated and reported.

2.4.4.5.3 Sensitivity

The sensitivity of the method is demonstrated by the lower limit of detection (LOD), and the lower limit of quantitation (LOQ) obtained from the standard deviation of the y-intercept and slope of the calibration curve.

2.4.4.5.4 Accuracy and Precision

The amount of phenytoin recovered from the tissue and plasma QC samples after sample preparation and HPLC analysis were compared to the theoretical values and used to report the accuracy of the method. The intraday variability was determined by replicate analysis of QC samples on the same day, by calculating and reporting the %co-variance (CV) and %bias. The accuracy and precision of the method were based on the %bias and %CV.

The inter-day variability was measured to represent the repeatability of the method. QC samples were analyzed on different days with one replicate being analyzed each day and the %CV and %bias were calculated and reported. A %CV and %bias within ±15 % were considered as acceptable for the plasma and tissue samples.

2.5 Statistical analysis

All results are expressed as mean ± SD. Where applicable, statistical analyses were conducted using an unpaired t-test or ANOVA on Prism 6 (GraphPad, USA). A P-value of < 0.05 was taken to be significant.

Chapter 3

Formulation and evaluation of TSP-microparticles

This chapter has been published as a peer-reviewed article:

Sasi B. Yarragudi, Robert Richter, Helen Lee, Greg F. Walker, Andrew N. Clarkson, Haribalan Kumar, Shakila B. Rizwan, Formulation of olfactory-targeted microparticles with tamarind seed polysaccharide to improve nose-to-brain transport of drug, *Carbohydrate Polymers*, 2017, 163: 216–226.

3 Formulation and evaluation of TSP-microparticles

As discussed in **Chapter 1**, this thesis aimed to develop a mucoadhesive microparticle system with specific size to efficiently target the olfactory region and enhance nose-to-brain delivery of drugs. In this **Chapter**, the selection of a mucoadhesive polymer, formulation of size tailored microparticles and the ability of such a microparticle system to load and release drugs was investigated.

3.1 Selection of a mucoadhesive polymer

Chitosan is the most popular polymer reported in the literature for the formulation of nose-to-brain micro and nanoparticle drug delivery systems (**Table 5**). It is proposed that the positively charged amino groups of chitosan interact with sialic acids in the mucous layers to form strong electrostatic bonds causing mucoadhesion. Also, chitosan can reversibly open the tight junctions by inducing changes in the transmembrane protein claudin-4 and the C-Jun NH_2-terminal kinase-dependent pathway to increase the permeability of the epithelial cells[231,260]. These characteristics have made chitosan the first choice among all other polymers. However, there have been reports of acute mucosal toxicity[261] believed to be due to the positive charge on chitosan, and there is very little known about the effect of long-term exposure to chitosan on the nasal mucosa.

Recently, tamarind seed polysaccharide (TSP) has gained some attention in drug delivery applications due to its mucoadhesion properties, broad pH tolerance, biocompatibility and high drug loading capacity[262,263]. Moreover, unlike chitosan, TSP is uncharged under physiological conditions [264] and therefore is less likely to cause nasal toxicity. TSP is classified as a generally recognized as safe (GRAS) substance and is approved by the FDA. It is commonly used as an excipient in food and pharmaceutical preparations and is available in the market as an eye drop formulation for treating dry eyes[264–266]. TSP is a naturally occurring and readily available polymer. These distinctive advantages and characteristics of TSP make it a potential polymer for nose-to-brain drug delivery purposes and hence, this thesis investigates TSP for the formulation of mucoadhesive microparticles.

3.1.1 Tamarind seed polysaccharide (TSP)

TSP is a high MW (720-880 kDa) polysaccharide isolated from the seed kernel of *Tamarindus indica* Linn. (Leguminosae)[267] and composed of a cellulose-like (1→4)-β-D-glucan backbone substituted with sidechains of α-D-xylopyranose units at 1→6 positions and β-D-galactopyranosyl units at 1→2 positions[268] as shown in **Figure 3.1** . TSP predominantly contains the sugars; glucose, galactose, and xylose in a molar ratio of 2.8:1:2.25[269,270]. The MW of TSP is based on the chain length which can vary from 300 to 3000 glucose units[271].

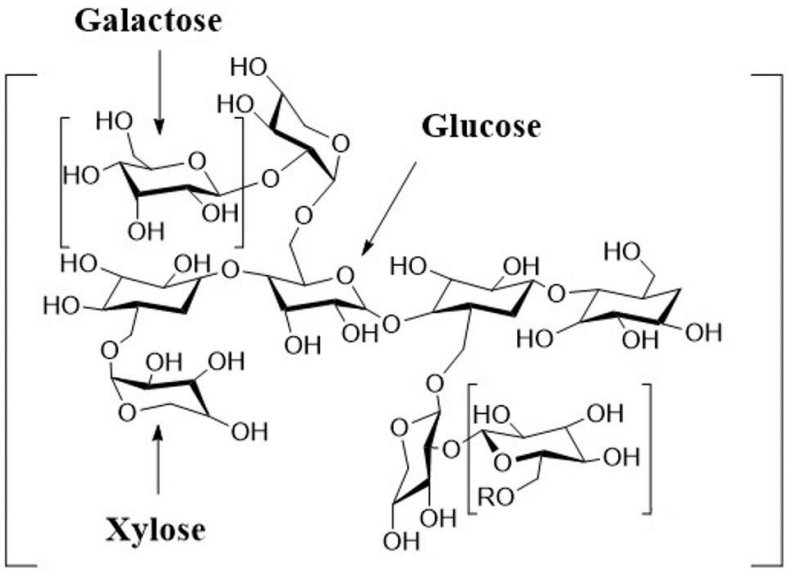

Figure 3.1 Chemical structure of TSP with xylose and galactose side chains attached on to the glucose backbone.

As a result of inter-chain interactions promoted by the cellulose like β (1→4) backbone, TSP is a highly hydrophilic polymer. However, macromolecules in TSP are not adequately hydrated. Consequently, supramolecular aggregated species are present even in dilute solutions[235]. Xylose and galactose side chains are more hydrophilic than the glucose units and significantly affect the solubility of TSP. For example, removal of galactose side chains significantly decreases the solubility of TSP[272]. Given that modification of side chains shows a direct correlation with changes in solubility and rheological properties[273,274], this structure-

functional relationship may have potential in controlling the release of drugs when formulated using TSP.

The mucoadhesive properties of TSP are believed to be due to the secondary hydroxyl (OH) groups present in the molecule, which can interact with mucus to form hydrogen bonds, and Van der Walls attractions[221]. Also, the mucin-like configuration of TSP imparted by its branched structure aids in the interpenetration of chains between TSP and mucus resulting in mucoadhesion[275,276]. Due to the advantages it can offer, TSP has been investigated in drug delivery applications. **Table 5** lists the reported drug delivery applications of TSP and the critical observations in those studies.

Table 5. Drug delivery applications (preclinical and in-vitro) of TSP reported in literature grouped according to the formulation type.

Drug	Route	Observations	Ref
Solutions			
Gentamicin & ofloxacin	Ocular	• Enhanced drug absorption compared to simple suspensions was reported with TSP formulations in rabbits.	277
Timolol		• High ocular and low systemic drug concentrations compared to commercial eye drops were reported with TSP formulation in rabbits.	278
Ketotifen & Diclofenac sodium		• TSP significantly prolonged the drug residence in the precorneal area of rabbits.	279
Ketotifen fumarate & Diclofenac sodium		• Synergistic action between TSP and hyaluronic acid was utilized to prolong the residence time of drugs in the tear fluid of rabbits.	280
Rufloxacin		• A significant increase in the intra-aqueous penetration and the bioavailability of rufloxacin was reported by TSP formulations in rabbits.	281,282
Thermally reversible gels			
Indomethacin & Diltiazem	Rectal	• Modified-TSP was used as polymer: 44 % of galactose residues were removed from TSP by β-galactosidase to obtain thermally reversible gels. • Sustained Drug release was reported from TSP formulations	283
Pilocarpine	Ocular		284
Ibuprofen & Ketoprofen	Percutaneous		285
Mitomycin	Intraperitoneal		286
Indomethacin & Diltiazem	Oral		287
Cimetidine			288
Lidocaine Hydrochloride	Buccal	• TSP + Pluronic F 127 combination was used as the polymer. • Fast onset of drug action was reported with TSP formulations.	289

Tablets			
Aspirin	Oral (pH-dependent hydrogel)	• TSP was modified by grafting with polyacrylamide. • Significant enhancement in controlled release of aspirin was reported with grafted TSP formulations.	290
Aceclofenac	Oral	• TSP + Chitosan blend was used for the preparation of microparticles (91 to 498 µm) and compressed to tablets.	291
Famotidine	Oral (Gastro retentive)	• TSP and tamarind kernel powder (TKP) were compared. TKP was found to be more suitable for the gastro retention of famotidine.	292
Metformin hydrochloride	Oral (Gastro retentive)	• TSP and TKP were used to prepare the tablets. • TSP formulations were found to remain in the stomach for 12 h.	293
Simvastatin	Oral	• TSP was modified with cysteine to form thiomer. • Enhanced mucoadhesion and increased *ex-vivo* permeation was reported	294
Metformin	Oral	• TSP + methacrylamide-p-gellan combination was used as the polymer	295
Metformin	Oral (Gastro retentive)	• A significant increase of the drug release rate and swelling was reported.	296
Theophylline	Oral	• *In-vitro* drug dissolution studies showed the release of theophylline was sustained by TSP • The release of drug from tablets was directly proportional to the percentage of TSP	297

Large Particles			
Diclofenac sodium	Oral-Spheroids (690 µm)	• Microcrystalline cellulose + TSP combination was used as the polymer. • TSP spheroids sustained the drug release over 10 h	298
Diclofenac sodium	Oral-beads (710 to 1330 µm)	• TSP + sodium alginate combination was used as the polymer • The TSP beads were able to control the release of drug for 10 h	299
Glicazide	Oral-Beads (752 to 948 µm)	• TSP + sodium alginate combination was used as the polymer • The TSP beads were able to control the release of drug for 12 h • A significant hypoglycemic effect was reported in the rats	300
Diltiazem	Oral-Beads (1063 to 1269 µm)	• TSP + sodium alginate was used as the polymer. • Prolonged release of drug for 10 h was reported in rats.	301
Metformin hydrochloride	Oral-Beads (1930 µm)	• TSP + Pectin combination was used as the polymer. • A significant hypoglycemic effect in diabetic rats was reported	302
Metformin hydrochloride	Oral-Beads (1274 µm)	• TSP + sodium alginate combination was used as the polymer. • pH-dependent swelling & sustained release for 10 h	303
Metformin hydrochloride	Oral-Beads (1000 to 1560 µm)	• TSP + Gellan gum combination was used as the polymer. • Sustained and significant hypoglycemic effect in diabetic rats	304
Microparticles			
Aceclofenac	Oral-Microspheres (490 to 621 µm)	• TSP + Chitosan combination was used as the polymer. • The release of the drug was sustained over 10 h and sustained anti-inflammatory activity in rats was reported.	305
Glipizide	Oral-Microspheres (3 to 6 µm)	• The drug release was sustained for 10 h.	237

Montelukast sodium	Inhalation Microspheres (0.9 to 6 µm)	• Modified TSP was used as polymer: 47 % of galactose units were removed. • Enhanced *in-vivo* drug residence time in rats was reported	306
		Films	
Rizatriptan benzoate	Buccal	• TSP + Carbopol combination was used as the polymer.	307
Nystatin	Vaginal	• The sustained release was reported	308
Timolol maleate	Ocular	• TSP films were nonirritant and able to sustain the drug delivery	309
Ciprofloxacin			310
		Nanoparticles/Nanoaggregates	
Tropicamine	Ocular	• Increased drug absorption was reported in the *in-vitro* cell studies	311
Doxorubicin	NA/in-vitro	• Enhanced cytotoxic effects were reported in the cells with TSP formulations	312
		Gels	
Paracetamol	Oral	• Modified-TSP was used as polymer: removal of galactose residues • Sustained release of drugs by TSP gel was reported in rats.	313
Metronidazole		• Thiol-functionalized TSP was used as the polymer. • Mucoadhesion was increased by 6.85 folds after functionalization	268
Eriochrome Black T	Injectable implants	• Sustained drug release was reported for four days	314

Reports in the literature showcase the potential of TSP as an excipient and an active ingredient in drug delivery applications. The chemical modification of TSP with polyacrylamide[315], methyl methacrylate[316], polycaprolactone[317,318] and PLA[319] has been investigated for drug delivery purposes. Semi-synthetic derivatives of TSP such as thiolated-TSP[268,276,320] and carboxymethylated-TSP[321] have also been investigated for drug delivery applications. Several patents on the use of TSP as a polymer for drug delivery in opthalmic[322,323], topical[324] and cosmetic[325] areas have been filed. In addition to the drug delivery applications, TSP has also been shown to have wound healing[326], anti-tumor[327–329], anti-myocardial infraction[330] and immunomodulatory properties[329,331].Patent has also been filed for the use of TSP as a protecting agent for epithelial cells of the respiratory tract from damages induced by smoking[332]. TSP has been tested clinically with positive results for the treatment of dry eye syndrome[333] and is used in commercially available Visine Intensiv 1% eyedrops (Europe)[266].

The analysis of literature has shown some interesting trends in the use of TSP for drug delivery applications.

1. The drug carrying capacity of TSP in oral and ocular routes was well characterized in the reported publications (**Table 5**). However, the ability of TSP to act as a drug carrier via the nasal route has not been well reported.
2. The potential of TSP as a carrier of drug molecules with high MW has not been explored yet.
3. About 60 % of the reported publications have formulated TSP either with a combination of another polymer or modification of its structure with an aim to change properties like mucoadhesion and drug release. Consequently, this has resulted in considerable variations in reported drug release profiles ranging from 2 h to four days. Controlled release of drugs formulated in TSP in combination with other polymers or by chemical modification has been shown for at least 10-12 h *in-vitro* (**Table 5**). While this may be useful for other drug delivery purposes, for the nose-to-brain delivery purposes, the likelihood that any formulation is retained in the nasal cavity for periods longer than 12 h despite its mucoadhesive nature is unlikely and often not desired. Thus, examining unmodified TSP as a carrier of drugs may

decrease the time required to release the encapsulated drugs, offering advantages for nose-to-brain drug delivery purposes.

3.1.1.1 TSP as a carrier for nose-to-brain drug delivery

Two investigations have reported the potential of TSP as a carrier for brain targeting drugs via the nasal cavity. Kumar *et al.*,[275] formulated two anti-migraine drugs zolmitriptan and ketorolac tromethamine into thermally reversible gels using a blend of TSP, Pluronic F127 and PEG. The formulations were found to be mucoadhesive and sustained release of both drugs. The histopathological evaluation of sheep nasal tissue treated with the formulations suggested the formulations were safe to administer. *In-vivo* studies in rabbits compared the pharmacokinetic profiles of drugs between intranasal (gel), IV and oral (solutions) administrations. The TSP formulations were reported to have an almost 1.3-fold increase in absolute bioavailability compared to the oral route.

In the second study, Mahajan *et al.*,[334] reported the formulation of the anti-nausea agent ondansetron in a TSP thermally reversible gel. TSP was modified by the β-galactosidase enzyme to remove 45 % of the galactose units. The removal of galactose units imparted TSP with thermosensitive gel properties. The formulations were found to be mucoadhesive with sustain drug release over 6 h. Histopathological evaluation of rabbit nasal tissue treated with the formulations has shown no evidence of damage. *In-vivo* absorption studies compared intranasal (gel) and oral (solution) administration. TSP formulations were reported to produce an almost two-fold increase in absolute bioavailability.

In both studies, TSP was either chemically modified or used with another polymer. Both studies reported the safety of TSP for nasal administration and the ability of TSP formulations to improve residency of drugs in the nasal cavity. However, the drug concentrations in the brain were not quantified.

The capability of TSP as a mucoadhesive and safe polymer for nasal administration has been reported. Therefore, due to the advantages and potential of TSP, this thesis utilizes TSP as a mucoadhesive polymer for the preparation of solid microparticles intended for nose-to-brain delivery.

3.2 Method of preparation of microparticles

Freeze drying[206,207], emulsification-cross linking[137,208], and emulsification-solvent evaporation[193,205] are some of the methods reported in the literature for the preparation of microparticles for nose-to-brain delivery. Spray-drying has been the most popular method with about 70 % of the reported publications utilizing spray-drying for the formulation of microparticles intended for nose-to-brain delivery. The high yield rate and simple methodology of spray-drying are the main reasons for its popularity.

3.2.1 Spray-drying

Spray-drying is a process where a liquid (feed) is converted to a powdered solid (product) by spraying the feed into a gaseous drying medium[335]. It has been utilized in the food and pharmaceutical industry for the production of powders since its first patent in 1872[336]. There are three phases involved in the spray-drying process: first, the atomization phase where the pumped feed is sprayed as small droplets through the nozzle by the force of a compressed air/gas. The second is the drying phase where the droplets interact with hot gas in a chamber to evaporate the solvent, and third, a separation phase where the particles are separated from the gas for collection by filter or cyclone[337].

Spray-drying is a one-step method and produces reasonable yields of microparticles[338]. By controlling the spray-drying parameters, microparticle characteristics such as particle size, shape and density can be tailored to suit the requirements[339]. The parameters of composition of feed solution, velocity of the feed solution being pumped, velocity of the compressed air/gas (atomizing air flow), nozzle type, velocity of the drying gas (aspiration) and temperature of the drying gas (inlet temperature) can be examined.

As reported in Chapter 1 and previous sections spray-drying is the most widely used method to produce microparticles, which this can be attributed to the numerous advantages of spray-drying compared to the other methods. For example, compared to a commonly employed method, freeze-drying, it is economical and less time consuming due to the fact that spray-drying doesn’t have a deep cooling step which consumes significant time and

energy[340–342].Hence, spray-drying is being explored as an alternative to freeze-drying[343,344]. In addition, particle size and distribution can be well controlled by spray-drying compared to emulsification, solvent extraction, and crosslinking methods employed in the literature. Hence, a spray-drying method promises successful bench-to-bedside translation of microparticle produciton[345].

Although spray-drying has numerous advantages, low yield and loss of nano-sized particles are major limitations of the spray-drying process[345]. Low yields are generally associated with loss of particles in the walls of equipment and smaller particles passing into exhaust[346]. The production of nanometer-sized particles by spray-drying is a challenging task due to the low separation capacity of the cyclone and low forces of liquid atomization[345,347,348]. While few studies reported an increased capacity of the cyclone at industrial settings, more studies are required to address these challenges[345,349].

Due to the ability of spray-drying to control the particle size, this thesis employs spray-drying to investigate the optimum parameters to produce the 10 µm sized particles with TSP as a mucoadhesive polymer.

3.3 Design of experiments (DOE)

Rational DOE decreases the total number of experiments required to extract critical information of a complicated process and saves significant experimental time[238]. In this thesis variables of an experiment that may have an effect on the characteristics of the end product are termed '*independent factors*,' the characteristics that are being affected are termed '*responses*.' This chapter employs spray-drying to formulate size tailored TSP microparticles. The effect of spray-drying parameters at different levels on the particle size needs to be tested for these purposes to identify the optimum parameters. The relationship between one or more responses and one or more independent factors can be studied using response surface methods[350].

Central composite design and Box–Behnken experimental designs are two widely reported methods to identify optimum levels of independent factors to achieve a specific

response[238,239]. The central composite experimental design has axial points beyond the design space leading to increased levels of the independent factors to be tested. Due to the nature of the independent factors tested in this chapter, it might not be beneficial to test points beyond the design space. In contrast, Box-Behnken design does not require the axial points beyond design space to be tested. Also, it is experimentally more convenient as it requires fewer experiments to be performed. The Box-Behnken experimental design also ensures that all individual factors are not tested at their highest levels, simultaneously putting the experiments in a safe operating zone[350]. Thus, in this chapter, Box-Behnken experimental design is employed to examine and identify the optimum parameters to produce the 10 µm sized particles with TSP using the spray-drying method.

3.4 Model drugs

In this **Chapter,** the ability of TSP to load drugs and the release of drugs from the formulated microparticles are examined by incorporating fluorescein isothiocyanate-labeled dextran's (FITC-Dextrans) with MW of 3–5, 10, 20 and 40 kDa as model drugs. Use of FITC-Dextrans to study the drug release from the formulations and permeation across the mucosal barriers is well reported in the literature[351–353].

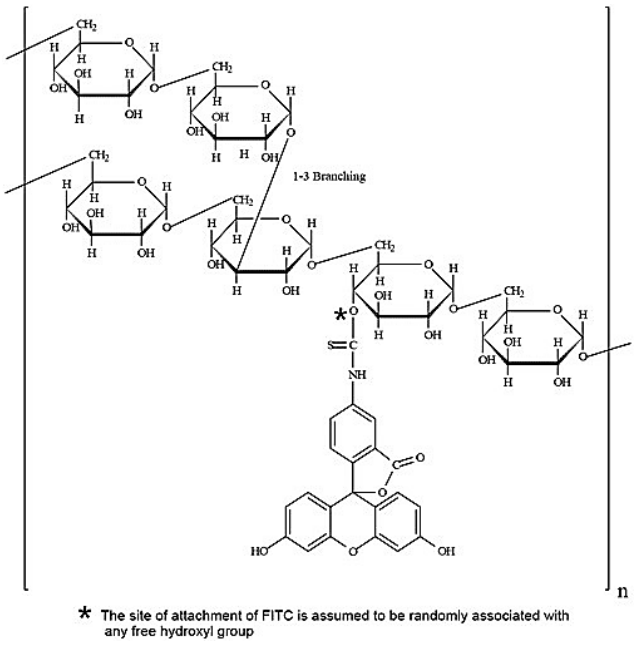

Figure 3.2 Structure of FITC-Dextran. The MW depends on the number of dextran molecules linked to each other. Figure adapted from website https://www.sigmaaldrich.com

Dextran is a polymer of anhydroglucose as shown in **Figure 3.2** It is comprised of approximately 95 % straight-chain α-D-(1→6) glycosidic linkages and the remaining α -D-(1→3) glycosidic linkages account for the branching of dextran[354]. The FITC is randomly conjugated to the free hydroxyl groups of the dextran at a frequency of 0.003 to 0.02 moles of FITC per mole of glucose. The number of dextran molecules determines the MW of the FITC-Dextrans and hence they are available in different MW. The FITC portion is responsible for the fluorescence of the compound, and hence it is utilized in permeation and release studies. It fluoresces with an excitation and emission wavelength of 498 nm and 520 nm, respectively.

3.4.1 Spray-dried TSP microparticles

As discussed in the previous sections, the advantages TSP can offer, its unexplored potential as a carrier of macromolecules and the ability of spray-drying to control the particle size combined poses the research question of whether drug loaded 10 µm sized TSP-particles can be formulated by spray-drying.

3.5 Hypothesis

The overall hypothesis tested in this chapter is that drug formulated into 10 µm TSP-microparticles will have increased olfactory targeting and residence.

3.5.1 Chapter aims

1. To formulate 10 µm sized TSP-microparticles loaded with high MW drugs by spray-drying.
2. To measure the mucoadhesion of the TSP-microparticles *in-vitro* and *ex-vivo*.
3. To establish the drug release profile from the TSP-microparticles.
4. To assess the safety of TSP-microparticles for nasal administration.
5. To assess the olfactory deposition of TSP-microparticles.

3.6 Results

3.6.1 Extraction of TSP from tamarind seed gum

TSP was extracted from tamarind seed gum with an average yield of 51 ± 11 %. The infrared (IR) spectra and x-ray diffractograms of the extracted TSP were analyzed and compared with the published data[355].

The IR spectra of TSP presented the characteristic broad peaks for stretching of the –OH group on the glucan backbone at 3331.62 cm^{-1} and 3282.07 cm^{-1} and the OH bending peaks were observed at 526.61 cm^{-1}. The alkane C-H stretching was observed by the peak at 2922.80 cm^{-1}. The cyclic ethers (C-O-C) stretching peak was observed at 1026.24 cm^{-1}. These peaks (**Figure 3.3 A**) indicate the characteristic functional groups of TSP and are agreement with the reported literature[355]. The x-ray diffractograms of TSP are presented in **Figure 3.3 B**. In agreement with the published literature for TSP, no sharp peaks were observed indicating its amorphous nature[355].

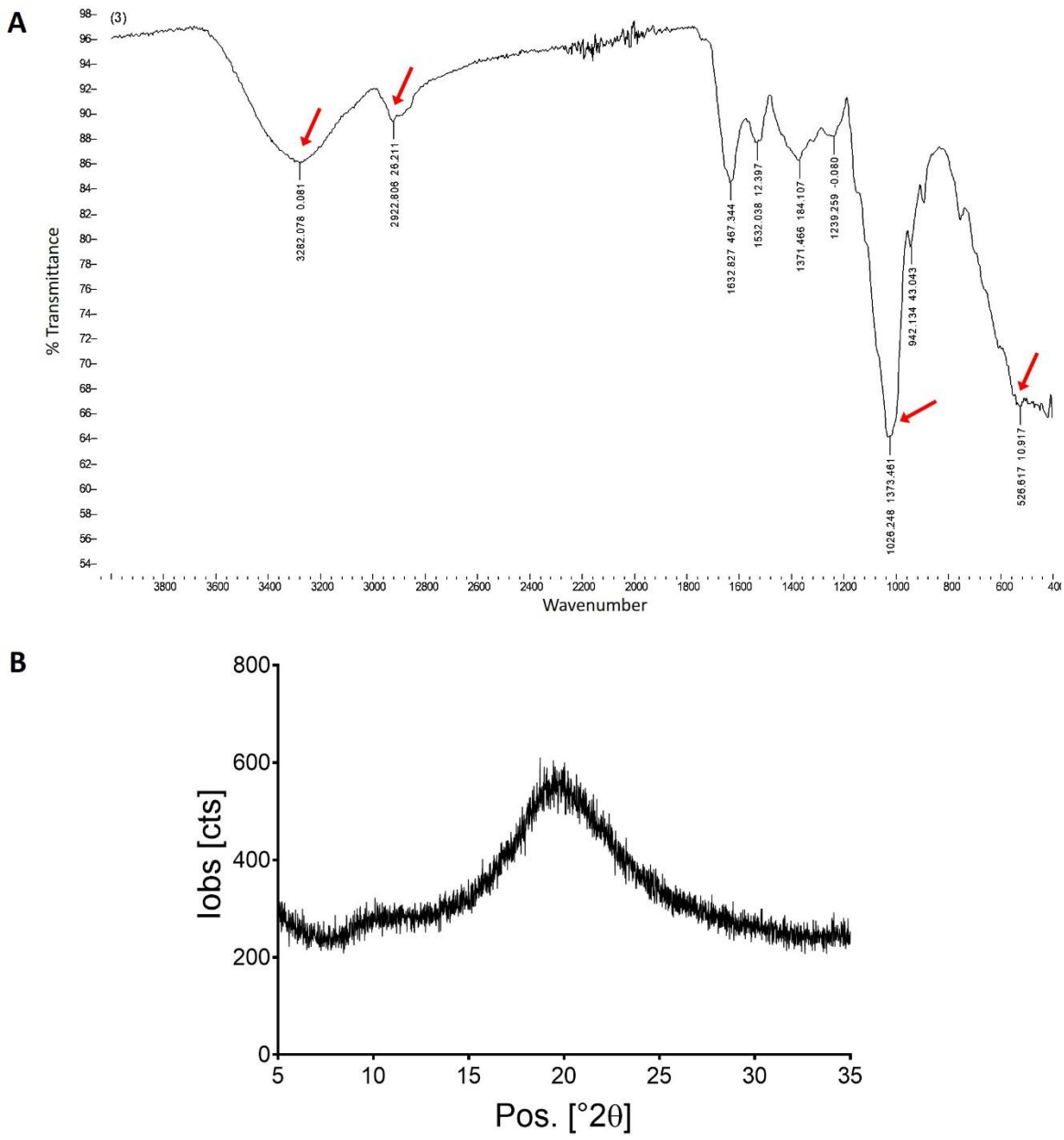

Figure 3.3 IR spectrum (A) and X-ray diffractogram (B) of TSP extracted from the tamarind gum. The red arrows show the characteristic peaks.

The surface morphology of TSP was observed under SEM and found to be similar to the published literature[356].

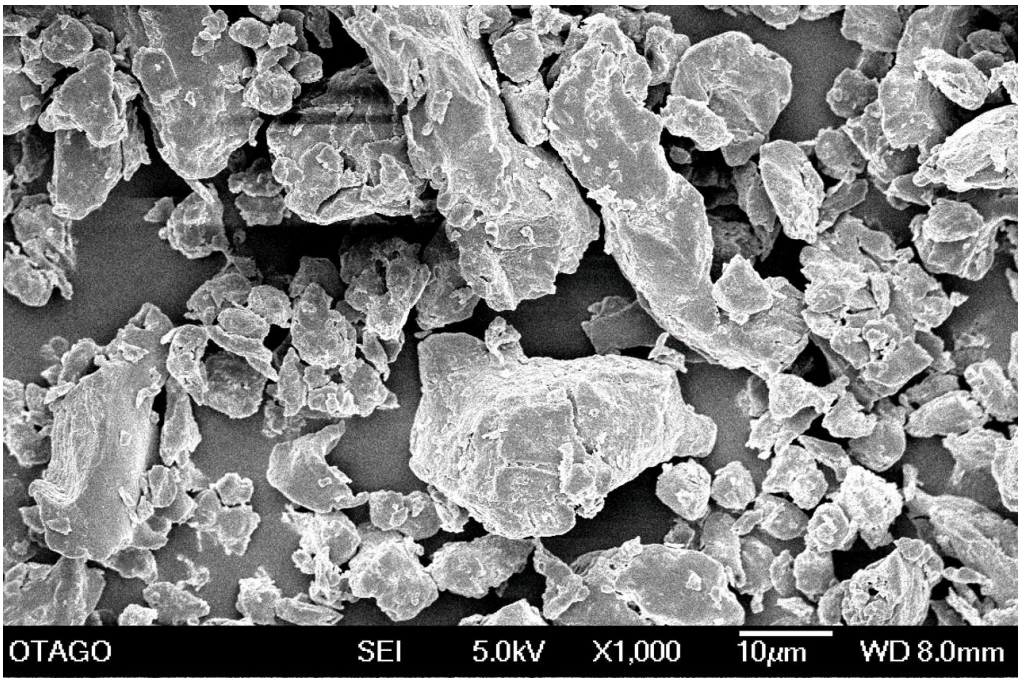

Figure 3.4 Representative micrograph showing the morphology of TSP (powder obtained from the crushed film) extracted from tamarind seed gum similar to the extraction procedure followed in this thesis.

3.6.2 Formulation of 10 µm sized TSP-microparticles loaded with FITC-Dextrans

3.6.2.1 Pilot studies

Pilot studies were conducted by trial and error to examine the ability of TSP to form microparticles. Initially, the process variables that might affect the characteristics of resultant particles were identified. These are referred to as formulation parameters (independent factors) in this thesis. The identified formulation parameters were: total solids (%) (w/w) in the feed solution, FITC-Dextran content (%), spray-drying conditions (atomizing airflow (L/h), inlet temperature and aspiration (%)). Formulation parameters employed in the preliminary studies and the resulting microparticle size and yield are presented in **Table 6.**

Table 6 Preliminary studies with TSP to examine the yield and size of microparticles with spray-drying.

Total solids (%) (TSP)	Atomizing airflow (L/h),	Inlet temperature	Aspiration (%)	Particle size (µm)	Yield (%)
1.0	742	130	100	2.1 ± 0.2	21 ± 4
1.5	742	130	100	2.8 ± 0.9	53 ± 1
2.0	742	130	100	2.2 ± 0.1	69 ± 4
1.0	246	100	20	NA	NA
1.5	312	110	30	16.3	13.0
2.0	384	120	40	13.2	35.0
2.0	425	130	50	11.9	67.0

TSP concentration higher than 2 % made the feed solution too viscous for spray-drying. Therefore, a 2 % TSP concentration (total solids content) was employed to prepare the feed solutions in subsequent studies. The % yield of the microparticles was found to increase with an increase in the % w/w of total solids.

The levels of other formulation parameters were too many to test with trial and error. Hence a DOE approach was followed to identify the significant formulation parameters affecting the particle size.

3.6.2.2 Optimization of formulation parameters using DOE

Box-Behnken experimental design was used to optimize the formulation parameters to produce a mode size of 10 µm sized TSP-microparticles.

A total of 29 combinations of different levels of formulation parameters were tested, the different levels of the formulation parameters and the resultant particle mode sizes are presented in **Table 7**. The effect of formulation parameters at different levels on the mode size of microparticles was analyzed using statistical methods.

Table 7 Box-Behnken design of experiments to optimize the formulation parameters.

	Formulation parameters (Independent Factors)				Response
Run	**Atomizing Airflow (L/h)**	**Aspiration (%)**	**FITC content (%)**	**Inlet temperature (°C)**	**Mode size (μm)**
1	494	50	0.10	110	12.99
2	246	60	0.20	120	12.98
3	494	60	0.10	120	9.48
4	494	60	0.20	110	8.63
5	494	70	0.20	100	8.61
6	494	60	0.20	110	7.27
7	246	50	0.20	110	11.32
8	742	60	0.10	120	4.79
9	742	70	0.20	110	5.24
10	742	60	0.20	100	5.24
11	494	50	0.25	110	14.14
12	742	50	0.20	110	5.47
13	494	60	0.20	110	12.96
14	494	60	0.10	100	9.46
15	494	60	0.25	120	12.40
16	494	60	0.25	100	6.27
17	742	60	0.20	120	5.47
18	494	60	0.20	110	10.32
19	494	50	0.20	120	12.96
20	246	60	0.20	110	8.23
21	494	60	0.20	110	10.32
22	494	50	0.20	100	11.28
23	494	70	0.20	110	10.32
24	246	60	0.20	110	10.80
25	742	60	0.25	110	8.23
26	494	70	0.25	110	7.89
27	494	60	0.10	110	11.84
28	246	60	0.25	110	12.39
29	494	70	0.10	110	5.50

ANOVA was performed to determine the validity of the experimental design used and the effect of each of the independent factors on mode size of the particles. The sequential model sum of squares and lack of fit tests were performed to determine whether the experimental design model is valid to navigate the design space. Lack of fit provided a mean response and an estimate of real experimental uncertainty and was found to have a value of $P = 0.5613$ (**Table 8**). An insignificant *P*-value for lack of fit indicates that any errors caused by design were too insignificant to influence the desired outcome.

*Table 8 Effect of independent factors on mode size of the microparticles and the validity of design model was determined by ANOVA. DF: degrees of freedom. *P-value of < 0.05 was taken to be significant.*

Source	Sum of Squares	DF	Mean square	F-value	P-value
Model	128.64	4	32.16	7.49	0.0005*
Atomizing Airflow	92.47	1	92.47	21.53	0.0001*
Aspiration	35.16	1	35.16	8.19	0.0086*
TSP:FITC-Dextran	1.97	1	1.97	0.46	0.5051
Inlet Temperature	3.50	1	3.50	0.81	0.3759
Residual	103.07	24	4.29		
Lack of Fit	81.42	19	4.29	0.99	0.5613
Pure Error	21.65	5	4.33		
Cur Total	231.71	28			

The atomizing airflow and aspiration were found to significantly influence microparticle size, with P-values of 0.0001 and 0.0086, respectively (**Table 8**). The three levels of inlet temperature used in the study were high enough to dry the microparticles in the spray-drying chamber and did not influence the mode size. Additionally, the amount of FITC-Dextran did not have a significant effect on the size of the microparticles. The 2D contour plots representing the effect of significant factors on the mode size are presented in **Figure 3.5.**

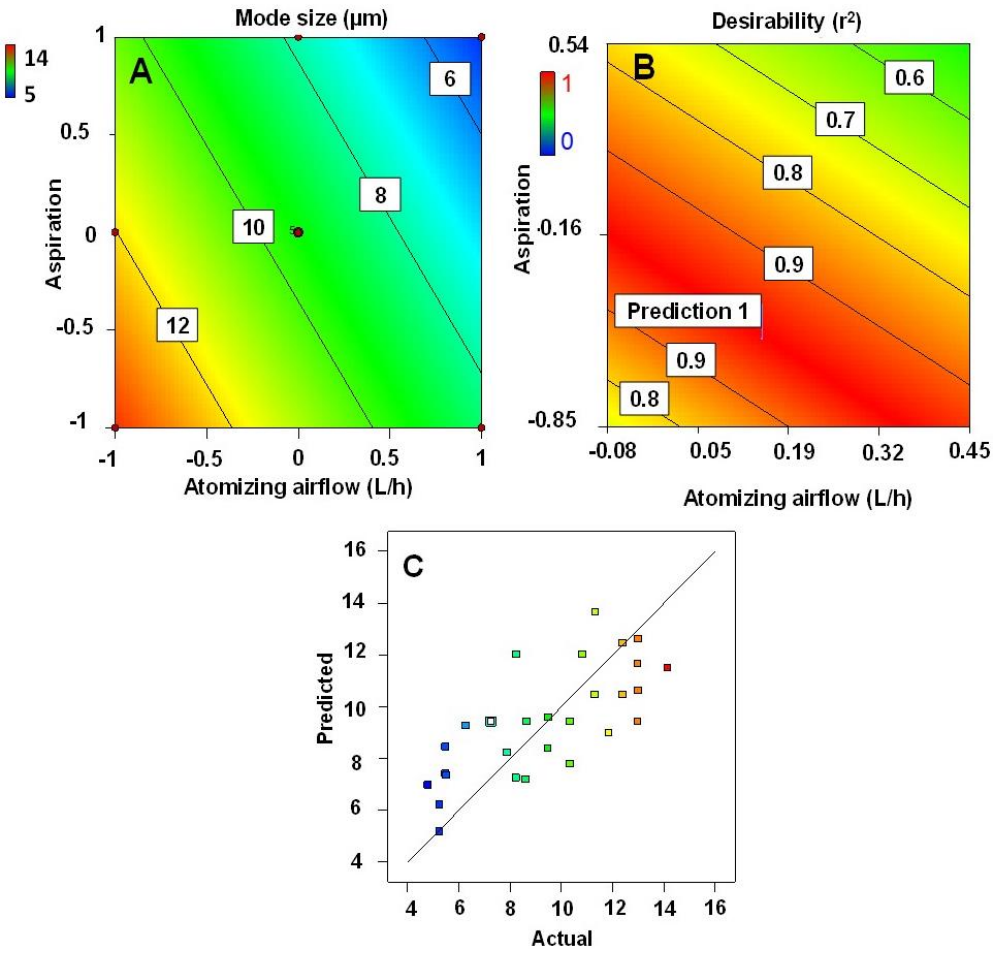

Figure 3.5 Contour plots showing the effect of the atomizing airflow and aspiration on the mode size of TSP-microparticles (A) which was further optimized to obtain microparticles with a mode size of 10 µm (B). A plot showing the correlation between the predicted mode of TSP-microparticles sizes against experimentally determined values (C).

Response surface methodology was used predict the optimal formulation parameters required to produce 10 µm sized microparticles based on their effect on the size. A correlation between the predicted mode size of TSP-microparticles and experimentally determined values was found to exist and is presented in **Figure 3.5 C**. The desirability plot shown in **Figure 3.5 B**, constructed based on the predictions of response surface methodology shows the desirable regression ranges for the atomizing airflow and aspiration to produce 10 µm microparticles. Optimum values of atomizing airflow and aspiration, to produce 10 µm microparticles were determined to be 547 L/h and 55 %, respectively, while the inlet temperature and amount of FITC-Dextran were set at 120 ºC and 0.25 % w/w, respectively.

All predicted values were validated by preparing the microparticles using the optimized spray-drying conditions, and the mode size of the particles was determined. Further, the microparticles loaded with different MW FITC-Dextrans were prepared using the optimized spray-drying conditions. The mode size of all microparticles formulated using optimized process variables as described above are presented in **Table 9**

Table 9 Mode size of formulations containing FITC-Dextran's prepared using optimized spray-drying conditions. Data presented is the mean of three independent experiments ± SD.

Formulation	Mode size (µm)
F5	10.5 ± 0.2
F10	10.3 ± 0.4
F20	10.1 ± 0.2
F40	10.2 ± 0.2

The formulations were identified as F5, F10, F20, and F40, with the numerical value representing the MW of the dextran (in kDa). The mean diameters of the microparticles were in the range of 9 to 12 µm as shown in **Figure 3.6** indicating uniformly sized formulations suitable for nasal administration[226,236].

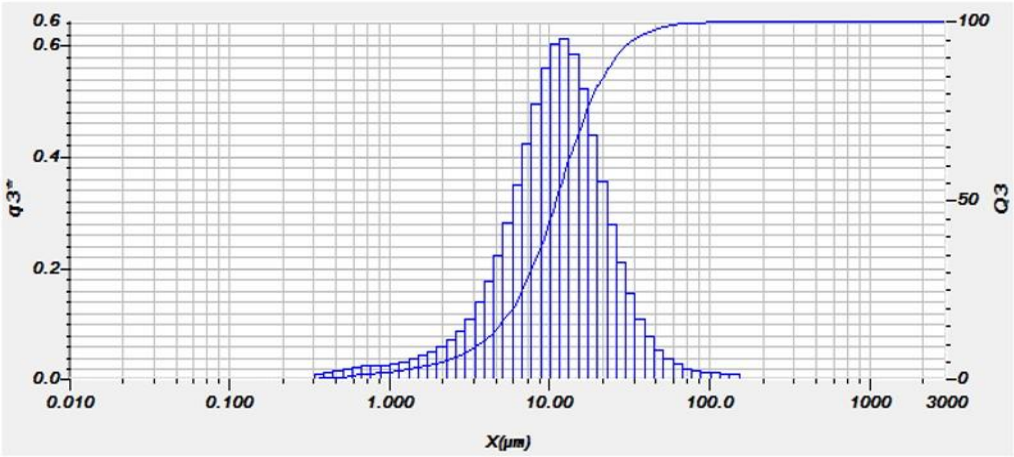

Figure 3.6 Representative particle size distribution of TSP-microparticles spray-dried using optimized formulation parameters.

3.6.2.3 Morphology of TSP-microparticles

The morphology of the microparticles was investigated using SEM. The spray-drying conditions used in pilot studies were able to produce microparticles successfully as shown in **Figure 3.7.** The TSP-microparticles were spherical and corrugated in shape. The majority of the larger particles (> 15 µm) were spherical as shown in **Figure 3.7 A** and the smaller particles (< 5 µm) were corrugated in shape (**Figure 3.7 B).** All particles had a smooth surface.

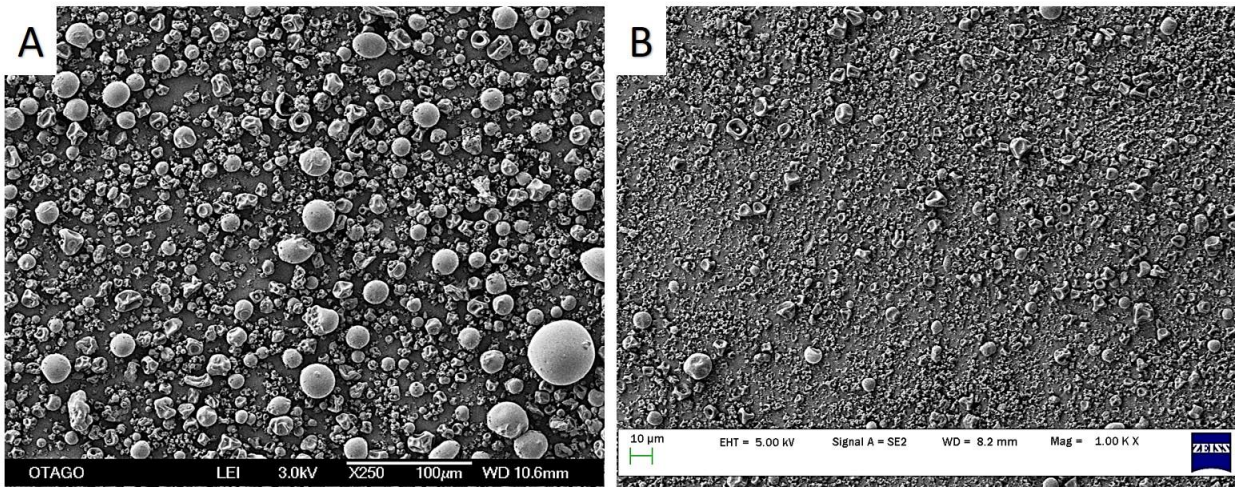

Figure 3.7 Representative SEM micrographs from the pilot studies showing the microparticle formation with TSP alone. Huge variation in particle size (large >15 µm (A) and small < 5 µm (B)) was observed at different levels of formulation parameters.

The morphology of TSP-Microparticles containing FITC-Dextrans obtained by spray-drying with optimized formulation parameters is shown in **Figure 3.8**. Addition of FITC-Dextrans also produced microparticles with corrugated shape and smooth surface. No significant morphological differences were observed with the particles containing different FITC-Dextrans.

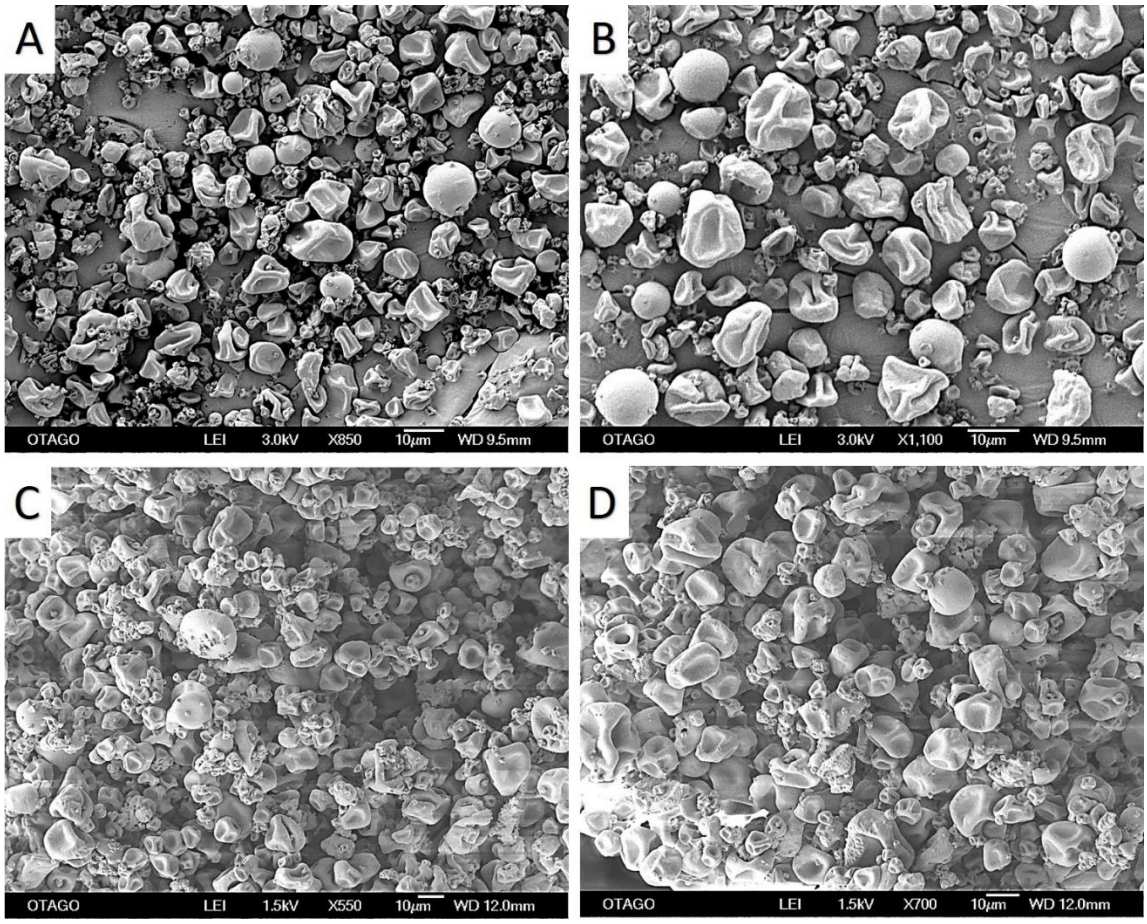

Figure 3.8 Representative SEM micrographs of TSP-microparticles containing FITC-Dextran (A) 5 kDa, (B) 10 kDa, (C) 20 kDa and (D) 40 kDa. All the formulations were similar in appearance and the microparticles were corrugated in shape.

Microparticles were physically broken using a mortar and pestle and observed under SEM to examine their core. The TSP-microparticles produced were hollow (**Figure 3.9 B)**.

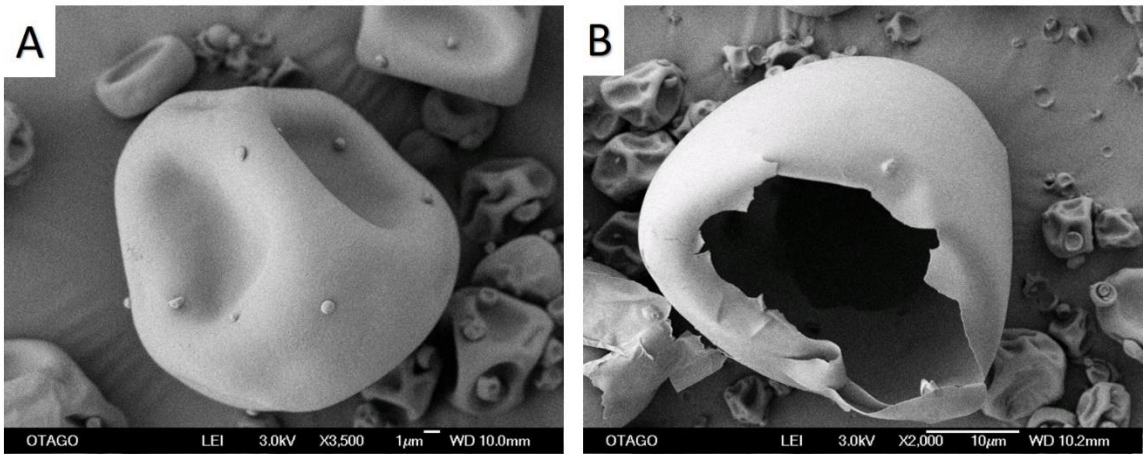

Figure 3.9 Representative electron micrographs of TSP-microparticles showing the smooth rupture free surface (A) and showing the hollow core (B). The microparticles were physically broken and examined under SEM to reveal the hollow core.

3.6.2.4 FITC-Dextran content

Quantification of FITC-Dextrans encapsulated in TSP-microparticles was carried out by fluorescence spectroscopy. A series of standard curves were prepared with FITC-Dextrans and used to calculate the fluorescence of unknown samples, as presented in **Figure 3.10.** The background fluorescence from TSP was normalized to construct the standard curves.

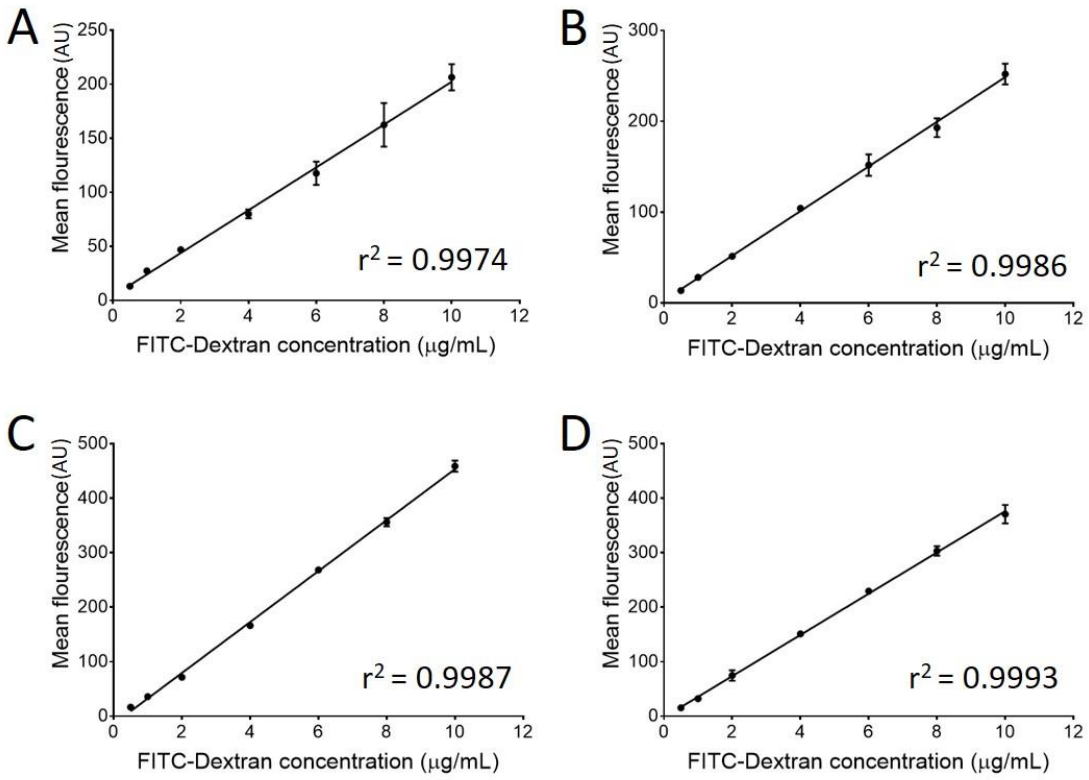

Figure 3.10 Standard curves and r^2 values of FITC-Dextrans with a MW (A) 3-5 kDa, (B) 10 kDa, (C) 20 kDa and (D) 40 kDa. (AU = arbitrary units)

The fluorescence was used to quantify the amount of FITC-Dextran entrapped in the microparticles. **Table 10** presents the entrapment efficiency (%) and drug loading (%) of microparticles for all the FITC-Dextrans used.

Table 10 Drug loading and encapsulation efficiency of 3-5 kDa (F5), 10 kDa (F10), 20 kDa (F20) and 40 kDa (F40) FITC-Dextrans in TSP-microparticles. Data presented is the mean of three independent experiments ± SD.

Formulation	Drug loading (%)	Encapsulation efficiency (%)
F5	20.6 ± 0.1	82.6 ± 0.5
F10	19.8 ± 0.3	79.3 ± 1.1
F20	24.2 ± 0.6	75.7 ± 0.5
F40	18.2 ± 0.3	72.8 ± 1.9

The FITC-Dextran loading of TSP-microparticles was also determined qualitatively under fluorescence microscopy. The green fluorescence produced by the FITC is shown in **Figure 3.11**.

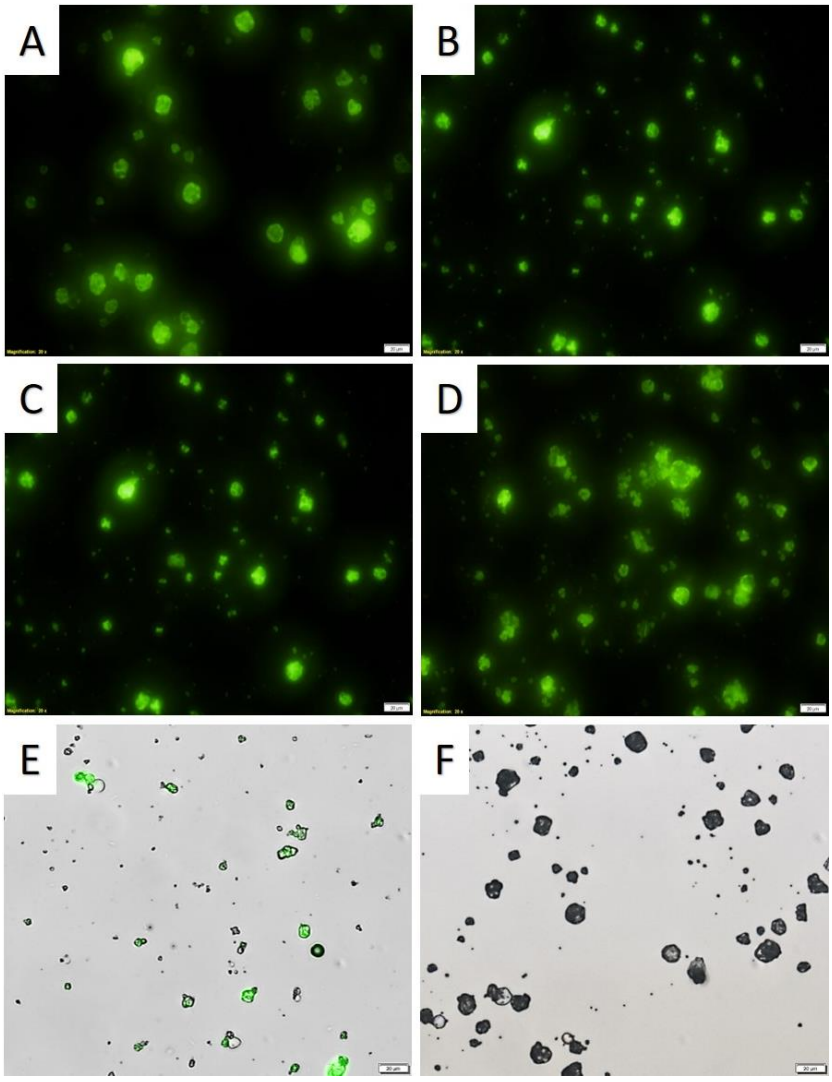

Figure 3.11 Representative fluorescence micrographs (20X magnification) of TSP-microparticles containing FITC-Dextran; (A) 5 kDa; (B) 10 kDa; (C) 20 kDa; and (D) 40 kDa. Representative overlapped fluorescence and light micrographs of TSP-microparticles containing FITC-Dextran (E) and Blank TSP-microparticles (F). FTIC-Dextran loaded in microparticles produces green fluorescence when excited with the fluorescence illuminator suggesting its incorporation into the TSP-microparticles. However, the green fluorescence is not observed in the blank microparticles (Scale bar = 20 µm).

3.6.3 The mucoadhesive potential of TSP-microparticles

A combination of *in-vitro* and *ex-vivo* techniques was used to investigate the interaction of TSP-microparticles with mucin as an indicator of mucoadhesiveness. The percentage of FITC-Dextran that remained adhered to a piece of filter paper saturated with mucin after application of an air load was quantified and expressed as a percentage of the original amount of FITC-Dextran applied (**Figure 3.12 A**). Applying an air load is a useful way to determine, *in-vitro*, the effect breathing may have on the clearance of microparticulate formulations from the nasal cavity ('nasal retention') after administration. The percentage of FITC-Dextran that remained adhered to the filter paper was comparable across all microparticle formulations. However, it was higher when compared to unformulated FITC-Dextran powders, which were used as controls ($P < 0.001$). Mucoadhesive strength was determined *ex-vivo* using porcine mucosa and a tensile strength apparatus and the results are shown in **Figure 3.12 B**. The strength required to detach (mucoadhesion strength) the microparticles from the mucosa was significantly ($P < 0.0001$) higher than the mucoadhesion strength of unformulated FITC-Dextran powders. The mucoadhesion strength of all the formulations containing different MW FITC-Dextrans was comparable and also was comparable to the *in-vitro* studies using the mucin-saturated filter paper.

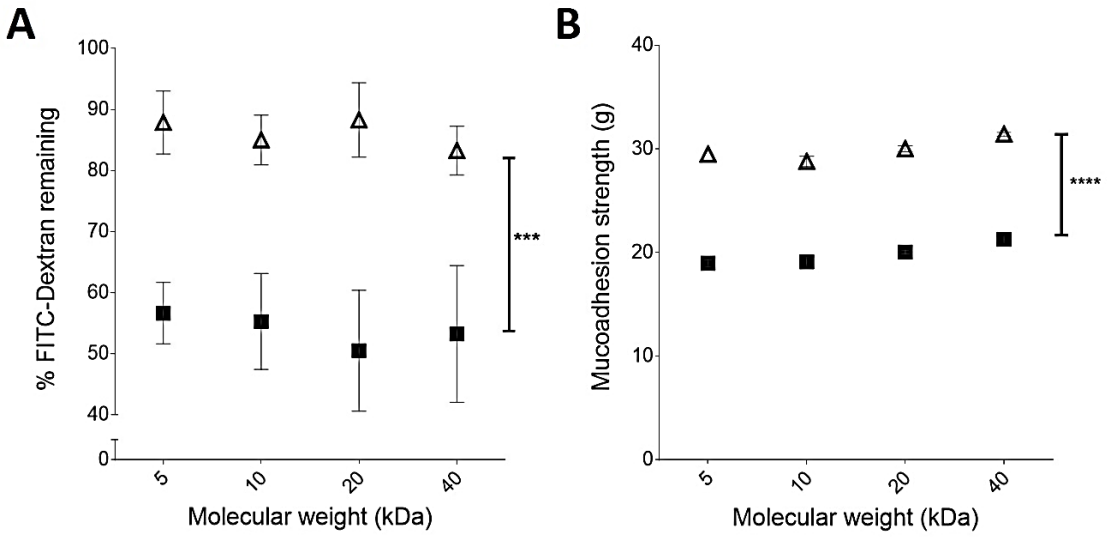

*Figure 3.12 Mucoadhesive properties of FITC-Dextran containing TSP-microparticles (triangle) or unformulated FITC-Dextrans (square) in-vitro (A) and ex-vivo (B) as a function of the MW of the FITC-Dextran. Data presented is the mean of three independent experiments ± SD. (***P < 0.001 and **** P < 0.0001).*

3.6.3.1 Mechanism of mucoadhesion determined by cryo-FESEM

The interaction of TSP-microparticles with mucin was investigated microscopically by plunge freezing a sample of mucin with microparticles deposited on it. Samples were viewed at pre-determined time intervals under the cryo-FESEM (**Figure 3.13**). The time-series cryo-FESEM micrographs show the initial contact (**Figure 3.13 B**, white arrowhead) followed by gradual formation of a gel-like layer due to the interaction between the TSP-microparticles and the mucin layer (**Figure 3.13 C** and **D**, white arrows). The rough surface features of the mucin layer as shown in **Figure 3.13 A** gradually changes to a smoother surface after interacting with TSP-microparticles (**Figure 3.13 C** and **D**, red arrows)

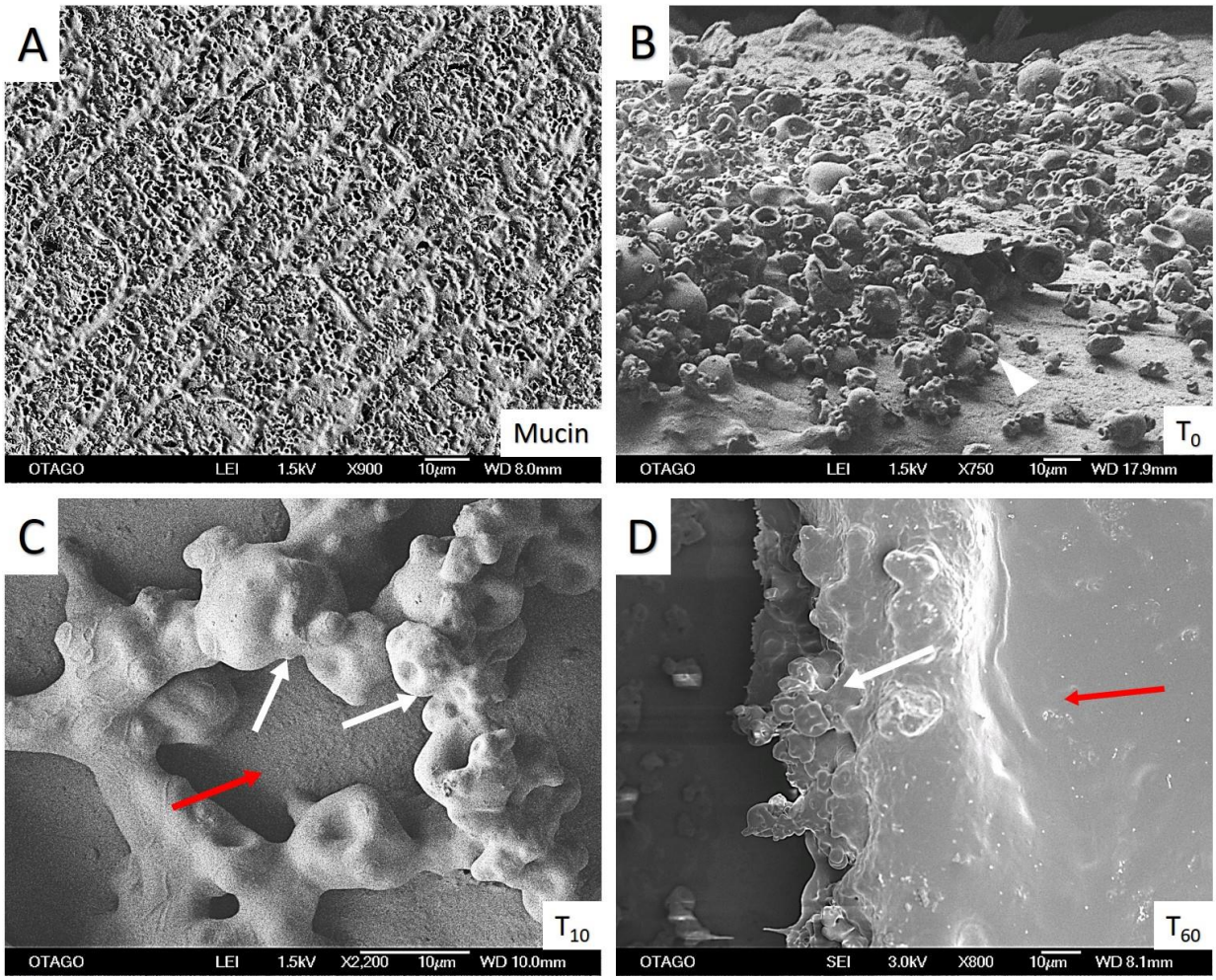

Figure 3.13 Representative cryo-FESEM micrographs of a 2 % w/v solution of mucin only (A) or mucin over 60 min (T_0-T_{60}) after deposition of TSP-microparticles on it (B-D). The initial contact stage between mucin and TSP-microparticles (B, arrowhead) is followed by interaction of the microparticles with the mucus layer (consolidation stage, white arrows) and gradual formation of a smooth gel layer (red arrows) (C and D).

3.6.4 The release of FITC-Dextrans from TSP-microparticles

Any drug incorporated into the microparticles must first be released from it to permeate across the nasal mucosa to have a biological effect in the CNS. *In-vitro* permeability studies are a useful tool for understanding the drug release potential of a formulation. Cumulative release profiles of FITC-Dextrans (3-40 kDa) from TSP-microparticles across a cellulose acetate membrane are shown in **Figure 3.14**. The unformulated FITC-Dextran solution was used as a control. It is evident from the data that incorporation into TSP-microparticles sustains the release of the FITC-Dextran molecules ($P < 0.01$) particularly over the first hour (**Figure 3.14 inset**). However, the release profiles of formulated and unformulated FITC-Dextrans were comparable after 2 h, and the effect of the MW of FITC-Dextrans on release was insignificant. The initial burst release of FITC-Dextrans from TSP microparticles reported within the first 15 min is likely a result of the desorption of a small proportion of FITC-Dextrans weakly associated with or adsorbed to the surface of TSP-microparticles upon contact with the dissolution medium.

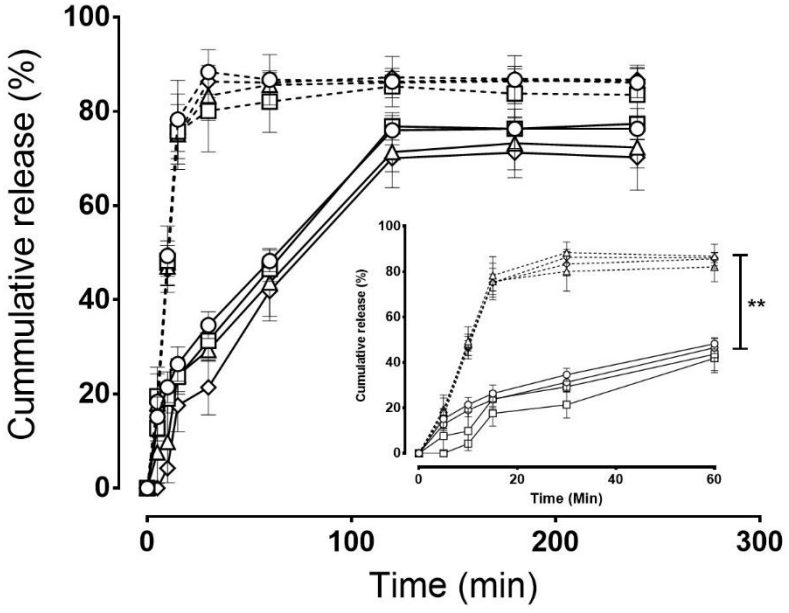

*Figure 3.14 Cumulative release over time of 3-5 kDa (circle), 10 kDa (square), 20 kDa (triangle) and 40 kDa (diamond) FITC-Dextrans formulated in TSP-microparticles (solid lines) or as an unformulated solution (dotted line). The inset shows release within the first 60 min of the study. Data presented is the mean of three independent experiments ± SD. (** $P < 0.01$).*

The *in-vitro* drug release results for the first hour were fitted into zero-order, first-order, Higuchi, and Korsymeyers-Peppas models to determine the release kinetics and presented in **Table 11.**

Table 11 Kinetics of FITC-Dextran release from TSP-microparticles.

Formulation	Zero-order (r^2)	First order (r^2)	Higuchi (r^2)	Korsmeyer-Peppas (r^2)
F 5	0.865	0.874	0.996	0.996
F 10	0.902	0.879	0.998	0.915
F 20	0.905	0.749	0.948	0.822
F 40	0.948	0.691	0.876	0.985

3.6.5 Permeability of FITC-Dextrans across a porcine nasal mucosa

Ex-vivo studies were conducted to determine if drug released from TSP-microparticles can then permeate across the nasal mucosa. Freshly acquired porcine nasal mucosa was used in these studies due to its morphological similarities with the human nasal mucosa[357]. The permeability of FITC-Dextrans formulated in TSP-microparticles across the porcine nasal mucosa shown in **Figure 3.15 A-D** was significantly slower compared to a solution of the FITC-Dextrans ($P < 0.05$). The cumulative amount of FITC-Dextran from TSP-microparticles penetrating the mucosa per unit area (cm^2) versus time was plotted.The steady state flux (J_{ss}) was calculated from the slope of the linear portion of the curves and is shown in **Figure 3.15 E**. The plot shows that J_{ss} of FITC-Dextran incorporated in microparticles across the porcine nasal mucosa is inversely proportional to its size.

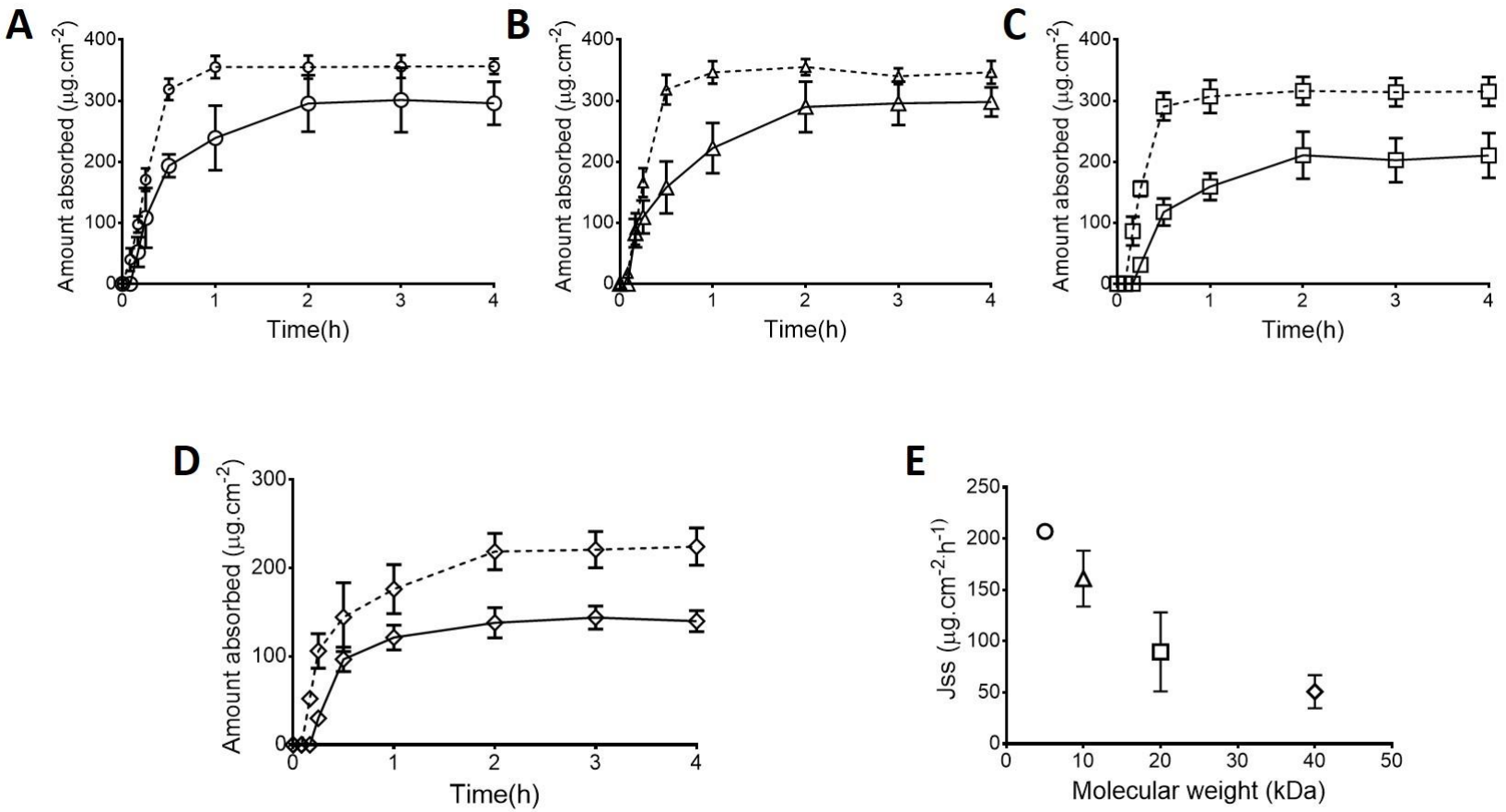

Figure 3.15 Permeability across porcine nasal mucosa over time of 3-5 kDa (A), 10 kDa (B), 20 kDa (C) and 40 kDa (D) FITC-Dextrans formulated in TSP-microparticles (solid lines) or as an unformulated solution (dotted line). Flux (Jss) as a function of the MW of FITC-Dextrans across porcine nasal mucosa (E). Data presented is the mean of three independent experiments ± SD.

3.6.6 Olfactory deposition of 10 µm sized TSP-microparticles containing FITC-Dextrans

To determine if 10 µm sized TSP-microparticles are capable of depositing in the olfactory region of humans after intranasal administration, they were nebulized under normal breathing conditions and administered into a 3D printed cast of a human nasal passage, the experimental setup constructed, validated and used for the deposition studies is shown in **Figure 3.16**.

The nasal cast was air sealed except for the nostrils and throat. The vacuum pipe was inserted into the throat of the nasal cast. The vacuum pump was adjusted to produce ~20 L min^{-1} inhalational airflow rate. The flow rate was monitored before and after the experiment by an anemometer. The microparticles were nebulized for 2 sec in one of the nostrils using an air compressor acting at low airflow rates (~5 L min^{-1}). Consequently, the nasal cast was disassembled and the particles deposited in the olfactory region were carefully collected. The FITC content was quantified using fluorescence spectroscopy and used to calculate the deposition efficiency.

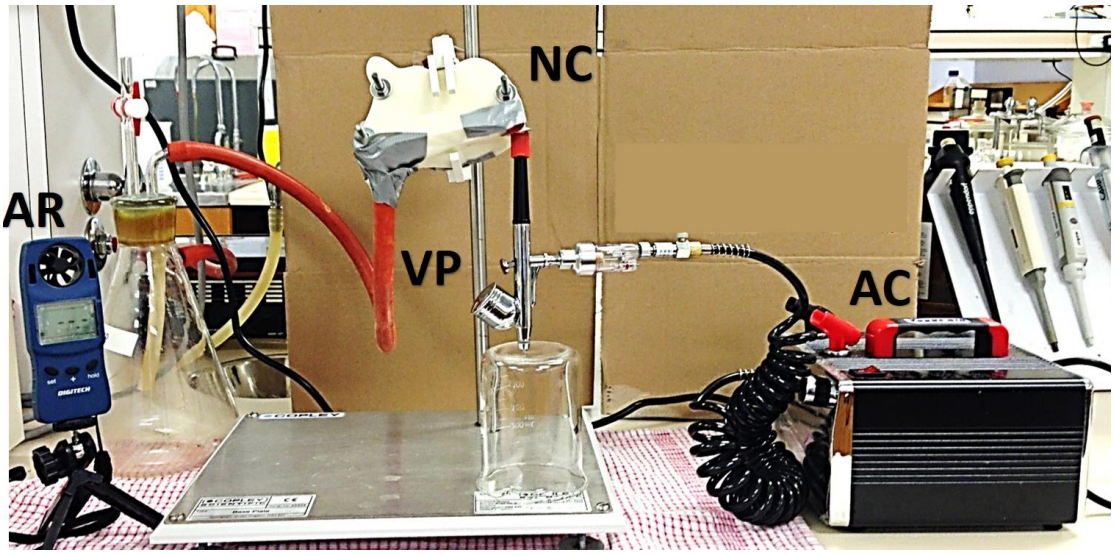

Figure 3.16 Experimental set up used for particle deposition experiments. [anemometer: AR, vacuum pipe: VP connected to a vacuum pump, nasal cast: NC, and air compressor: AC]. The equipment was air sealed with duct tape.

The deposition of microparticles in the 3D printed human nasal cast after nebulization is shown in **Figure 3.17.** The amount of FITC-Dextrans was used to indirectly quantify the extent of microparticle deposition in the olfactory region of the nasal cast.

Figure 3.17 Representative picture showing the deposition of TSP-microparticles containing FITC-Dextrans in the nasal cast, the yellow color observed was due to the FITC.

All formulations were compared against 2 µm sized TSP-microparticles containing FITC-Dextrans. Powder-based formulations of 2 µm in size are known to deposit preferentially in the lung due to their smaller size, therefore used as a control[213]. The deposition efficiency of the TSP-microparticles is shown in **Figure 3.18.**

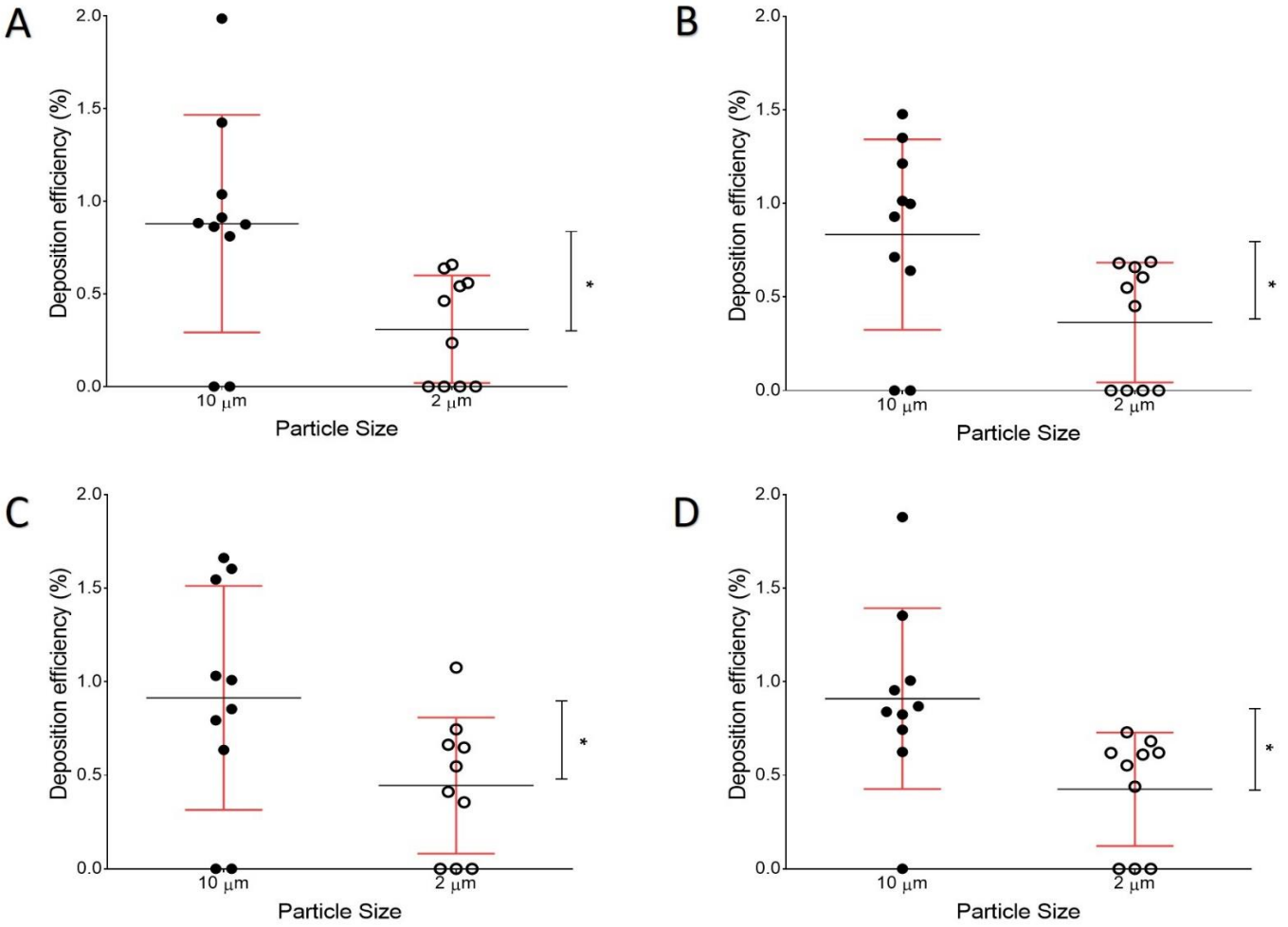

Figure 3.18 Deposition efficiency of 10 µm versus 2 µm TSP-microparticles containing 5 kDa (A), 10 kDa(B), 20 kDa(C) and 40 kDa(D) FITC-Dextrans in the olfactory region of a human nasal replica 3D printed cast when nebulized under normal breathing conditions (20 L/min). Data presented is the mean of 10 independent experiments ± SD. ($P < 0.05$).*

Deposition in the olfactory region is reported as deposition efficiency and the data is presented in **Figure 3.18**. Deposition efficiency ranged from 0 to 1.9 % with 10 µm microparticles as compared to 0 to 0.7 % with 2 µm microparticles. In some experiments, olfactory deposition of microparticles was negligible, so for these experiments, the deposition efficiency is reported as zero. Consequently, a large number of independent experiments were conducted to ensure reproducible and statistically robust data. Overall, microparticles with a mode size of 10 µm showed significantly higher deposition efficiency (****$P < 0.0001$) in the olfactory region compared to the 2 µm particles.

3.6.7 Safety of TSP-microparticles for nasal administration

Histopathological analysis of porcine nasal mucosa at the completion of the *ex-vivo* studies (**Section 3.6.5**) is shown in **Figure 3.19**. Freshly acquired, untreated nasal mucosa was used as a control as shown in **Figure 3.19 A**. Mucosal structures such as the surface epithelium, the underlying connective tissue, and serous glands are evident in the micrographs as shown in **Figure 3.19 B-E**. The cylindrical appearance of epithelial cells retaining their overall polarity is a good indicator of structural integrity[250]. No visual evidence of epithelial cells detached from the mucosa or large vacuolated regions, necrosis, hemorrhage or ulceration (large red colour spots), were identified in tissues treated with TSP-microparticles as shown in **Figure 3.19 B-E** and these were comparable to the negative control. Marked alterations to the epithelium with a detachment of the epithelial layer, the presence of rounded epithelial cells and loss of polarity could be seen in the histopathology of the positive control as shown in **Figure 3.19 F**. The histopathlogy of nasal mucosa in this case is in agreement with other reports of the toxic effect of nitric acid on the nasal mucosa[171,358,359].

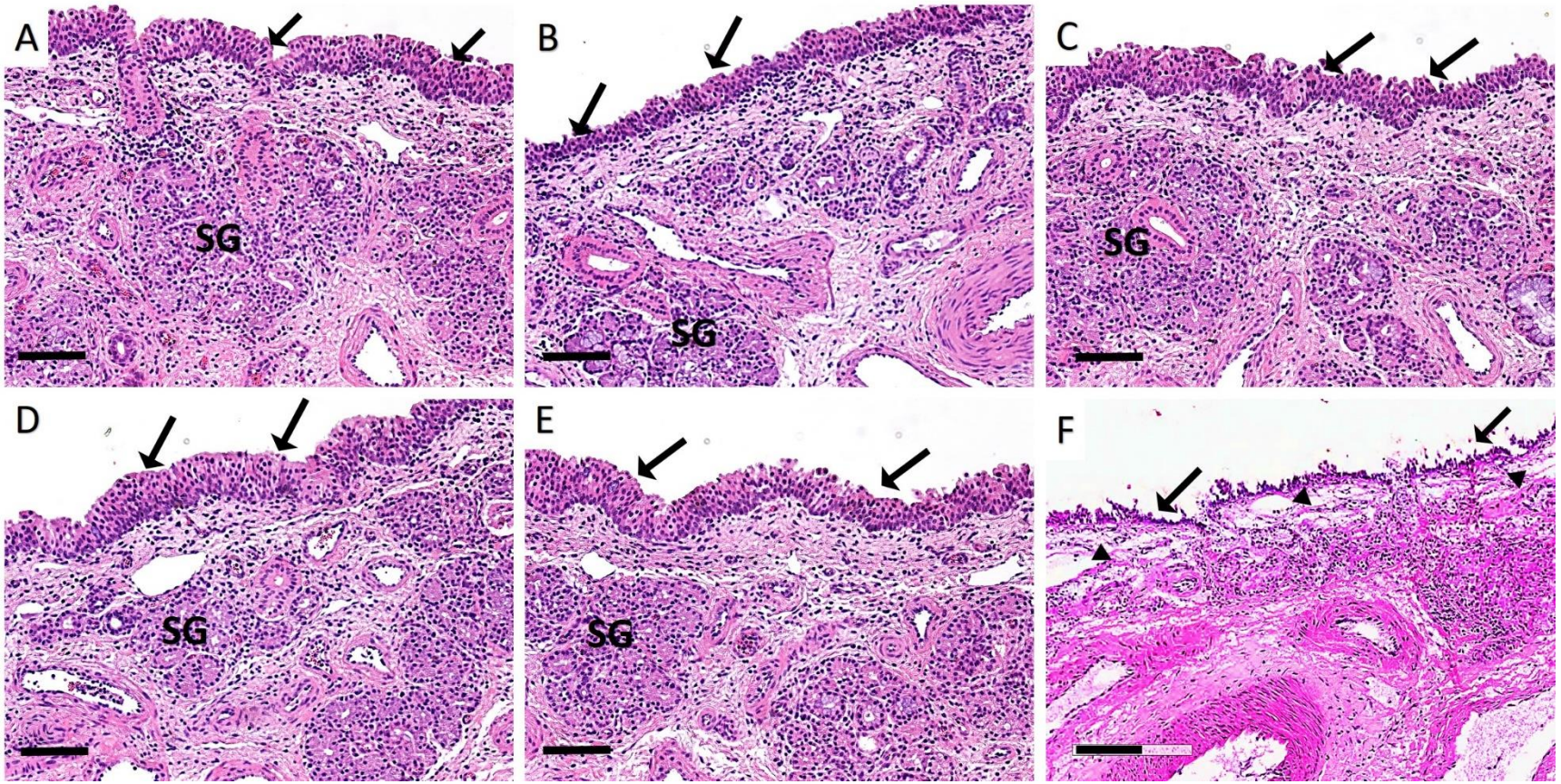

Figure 3.19 Representative light micrographs of porcine olfactory nasal mucosa after exposure to TSP-microparticles containing FITC-Dextran (B) 5 kDa, (C) 10 kDa, (D) 20 kDa and (E) 40 kDa. Freshly acquired nasal mucosa was used as negative control (A) while mucosa treated with 37 % v/v nitric acid served as a positive control (F). (SG: serous glands). The arrows and arrowhead indicate histopathology of the olfactory epithelium and large vacuoles, respectively. (Scale bar = 100 µm).

3.7 Discussion

The potential advantages that TSP formulated as microparticles can offer to the nose-to-brain delivery of drugs, the unexplored potential of TSP as a macromolecular drug carrier, and the understated nasal drug carrier properties of TSP are the driving factors for the research presented in this **Chapter**.

The majority of the literature has followed the extraction of TSP described by Rao *et al*[233]. Since it is an easy and straightforward method, it was used in this chapter for the extraction of TSP from tamarind seed gum. The IR spectrum of extracted TSP produced characteristic functional group IR peaks, and the x-ray diffractograms showed no sharp peaks indicating the amorphous nature of the TSP. The IR spectrum and the x-ray diffractograms were comparable to the data available in literature[355]. Furthermore, the SEM observation of TSP revealed a smooth surface and was similar to the published literature[356]. In addition, no batch variation was observed between TSP extracted on different days, x-ray diffractograms and IR spectrum were identical. Published scientific reports identified similar properties for polysaccharides with no batch variation when a similar method of extraction has been used[360,361].

Formulating TSP as microparticles and optimizing the microparticle size to 10 µm was one of the research aims of this chapter. In this thesis, the size of particles is reported as "mode size" the most common size within a particle population. Pilot studies and a DOE approach (Box-Behnken experimental design) was employed to optimize the formulation parameters. The effect of formulation parameters on the microparticle size was analyzed by ANOVA to understand their effect and atomizing airflow and aspiration were found to be significant factors affecting the particle size. The velocity of the compressed air passing through the nozzle (atomizing air flow) can significantly affect the particle size by determining the size of droplets formed from the feed solution[339,362]. The velocity of the drying gas (aspiration) determines the time of droplet drying in the chamber which might have affected the size of the particles[339]. Among the formulation parameters tested, FITC-Dextran concentration and inlet temperature did not significantly affect particle size.

The reason for this can be attributed to the low amount of FITC-Dextrans used in this study and that the temperatures were higher and sufficient to dry the solvent (water) quickly, resulting in an insignificant effect on the resultant microparticle size.

To identify the optimal levels of formulation parameters to produce the 10 µm particles the Design Expert software was used. Design Expert provides a user interface to target the particle size to a specific range manually and predicts the optimal levels of formulation parameters required to produce the target range of particle size. The particle size target was set to 10 µm and the predictions of formulation parameter levels acquired from Design Expert. The levels of two significant parameters: atomizing airflow and aspiration, were predicted to be 547 L/h and 55 % respectively, in order to produce 10 µm sized particles. These predictions were tested practically and resultant particle size was measured. The optimized levels of formulation parameters were found to produce the 10 µm sized particles reproducibly. FITC-Dextran with MW 3-5 kDa was employed for these studies. Microparticles were prepared using the optimized levels of formulation parameters with all the other FITC-Dextrans. The MW of the FITC-Dextran did not show any effect on the particle size. This could have been be due to the constant amount of the FITC-Dextrans (0.25 % w/w) used in all the formulations. Spray-Drying TSP with FITC-Dextrans of different MW at the optimized levels of formulation parameters produced 10 µm sized TSP-microparticles containing FITC-Dextrans.

Spray-dried TSP-microparticles containing FITC-Dextrans were corrugated in shape and hollow. Corrugated particle shape has been reported to lower the true area of contact between the particles thereby reducing the cohesiveness between particles which is the desired quality for intranasal administration[363,364]. Hollow particles improve the dispersibility of the solid microparticles[339] which can be a desirable property for intranasal delivery end use aimed for in this thesis. The surfaces of the microparticles observed were rupture free, which is desirable as such microparticles have been reported to have proper deposition and delayed clearance from the nasal cavity[365]. There were no significant differences observed between the morphology of the TSP-microparticles containing different MW FITC-Dextrans.

The FITC-Dextran content in the microparticles was determined by fluorescence spectrophotometer. The results indicated that TSP could successfully load high MW dextran

molecules up to 40 kDa. The molecular interactions of dextran chains with TSP and the low drug loss in the spray-drying process might have contributed to the high encapsulation efficiency of the TSP-microparticles. The green fluorescence of the FITC in TSP-microparticles observed with fluorescence microscopy confirmed the loading of FITC-Dextrans. These results suggest that TSP can be a potential macromolecular drug carrier for drug delivery applications.

One of the beneficial features of TSP for intranasal drug delivery is its potential ability to resist mucociliary clearance. The mucoadhesive potential of TSP was evaluated to identify the potential of TSP-microparticles to increase their residence time in the nasal cavity. In the present study, two *in-vitro* approaches and an *ex-vivo* approach were used to confirm the mucoadhesive properties of FITC-Dextran loaded TSP-microparticles. Firstly, the amount of TSP-microparticles containing FITC-Dextran that adhered to a piece of filter paper saturated with mucin after application of an air load was determined by quantifying the amount of FITC-Dextran and represented as *in-vitro* mucoadhesion. It is a quick and useful approach to determine the effect of air-flow on nasal clearance of microparticulate formulations after their administration into the nasal cavity. Previously reported techniques for *in-vitro* mucoadhesion had applied the air load only one-way to simulate the process of inhalation but not exhalation[209]. In, the current study, respiration was simulated by incorporating the airflow from two directions in an attempt to better represent the respiratory conditions when a formulation is inhaled. *In-vitro,* TSP-microparticles showed significantly higher mucoadhesion compared to the unformulated FITC-Dextran powders. The mucoadhesive potential of TSP can be attributed to the hydrogen bonding capacity of –OH groups on the side chains of TSP. These functional groups interact with other electronegative atoms in mucin and form a hydrogen bond. Furthermore, van-der-Waals bonds may also arise due to the dispersion forces in TSP contributing to the mucoadhesion.

Ex-vivo mucoadhesion studies using the tensile strength apparatus complemented the *in-vitro* study and demonstrated the potential of TSP-microparticles to adhere to the mucosa in the nasal cavity. Tensile strength is, a widely employed method for the assessment of mucoadhesion[366]. In this chapter, the force required to detach the microparticles from porcine nasal mucosa was represented as mucoadhesive strength. Assessing mucoadhesion of

microparticles is challenging due to the small size of the particles. In this study, an industrial grade strong adhesive epoxy was employed to ensure the firm adhesion of microparticles to the probe. This prevented the loss of microparticles onto mucosa when the probe measured the detaching force. The exclusively designed mucoadhesion rig minimized any equipment errors. TSP-microparticles demonstrated significantly high mucoadhesion strength compared to the unformulated FITC-Dextran powders. Mucoadhesive properties were comparable across all microparticle formulations in *in-vitro* and *ex-vivo* studies and are most likely the result of the constant amount of polymer and FITC-Dextran used in each of the formulations investigated (2 % of total solids)[367].

Cryo-FESEM was used to investigate the interaction between TSP-microparticles and mucin. This work is the first electron microscopy study to identify the two critical stages which have been hypothesized to occur during the mucoadhesion process; contact and consolidation[221]. In the initial contact stage, contact between microparticles and the mucus layer was visible, and no apparent changes were seen in the morphology of the microparticles or the mucin. In the following consolidation stage, the interaction of TSP-microparticles with the mucus layer was evident. The interaction is most likely due to the moisture present in the mucin, which allows the TSP to swell and penetrate the mucin layer. Subsequently, the TSP conforms to the shape of the mucin by forming a gel-like layer most likely by weak Van der Waals attraction and hydrogen bonding [221,228].

While controlled release of a drug molecule is considered 'gold standard' in formulation science, the optimal release profile of a drug from an intranasal delivery system is dependent on several parameters, in particular, the drug molecule itself, the therapeutic indication and the required dose. Controlled release of drugs formulated in TSP in combination with other polymers has been shown for at least 10 to 12 h *in-vitro*. However, the release of drug molecules from TSP-only formulations was reported to be relatively quicker (approximately 6 h)[300,316]. The likelihood that any formulation is retained in the nasal cavity for periods as long as 10 to 12 h despite its mucoadhesive nature is unlikely and often not desired. Therefore, in the present chapter, release studies over a 4 h period were considered as a practical time frame which would most likely encompass the timeframe of any nasal clearance that occurs *in-vivo*. The mechanism of FITC-Dextran release was found to be

diffusion controlled as the data fit well with the Higuchi model of drug release. The mechanism of drug release from TSP can be compared to hydrogels as, the microscopy studies and previous reports in the literature show that TSP forms a gel-like viscous layer on contact with the mucin by absorbing water and simultaneously releasing the FITC-Dextrans loaded in the microparticles via diffusion[368,369]. However, the drug release from the F40 formulation fitted a Korsmeyer-Peppas model indicating that the drug release is by both diffusion controlled and erosion controlled mechanisms. Why this was the case for the F40 remains unclear.

Furthermore, *ex-vivo* studies using porcine nasal mucosa were conducted as such studies provide useful data about the permeability of drug molecules across a mucosal barrier before testing *in-vivo*. The permeation of FITC-Dextrans released from TSP-microparticles was dependent on MW. The FITC-Dextrans employed in this chapter were ≤ 40 kDa in size and their *ex-vivo* permeation flux decreased with increase in MW as their permeation across the mucosa was diffusion dependent. It has been reported that FITC-Dextrans with MW lower than 40 kDa cross biological barriers primarily by diffusion and in small amounts by pinocytosis[370].

Collectively, the *in-vitro* data suggest that release of hydrophilic molecules (≤ 40 kDa) from TSP-microparticles was independent of MW and followed a typical biphasic profile. The initial burst release reported was most likely surface-associated molecules that dissolved quickly upon contact with the solvent. This is supported by the near 100 % release reported with FITC-Dextrans in solution. However, unlike FITC-Dextrans in solution, the release of FITC-Dextrans formulated in TSP-microparticles was significantly slower which was most likely because the FITC-Dextrans had to diffuse through the gel layer which is rapidly formed when TSP-microparticles interact with mucin, as was seen by cryo-FESEM. The *ex-vivo* studies show that permeability of molecules across the nasal mucosa is strongly dependent on their MW. The size-dependent permeability of FITC-Dextrans across the olfactory mucosa and into the brain after intranasal administration has been demonstrated *in-vivo* [371].

Another objective of this **Chapter** was to investigate the deposition of 10 µm sized particles in the olfactory region of the human nasal cavity. A 3D human nasal replica cast

coated with 2 % w/w mucin solution inside the nasal passages was employed for this purpose. Deposition of particles in the geometrically complex human nasal cavity has been shown to be influenced by particle size, the inhalational flow rate and the position in the nasal cavity from where the drug is administered[76]. Particles 10 µm in size have recently been demonstrated to have an optimum deposition in the olfactory region of the nasal cavity[215]. TSP-microparticles (2 and 10 µm) were nebulized at the nostrils in a 3D printed human nasal cast under a normal inhalational flow rate (20 L/min). Such *in-vitro* studies provide useful data on the regional nasal deposition of particles before human testing. The influence of size on particle deposition in the olfactory region was reported in the present study, with 10 µm-sized microparticles showing better deposition than 2 µm-sized microparticles. The better deposition can be attributed to the inertia of the particles, where particles with 10 µm size have the optimum inertia to reach the upper narrow olfactory region. Deposition of microparticles was independent of the MW of the incorporated FITC-Dextrans. This study demonstrated that formulating microparticles to 10 µm size can enhance their deposition in the olfactory region of the human nasal cavity. In this chapter, the safety of TSP-microparticles containing FITC-Dextrans was assessed *ex-vivo* on the porcine nasal mucosa. Structural integrity and epithelial cell structure were preserved in the mucosae treated with TSP-microparticles demonstrating the safety of TSP-microparticles for intranasal administration. These results agree with the previously reported safety data of TSP for intranasal applications[275,334].

Collectively, this **Chapter** evaluated the potential of TSP as a nasal drug carrier and macromolecular drug carrier. The combined formulative approach of formulating mucoadhesive microparticles as 10 µm particles improved their deposition in the olfactory region and the mucoadhesive potential of TSP may increase the intranasal residence time of the drug. A significant advantage of TSP is that it is structurally very similar to mucin and demonstrates mucoadhesive properties. Furthermore, the established tolerability of TSP in humans makes it a great candidate for a nasal preparation[266].

3.8 Key findings

This chapter of the thesis tested a simple formulative approach of incorporating drug molecules in 10 µm-sized mucoadhesive microparticles to target them to the olfactory region of the nasal cavity. Collectively, the data reported in this chapter suggest that the TSP can act as a carrier for the high MW drugs and can be formulated as 10 µm-sized particles by spray-drying technique. TSP-microparticles have the potential to increase the residence time of drugs in the nasal cavity by mucoadhesion and are safe to the nasal mucosa after acute nasal administration. The 10 µm-sized TSP-microparticles can improve the olfactory deposition at normal inhalation rates.

3.9 Future directions

Although enhanced olfactory deposition with size tailored particles has been reported in this study, further human studies are required to correlate increased deposition efficiency with the biological relevance. Critical research quesitons such as, does increased depositon in the olfactory region affect brain uptake of drugs? Is the increase in depositon sufficient to produce a biological effect? need to be answered in future studies.

Although the safety of TSP has been reported *ex-vivo*, further studies investigating the safety and tolerability of TSP-microparticles *in-vivo* after acute and chronic intranasal administration are required to progress this drug-delivery platform. The drug release and permeation across the nasal mucosa to reach the brain have to be examined *in-vivo* to further understand the potential of TSP-microparticles in nose-to-brain drug delivery. In addition, the FITC-Dextrans used as model drugs in this study are hydrophilic and the MW tested is only till 40 kDa. Such limitations of this study raise research questions on the potential of the TSP-microparticle delivery system for use with larger and or hydrophobic drugs, which need to be addressed by future studies. Also, study of effect of the surface charge of particles on drug delivery and mucoadhesion needs to be addressed in future work.

Several drug delivery devices that aim to target drug formulations to the olfactory mucosa are already in various stages of clinical trials. While still at a conceptual stage, it would be interesting to explore if this formulative approach used in combination with an

intranasal device can augment olfactory targeting and enable enhanced delivery of therapeutic molecules to the brain via the nose.

Chapter 4

Formulation and In-vivo characterization of TSP-microparticles containing phenytoin

4 Formulation and *in-vivo* characterization of TSP-microparticles loaded with phenytoin

4.1 Introduction

Results from **Chapter 3** demonstrate that TSP can be formulated as mucoadhesive microparticles. This chapter investigates the ability of the TSP microparticle system to load and release an anti-epileptic drug (AED) phenytoin *in-vitro* and its biodistribution in rats following intranasal administration.

4.1.1 Sub therapeutic brain concentrations of drugs in epilepsy

More than 70 million people worldwide are affected by epilepsy, making it one of the most common neurological disorders[372,373]. Unprovoked and recurrent seizures are observed in epileptic patients which are either focal or general in nature[374]. AEDs are the first line of treatment in controlling seizures. However, about one-third of epilepsy patients suffer from uncontrolled seizures despite treatment with at least two or three AEDs. Such a condition is termed 'drug-resistant epilepsy'[375].

One possible reason for treatment failure is inadequate levels of AEDs reaching the brain due to overexpression of the multidrug efflux transporter P-glycoprotein (Pgp) at the blood-brain barrier (BBB) in the tissues surrounding the epileptic focus [376–378]. Along with Pgp various types of multidrug efflux transporters present at the BBB are shown in **Figure** 4.1**.** It is hypothesized that in patients with drug-resistant epilepsy, multidrug efflux transporters at the BBB efflux AEDs at a significantly higher rate, which results in lower brain concentrations of the AEDs[376,377,379]. Overexpression of such efflux transporters severely limit the AED penetration into the brain so that the concentrations of AEDs in the brain cannot become sufficiently high for therapeutic efficacy[380,381]. Consequently, AEDs fail to control the seizures in drug-resistant epilepsy. To improve the efficacy of AEDs simultaneous use of Pgp inhibitors with AEDs has shown promise[382]. However, the

long-term use of Pgp inhibitors can be associated with several intolerable side-effects and development of resistance to the Pgp inhibition[383].

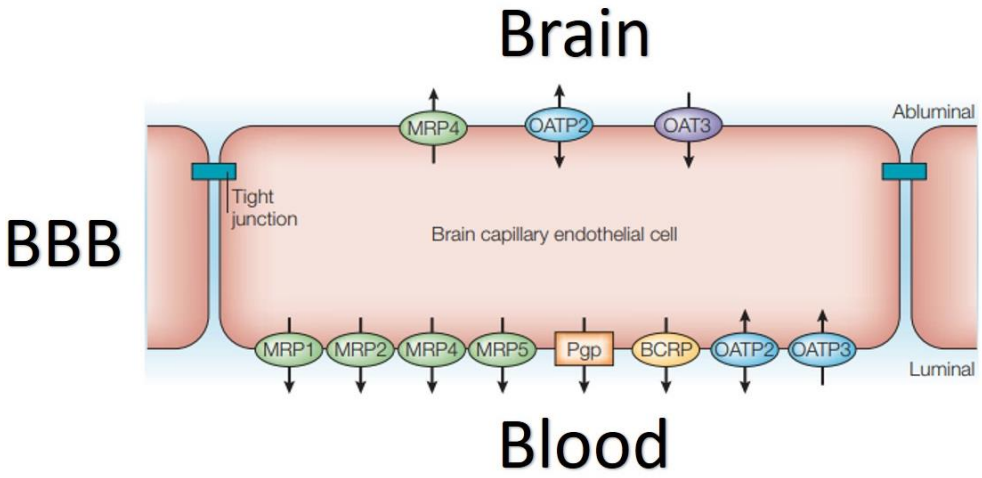

Figure 4.1 Localization of multidrug efflux transporters at the BBB. The efflux transporters at the luminal side are mainly responsible for the restriction of drug entry into the brain. However, transporters at the abluminal side can sometimes act in conjunction with the transporters on the luminal side to enhance the extrusion of drugs from the brain. Arrows indicate the direction of transport of drugs. BCRP, breast cancer resistance protein; MRP, multidrug resistance protein; OAT3, organic anion transporter 3; OATP2/3, organic anion transporting polypeptide 2/3 and Pgp, P-glycoprotein. Figure modified with permissions from Loscher et al[381].

4.1.2 Strategies to enhance the brain concentrations of drugs in epilepsy

In order to overcome the BBB and the effect of multidrug efflux transporters, drugs are administered to the brain by several strategies. Direct brain delivery of drugs by invasive methods such as intrathecal[378], intracerebral implants[384], and BBB disruption techniques[385] are reported. However, invasive methods have been reported to have significant disadvantages such as local toxicity, poor and unpredictable distribution, and low patient compliance[385]. Non-invasive methods such as chemical modification of drugs[386,387], receptor-mediated delivery, cell penetrating peptide-mediated delivery, and intranasal delivery are reported in the literature. As discussed in **Chapter 1,** neurological pathways in the olfactory region can deliver the drugs to the brain while bypassing the BBB and multidrug efflux transporters. Hence, intranasal delivery of AEDs can be advantageous. For example, AEDs such as midazolam administered as an intranasal solution have been shown

to produce enhanced anti-seizure effect compared to IV diazepam in humans[388,389]. Administering the AED lamotrigine[390] and clobazepam[391] intranasally has been reported in literature to achieve higher *in-vivo* brain concentrations. Also, intranasal administration of lorazepam demonstrated favorable pharmacokinetics in humans in relation to IV and IM routes[392].

Formulation strategies to improve AED bioavailability for effective anti-seizure activity has been reported in the literature. For example, formulation of carbamazepine as a β-cyclodextrin-carbamazepine complex has been shown to significantly improve the anti-epileptic activity and bioavailability in rats compared to unformulated AED after intraperitoneal and oral administrations[393,394]. Co-polymerization and co-precipitation of AEDs with polymers have been reported to improve the dissolution and solubility profiles consequently enhancing the bioavailability[395,396]. Formulating AEDs such as stiripentol,[397] carbamazepine,[398–400] rufanimide[401] and phenytoin[402] as solid dispersions has been shown to improve their dissolution profiles.

Delivery of AEDs formulated as nanoparticles have been reported with promising results towards increasing the bioavailability of AEDs[403,404]. For example, polysorbate-80 coated nanoparticles of gabapentin have shown an enhanced concentration in the brain after intraperitoneal administration[405]. Another study where clonazepam was formulated as solid lipid nanoparticles demonstrated improved anticonvulsant activity by enhanced BBB permeability of nanaoparticles[406]. Wang *et al.* reported that hydrogel nanoparticles of phenytoin sodium improve antiepileptic effects by enhancing the brain concentrations[407] and on-demand delivery of phenytoin sodium into the brain by electro responsive nanoparticles in generalized tonic-clonic seizures[408].

Combining formulation strategies with intranasal administration has been reported to produce high brain targeting of AEDs in the literature. For example, Eskandari *et al.* reported that intranasal administration of valproic acid formulated into nanostructures could enhance the brain concentration and consequently produce high anti-seizure activity compared to intraperitoneal administration[409]. Sharma *et al.* demonstrated enhanced brain delivery of lorazepam incorporated into nanoparticles after intranasal administration compared to intranasal solution and intraperitoneal administrations[410]. Vyas *et al.* demonstrated

mucoadhesive microemulsions could significantly increase the direct nose-to-brain transport of clonazepam compared to a solution or non-mucoadhesive microemulsions, into rabbit brain. The brain targeting efficiency of mucoadhesive microemulsions was tested by measuring the radioactivity of administered ^{99m}Tc-labeled clonazepam. Mucoadhesive microemulsions produced higher radioactivity in the brain demonstrating the high targeting efficiency of the mucoadhesive microparticles[411].

Interestingly, the reports on AEDs formulated as intranasal microparticles are scarce. One study reported spray-dried microspheres loaded with phenytoin. The *in-vitro* characteristics of the formulation and the sustained release of phenytoin from microspheres was reported, but no *in-vivo* data was provided[412]. In another study, alginate-chitosan microparticles of phenytoin were formulated. Nonetheless, the study did not report any significant advantage of formulating phenytoin as alginate-chitosan microparticles and concluded that the formulation requires more modifications[413].

Considering the advantages of intranasal administration of AED formulations and the potential of mucoadhesive microparticles as discussed in **Chapter 1**, this chapter investigates the formulation of an AED (phenytoin) into microparticles and its intranasal administration in rats. Phenytoin was selected as a model drug as it is an effective first-line AED and is a substrate of the Pgp multidrug efflux transporter. Over expression of Pgp in drug-resistant epilepsy severely limits the uptake of phenytoin into the brain leading to sub therapeutic levels and treatment failure[414]. Therefore this **Chapter** utilizes phenytoin as a model drug for formulation into the intranasal mucoadhesive microparticles.

4.1.3 Phenytoin

Phenytoin (**Figure 4.2**) was first developed during the 1930s, and it is still in use for the treatment of epilepsy despite the invention of many new AEDs[415]. In addition to its use as an AED, phenytoin is also used as antiarrhythmic[416]. Recently, neuroprotective activity of phenytoin in optic neuritis in patients with multiple sclerosis has been tested with positive results in a Phase II clinical study and new indications for phenytoin are still emerging[415,417].

Phenytoin exhibits anti-epileptic activity by blocking inactive sodium channels and reducing voltage-gated sodium and calcium channel currents[418,419].

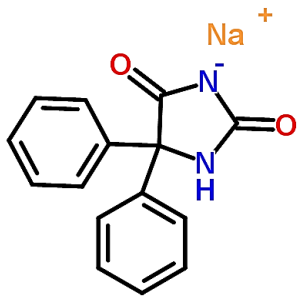

Figure 4.2 Chemical structure of phenytoin sodium (phenytoin).

Due to its poor water solubility (80 µmol/L), its sodium salt, phenytoin sodium, and ester prodrug, fosphenytoin, are used clinically[420,421]. Phenytoin (Sodium 2,5-dioxo-4,4-diphenylimidazolidin-1-ide) belongs to Class II of the Biopharmaceutics Classification System with low solubility and high permeability[422]. Phenytoin is available as a parenteral preparation solubilized at 50 mg/mL with 40 % propylene glycol (PG) and 10 % ethanol[421]. Sodium salt of phenytoin is a low MW (274.25 Da) crystalline powder, which converts into phenytoin when administered and exhibits its pharmacological activity. Phenytoin undergoes metabolism in the liver by cytochrome P450 enzymes to form its major metabolite '5-(4-Hydroxyphenyl)-5-phenyl-hydantoin'[423]. The amide groups (-NH) in the phenytoin molecule (**Figure 4.2**) are reported to interact with excipients by hydrogen bonding and improve the solubility of phenytoin[394,421,424].

4.1.4 TSP-microparticles loaded with phenytoin for nose-to-brain delivery

It is evident from a review of literature that there is still a need for studies to explore the potential of formulation strategies combined with intranasal administration for AEDs. With the advantages mucoadhesive microparticle formulation can provide as discussed in **Chapter 1**, and the supporting results from **Chapter 3**, formulating AEDs into

TSP-microparticles with 10 µm size could have the potential for enhancing nose-to-brain drug delivery of phenytoin and therefore forms the focus of this chapter. However, the low solubility and high crystallinity of phenytoin pose research questions:

- Whether phenytoin can be formulated as 10 µm sized TSP-microparticles?
- Whether phenytoin can affect the mucoadhesive potential of TSP-microparticles?
- How stable are the microparticle formulations?
- How much phenytoin administered as intranasal microparticles can reach the brain?

4.2 Hypothesis

The overall hypothesis of this chapter is that incorporating phenytoin into 10 µm sized TSP-microparticles can enhance nose-to-brain delivery of phenytoin in a rat model.

4.2.1 Chapter Aims

1. To formulate and optimize 10 µm sized TSP-microparticles loaded with phenytoin by spray-drying.
2. To assess the mucoadhesive potential and phenytoin release profile of TSP-microparticles.
3. To assess olfactory deposition efficiency of 10 µm sized TSP-microparticles loaded with phenytoin.
4. To assess nasal mucotoxicity of TSP-microparticles loaded with phenytoin in rats.
5. To assess the stability of microparticle formulations.
6. To develop an HPLC method to accurately quantify phenytoin in rat plasma, brain, and other tissues.
7. To quantify the uptake of phenytoin in plasma, brain, and peripheral tissues following intranasal administration of phenytoin in TSP-microparticles, IV and as an intranasal solution.

4.3 Results

4.3.1 Formulating 10 µm-sized TSP-microparticles containing phenytoin by spray-drying

4.3.1.1 Optimization of formulation parameters

The initial experimental trials were based on the optimized conditions for the TSP FITC-microparticles from **Chapter 3.** The effect of formulation parameters: total solids (%), TSP:phenytoin ratio, PG (%), and spray-drying conditions (Q-flow (L/h) & aspiration (%)) on particle size was examined. The inlet temperature was kept constant at 120 ºC. **Table** 12 lists various formulation parameters and the resulting particle size. A total of 12 combinations of different levels of formulation parameters were tested.

The optimized formulation parameters from **Chapter 3** failed to produce the same particle size when the FITC-Dextran was replaced with phenytoin. Instead an increased particle size of 14 µm was observed. It has been reported that factors like the properties of drug, excipients, and drug to excipient ratio can affect the spray-drying process[362,425]. Phenytoin is a poorly soluble crystalline drug, unlike amorphous hydrophilic dextrans and the addition of PG may have affected the spray-drying process. Thus suitable formulation parameters to produce 10 µm sized TSP-particles containing phenytoin were identified by trial and error.

The analysis of the spray-drying results from **Chapter 3** revealed that atomizing airflow and aspiration are two significant factors that control particle size. As a first step, the atomizing airflow was changed, and the size of the resultant particles was analyzed. A decrease of atomizing air flow < 547 L/h lead to larger particle size (> 14 µm). Furthermore, the phenytoin was not completely formulated into microparticles as identified by SEM (**Figure 4.3**). Increasing the atomizing airflow to the next possible level (> 547 L/h) resulted in very fine atomization of the feed solution and consequently a decrease in the particle size (6 ± 0.3µm) and its distribution. Hence, the atomizing airflow rate was kept constant at 547 L/h while the aspiration was increased gradually and the resultant particle size was

analyzed. An increase in the velocity of the drying gas decreased particle size gradually, and at the maximum level of aspiration (100 %), the particle size was 11.6 ± 0.2 µm.

As the amount of drug and excipients can also affect spray-drying, the total solid contents in the feed solution was decreased from 2 % to 1.5 % without changing the TSP:phenytoin ratio. This further decreased the particle size to 11.2 ± 0.1 µm. Further decrease in total solids was not considered due to its potential implications on the mucoadhesive potential and phenytoin content of the microparticles. Instead, PG content was decreased from 10 % to 5 %, and the resultant particle size was analyzed. These conditions produced the required 10 µm particles. The optimized conditions are presented in **Table 12** and are highlighted with grey color.

Table 12 List of formulation parameters tested. Highlighted cells in gray color indicate the optimized, most suitable formulation parameters to obtain microparticles with a size of 10 µm. Particle size data presented is the mean of three independent experiments ± SD.

Total solids (%)	TSP: Phenytoin	Spray-drying conditions		PG (%)	Particle size (µm)
		Atomizing airflow (L/h)	Aspiration (%)		
2.0	3:1	425	55	10	17.8 ± 0.3
2.0	3:1	487	55	10	17.8 ± 1.0
2.0	3:1	547	55	10	14.0 ± 1.0
2.0	3:1	607	55	10	6.0 ± 0.3
2.0	3:1	668	55	10	4.2 ± 0.1
2.0	3:1	547	60	10	19.4 ± 0.1
2.0	3:1	547	75	10	14.3 ± 0.8
2.0	3:1	547	95	10	12.2 ± 0.5
2.0	3:1	547	100	10	11.6 ± 0.2
1.5	3:1	547	100	10	11.2 ± 0.1
1.5	3:1	547	100	5	9.8 ± 0.4 10.1 ± 0.1 10.3 ± 0.3
1.5	1:1	547	100	5	9.7 ± 0.7
1.5	1:3	547	100	5	11.0 ± 1.0

The optimized conditions were validated by analyzing the particle size data obtained under these conditions on three different days and during three different times within a day. Statistical analysis of these results by a student t-test identified no significant difference in the particle size ($P>0.05$) confirming that these conditions were suitable to produce 10 µm-sized TSP-microparticles containing phenytoin. Then, with an aim to further increase the drug concentration in microparticles, the concentration of phenytoin was increased from

25 % to 50 % and 75 %. These changes did not result in significant particle size changes ($P > 0.05$).

Figure 4.3 A & B show the morphology of the unformulated phenytoin powder (**A**) and spray-dried phenytoin (**B**). **Figure 4.3 C-F** show representative SEM micrographs of TSP-microparticles containing phenytoin where the effect of formulation parameters can be observed in the morphological features of the particles. The effect of spray-drying parameters are shown in **Figure 4.3 C & D** and indicate that the larger particles are produced at lower atomizing air flow ($\leq$ 487 L/h) rates. Also, at these levels, phenytoin was not completely incorporated into TSP-microparticles. The unformulated phenytoin crystals could be observed as shown in **C**. Higher atomizing airflow ($\geq$ 607 L/h) led to particles with smaller size as shown in **Figure 4.3 D**. **Figure 4.3 E & F** demonstrate the effect of the TSP: Phenytoin ratio on microparticles. With increases in the concentration of phenytoin (50 %), the surface of the microparticles shows crystalline fractions of the phenytoin as a textured surface, as shown in **Figure 4.3 E**. Further increase in phenytoin level (75 %) results in increased fractions of crystalline phenytoin on the surface of the microparticles as shown in **Figure 4.3 F**. Large variations in the particle size and presence of crystalline phenytoin in the formulations and on the surface of microparticles observed under SEM emphasize the importance of formulation parameters on the particle size and morphology of the microparticles.

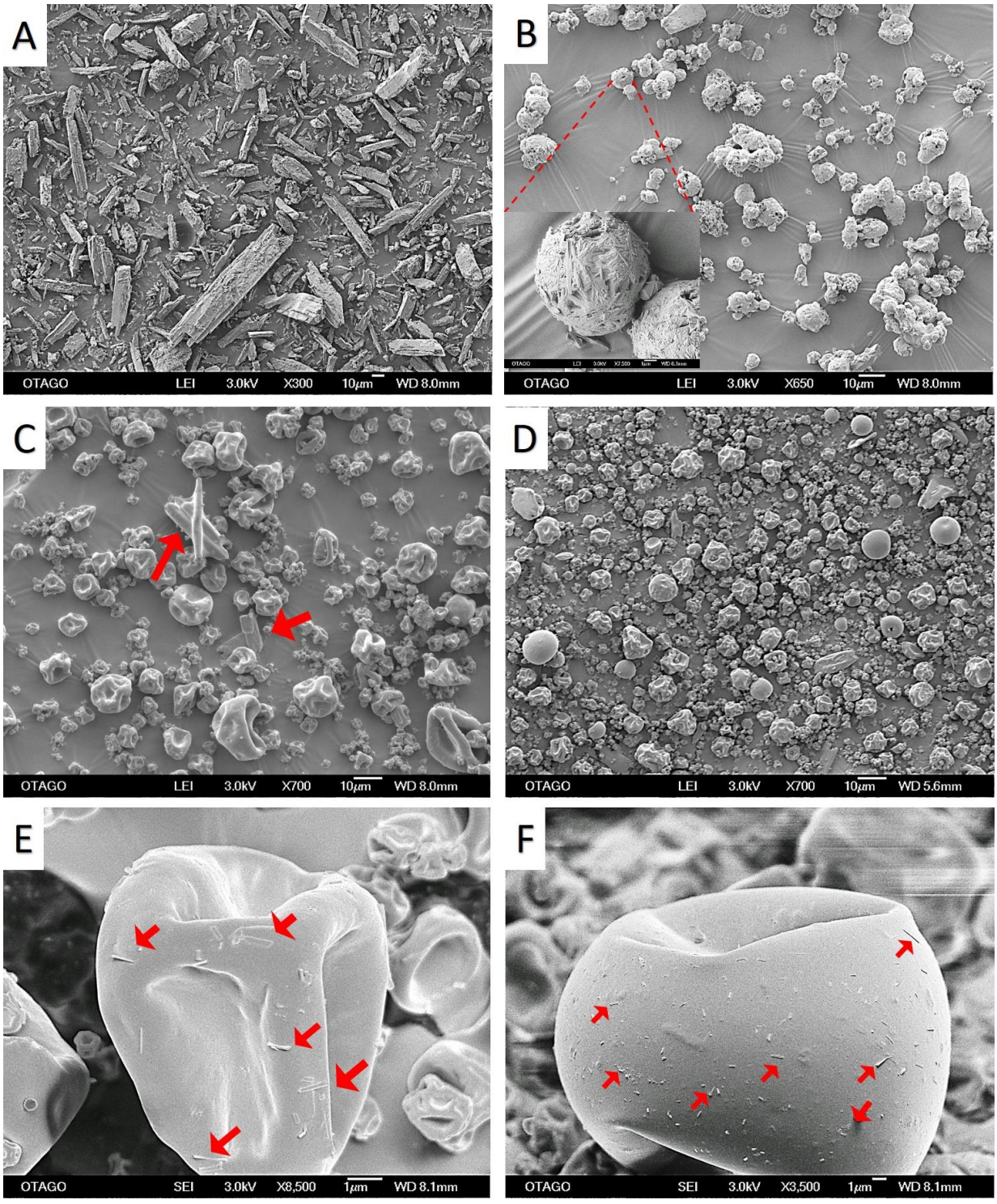

Figure 4.3 Representative micrographs of (A) crystalline unformulated phenytoin powder and (B) spray-dried phenytoin. Representative micrographs of TSP-microparticles demonstrating the effect of spray-drying parameters: (C) unformulated crystalline phenytoin observed after spray-drying with TSP and (D) smaller particle size at the higher levels (≥ 607 L/h) of spray-drying parameters. Representative micrographs of TSP-microparticles demonstrating the effect of an increase in phenytoin concentration (E and F). Arrows indicate the visible crystalline fractions of phenytoin.

Figure 4.4 shows the morphology of TSP-microparticles containing phenytoin produced using the optimized spray-drying conditions. These microparticles had uniform size distribution compared to the microparticles produced with non-optimized formulation parameters (**Figure 4.3**). The particles had corrugated shape. The surface appeared smooth and with no visible fractions of crystalline phenytoin as shown in **Panel B**.

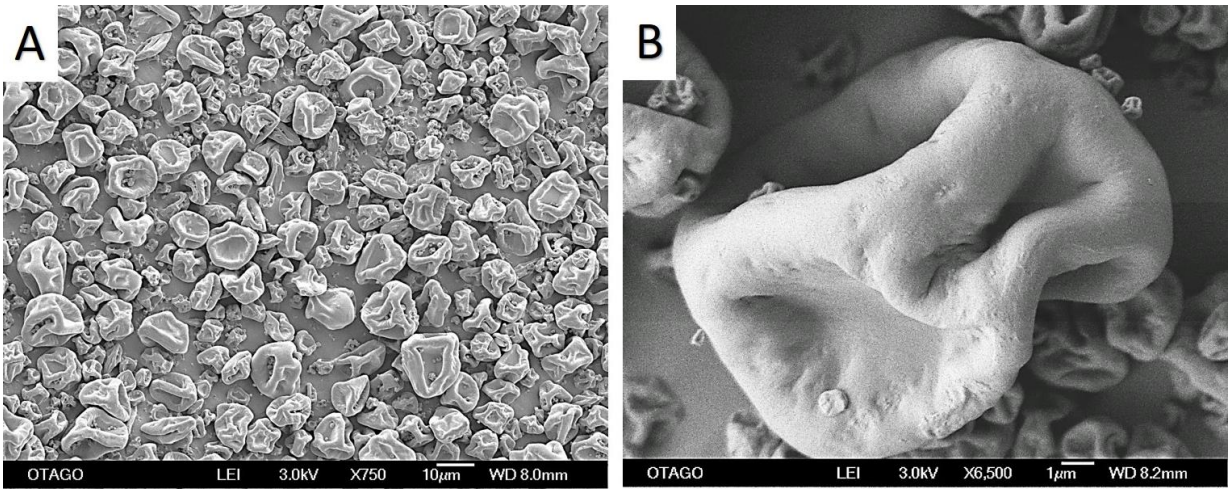

Figure 4.4 Representative micrographs showing the morphology of TSP-microparticles containing phenytoin (C) and corrugated microparticles with smooth the surface (D).

These TSP-microparticles with a mode size of 10 µm, containing phenytoin produced with optimized spray-drying conditions were used for further studies. They are, herein referred in this thesis as TSP-microparticles containing phenytoin.

4.3.1.2 Analysis of phenytoin content in TSP-microparticles

The amount of phenytoin incorporated in TSP-microparticles was analyzed by a previously validated HPLC method (Younus et al, unpublished data). **Figure 4.5 A,** shows the peak for separation and identification of phenytoin. Phenytoin was quantified using the standard curve in **Figure 4.5 B** ($r^2 = 1$). The encapsulation efficiency of optimized microparticle formulations was found to be 96.13 ± 0.37 %, and the drug loading was 24.20 ± 0.02 %.

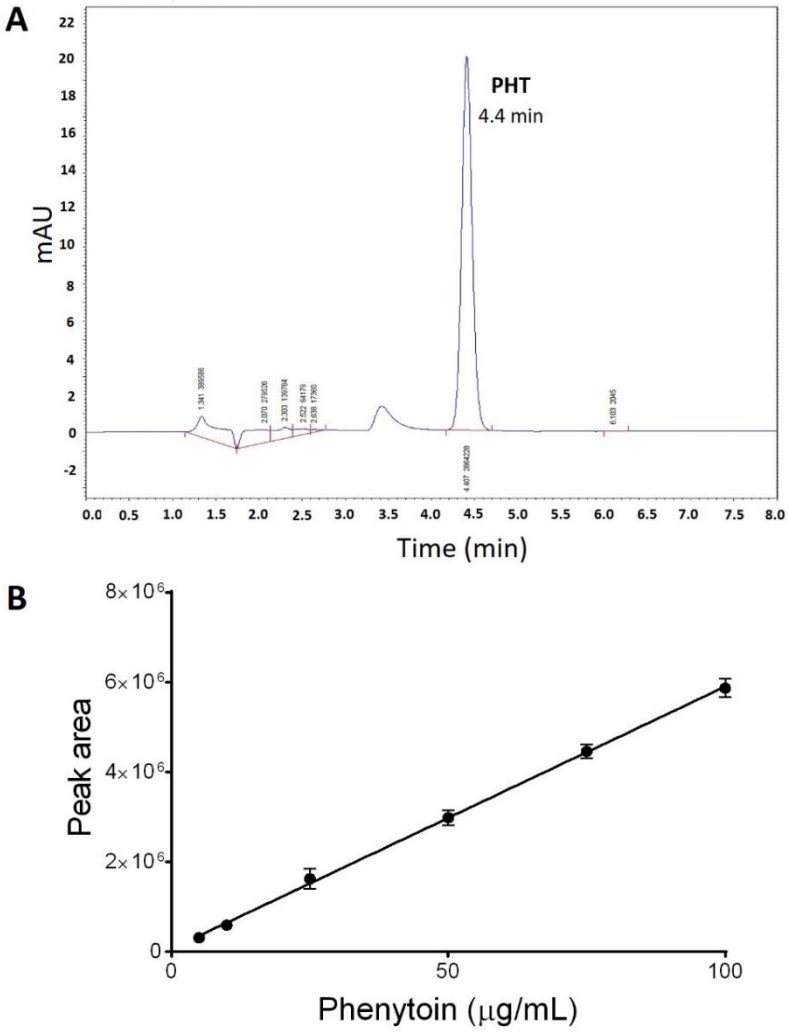

Figure 4.5 (A) HPLC chromatogram showing the phenytoin (PHT) peak with a retention time of 4.4 min. (B) A standard curve of phenytoin where data presented are the mean of three independent experiments ± SD

4.3.2 Mucoadhesive properties of TSP-microparticles containing phenytoin

The mucoadhesiveness of TSP-microparticles containing phenytoin was investigated using the *in-vitro* and *ex-vivo* methods described in **Chapter 3**. Phenytoin solution and unformulated phenytoin powders were used as controls.

Figure 4.6 shows that TSP-microparticles show significantly higher mucoadhesion under both the *in-vitro* ($P < 0.01$) and *ex-vivo* conditions ($P < 0.001$) compared to the unformulated phenytoin powder and phenytoin solution. Interestingly, there was no significant difference between the *ex-vivo* mucoadhesion strengths of phenytoin solution and phenytoin powder.

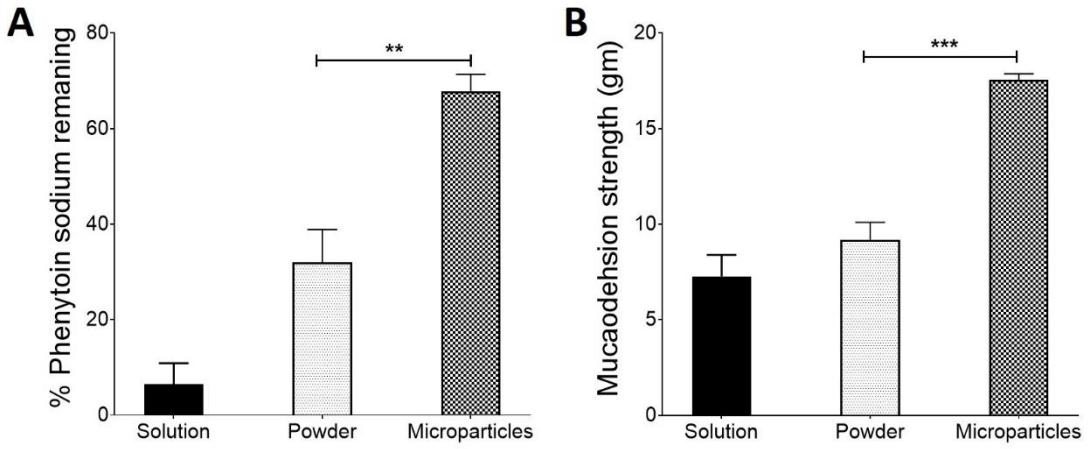

*Figure 4.6 In-vitro (A) and ex-vivo (B) mucoadhesive properties of TSP-microparticles containing phenytoin compared to the unformulated phenytoin sodium powder and solution. Data presented is the mean of three independent experiments ± SD. (** P < 0.01, ***P < 0.001).*

4.3.3 Release of phenytoin from TSP-microparticles *in-vitro*

The cumulative release profile of phenytoin from TSP-microparticles across a cellulose acetate membrane is presented in **Figure 4.7**. Unformulated phenytoin powder and phenytoin solution were used as controls. The results suggest that the microparticles significantly sustain the release of phenytoin. The initial burst release of phenytoin from microparticles and faster release in the first 5 min was observed compared to the phenytoin powder.

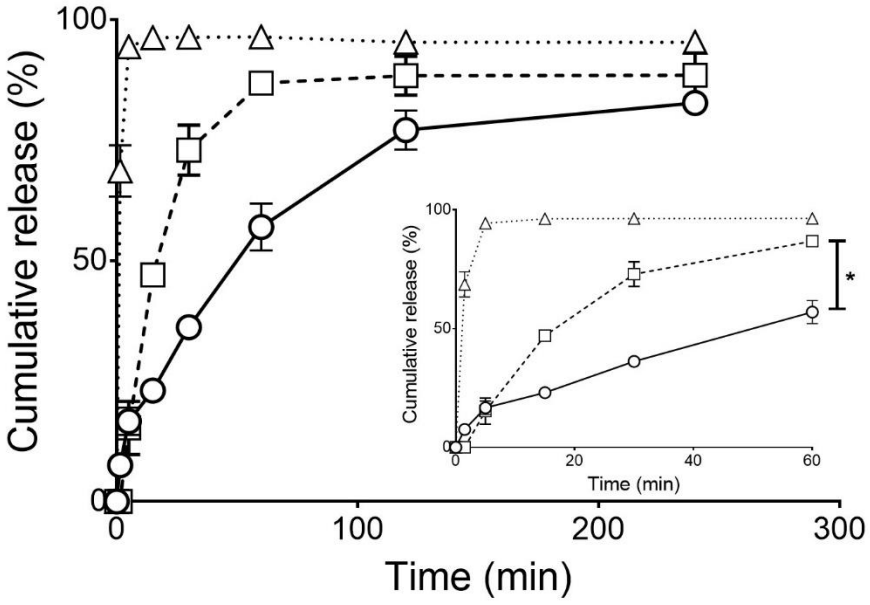

Figure 4.7 Cumulative release of phenytoin as a function of time from solution (triangle, dotted line), unformulated powder (square, dashed line) and microparticles (circle, solid line). The inset shows the initial burst release from the microparticles due to the amorphous surface drug releasing instantly upon contact with the medium and sustained release of phenytoin over the first 60 min. Data presented is the mean ± SD of three independent experiments ($P < 0.05$).*

The *in-vitro* drug release results for the first hour were fitted into zero-order, first-order, Higuchi, and Korsymeyers-Peppas models to determine the release kinetics. The release was found to follow a diffusion controlled release (Higuchi, $r^2 = 0.998$).

The results from *in-vitro* drug release suggest that phenytoin from microparticles is slowly released during the first 60 min. In addition, an initial burst release of phenytoin was observed. Whilst *in-vitro* and *in-vivo* correlations are not always accurate, based on these results it is hypothesized that any brain uptake of phenytoin should be observable within 60 min after administration of intranasal-microparticles *in-vivo*. Using this data in combination with the average nasal residence time of 8-15 min in healthy humans[48,52,426] the time points of 15, 30, 45 and 60 min were established for the *in-vivo* study described in this chapter.

4.3.3.1 Investigating the spray-drying induced change in physical state of phenytoin

The initial faster release of phenytoin from microparticles could be due to a change in the physical state of phenytoin due to spray-drying with TSP. The XRPD diffractograms of phenytoin powder and microparticle formulations were obtained to investigate any changes in the physical state of phenytoin. **Figure 4.8 A** shows the XRPD diffractograms of unformulated phenytoin powder containing crystalline peaks. **Figure 4.8 B** shows representative XRPD diffractograms of TSP-microparticles containing phenytoin. The absence of any crystalline peaks in the microparticles indicates that the spray-drying has converted crystalline phenytoin to an amorphous phase in the microparticle formulations. Representative DSC thermograms in **Figure 4.8 C** show the thermal behavior of unformulated phenytoin powder with microparticles. The absence of a thermal peak in the microparticle formulations suggests a change from crystalline form to a high-energy amorphous phase.

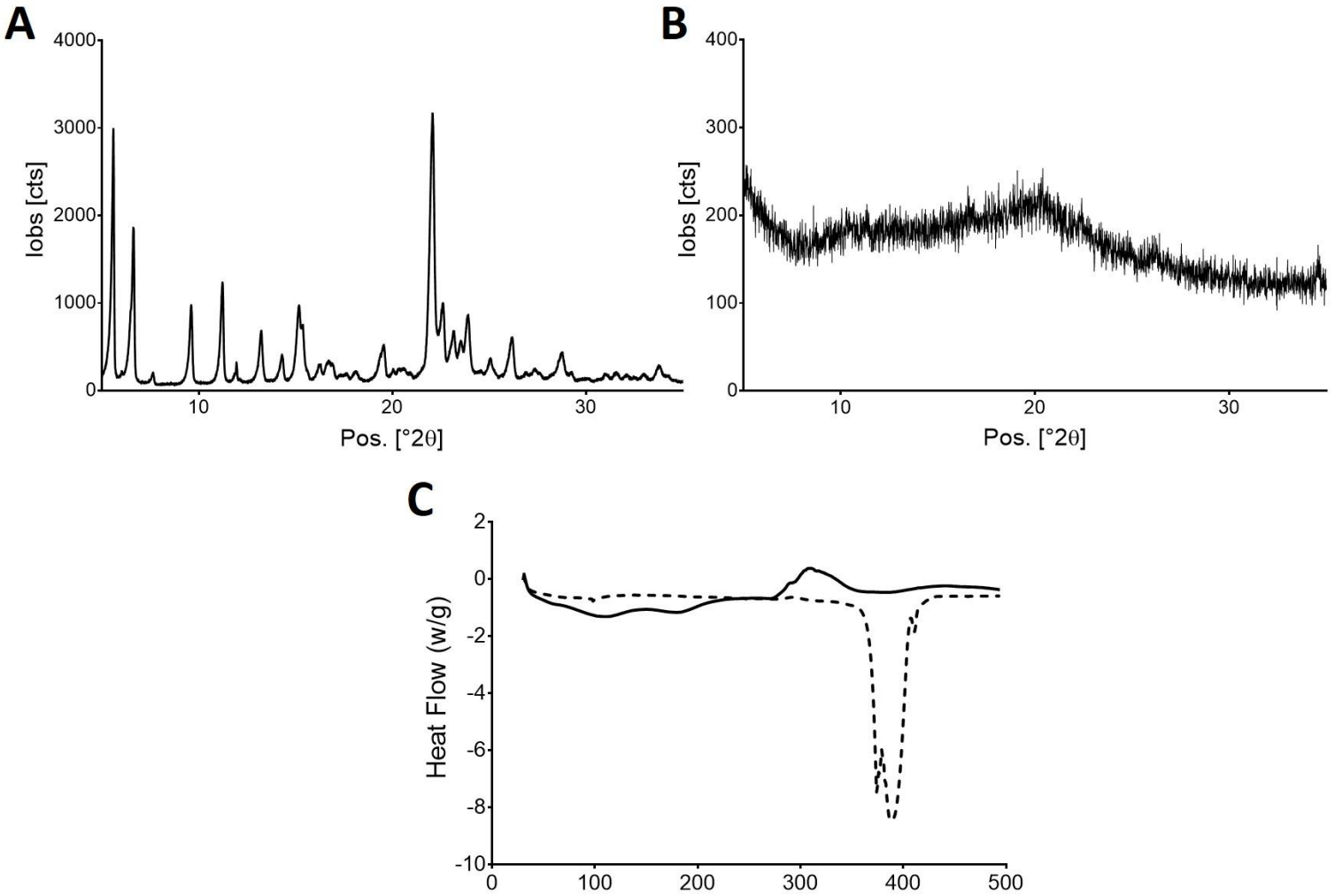

Figure 4.8 XRPD diffractograms of unformulated phenytoin powder (A) and TSP-microparticles containing phenytoin (B). DSC thermograms comparing the thermal behavior of unformulated phenytoin (dashed line) with TSP-microparticles containing phenytoin (solid line) (C).

4.3.4 The permeability of phenytoin across porcine nasal mucosa *ex-vivo*

Permeation of phenytoin across the porcine nasal mucosa was studied to determine if drug released from TSP-microparticles can then permeate a biologically relevant mucus barrier. Unformulated phenytoin powder and phenytoin solution were used as controls. The permeability of phenytoin as shown in **Figure 4.9** from microparticles during the first 2 h was significantly slower compared to the powder and solution ($P < 0.05$). The steady state flux (J_{ss}) of phenytoin permeation across the porcine mucosa released from TSP-microparticles was calculated to be 55.9 ±2.808 µg cm^{-2} h^{-1}. The J_{ss} of phenytoin solution and phenytoin powder was found to be 210.10 ± 68.89 and 87.99±40.77 µg cm^{-2} h^{-1} respectively.

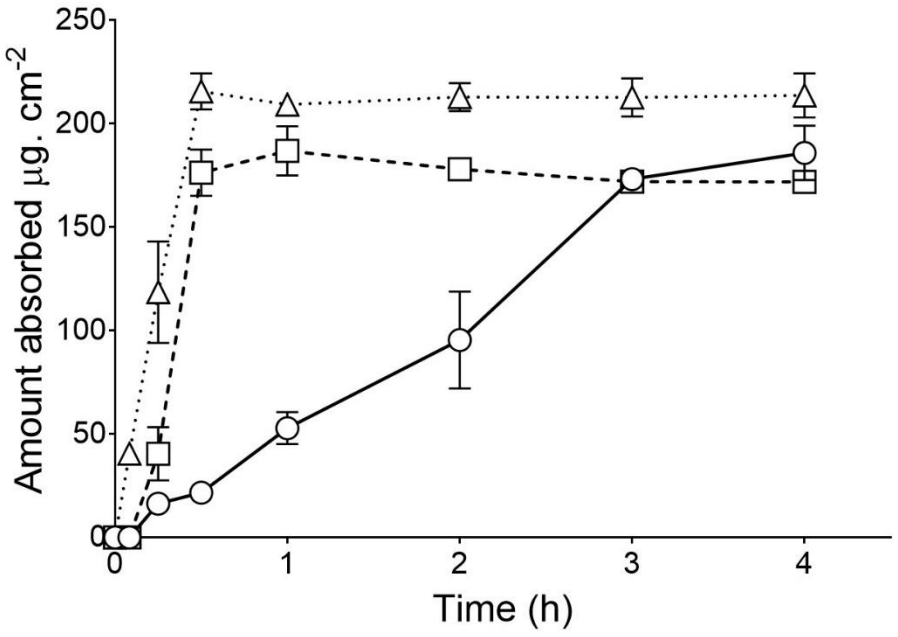

Figure 4.9 Permeability of phenytoin across porcine nasal mucosa over time. The permeation of phenytoin formulated as TSP-microparticles (circle, solid line) was compared with phenytoin solution (triangle, dotted line) and unformulated phenytoin powder (square, dashed line). Data presented are the mean ± SD of three independent experiments.

4.3.5 Olfactory deposition of TSP-microparticles containing phenytoin

The extent of olfactory targeting by microparticles under normal breathing conditions of 20 $Lmin^{-1}$ was determined by the amount of phenytoin depositing in the olfactory region of the 3D nasal cast. The 4 µm sized microparticles produced from one of the trial runs in the formulation optimization process was used as a control due to their ability to escape deposition in the nasal cavity. The deposition efficiencies of microparticles are reported in **Figure 4.10**. In some experiments, olfactory deposition of microparticles was negligible, so for these experiments, the deposition efficiency is reported as zero. Overall, microparticles with a mode size of 10 µm showed significantly higher ($P < 0.0001$) deposition efficiency in the olfactory region compared to the 4 µm particles. The results are comparable to the deposition of TSP-FITC-Dextran microparticles described in **Chapter 3**.

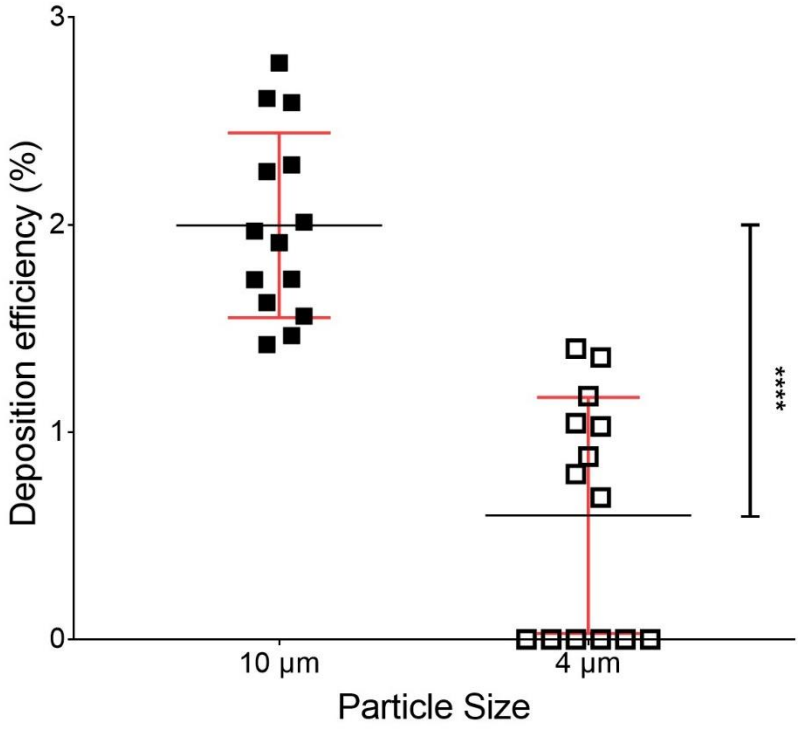

*Figure 4.10 Deposition efficiency of 10 µm versus 3 µm TSP-microparticles containing phenytoin in the olfactory region of a human nasal replica 3D printed cast when nebulized under normal breathing conditions (20 L/min). Data presented is the mean ± SD of ten independent experiments. (**** $P < 0.0001$).*

4.3.6 Stability of TSP-microparticles containing phenytoin

The stability of TSP-microparticles containing phenytoin was tested according to the ICH guidelines for finished products[248]. Phenytoin content, moisture content and XRPD diffractograms of all microparticle formulations stored at specified conditions were recorded at predetermined points. **Table 13** shows the drug and moisture content of the formulations. No significant difference in encapsulation efficiency and moisture content of microparticles was observed over six months of storage.

Table 13 Drug and moisture contents of TSP-microparticles containing phenytoin over a period of six months.

Storage conditions	Day	Encapsulation efficiency (%)	Moisture content (%)
Freshly prepared	0	96.54 ± 0.25	1.73 ± 0.15
25ºC and 60 % RH	30	96.83 ± 1.47	3.20 ± 0.77
	60	94.95 ± 2.11	3.73 ± 1.22
	90	94.74 ± 2.01	3.68 ± 1.02
	180	94.04 ± 1.21	4.51 ± 1.01
40ºC and 75 % RH	30	95.21 ± 2.01	4.87 ± 1.91
	60	94.87 ± 1.95	4.66 ± 0.85
	90	95.07 ± 1.76	4.80 ± 1.02
	180	94.11 ± 2.87	4.61 ± 0.21

Figure 4.11 A & B show the XRPD diffractograms of TSP-microparticles containing phenytoin after a storage period of three months. **Figure 4.11 A** represents TSP-microparticles stored under ambient conditions whilst **Figure 4.11 B** represents TSP-microparticles stored under accelerated conditions. The XRPD diffractograms in **Figure 4.11 C & D** show that crystalline peaks began to reappear after six months. In addition, the intensity of the peaks also increased. This can be attributed to the recrystallization process of phenytoin in the microparticles stored for six months.

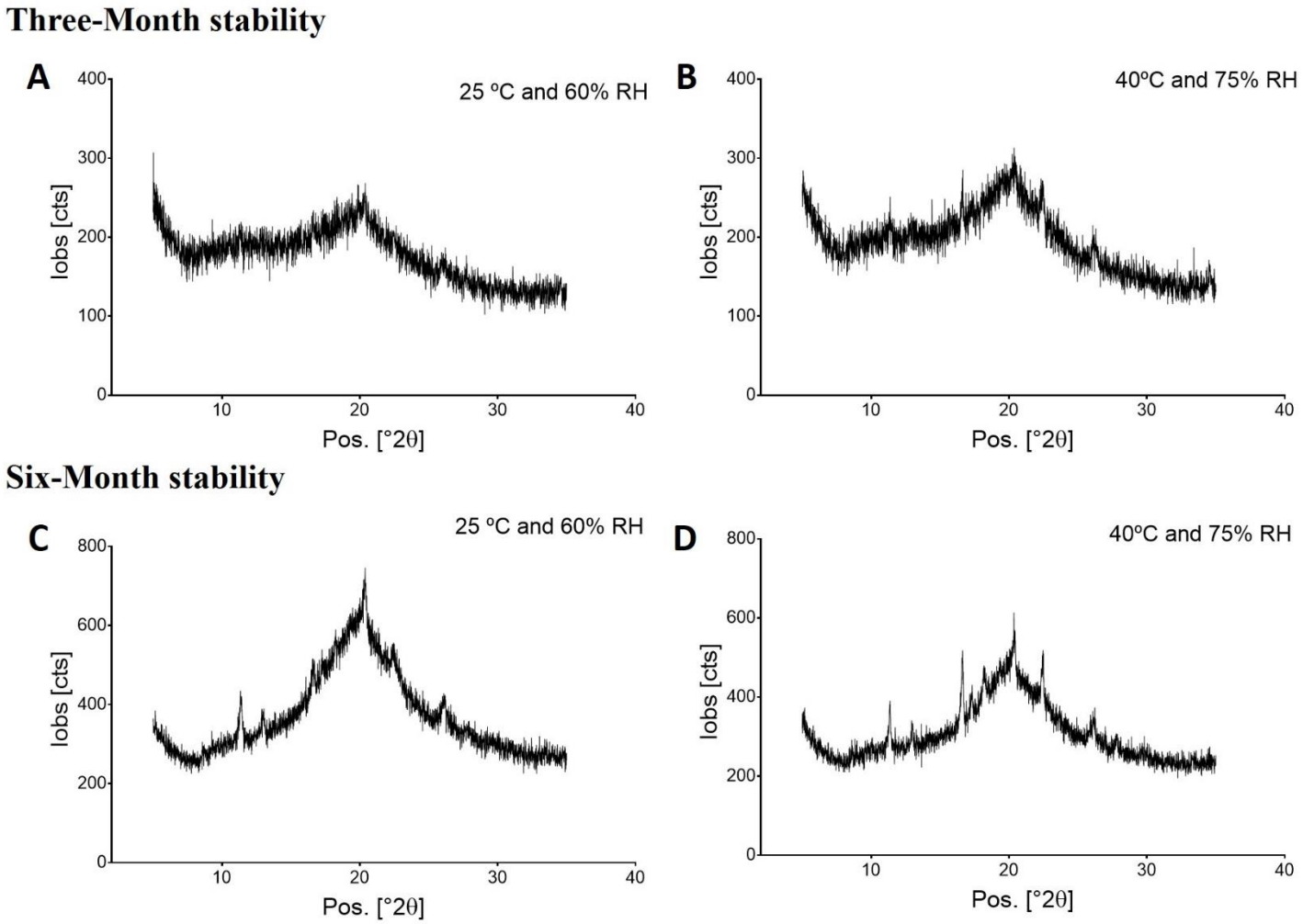

Figure 4.11 Representative XRPD diffractograms of TSP-microparticles containing phenytoin stored at 25 ºC and 60 % RH for three (A) and six months (C) and of microparticles stored at 40ºC and 75 % RH for three months (B) and six months (D).

4.3.7 Evaluation of nasal toxicity and drug-related behavioral adverse effects of phenytoin loaded TSP-microparticles after intranasal administration

The effect of TSP-microparticles loaded with phenytoin on rat nasal mucosa was examined *in-vivo*. No potential signs of nasal irritation such as frequent sneezing, noisy breathing, red (porphyrin) discharge, nose-rubbing or general signs of pain/discomfort were observed over the time between administration and euthanasia. The histological micrographs of the olfactory mucosa of rats 1 h after administration of TSP-microparticles containing phenytoin is shown in **Figure 4.12**. The olfactory mucosa of a rat treated with saline was used as a negative control and is shown in **Figure 4.12 A**. The structural integrity of the olfactory mucosa treated with microparticles is evident in the micrographs as shown in **Figure 4.12 B**. The structure and appearance of the epithelial cells and tissue integrity is comparable to the negative control. No evidence of necrosis or structural damage exists, unlike in the positive control (**Figure 4.12 C)** which was rat nasal mucosa treated with sodium deoxycholate. Damage to the epithelial cells, rupture of the epithelial tissue and large vacuoles are observed in the positive control tissues. These studies suggest that the TSP-microparticles loaded with the phenytoin do not cause any nasal mucosal toxicity in rats up to 60 min after administration.

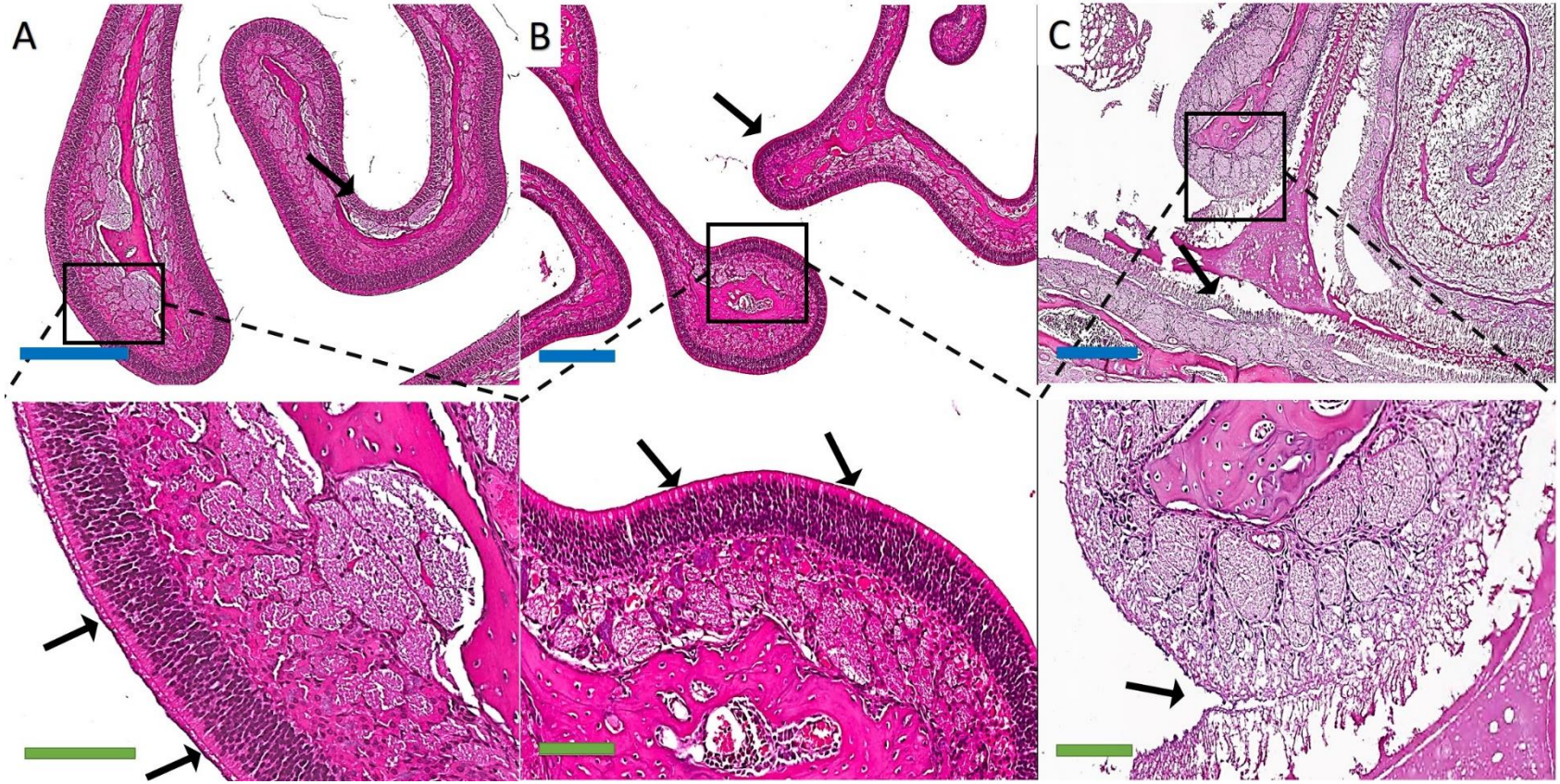

Figure 4.12 Representative light micrographs of rat nasal mucosa treated with saline (A) (negative control), phenytoin containing TSP-microparticles (B), and sodium deoxycholate (C) (positive control). The arrows indicate histopathology of the olfactory mucosa. A, B, C were captured at 4X magnification (scale bar (blue) = 400 µm) and their zoomed micrographs were captured at 10X magnification (scale bar (green) = 100 µm).

4.3.8 *In-vivo* characterization of TSP-microparticles containing phenytoin

4.3.8.1 Development of an HPLC method for quantification of phenytoin

A reliable analytical method to quantify phenytoin in blood and tissues was a vital part of characterizing the formulations *in-vivo*. The aim of this part of the chapter is to develop and validate an HPLC method to quantify the phenytoin in rat plasma, brain, and other tissues. Due to high selectivity and sensitivity, HPLC can enable quantification of phenytoin in the presence of complex matrices.

4.3.8.1.1 Optimization of chromatographic conditions

The HPLC conditions such as mobile phase, pH of the mobile phase, column temperature, flow rate, injection volume, runtime and UV detection wavelength were optimized based on literature values[257,258] and by trial and error. The effect of all these conditions was tested and the optimal conditions for separation and quantification of phenytoin and metabolite peaks were identified. The optimized chromatographic conditions are presented in **Table 14.**

Table 14 Optimized chromatographic conditions for the identification and quantification of phenytoin and its metabolite (5-(4-Hydroxyphenyl)-5-phenyl-hydantoin).

Chromatographic parameters	Optimized conditions
Mobile phase	Phosphate buffer (10 mM) and acetonitrile (pH 5.8)
Column temperature	40 ºC
Flow rate	0.2 mL/min
Injection volume	10 µL
Runtime	22 min
UV detection	210 nm

At these optimized conditions, phenytoin and metabolite peaks were identified and separated as shown in **Figure 4.13.** Retention time for the phenytoin peak ranged between 13.4 to 13.6 min, the metabolite peak between 10.4-10.6 min and the internal standard peak between 14.6 min and 14.8 min in various tissues and plasma.

4.3.8.1.2 Validation

The assay was validated in plasma, brain tissue and peripheral tissues such as lung, liver, spleen, heart, kidney, and spleen. The plasma and brain tissue validation data are presented in detail in this chapter, and the validation data in other tissues is given in **Appendix E.**

4.3.8.1.2.1 Specificity

The specificity of the HPLC method was determined by comparing the chromatograms of plasma and brain samples with no phenytoin, metabolite and internal standard to those obtained from plasma and brain samples spiked with known amounts of phenytoin, metabolite and internal standard. The blank samples had no peaks at the retention times expected for phenytoin, metabolite or internal standard as shown in **Figure 4.13 A & C**. The spiked samples had separate peaks for phenytoin, metabolite or internal standard as shown in **Figure 4.13 B & D**, suggesting the specificity of the method.

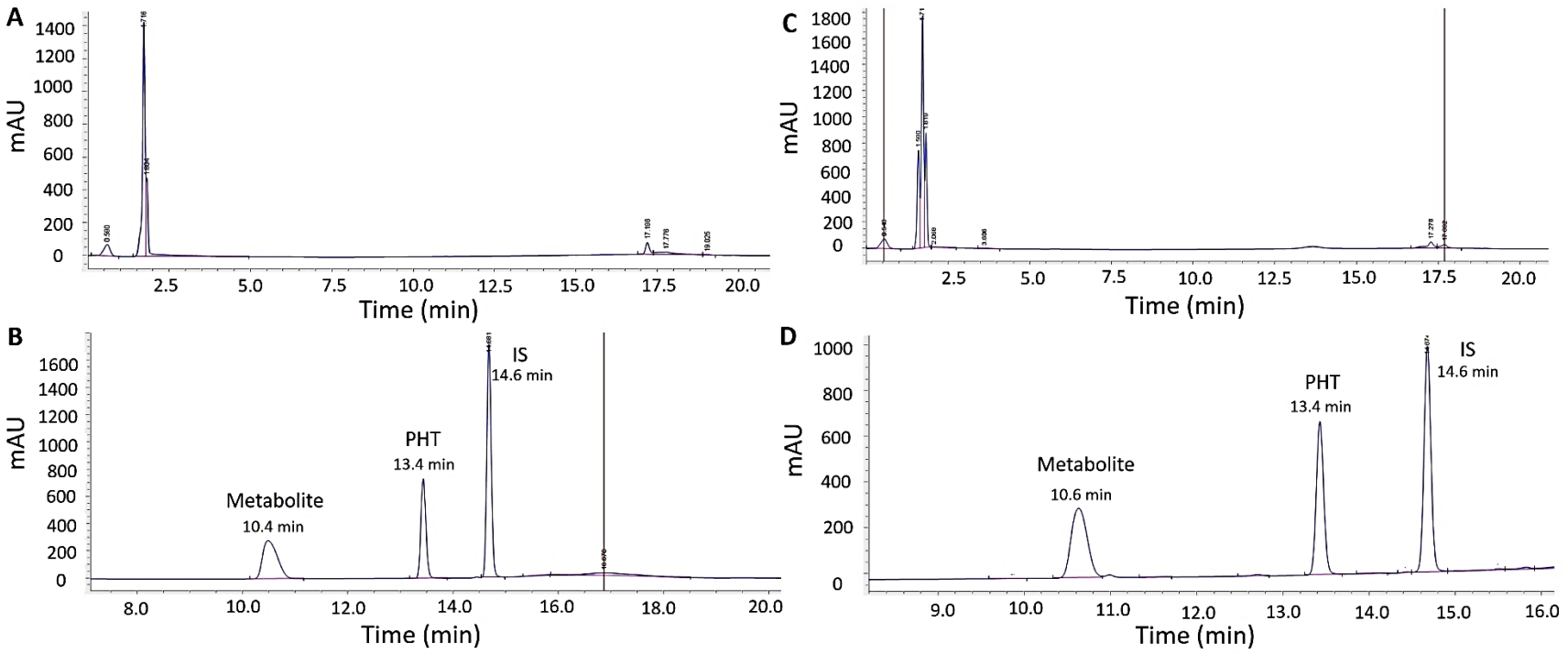

Figure 4.13 HPLC chromatograms of (A) blank plasma (B) plasma sample spiked with metabolite, phenytoin (PHT) and internal standard (IS), (C) blank brain tissue and (D) brain sample spiked with metabolite, phenytoin (PHT) and internal standard (IS). The chromatograms show clear separation of metabolite, phenytoin and IS in both plasma and brain tissue, only retention times near peaks are shown in the chromatograms.

4.3.8.1.2.2 Linearity

Plasma and brain standard samples were measured with the HPLC method to determine the linearity of the peak ratio. The peak ratio of the standard samples was a linear function of the phenytoin and metabolite concentration in the range of examined concentrations as shown in **Figure 4.14**. The linear regression correlation coefficient (r^2) values for metabolite and phenytoin in plasma and tissue were all > 0.998 and the y-intercepts did not significantly deviate from zero (P > 0.05).

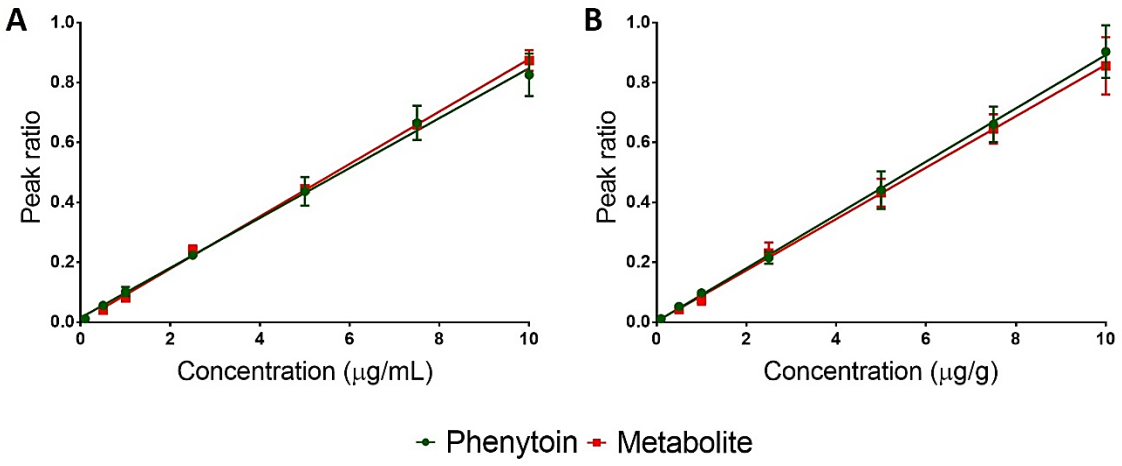

Figure 4.14 Standard curves of phenytoin and metabolite in rat plasma (A) and brain (B). Data shown are the mean of three independent sets of standards ± SD.

4.3.8.1.2.3 Sensitivity

The LOD and LOQ are used to assess the sensitivity of the HPLC assay. These were calculated from the slope and the SD of the y-intercepts from the standard curves. The LOQ and LOD for phenytoin were 0.016 µg/mL, and 0.048 µg/mL in plasma, and in brain were 0.027 µg/g, and 0.084 µg/g respectively. The LOQ and LOD for metabolite were 0.061 µg/mL, and 0.185 µg/mL in plasma, and in brain were 0.140 µg/g and 0.441 µg/g respectively.

4.3.8.1.2.4 Accuracy and precision

The accuracy of the assay was determined by comparing the amount of phenytoin and metabolite recovered in quality control (QC) samples spiked with known concentrations. The precision of the assay was then determined by calculating the coefficient of variation (CV) and bias (%). Accuracy and precision of plasma and brain samples are reported in **Table 15** and **Table 16**. Deviations from theoretical concentrations were less than 8 % for all the intraday and inter-day QC samples tested. The CV and bias for all QC samples tested were within 13 % for both the intraday and inter-day. These values for accuracy and precision are with a range which is acceptable for HPLC analysis according to FDA guidelines[427].

Table 15 Intraday and inter-day accuracy and precision of phenytoin and its metabolite in plasma (n = 6, mean ± SD).

	Nominal concentration (µg/mL)	**Nominal concentration observed (µg/mL)**	**%CV**	**%bias**	**Accuracy %**
Intraday	Metabolite				
	1	0.9694 ± 0.118	12.19	3.05	96.94
	5	5.2133 ± 0.472	8.98	-4.11	104.10
	10	10.3010 ± 0.380	3.64	-3.03	103.01
	Phenytoin				
	1	0.9237 ± 0.064	7.00	7.63	92.37
	5	5.1423 ± 0.301	5.82	-2.85	102.84
	10	10.3600 ± 1.050	10.17	-3.61	103.60
Inter-day	Metabolite				
	1	0.8875 ± 0.081	9.80	11.24	88.75
	5	5.3347 ± 0.413	7.73	-6.61	106.69
	10	9.9878 ± 0.922	9.32	0.17	99.878
	Phenytoin				
	1	1.0492 ± 0.074	7.17	-4.92	104.92
	5	5.2641 ± 0.500	9.50	-5.21	105.28
	10	10.1724 ± 1.031	10.37	-1.70	101.72

Table 16 Intraday and inter-day accuracy and precision of phenytoin and its metabolite in brain tissue (n = 6, mean ± SD).

	Nominal concentration (µg/mL)	**Nominal concentration observed (µg/mL)**	**%CV**	**%bias**	**Accuracy %**
Intraday	Metabolite				
	1	0.8883 ± 0.065	7.40	11.16	88.83
	5	4.7934 ± 0.497	10.25	4.22	95.86
	10	9.8697 ± 0.304	3.04	1.41	98.69
	Phenytoin				
	1	1.0633 ± 0.035	3.32	-6.33	106.33
	5	4.9074 ± 0.561	11.41	2.00	98.14
	10	10.1891 ± 1.276	12.44	-1.77	101.89
Inter-day	Metabolite				
	1	0.8795 ± 0.089	10.28	12.04	87.95
	5	5.0187 ± 0.514	10.18	-0.14	100.37
	10	10.1734 ± 0.600	5.82	-1.72	101.73
	Phenytoin				
	1	1.0753 ± 0.084	7.81	-7.52	107.53
	5	4.7299 ± 0.491	10.34	5.53	94.59
	10	10.2224 ± 1.113	10.87	-2.15	102.22

4.3.8.2 Uptake of phenytoin into the rat brain.

The uptake of phenytoin into the brain 60 min after intranasal administration of phenytoin-loaded microparticles was compared with IV and intranasal solution administration and is shown in **Figure 4.15**.

IV administration showed comparatively low brain uptake of phenytoin with a maximum phenytoin concentration of 0.21 ± 0.09 µg/g observed at 15 min post administration. Thereafter, no statistically significant difference between the brain concentrations of phenytoin over the remaining 45 min was observed. The highest phenytoin concentration of 1.25 ± 0.44 µg/g in the brain was at 30 min after administration of intranasal solution. Again, like the IV administration, no statistically significant difference in the brain concentrations of phenytoin over the remaining 45 min was observed. Intranasal microparticles produced a continuous increase in the brain concentrations of phenytoin over time with a maximum of 1.22 ± 0.39 µg/g at 60 min. Phenytoin concentrations in the brain were significantly higher at 60 min (**P = 0.0037) compared to initial time points.

The efficiency of the formulation for nose-to-brain delivery of phenytoin was analyzed by comparing the brain concentrations obtained after administration of intranasal solution versus intranasal microparticles. The efficiency of the route of administration was analyzed by comparing brain concentrations after administration as IV solution versus intranasal solution and the results are reported in **Table 17**. The statistical analysis indicates that initially the administration of the intranasal solution led to significantly higher concentrations of phenytoin in the brain at the 15, 30 and 45 min time points compared to IV and at 15 and 30 min ($P < 0.05$) compared to intranasal microparticle administrations. However, at 60 min post administration, microparticles were shown to produce significantly higher phenytoin brain concentrations compared to the intranasal solution at 60 min. The analysis of phenytoin brain concentrations shows the intranasal route can offer high brain concentrations of phenytoin compared to the IV route and furthermore administration of phenytoin as intranasal microparticles can preferentially increase the brain concentrations compared to the intranasal solution.

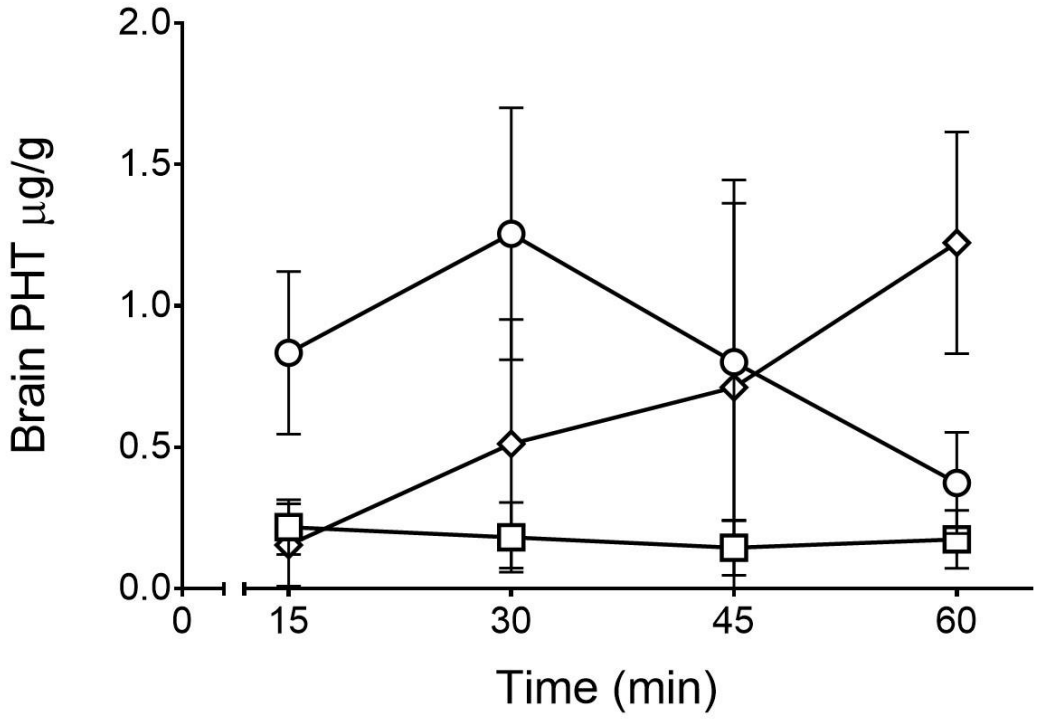

Figure 4.15 Concentration of phenytoin (PHT) in the rat brains after IV solution administration (square), intranasal administration of solution (circle) and intranasal microparticles (diamond) over time. Data expressed are the mean of minimum three independent experiments ± SD with at least n=5 rats in each time point.

Table 17 P-values indicating the statistical significance of brain phenytoin concentrations after (IN; intranasal and IV; intravenous) over time.

	15 min	**30 min**	**45 min**	**60 min**
IV solution vs IN solution	*P = 0.0129	**P = 0.0074	*P = 0.0328	P = 0.1072
IN solution vs IN microparticles	**P = 0.0037	*P = 0.0411	P = 0.8511	* P = 0.0270

4.3.8.2.1 Uptake of phenytoin in the olfactory bulb

The concentration of phenytoin in the olfactory bulb after intranasal administration can be an indicator of direct nose-to-brain delivery. **Figure 4.16** shows the concentration of phenytoin in the olfactory bulb after IV and intranasal administration of phenytoin as a solution and intranasal administration as microparticles. The olfactory bulb phenytoin concentration following IV administration could not be quantified. Consequently, only data from intranasal solution and intranasal microparticle experiments are presented here.

Administration of phenytoin as an intranasal solution produced significantly higher concentrations in the olfactory bulb at initial points (15 and 30 min) with maximum phenytoin concentration of 0.83 ± 0.26 µg/g at 15 min. However, at 45 min there was no significant difference between an intranasal solution and intranasal microparticles. At 60 min, intranasal microparticles produced significantly higher brain concentrations of phenytoin than the intranasal solution (**Table 18**) with maximum concentration of 0.53 ± 0.09 µg/g. However, there was no significant difference observed between the maximum concentrations produced by intranasal solution (15 min) and intranasal microparticles (60 min) in the olfactory bulb ($P > 0.05$). The phenytoin concentrations in the olfactory bulb decreased significantly over time (**$P = 0.0013$) when administered as an intranasal solution while the concentrations increased significantly over time (***$P = 0.0006$) when administered as intranasal microparticles. These results indicate that the phenytoin concentrations in olfactory bulb increase with time when administered as microparticles and are in correlation with the increasing concentrations of phenytoin in the brain over time.

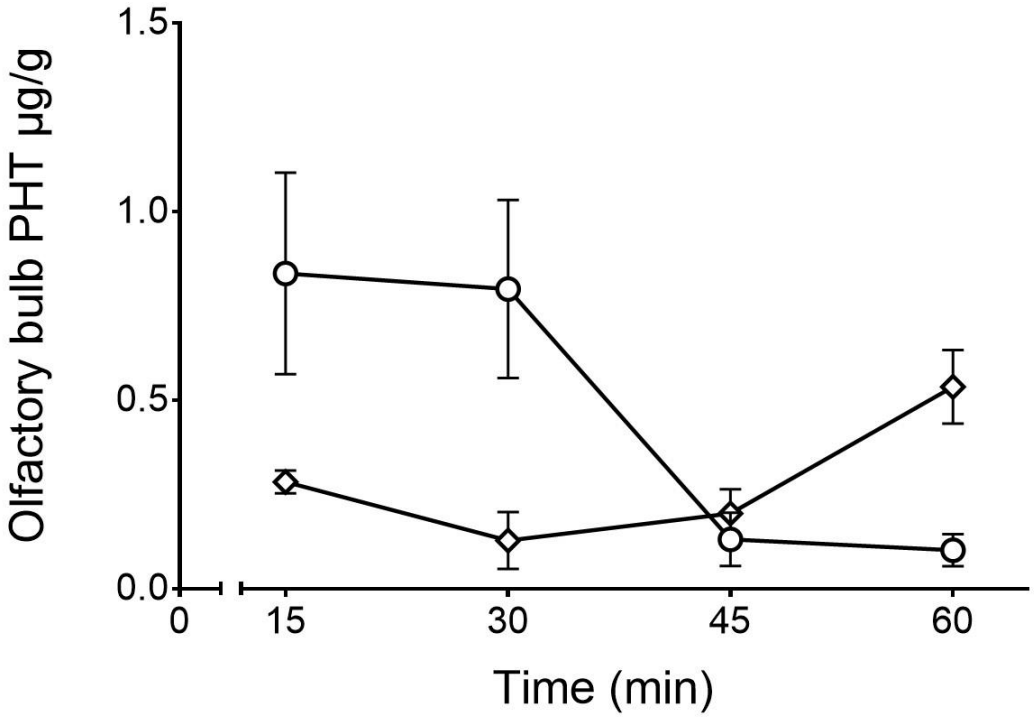

Figure 4.16 The olfactory bulb-time concentration curves of phenytoin (PHT) in rats after intranasal administration of solution (circle) and microparticles (diamond). Data expressed are the mean of three independent runs ± SD with at least n=5 rats in each time point.

Table 18 P-values indicating the statistical significance of olfactory bulb phenytoin concentrations. (IN: intranasal) over time.

	15 min	**30 min**	**45 min**	**60 min**
IN solution vs IN microparticles	* P = 0.0236	** P = 0.0097	P = 0.2800	** P = 0.0021

4.3.8.3 The plasma-time concentrations of phenytoin

The plasma concentration of phenytoin over a period of 60 min after IV, intranasal solution and intranasal microparticle administration was quantified and is shown in **Figure** 4.17. A trend of increase in plasma concentration of phenytoin over time when administered as intranasal microparticles and intranasal solution was observed with maximum concentrations of 1.29 ± 0.36 and 0.97 ± 0.45 µg/mL at 60 min respectively. No significant difference was observed in plasma phenytoin concentrations for the time points tested with intranasal solution and intranasal microparticle administrations.

With IV administration, the maximum phenytoin concentration of 2.74 ± 0.27 µg/mL was observed at the initial 15 min time point, then the plasma concentrations decreased over time reaching a minimum of 1.85 ± 0.32 µg/mL at 60 min. The plasma phenytoin concentration decreased significantly (*P = 0.0239) over 60 min after IV administration. Plasma concentrations of phenytoin with IV administration were compared with intranasal solution to determine the statistical significance between administration routes. Also, intranasal solution and intranasal microparticle administrations were compared to assess the effect of formulation strategy and the results are reported in **Table 19**. The statistical analysis revealed that as expected, IV administration led to a significantly higher phenytoin plasma concentration than the intranasal solution and intranasal microparticles at all the time points. Significantly higher phenytoin plasma concentrations for intranasal solution compared to intranasal microparticles for the first 30 min were observed, but intranasal microparticles were then able to produce similar phenytoin plasma concentrations. The plasma phenytoin concentrations show that the intranasal route reduces the plasma exposure when compared to the IV route and furthermore administering intranasal microparticles produces low plasma phenytoin concentration for 60 min compared to the intranasal solution.

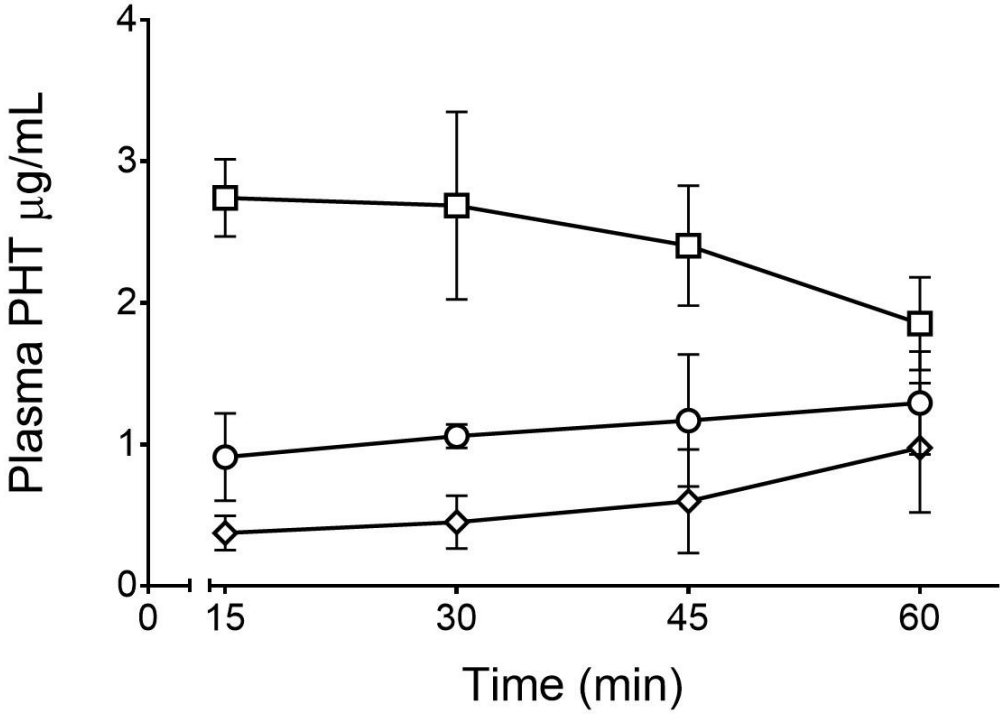

Figure 4.17 Plasma phenytoin (PHT) concertation in rats after IV solution administration (square), intranasal administration of solution (circle) and intranasal microparticles (diamond) overtime. Data expressed are the mean of minimum three independent experiments ± SD with at least n=5 rats in each time point.

Table 19 P-values indicating the statistical significance of plasma phenytoin concentrations (IN; intranasal and IV; intravenous).

	15 min	**30 min**	**45 min**	**60 min**
IV vs IN solution	**** P < 0.0001	***P = 0.0003	** P = 0.0023	* P = 0.0338
IN solution vs microparticles	*P = 0.0144	*** P = 0.0006	P = 0.0639	P = 0.3182

4.3.8.4 The brain targeting efficiency of TSP-microparticles containing phenytoin

The brain-plasma ratio can be used as a good indicator of the brain-targeting efficiency for intranasally delivered drugs[428–430]. The brain-plasma ratio at each time point was calculated as the ratio of phenytoin concentration in the brain (µg/g) to the phenytoin concentration in plasma (µg/mL) and presented in **Figure 4.18**. While calculating the brain-plasma ratio, the phenytoin concentration in the olfactory bulb was also considered as the phenytoin concentration in the brain.

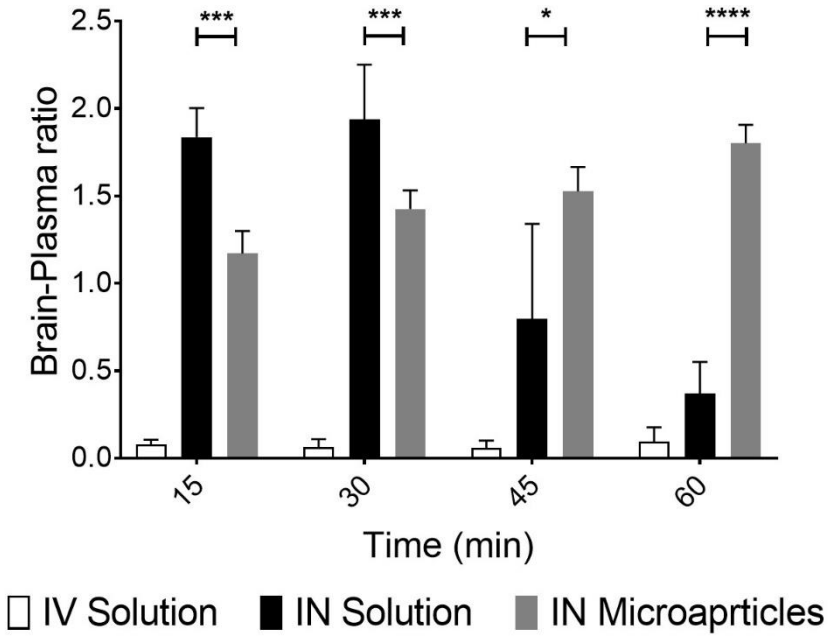

*Figure 4.18 Brain-plasma ratios of phenytoin after administration as IV solution, intranasal (IN) solution and intranasal (IN) microparticles. Data presented are the mean of at least three independent experiments ± SD. (*P < 0.05, ***P < 0.001, and ****P < 0.0001).*

The brain-plasma ratio of phenytoin was significantly higher after intranasal solution during the first 30 min, however in the latter time points intranasal microparticles were found to produce a significantly higher brain-plasma ratio of phenytoin as shown in **Figure 4.18** suggesting a greater targeting of phenytoin to the brain due to the ability of microparticles to withstand mucociliary clearance.

4.3.8.5 Peripheral tissue distribution of phenytoin

Figure 4.19 shows the peripheral tissue concentrations of phenytoin following IV solution (**A**), intranasal solution (**B**) and intranasal microparticle (**C**) administrations. The peripheral tissues (liver, lung, kidney, spleen, and heart) were analyzed for phenytoin content. The results show that the phenytoin administered as intranasal microparticles underwent reduced distribution to the peripheral tissues.

Phenytoin was rapidly distributed into the liver following IV and intranasal solution administration with the highest concentrations of 1.41 ± 1.12 µg/g and 1.98 ± 0.84 µg/g at 15 min which then decreased with time. However, intranasal microparticles produced a different profile. The initial concentrations of phenytoin in the liver were low at 15 min after administration of intranasal microparticles and increased with time reaching 0.331 ± 0.21 µg/g at 60 min.

The lungs received 0.68 ± 0.21, 0.58 ± 0.30, and 0.59 ± 0.09 µg/g concentrations of phenytoin with the IV, intranasal solution and intranasal microparticles at 15 min respectively. The concentration of phenytoin in the lungs was comparable between the time points with no significant difference for IV and intranasal solution administration. However, the lung concentration of phenytoin significantly decreased (****$P < 0.0001$) overtime for intranasal microparticle administration reaching to 0.14 ± 0.09 µg/g at 60 min.

A maximum phenytoin concentration of 1.89 ± 0.43 µg/g in the kidney was produced by IV administration followed by intranasal solution (1.06 ± 0.25 µg/g) and intranasal microparticles (0.64 ± 0.55 µg/g) at 15 min. Concentrations of phenytoin in the kidney remained comparable with no significant difference over 60 min for all administrations.

IV administration of phenytoin produced significantly higher concentrations (**$P = 0.0042$) in the heart at 30 min (~1.9 µg/g) post administration compared to intranasal solution (~1 µg/g) and intranasal microparticle (~0.14 µg/g) administrations. Concentrations of phenytoin in the heart remained unchanged with no significant difference over 60 min for all administrations. However, the intranasal microparticle administration produced

significantly lower concentrations (*P = 0.0264) of phenytoin in the heart than IV and intranasal solution.

The spleen received a comparatively higher concentration of phenytoin following IV administration. The highest concentrations of 0.12 ± 0.06 µg/g, 0.07 ± 0.03 µg/g and 0.05 ± 0.01 µg/g phenytoin in the spleen was observed at 30 min with IV, intranasal solution and intranasal microparticle administrations respectively. Concentrations of phenytoin in the spleen remained comparable with no significant difference over 60 min for all administrations. However, the intranasal microparticle administration produced significantly lower concentrations (*P = 0.0135) of phenytoin in spleen than IV and intranasal solution.

The results from the peripheral distribution study show that phenytoin distribution in peripheral tissues is significantly decreased by administering it as intranasal microparticles over a period of 60 min. These results were consistent with the plasma-time concentrations of phenytoin.

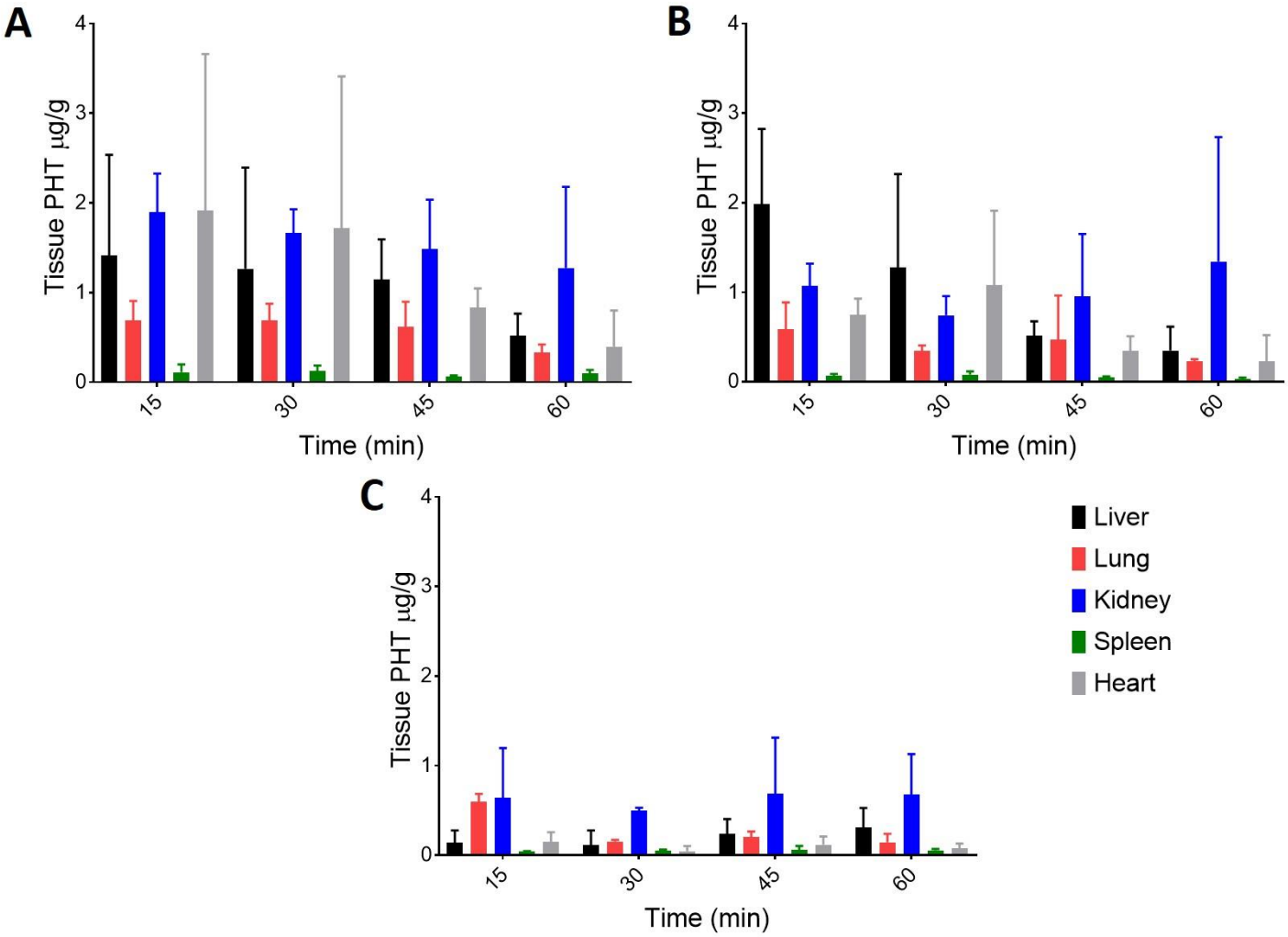

Figure 4.19 Comparison of phenytoin distribution over time in peripheral tissues after administration as intravenous solution (A), intranasal solution (B) and intranasal microparticles (C). (PHT: phenytoin).

4.4 Discussion

In **Chapter 3** the formulation using spray-drying and the characterization of TSP-microparticles loaded with model drugs was presented. The aim of this chapter was to formulate TSP-microparticles containing phenytoin and study the *in-vivo* brain uptake and biodistribution of the phenytoin formulated into TSP-microparticles.

Formulating TSP-microparticles loaded with phenytoin and optimizing their size to 10 µm was one of the research aims of this chapter. TSP-microparticles containing phenytoin were produced with the spray-drying method, and particle size was optimized to 10 µm The SEM analysis of the microparticles produced at optimized formulation parameters identified microparticles with a corrugated morphology and smooth and rupture free surface. A corrugated shape and rupture free surface has been reported to be advantageous for intranasal administration of microparticles[363–365]. The shape and texture of the microparticles had comparable features to TSP-microparticles containing FITC-Dextrans (**Chapter 3)**. The phenytoin content analysis showed very high encapsulation efficiency in the TSP-microparticles, and these results corroborate with the literature reporting high drug contents of spray-dried products[431,432].

Evaluating the mucoadhesive potential of TSP-microparticles containing phenytoin was an important research aim of this chapter. As in **Chapter 3,** *in-vitro* and *ex-vivo* methods were applied to investigate the mucoadhesive potential of the microparticles. In the *in-vitro* method, phenytoin microparticles have shown significantly higher mucoadhesion than the phenytoin powder or solution. The complementary *ex-vivo* studies also have shown similar results. These results demonstrate that the TSP-microparticles are mucoadhesive, the mucoadhesiveness of TSP might help microparticles to withstand mucociliary clearance in the nasal cavity.

The mucoadhesive potential of TSP-microparticles containing phenytoin was compared with the TSP-microparticles containing FITC-Dextrans. The ratio of the *ex-vivo* mucoadhesive strength of the microparticles to the unformulated powders was used to compare the mucoadhesive potential between TSP-microparticles containing FITC-Dextrans

and phenytoin. Lack of a statistically significant difference between TSP-microparticles containing phenytoin or dextrans indicates that the mucoadhesive potential of TSP-microparticles did not change with the addition of phenytoin.

Assessing phenytoin release from the microparticles represented the drug releasing behavior from TSP-microparticles and was one of the research aims of this **Chapter**. The *in-vitro* studies were performed for a duration of 4 h as it was hypothesized that the *in-vivo* formulation residence time in the nasal cavity was unlikely to be longer than this. Analysis of *in-vitro* drug release data revealed that the release of phenytoin from microparticles was diffusion dependent. The data best fitted to Higuchi's model for drug release, indicating diffusion of drug through polymer matrix was the rate-limiting step in the release of phenytoin from TSP-microparticles[433]. These results are supported by the cryo-FESEM studies discussed in **Chapter 3** where it was shown that TSP-microparticles form a gel-like layer on contact with mucin and the drug has to diffuse through this matrix. The formation of a gel-like layer during the mucoadhesion process is likely the key to the sustained release of phenytoin from TSP-microparticles compared to the phenytoin solution and phenytoin powder. TSP-microparticles significantly sustained the release of the phenytoin compared to the phenytoin solution or powder. About 60 % of the drug was released from the particles during the first 60 min and the drug release was sustained over 2 h. The drug release data from microparticles during the first 60 min was significantly slower compared to the solution and powder.

In-vitro drug release studies were supported by the *ex-vivo* permeation study in the porcine nasal mucosa. Due to the morphological similarities of porcine nasal mucosa to the human nasal mucosa, it was used in this chapter to evaluate drug permeation[357]. *Ex-vivo* permeation data showed evidence for sustained permeation of phenytoin from microparticles compared to the solution and powder. Due to its hydrophobic nature, phenytoin predominantly relies on the transcellular pathway to permeate across biological membranes[434]. However, the permeability of phenytoin solution data obtained in this study was slightly higher than literature[422], with the high JSS values observed in this study suggesting that the transport of phenytoin is supported by other mechanisms such as passive diffusion through paracellular pathways. The ability of solid microparticles to open tight

junctions was already reported and may have contributed to the drug permeation[228]. Collectively, the drug release data suggest that phenytoin was successfully released from the microparticles and is able to permeate across the nasal mucosa.

The initial burst release of phenytoin observed from the microparticles in the *in-vitro* studies is most likely attributed to surface-associated phenytoin molecules that can undergo rapid dissolution. Interestingly, in the first 5 min, the drug release from the microparticles was higher than the drug release from the phenytoin powder. The hypothesis is that this phenomenon was due to changes in the physical nature of the phenytoin when formulated into TSP-microparticles.

Phenytoin, when spray-dried with the polymers containing hydrogen donor and acceptor sites, is known to change from its crystalline state to an amorphous phase[395,424]. A change form a crystalline to an amorphous phase can improve solubility[75] and permit faster drug release which may be the reason for the faster release of phenytoin from TSP-microparticles than the crystalline powder.

Physical characterization of TSP-microparticles by XRPD and DSC revealed the change of crystalline phenytoin to a high-energy amorphous phase. The XRPD diffractograms of TSP-microparticles lack any crystalline phenytoin peaks, and the DSC analysis did not show any thermal peaks indicating an amorphous nature. The hydrogen donor and acceptor sites in polymers such as TSP can interact with the amide –NH protons in phenytoin and result in variation in nucleation and crystal growth inhibition[395]. TSP contains numerous -OH groups that can act as hydrogen bond donors or acceptors, which upon spray-drying with phenytoin can potentially interact with the amide groups and inhibit the association of drug molecules to form crystal nuclei and hold the drug in the amorphous phase[234,395]. Results from the stability studies demonstrate that phenytoin content and moisture content of the TSP-Microparticles did not change significantly over the period of six months ($P > 0.05$). However, the XRPD diffractograms showed that the phenytoin crystalline peaks begin to reappear after six months of storage. Phenytoin molecules have been reported to surface absorb and interact with the other phenytoin molecules via π-π interactions between phenyl rings and hydrogen bonding between amide and carbonyl groups during crystal growth[435]. A polymer with structurally similar hydrogen donor and acceptor groups can maintain the

amorphous phase for longer periods by competitive hydrogen bonding to inhibit the nucleation and crystal regrowth[395]. Hence it is reasonable to hypothesize that due to the lack of structurally similar hydrogen donor or acceptor groups in TSP the nucleation and crystal regrowth of phenytoin molecules occurred over time causing the reappearance of the crystal peaks in XRPD diffractograms. In future studies, it would be interesting to investigate how long TSP is able to retain the phenytoin in its amorphous phase, as it may have implications for the shelf life of TSP-microparticles.

Formulating size specific microparticles to target the olfactory region was a key focus of this thesis. Due to size-dependent aerodynamics and suitable impaction, 10 µm-sized particles have previously been suggested to target the olfactory region, as was observed in this study with TSP-microparticles[214]. Smaller particles (4 µm) owing to their small size tend to follow the air streamlines and escape the nasal cavity without depositing. These results reinforce the importance of particle size on nasal deposition and corroborate the olfactory deposition data for TSP-microparticles containing FITC-Dextrans.

Assessing the mucosal toxicity of formulations intended for mucosal applications is a crucial step in the formulation development process. Therefore, assessment of mucosal toxicity of TSP-microparticles containing phenytoin when administered intranasally was one of the research aims of this chapter. TSP has been reported to be nontoxic to the mucosa in previous reports in the literature[326] and results from **Chapter 3** corroborated these reports as TSP-microparticles containing FITC-Dextrans were found to be non-toxic to *ex-vivo* porcine nasal tissue. In this chapter, the safety of TSP-microparticles containing phenytoin following intranasal administration in rats was evaluated. The histopathological examination revealed no signs of necrosis or tissue damage and the olfactory mucosa treated with microparticles was comparable with the negative control. The structure of the nasal mucosa was well preserved and the olfactory epithelium displayed standard characteristics. Collectively, these results suggest that the TSP-microparticles containing phenytoin are safe for acute intranasal administration.

In addition to the results of *in-vitro* and *ex-vivo* studies, data from *in-vivo* studies are essential to predict the clinical outcome of a formulation[436]. An accurate, reliable analytical

method is required to obtain robust *in-vivo* data. Thus a sensitive HPLC method was developed to quantify the data in rat plasma and biological tissues.

As discussed previously, phenytoin is metabolized into its metabolite (5- (4-Hydroxyphenyl)-5-phenyl-hydantoin) in *in-vivo*, hence an HPLC assay that could simultaneously quantify phenytoin and its metabolite was developed. The chromatographic conditions were optimized by trial and error. The mobile phase reported by Potschka *et al*[257] was used and modified. The pH of the mobile phase was adjusted to 5.8 to facilitate the separation of phenytoin. The flow rate affected the retention time and a flow rate of 0.2 mL/min ensured the separation of the biological matrix from the phenytoin and metabolite. Adjusting injection volume to 10 µL provided an acceptable peak shape.

Sample preparation for HPLC analysis was optimized by trial and error. Use of perchloric acid to effectively solubilize lipids in the brain tissue to prepare HPLC samples has been reported in literature[437]. However, in this study, when perchloric acid was used, phenytoin recovery was low. The decreased pH caused by the addition of perchloric acid was likely causing the phenytoin to precipitate out resulting in the poor recovery. The 80 % ethanol solution and acetonitrile used to prepare the samples was sufficient to solubilize the lipids in the brain and other tissues effectively. In order to completely extract phenytoin from the plasma and tissues, tert-butyl methyl ether (TBME) was added to the extraction procedure for the samples. The HPLC assay developed in this chapter was validated for specificity, linearity accuracy and precision in plasma, brain, and other tissues prior to analysis of the *in-vivo* samples.

Brain, plasma and peripheral tissue uptake of phenytoin following administration as an IV solution, intranasal solution, and intranasal microparticles were obtained from *in-vivo* studies in rats. Brain concentrations of phenytoin were significantly higher for intranasal solution compared to the IV solution for the first 45 min, indicating transport through direct pathways to brain via olfactory and trigeminal neurons in the nasal cavity. As the 'rat intranasal catheter device' (Impel Neuro Pharma, USA) used for administration of intranasal solution in rats delivered the phenytoin solution directly to the upper dorsal olfactory region of the rat nose, it might have prevented the loss of drug in the vestibule and helped to increase the phenytoin uptake to the brain. The uptake of phenytoin in the olfactory bulb followed a

similar trend as the whole brain uptake. Intranasal solution produced maximum olfactory bulb concentration by 15 min suggesting fast transport by direct neuronal pathways. The brain and olfactory bulb phenytoin concentration gradually decreased with time after 30 min and a sudden drop in phenytoin concentrations was observed between 30 min and 45 min. The decrease in phenytoin concentration in the brain and olfactory bulbs can be postulated to be due to mucociliary clearance. With time, the intranasal solution was cleared from the nasal cavity by mucociliary clearance and/or by dripping and being swallowed resulting in a reduced dose of phenytoin available at the olfactory region for direct transport. Also, the increase in plasma phenytoin concentrations observed over time with the intranasal solution administration supports the idea of a solution being cleared or lost to swallowing. Comparing the brain concentrations of phenytoin after IV and intranasal solution administration clearly demonstrate the potential of intranasal administration to enhance the brain uptake of phenytoin.

The concentrations of phenytoin in the brain after intranasal microparticle and intranasal solution administrations were compared to evaluate the effect of formulation on the brain uptake of phenytoin. The brain concentrations administered as a solution were significantly higher than microparticles within the first 30 min post administration. The high brain concentrations in the initial time points with an intranasal solution can be linked to the phenytoin dose available at the olfactory region for direct transport. The intranasal solution in this chapter was directly delivered to the olfactory region with a special rat intranasal catheter device and was readily available for absorption resulting in high dose availability in the olfactory region. In contrast, although the microparticles were delivered to the olfactory region, release of phenytoin from the microparticles requires time as suggested by the *in-vitro* release studies in **Section 4.3.3**. Hence, the available dose of phenytoin at the olfactory region for absorption during the first 30 min was likely less than the intranasal solution.

At the later time points, the brain and olfactory bulb phenytoin concentrations with intranasal microparticles steadily increased while the phenytoin concentrations from intranasal solution decreased. At 45 min there was no significant difference between solution and microparticle administrations. Then by 60 min, the brain and olfactory bulb

concentrations of the phenytoin from microparticles were significantly higher than from the solution. This increase in the brain and olfactory bulb concentrations could have been due to the continued availability of phenytoin administered as microparticles at the olfactory region due to the mucoadhesive nature of the microparticles. As demonstrated in **Section 4.3.2**, TSP-microparticles are mucoadhesive and can withstand mucociliary clearance. Therefore it is possible that they provide a continuous release of phenytoin at the olfactory region whereas, the solution is likely to have been cleared from the nasal cavity by mucociliary clearance resulting in a reduced dose of phenytoin being available for absorption. The brain-plasma ratio results suggest an increase in drug targeting efficiency to the brain over the time with microparticles, which is likely due to their mucoadhesive nature.

Within the olfactory bulb, a higher concentration of phenytoin was observed at 15 min than 30 min with intranasal microparticles. This could have been due to the *in-vitro* burst release and the availability of phenytoin due to desorption of the phenytoin from the surface of the microparticles. Once the surface phenytoin was exhausted, the uptake was dependent on the phenytoin release from the microparticles. Thus at 30 min, lower olfactory bulb concentrations of phenytoin were observed.

Interestingly, the brain concentrations of phenytoin from intranasal microparticles at 60 min was comparable to the maximum brain concentration obtained by intranasal solution at 30 min ($P = 0.9208$). *In-vitro* release data reported approximately 60 % phenytoin release from microparticles at 1 h. Comparing the brain concentrations suggests that 60 % of phenytoin dose released from microparticles can produce the brain concentrations equivalent to 100 % of phenytoin dose from intranasal solution. This can be explained by the dose of the phenytoin available at the olfactory region. Due to the mucoadhesive nature of the microparticles, the phenytoin dose available at the olfactory region for direct transport to the brain might have been higher than the intranasal solution resulting in comparable brain uptakes. Since the blood volume in the brain is very low (47 ± 1µl/g)[438] and the dose administered was also low (1.5 mg) the amount of phenytoin attributed to blood traces can be assumed to be very low and hence not considered in this study. In addition, in rats, for intranasal administration of small molecules, it has been reported that the blood-brain ratio is not significantly affected by perfusion of the brain[439].

Collectively, these results suggest that the mucoadhesive nature of the microparticles can withstand mucociliary clearance ensuring drug (in this case phenytoin), available for brain uptake at the olfactory region whilst the intranasal solution is cleared quicker. Therefore, formulating drugs into TSP-microparticles has potential in nose-to-brain drug delivery. These results are in corroboration with previous works on mucoadhesive microparticles[173–175,189,440].

The plasma concentrations of phenytoin at all-time points were significantly higher following IV administration compared to intranasal solution and microparticles. Although phenytoin plasma concentrations showed a decreasing trend over time after IV administration, they did not vary significantly between the time points which is likely due to the ~64 min half-life of phenytoin in rats, which extends beyond the time points employed in this study[441]. IV administration is also expected to lead to accumulation of phenytoin in the peripheral tissues which is supported by the high phenytoin concentrations observed in the peripheral tissues in this study.

The phenytoin plasma concentrations following intranasal solution administration were significantly higher for the first 30 min compared to those after intranasal microparticle administration. The amount of phenytoin available for absorption into blood is likely much higher when formulated as solution compared to microparticles where the amount of phenytoin is limited by its release from the microparticles. The high vasculature and surface area of the nasal cavity might have promoted the absorption of the administered phenytoin solution into the bloodstream. In addition, ethanol present in the phenytoin solution might have enhanced the phenytoin absorption by causing vasodilation which explains the steady increase in the plasma concentration over time after intranasal solution administration The peripheral tissue phenytoin concentrations following intranasal solution administration are comparable to those following IV administration which supports the hypothesis of phenytoin being lost to dripping, nasally absorbed or lost to swallowing and eventually entering the blood.

Plasma uptake of phenytoin administered as intranasal microparticles steadily increased with time. The lower plasma levels of phenytoin from microparticles can be explained by the controlled release of phenytoin from the TSP-microparticles. Interestingly, plasma

concentrations of phenytoin after intranasal microparticles and intranasal solution did not show any significant difference at 45 min and 60 min. This can be correlated to the phenytoin dose available for the absorption into the blood at respective time points. The intranasal solution, as mentioned before may have been cleared from the nasal cavity before 45 min and/or dripped and swallowed by the rat which would most likely lead to absorption into the blood. However, the mucoadhesive microparticles retain the drug in the nasal cavity and the dose of phenytoin available for the absorption might not have changed over time. Therefore, at the 45 min and 60 min time points the effective phenytoin dose available for absorption from both the formulations could have been similar. Consequently, this might have resulted in the comparable plasma concentrations of phenytoin from intranasal solution and intranasal microparticles. The hypothesis is supported by the comparable phenytoin concentrations in the kidney, liver, and lung observed with an intranasal solution and microparticle administrations at the 45 min and 60 min time points.

The peripheral tissue phenytoin concentrations suggest that the systemic exposure of phenytoin can be reduced by administering the drug as intranasal microparticles. The increase in plasma concentrations over time with intranasal microparticle administration is correlated with the increase in phenytoin concentration in the peripheral tissues over time. The high phenytoin concentrations at 15 min following intranasal microparticle administration is a noteworthy observation in this study. This is possibly due to the deposition of microparticles in the lung while administering with the insufflator, resulting in high lung concentrations at 15 min. This might have affected the plasma concentrations of phenytoin, and it would be reasonable to expect much lower plasma concentrations of phenytoin from intranasal microparticles without the deposition in the lungs. Interestingly, the lung phenytoin concentrations at later time points were significantly lower than at 15 min (****$P < 0.0001$). With the ability of microparticles to sustain the release of phenytoin, if the microparticles are deposited in the lung, a steady increase of the phenytoin concentration is expected over time. However, the phenytoin concentration decreases significantly. One of the possible reasons could be the presence of surface phenytoin. Assuming only a small fraction of microparticles are deposited in the lungs, the presence of surface phenytoin which quickly dissolves could have spiked up the phenytoin concentration at 15 min. Nevertheless,

evaluation of the TSP-microparticle release in the lungs is required in future to progress this delivery system.

4.4.1 Key findings

Collectively, the data presented in this chapter suggests that TSP can be formulated as 10 µm-sized particles containing phenytoin by a spray-drying technique. TSP-microparticles control the extent of release of phenytoin and improve the olfactory deposition at normal inhalational rates. TSP-microparticles are mucoadhesive and do not cause any nasal mucosa toxicity in rats. TSP-microparticles containing phenytoin were found to be stable up to 3 months of storage. I*n-vivo* studies identified the enhanced the brain uptake and direct nose-to-brain delivery of phenytoin when administered as intranasal TSP-microparticles.

4.4.2 Future directions

Considering the enhanced brain uptake of phenytoin from the TSP-microparticles, it would be interesting to explore the efficacy of such microparticles in a rat epilepsy model. Such studies can provide critical data for the translation of formulations from bench to bedside. In addition, this study considered drug concentrations due to blood traces in brain and other organs are negligible, however, it can be a limitation and future work needs to address this by employing techniques such as perfusion of blood.

The stability data in this chapter revealed the recrystallization on storage of TSP-microparticles for 6 months. Chemical modification of TSP to incorporate more structurally similar hydrogen donor or acceptor sites similar to phenytoin might prolong the storage time for TSP-microparticles. Furthermore, drugs with structurally similar hydrogen donor or acceptor sites could be ideal candidates for microparticle formulation with TSP.

Therefore, the data from this chapter provides evidence for a brain targeting effect of TSP-microparticles after intranasal administration. It would be interesting to further explore the organ toxicity, elimination profiles and pharmacokinetics of the drug absorbed systemically from the TSP-microparticles.

Chapter 5

Computational measurements of micro particle deposition in human nasal cavities

5 Computational measurements of microparticle deposition in human nasal cavities

Results from **Chapter 3** and **Chapter 4** of this thesis demonstrated that size-specific microparticles could enhance deposition in the olfactory region. It would be beneficial to study this formulative approach in combination with an intranasal delivery device to augment olfactory targeting. Intranasal devices carry the significant advantage of self-administration. This **Chapter** investigates microparticle deposition in three human nasal cavities using two conventional drug delivery approaches; firstly, a standard nebulizer that uses normal inhalational air flow, and secondly, a modern bi-directional air flow delivery technique.

5.1 Introduction

A recent 2017 report[442] from the Food and Drug Administration (FDA) stressed the importance of *in-silico* models in drug delivery. The statement "It is the use of *in-silico* tools in clinical trials for improving drug development and making regulation more efficient,this enables safe and effective new therapeutics to advance more efficiently through the different stages of clinical trials" from this report highlight the importance of *in-silico* models in drug development.

In recent years, *in-silico* experiments have suggested new lines of basic research and opened up new possibilities in various research areas like cardiovascular studies[443], ophthalmology[444], toxicology[445], dermatology[446], cancer studies[447,448], genetic assays[449], intra-cellular mechanisms[450], bone remodelling[451] and organ studies[452]. Computational simulations offer an inexpensive method to test a hypothesis which might be challenging to investigate experimentally in animals or human subjects[453].

Quantification of particle deposition in the olfactory region of the geometrically complex human nasal cavity is experimentally very hard to measure due to practical and ethical issues. Thus, *in-silico* methods such as computational fluid-particle dynamics (CFPD) offer a

practical, noninvasive and inexpensive means of predicting nasal particle deposition. CFPD allows prediction of particle deposition by varying physical conditions such as inhaled velocity profile[454,455] and particle size. It also helps obtain information on regional deposition within the nasal cavity[456–460].

5.1.1 Nebulized (inhalation-driven) deposition in the nasal cavity

Nebulizers have been commonly used for many years for the administration of drug solutions as aerosols. Nebulizers use a facemask, or a mouthpiece for the administration of drug aerosols and the driving force for drug administration is inhalation. Commonly available nebulizers in the market are divided into three types based on their working principle: jet nebulizers, ultrasonic nebulizers and mesh nebulizers.

Nasal airflow characteristics determine the intranasal deposition of particles through nebulization. Nasal airflow patterns are well described in the literature. Laminar flows are observed at normal inhalational rates of 5-20 L/min [461] as shown in **Figure 5.1**. The majority of air flows through middle and inferior regions, while dorsal posterior regions like the olfactory region receive little air flow[462]. The results obtained from the simulations were in partial agreement with experimental results from cadavers[463] and the nasal casts[464–466].

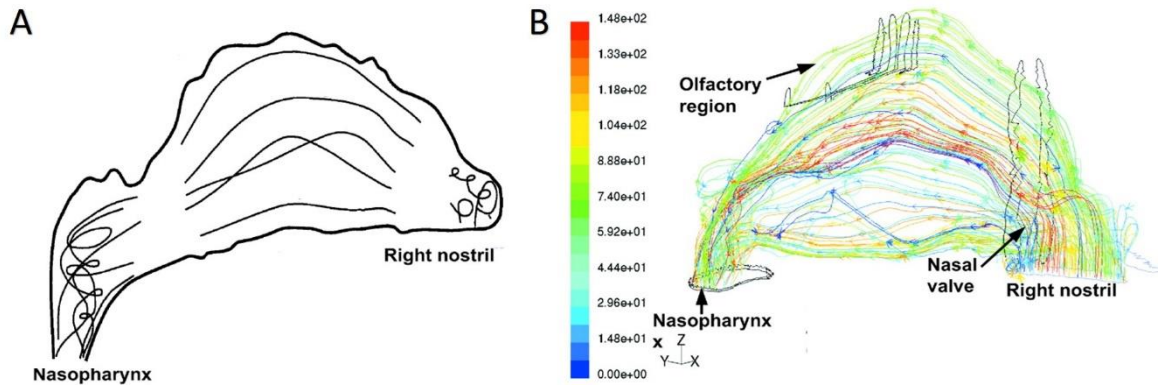

Figure 5.1 Schematic representation of airflow streamlines in the human nasal cavity obtained by computational simulations. (A) represents the simple flow lines from one of the early studies by Subramaniam et al.[467] and (B) represents the flow lines from an advanced CFPD model, with the color map indicating the velocity of the airflow (Figure adapted with permissions from Subramaniam et al.[467] and Zhao et al.[468]).

Alterations in nasal airflow patterns within human population have also been successfully characterized[469–471]. These results identified that 5 to 20 L min^{-1} are the physiological inhalation flow rates[215,472]. Zhu *et al.*[473] identified the difference in airflow patterns between two nasal models based on different ethnic origins. The study reported a lower flow in the olfactory region for the Indian model (about 1 %) compared to the Caucasian (about 6 %) and Chinese (about 5 %) models. The Caucasian nasal model showed high flow (35 %) through the middle passage and high flow (about 34 %) in the inferior portion of the Indian nasal model.

5.1.2 Particle deposition in the nasal cavity

5.1.2.1 Experimental measurements

Many studies have reported particle deposition in adult human nasal replica casts[474,475] at various air flow rates (4 to 50 L min^{-1}) and particle sizes (4 nm to 12 µm)[476–479]. The results from these studies have observed a common trend defining deposition in the nasal cavity. Total deposition fraction of particles in the nasal passages is a function of inertial impaction. The inertial particle deposition increases with the particle mean diameter and air flow rate and is expressed in terms of impaction parameter (IP)[480–482].

$$IP = d_a^2.Q \qquad Equation\ 6$$

Where d_a is the particle aerodynamic diameter and Q is the volumetric airflow rate. Hence, inertial particle deposition increases with the particle mean diameter and air flow rate.

5.1.2.2 Computational simulations

Computational simulations couple airflow and particle trajectories in order to compute deposition of particles in human nasal cavities. Airflow in the nasal cavities is typically solved using a set of coupled partial differential equations called the Navier-Stokes equations which yields air flow velocity and pressure. Microparticle movement is usually tracked using

the Lagrangian approach by taking into account various forces acting on a particle. For example, Li *et al.*[483] investigated microparticle deposition during normal inhalation for health-risk assessments associated with particle inhalation. Shang *et al.*[484] compared the deposition of microparticles between human and rat nasal cavities with an aim to improve extrapolation of particle deposition data between inter-subject species. The total nasal deposition under the effect of dynamic air flow was studied by Karakosta *et al.*[458] and they identified that dynamic flow has a significant effect on the microparticle deposition. It has been applied successfully to examine deposition of particles from nasal sprays[485–488] and the effects of ethnic groups[489], spray orientation[459] etc.

Shanely *et al.*[490] investigated region specific deposition of particles at inhalational air flow rates of 2 to 7 L min^{-1} in one healthy adult human subject. The nasal deposition was reported as a function of Stokes number in the vestibule, valves, and main airways. Liu *et al.*[491] investigated deposition of 1.71 to 10.00 μm sized microparticles at higher inhalation flow rates of 30, 60 and 90 L min^{-1} in one healthy adult human subject. This study divided the nasal cavity into an anterior, middle and posterior region. Particle deposition was reported to be dependent on particle size and flow rates. This study reported a preferential deposition of 10 μm particles at approximately 60 % of the distance into the cavity (from nostrils) at an airflow rate of 30 L min^{-1}. The particles between 5.77 to 10.00 μm were reported to significantly deposit in the first 30 % of the length of the nasal cavity at flow rates of 30, 60, and 90 L min^{-1}. Ghalati *et al.*[492] studied the deposition of microparticles (1 to 30 μm) at flow rates of 5, 10 and 15 L min^{-1} in one healthy adult human subject. This study predicted deposition in the vestibule, nasal valve, main airway, and nasopharynx regions of the human nasal cavity. Although these studies have reported critical data on region-specific deposition, the olfactory region was not identified.

Shi *et al.*[215] reported deposition of microparticles in the olfactory region. This study divided the nasal cavity into the anterior part, olfactory, middle meatus and inferior meatus and tested the deposition of microparticles at 7.5 and 20 L min^{-1}. The results of this study reported that relatively more particles pass through the olfactory and lower middle meatus regions, compared to the inferior meatus region with an increase in particle size (from 2 μm to 20 μm) due to the centrifugal force effect. The effect of gravity is negligible for flow rate

≥ 20 L min^{-1} due to inertia dominating, and the effect of gravity is higher for lower flow rates ≤ 7.5 L min^{-1} and particle size > 10 µm. This study identified that there is an optimal IP to enhance deposition in the olfactory region (**Figure 5.2**).

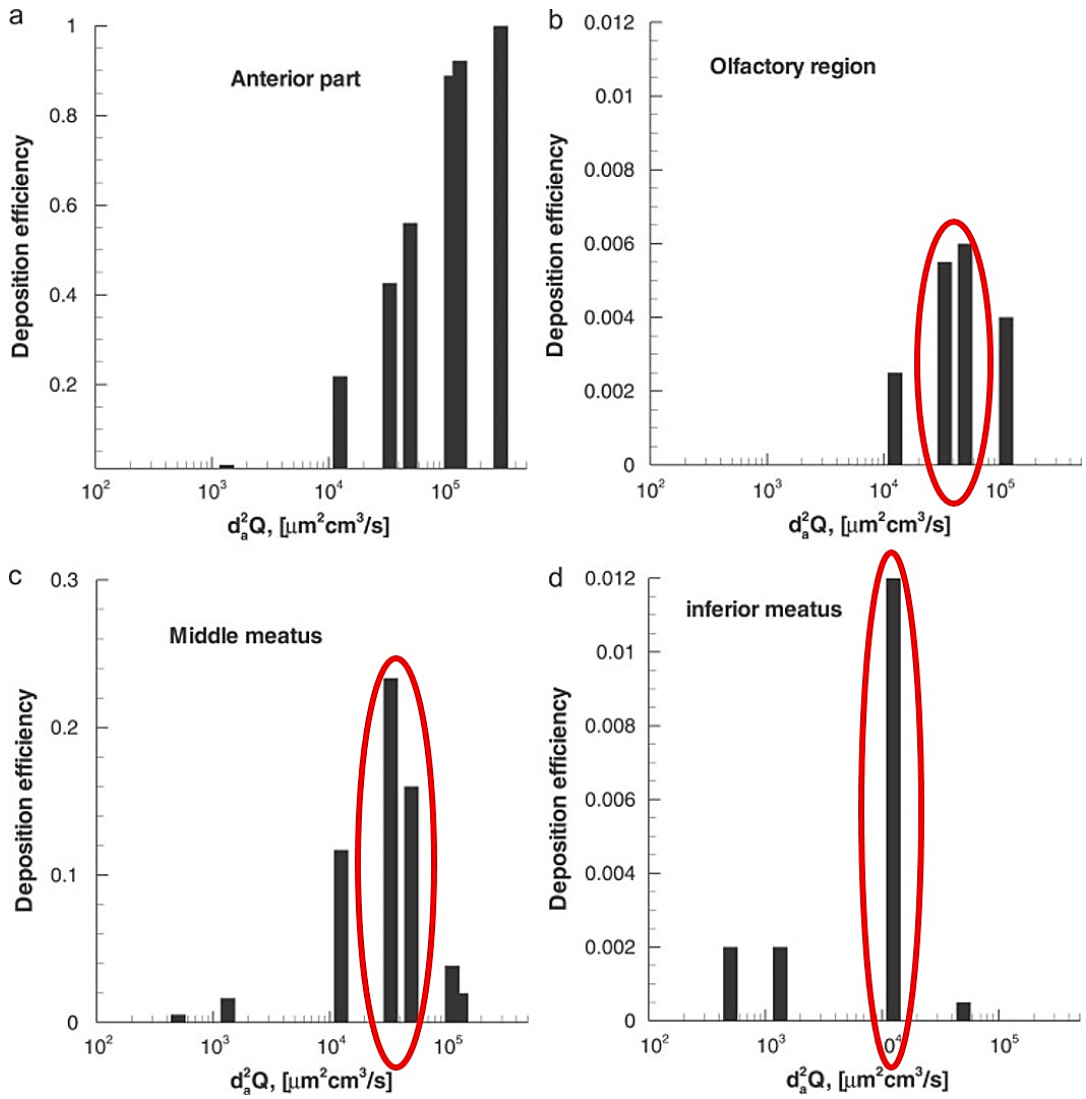

Figure 5.2 The region-specific deposition of microparticles as a function of IP reported by Shi et al. Circle represents the identified optimal IP to enhance the deposition in different regions of the nasal cavity. (Figure adapted with permission from Shi et al.[215]*).*

Xi *et al.*[493] compared drug deposition in human nasal replica casts with different nasal devices (sprays and nebulizers). This study reported that only 4.6 % of the particles released from spray pumps had reached the olfactory region whereas up to 9 % release was observed near the olfactory region with the pointed release administration by nebulizers.

Schroeter *et al*[214] reported detailed local deposition patterns in the human nasal cavity. Deposition of particles with size 2.6 to 14.3 μm at an inhalation flow rate of 7.5, 15.0, and 30.0 L min^{-1} in one healthy adult human subject were examined. Both the computational simulations and nasal replica cast deposition studies were reported. This study divided the nasal cavity into six regions; 1) nasal vestibule containing the anterior portion of the nose, 2) nasal valve region containing the anterior part of the nasal cavity with minimum cross-sectional area, 3) anterior turbinates encompassing the anterior sections of the middle and inferior turbinates, 4) olfactory region, 5) turbinates containing the middle and posterior parts of the inferior and middle turbinates, and 6) nasopharynx. Deposition efficiency as a function of particle size was reported in this study. The results from this study identified the optimal particle size for enhancing the deposition in specific regions of the nasal cavity. As stated in **Chapter 1,** this study identified that a particle size around 10 μm is optimal for maximizing the deposition in the olfactory region as shown in **Figure 5.3**.

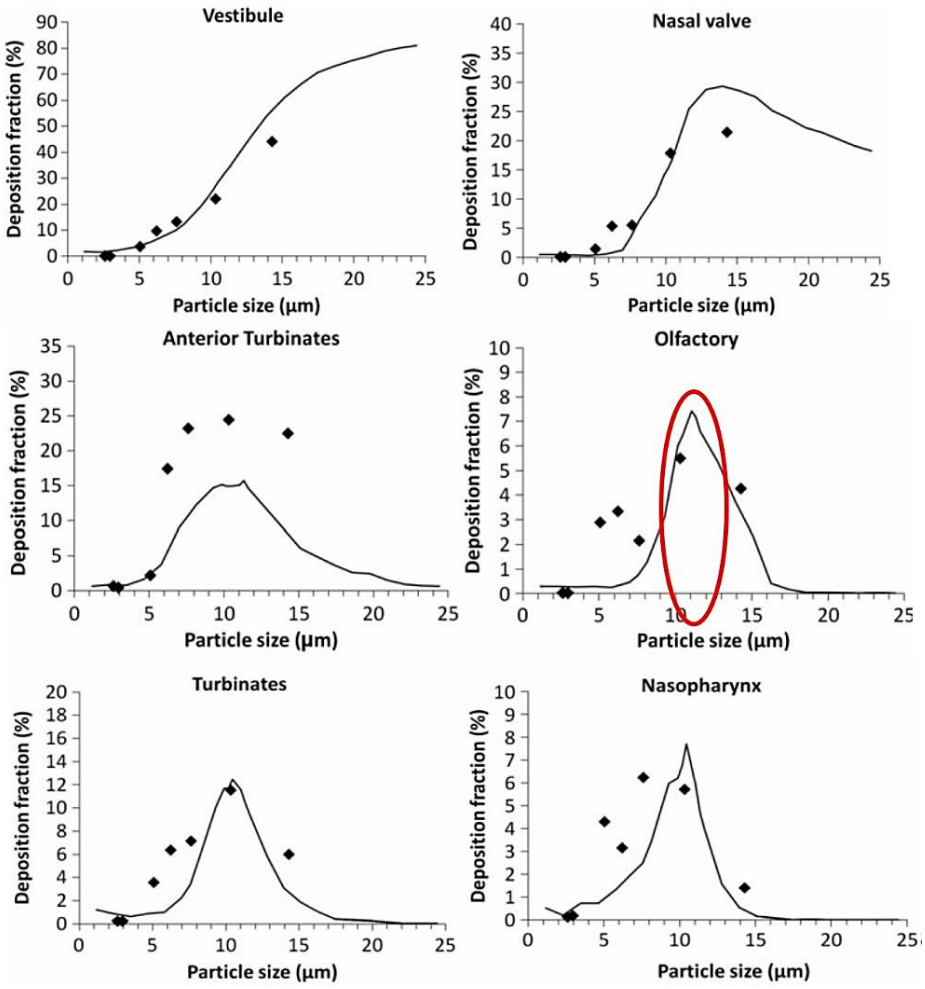

Figure 5.3 Deposition of microparticles in specific regions in the nasal cavity as a function of particle size. The solid line represents the data from computational simulations and symbol (diamond) represents the data from in-vitro nasal replica cast studies. The region-specific analysis identified the optimal particle size to maximize the deposition. Circle indicates the optimal size of particles for enhanced deposition in the olfactory region. (Figure adapted with permission from Schroeter et al.[214]*).*

In summary, the particle deposition in the nasal cavity was shown to be a function of its size. Also, all these studies investigated the region specific deposition in only one human subject and did not account for the inter-subject variability. Hence, there is a need to investigate the variability of deposition in the olfactory region of more than one human subject to examine if the same particle size range is enhancing the deposition. Therefore, this Chapter examines the effect of particle size on the region-specific deposition of particles in three human subjects with emphasis on the olfactory region.

5.1.3 Modern targeting devices

As mentioned in **Chapter 1**, POD technology, Kurve technology, and the OPTINOSE bi-directional delivery technique can improve the deposition in the nasal airways particularly near the olfactory region. Nebulisation often leads to a significant loss of the administered drug dose to the lungs resulting in low drug deposition in the olfactory region. Hence, the use of novel drug delivery device technologies for targeting formulations to the olfactory region is gaining traction. Among the targeting devices, the OPTINSOE 'Bi-directional delivery technique' shown in **Figure 5.4** has been popular and the recently FDA approved drug sumatriptan powder (Onzetra Xsail®) for nose-to-brain delivery is based on this delivery technique.

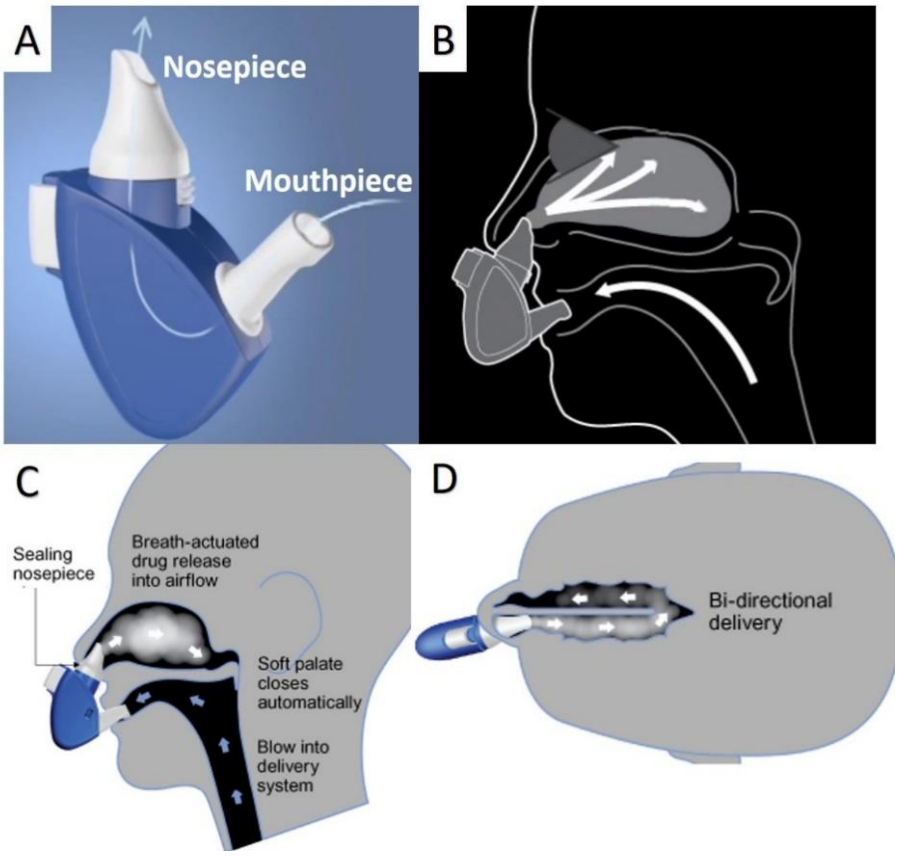

Figure 5.4 Illustration of breath powered bi-directional delivery technique. (A) OPTINOSE® device (B) with air flow into nasal cavity from the mouth through the device. (C) Steps involved in the delivery technique and (D) direction of air flow entering from one nostril and exiting from other. (Figure adapted with permission from Tepper et al.[494]).

Optinose Inc. (Oslo, Norway) developed the breath powered bi-directional delivery technique. The device consists of two parts: a sealing nosepiece and an adjustable mouthpiece. The nosepiece is inserted into one nostril, and the subject blows into the mouthpiece. Due to the positive pressure during exhalation, the soft palate closes and forms a communication pathway between two nostrils near the nasopharynx region. Under these circumstances, airflow enters via one nostril and leaves by the other, hence the name 'bi-directional delivery technique' as shown in **Figure 5.4**. The closure of the nasopharynx also prevents the loss of drug molecules into the lungs[495].

The bi-directional delivery technique has shown the potential to improve drug delivery to the olfactory region and consequently enhance nose-to-brain drug delivery. The bi-directional delivery technique has been tested with successful results in the treatment of migrane[494,496–498], nasal polyps[499,500], rhinosinusitis[501]. It has also shown evidence for direct nose-to-brain transfer of oxytocin by decreasing the dose required in a human study to improve social-cognitive behaviour[218] and might have implications in the treatment of complex CNS disorders[502].

Skretting *et al.*[503] identified the deposition of radiolabelled particles in the human nose administered by bi-directional delivery technique and showed that the bi-directional delivery could improve deposition in deep regions of the nasal cavity. Djupesland *et al.*[1] demonstrated an improved deposition in the upper nasal cavities and less deposition in the nasal valve and vestibule region using the bi-directional delivery technique. Djupesland *et al.*[504,505] compared the depositions of traditional spray pump in the human nasal cavity with bi-directional delivery technique and concluded that the bi-directional delivery could significantly improve the deposition of particles in the upper posterior segment of the nasal cavity near to the olfactory region.

5.1.4 Computational simulations in literature

Kleven *et al.*[506] were first to simulate bi-directional delivery at 6 L min^{-1} and uniform particle size of 3.5 µm as a part of the development process of this delivery technique. The particles were released near the nasal valve in the form of a spray. Under these conditions, the bi-directional delivery leads to 55.4 % total nasal deposition. The air flow velocity was observed to be greatest at the nasal valve regions of exit nostrils. The velocity at the inlet nasal valve was not high due to the placement of the delivery device. This study also tested the deposition of 10 µm sized particles and reported that the whole nasal deposition improved to 69.2 % due to the increase in particle size.

Xi *et al.*[507] compared the deposition of particles from two nebulizers vibrating mesh and jet nebulizer in one healthy human subject by inhalational and bi-directional delivery techniques. The particles released at the nostrils with size 1.5-3.2 µm and the air flow rates tested were 6, 12, 18 L min^{-1}. The nasal cavity was separated into the olfactory region and vestibule-turbinate region to estimate the deposition. The results of this study reported up to 6 % of olfactory deposition using the bi-directional delivery technique.

Recently, Dong *et al.*[508] simulated and compared the deposition pattern of particles (1 nm to 10 µm) released near the nasal valve in one healthy human subject by inhalational and bi-directional delivery techniques. The airflow rates tested in this study were 7.5 and 15 L min^{-1}. The deposition of particles near the olfactory region and the effects of exhalation flow rate were investigated. The results of this study were also in agreement with increased deposition of particles in the olfactory region by bi-directional delivery technique.

In summary, although bi-directional delivery was shown to improve the drug delivery in the olfactory region, no report has attempted to study the effect of particle size on the olfactory deposition by bi-directional delivery technique. Also, the detailed region-specific deposition of the bi-directional delivery that might have implications in toxicity and drug delivery studies has not yet been reported. Moreover, all these studies investigated the deposition in only one subject and did not assess variability between subjects.

5.2 Objectives

The computational simulations in this **Chapter** aim to study the effect of particle size on the regional deposition of particles in three human subjects and consequently the nose-to-brain delivery of the drugs. To this effect, the following are the two objectives of this chapter:

1. To study the effect of particle size combined with inhalation-driven (nebulized) delivery on the region-specific deposition of microparticles in the human nasal cavity with emphasis on the olfactory targeting of microparticles and study the variability between subjects in this study.
2. To study the effect of particle size combined with bi-directional delivery technique on the region-specific deposition of microparticles in the human nasal cavity with emphasis on the olfactory targeting of microparticles.

5.2.1 Chapter aims

The overall aim of this **Chapter** is to investigate the interaction between particle size and two different intranasal delivery mechanisms.

1. To analyze olfactory particle deposition in three human subjects under nebulization.
    a. By reconstructing the human nasal cavities *in-silico* using CT-scan images.
    b. By simulating the **inhalational airflow** and dynamics of particle deposition within the nasal passage.
    c. By analyzing and comparing the regional deposition data to identify the similarity in the deposition of the particles between three human subjects.
2. To identify the ideal particle size to improve the olfactory targeting under bi-directional delivery technique.
    a. By simulating the **bi-directional airflow** and dynamics of particle deposition at various particle sizes within the nasal passages.
    b. By analyzing the deposition data to identify the suitable particle size for enhancing the olfactory deposition.

5.3 Methods

5.3.1 Subjects used in this study

Axial head and neck computed tomographic (CT) scans of three adult normal healthy human subjects were used to reconstruct the anatomically accurate nasal airways. A Philips CT scanner was employed to obtain the scans. Scans were comprised of stacks of horizontal slices with 6.0000 pixels per mm resolution, and the voxel size was 0.1667x0.1667x0.5 mm^3. Subject 1 was a 40-year-old healthy male, Subject 2 was an 88-year-old male, and Subject 3 was a 60-year-old healthy male. Patients were imaged awake, in a supine position. CT scans were obtained following approval from New Zealand Health and Disability Ethics committee protocol NTX/08/12/26. All the raw image files of CT scans were provided by the Department of Surgery at the University of Auckland. Further processing of raw image files to generate in-silico nasal airways and simulation studies were performed at the University of Otago and Auckland Bioengineering Institute.

5.3.2 Image-based reconstruction of human nasal airways and mesh generation

Using ITK-SNAP 3.5.0, CT-scan images were segmented, and the airways in the nasal passage were identified. The segmented images were then converted to a 3D surface and smoothed using MESHLAB®. The resulting 3D nasal airways meshed with high-quality computational elements, surface and volume mesh were generated by ICEM-CFD® (ANSYS, Inc., Canonsburg, PA) for numerical analysis. The final 3D geometry was divided into six anatomical regions similar to Schroeter *et al.*[214] as shown in **Figure 5.5** to identify the region-specific deposition of particles.

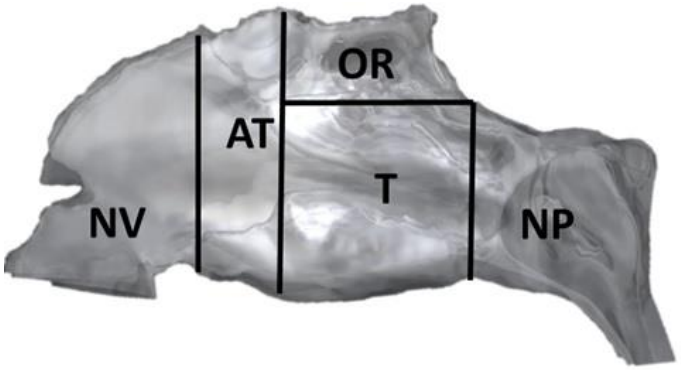

Figure 5.5 A representative 3D nasal cavity identifying the regions; nasal vestibule and valve (NV), anterior turbinates (AT), turbinates (T), olfactory region (OR), and nasopharynx (NP).

5.3.1 Governing equations

Assuming steady, laminar, incompressible and isothermal flow, the governing equations for air flow can be given as

Continuity

$$\frac{\partial u_i}{\partial x_i} = 0 \qquad |Equation\ 8$$

Momentum

$$\frac{\partial u_i}{\partial t} + u_j \frac{\partial u_i}{\partial x_j} = -\frac{1}{\rho}\frac{\partial p}{\partial x_i} + \frac{\partial}{\partial x_j}\left[v\left(\frac{\partial u_i}{\partial x_j} + \frac{\partial u_j}{\partial x_i}\right)\right] \qquad |Equation\ 9$$

Where u_i is the air velocity, ρ is the fluid density, p is the pressure and v is the air kinematic viscosity.

One-way coupling between fluid and particle phase was assumed. This assumption implies that the fluid phase affects particle phase. However, the particle does not influence the fluid flow. This assumption is valid for dilute suspensions. The governing equations for the microparticle transfer are given by

$$\frac{d\vec{x}_p}{dt} = \vec{u}_p \qquad |Equation\ 10$$

and

$$m_p \frac{d\vec{u}_p}{dt} = \frac{1}{8}\pi\rho_g d_p^2 C_D\left(\vec{U}_g - \vec{u}_p\right)\left|\vec{U}_g - \vec{u}_p\right| + \vec{G} \qquad |Equation 11$$

Where, $\vec{x}_p$ is the particle position; $\vec{u}_P$ and $\vec{U}_g \equiv u_i$ is the particle and airflow velocity vectors, m_p is the particle mass; ρ_g is the gas density; $\vec{G}$ is the gravitational force; C_D is the drag coefficient; and d_p is the particle diameter, each particle represents the group of particles possessing the same characteristics[215].

The air flow and particle deposition simulations were conducted with an air density of 1.225 kg/m^3, dynamic air viscosity of 1.8 X 10^{-5} kg/m.sec, absolute air temperature of 293 K and a particle density of 1350 kg/m^3.

5.3.2 Simulation of airflow and particle deposition

Steady incompressible, laminar and isothermal airflow was simulated in the three-dimensional (3D) nasal airways. The inhalational airflow rates of 5, 10, and 20 Lmin^{-1} and a bi-directional airflow rate of 6 Lmin^{-1} were simulated in this study. For the inhalation simulations boundary conditions were defined as, rigid airway walls with no-slip and perfect absorption, zero pressure at the nostrils and a negative pressure at the outlet. Outlet pressure was specified to attain the required flow rate.

Boundary conditions for bi-directional delivery technique were defined as follows: nostrils were defined as inlet and outlet. Each subject was simulated twice with one nostril serving as inlet once. Rigid airway walls with no-slip and perfect absorption, zero pressure at the outlet were specified. Airflow was simulated at 6 Lmin^{-1} at an upward angle of 60° through the inlet. All the simulations were performed by numerically solving the incompressible Navier-stokes equations using the finite volume method with commercial software ANSYS-CFX V16.0® (Canonsburg, PA).

Particle sizes of 2, 4, 6, 8, 10, 12, 14, 16, 18 and 20 µm were simulated in this thesis. Particles of 2-20 µm were selected to represent ideal size range to target olfactory region. The numerical computations of particle dynamics were performed with the low Reynolds number k-ω model; this model has demonstrated accurate solutions for laminar airflow[509].

Particles were released at both the nostrils when simulating nebulization. Particles were released at one of the noses for bi-directional delivery. In both cases, particles were released from uniformly distributed points across a surface. Total nasal deposition fraction was computed as the ratio of some particles deposited in the nose to the number of particles released. Region-specific deposition fractions were computed as the ratio of the number of particles deposited in each region by the total number of particles released. All the simulations were performed with commercial software ANSYS-CFX V16.0® (Canonsburg, PA). The deposition efficiency of particles according to the nasal regions was calculated, analyzed and reported.

$$DE(\%) = \frac{Number\ of\ particles\ deposited\ in\ the\ specific\ nasal\ region}{Total\ number\ of\ particles\ released\ into\ the\ nasal\ cavity} \quad |Equation\ 12$$

5.3.3 Statistical analysis

Where applicable, statistical analyses were conducted using an unpaired t-test or ANOVA on Prism 6 (GraphPad, USA). A *P*-value of < 0.05 was taken to be significant.

5.4 Results

5.4.1 Subjects used in this study

Three 3D-human nasal cavity models created from the three CT-Scans are shown in **Figure 5.6,** and their respective geometrical surface areas are presented in **Table 20**.

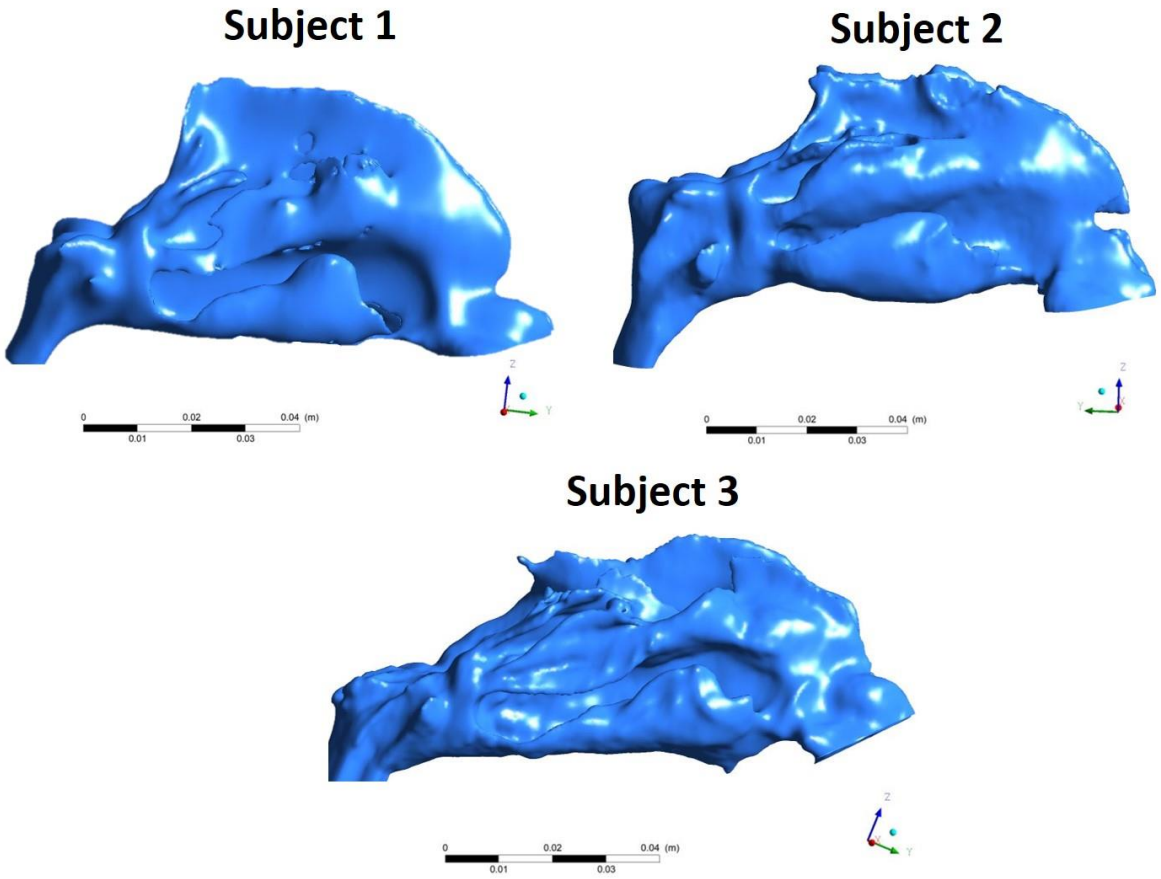

Figure 5.6 The 3D-human nasal replica model geometries of three subjects generated from CT-scan images.

Table 20 Geometrical surface area of the nasal regions in the 3D-human nasal cavity models.

Anatomical region	**Surface area (cm^2)**		
	Subject 1	**Subject 2**	**Subject 3**
Nasal valve and vestibule	34.50	38.85	29.02
Anterior turbinates	40.39	28.60	27.21
Olfactory region	40.59	37.82	27.91
Turbinates	96.49	102.91	113.47
Nasopharynx	32.97	35.47	22.56
Total	244.94	243.65	220.17

Cross-sectional areas of the nasal passage (inferior/middle/posterior meatuses) of the individual subjects were compared with cross-sectional results published in the literature to assess deviation from population data[510]. The cross-sectional areas of the three subjects used in this thesis were compared to the cross-sectional areas of normal subjects available in the literature[511–513] and are presented in **Figure 5.7**. Cross-sectional areas of all the three subjects were within the natural range of variation and, they reflect the trends of changing cross-sectional area at different positions along the cavity.

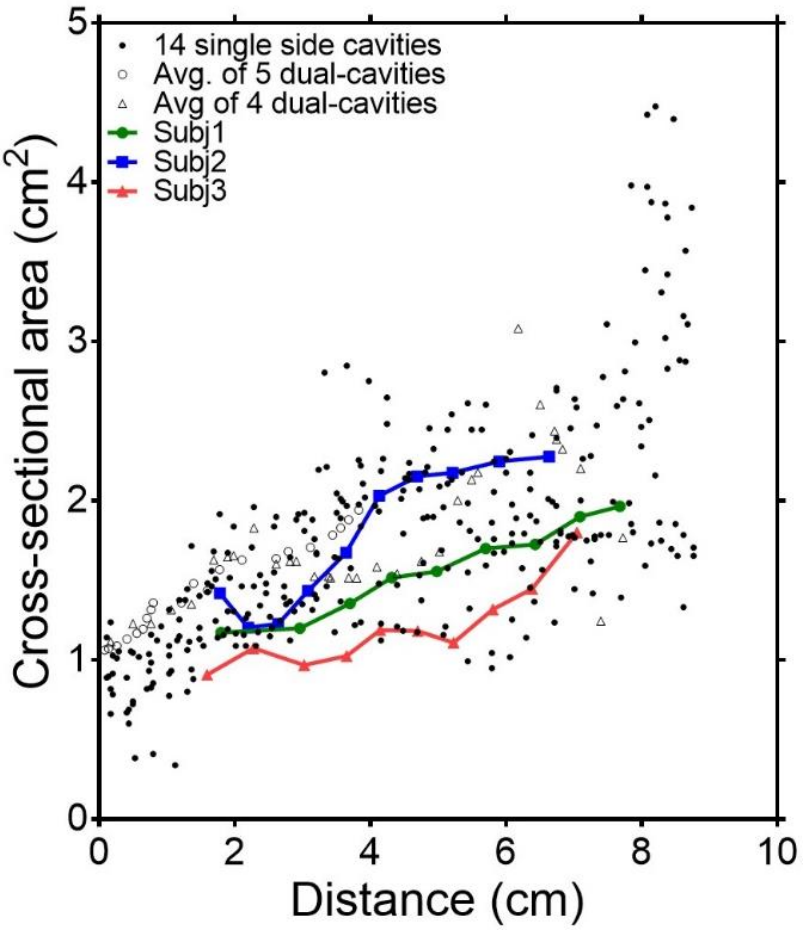

Figure 5.7 Comparison of the average cross-sectional area of the three individual subjects with published data from the literature. The horizontal axis is the distance from the anterior tip of the nostril.

The nasal airways were divided into tetrahedrons (Volume mesh) by ICEM-CFD. This mesh generation helps solve fluid flow and particle motion. Also, near to the nasal wall, a prism mesh consisting of three-layer tetrahedral or pentahedral elements was generated as shown in **Figure 5.8** to accurately calculate deposition and wall turbulence effects. The final mesh features about 89668 nodes, and 179086 elements for subject 1, 90000 nodes, and 179726 elements for Subject 2, and 86528 nodes, and 172771 elements for Subject 3.

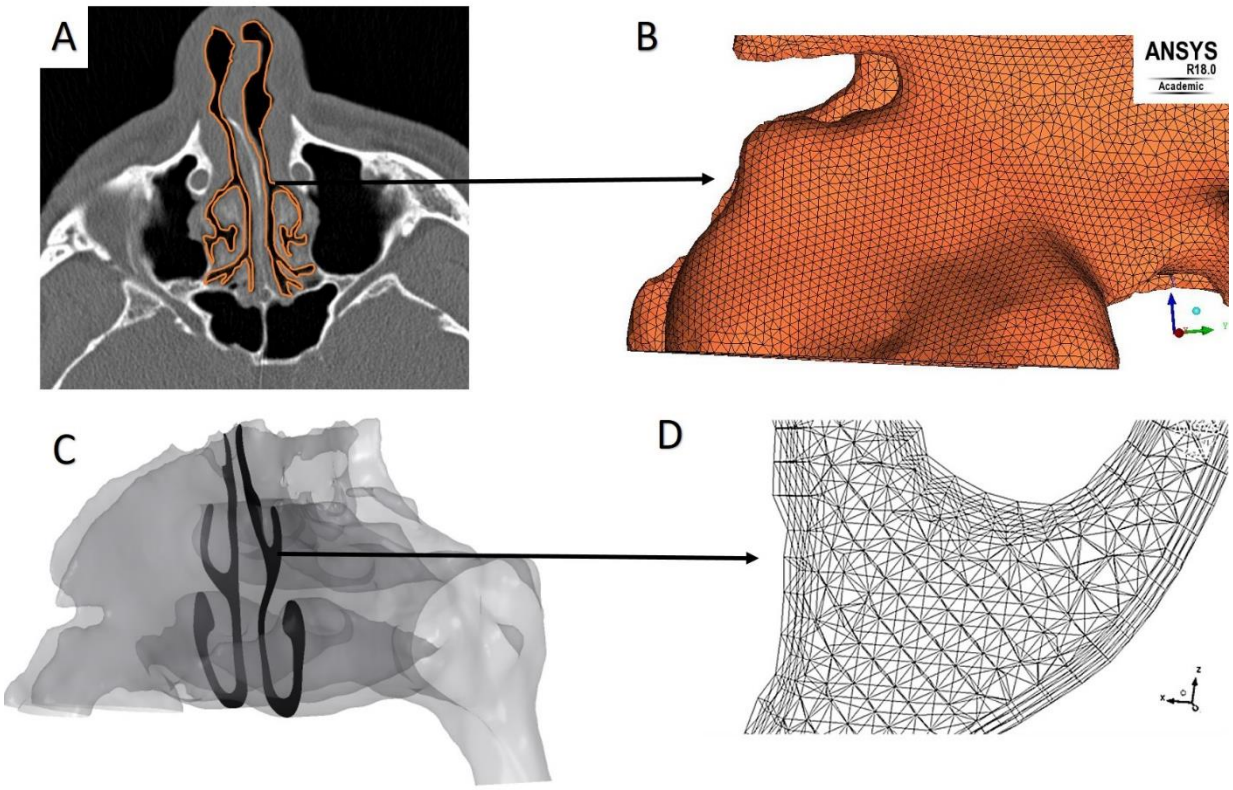

Figure 5.8 Reconstruction of human nasal cavities in-silico. (A) Segmentation of nasal airways in a CT-scan image (B) reconstruction of surface and generation of surface mesh (C) reconstructed nasal cavity model showing complex airways and (D) volume mesh generated in the airways and a three-layer prism mesh at the borders.

5.4.2 Model validations

Our predictions were overall in agreement with reported values from the literature. Particle deposition data from Kelly *et al.*[481] and Schroeter *et al.*[214] were selected to validate the data as they feature similar inlet conditions and anatomical descriptions of the regions in the nasal cavity. The whole nose deposition data as a function of IP from the current simulations were compared with the experimental data from nebulization simulations in a human nasal cast by Kelly *et al.*[481] and shown in **Figure 5.9.**

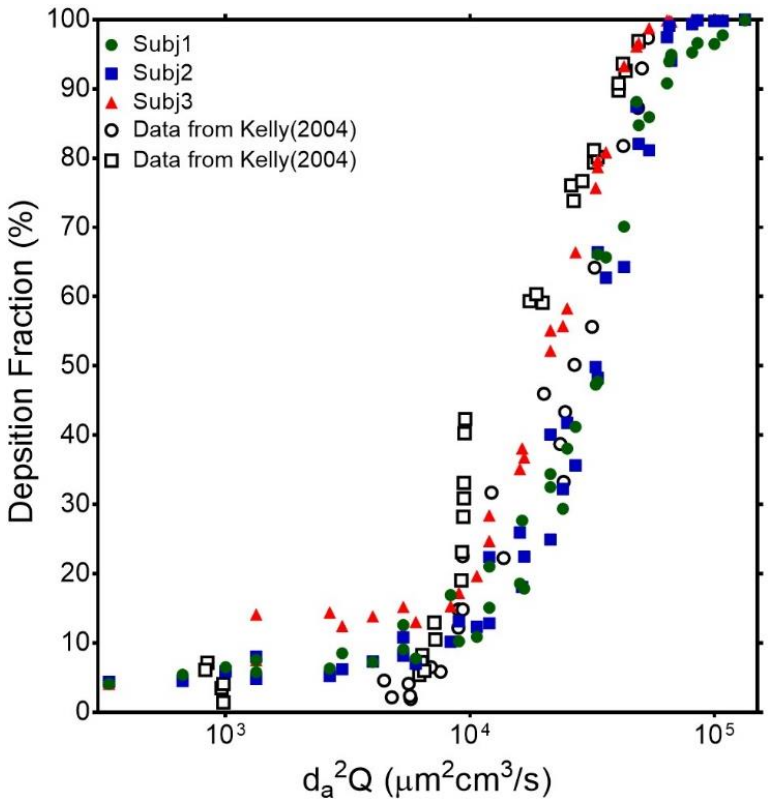

Figure 5.9 Whole nose deposition efficiency prediction of the three subjects for particle size between 2 to 20 μm (inhalation flow rates ranging from 5 to 20 L min^{-1}) as a function of IP compared to the published data from Kelly et al.[481].

Four inhalational flow rates (5, 7.5, 10, 15, and 20 L min^{-1}) and particle sizes from 2 to 20 μm were investigated in this study in each subject. The whole nasal deposition data of three subjects in this study were compared to the two nasal cast deposition data from Kelly *et al.* [481] as a function of IP. The total nasal deposition curve of all the three subjects was sigmoidal in shape and was in good agreement with experimental data. The minimum deposition of 4 % was observed with 2 μm particles at a lower airflow rate of 5 L min^{-1}. The deposition fraction of 2 μm particles increased to 8 % at a higher airflow rate of 20 L min^{-1}. The maximum deposition rate was 78 % for 20 μm particles at an airflow rate of 5 L min^{-1}. Near 100 % deposition was achieved for 20 μm, 14 μm, 12 μm particles at 10 L min^{-1}, 15 L min^{-1} and 20 L min^{-1} airflow rates respectively. The preferential deposition in the anterior parts of the nasal cavity was observed with the increase in particle size as shown in **Figure 5.10.**

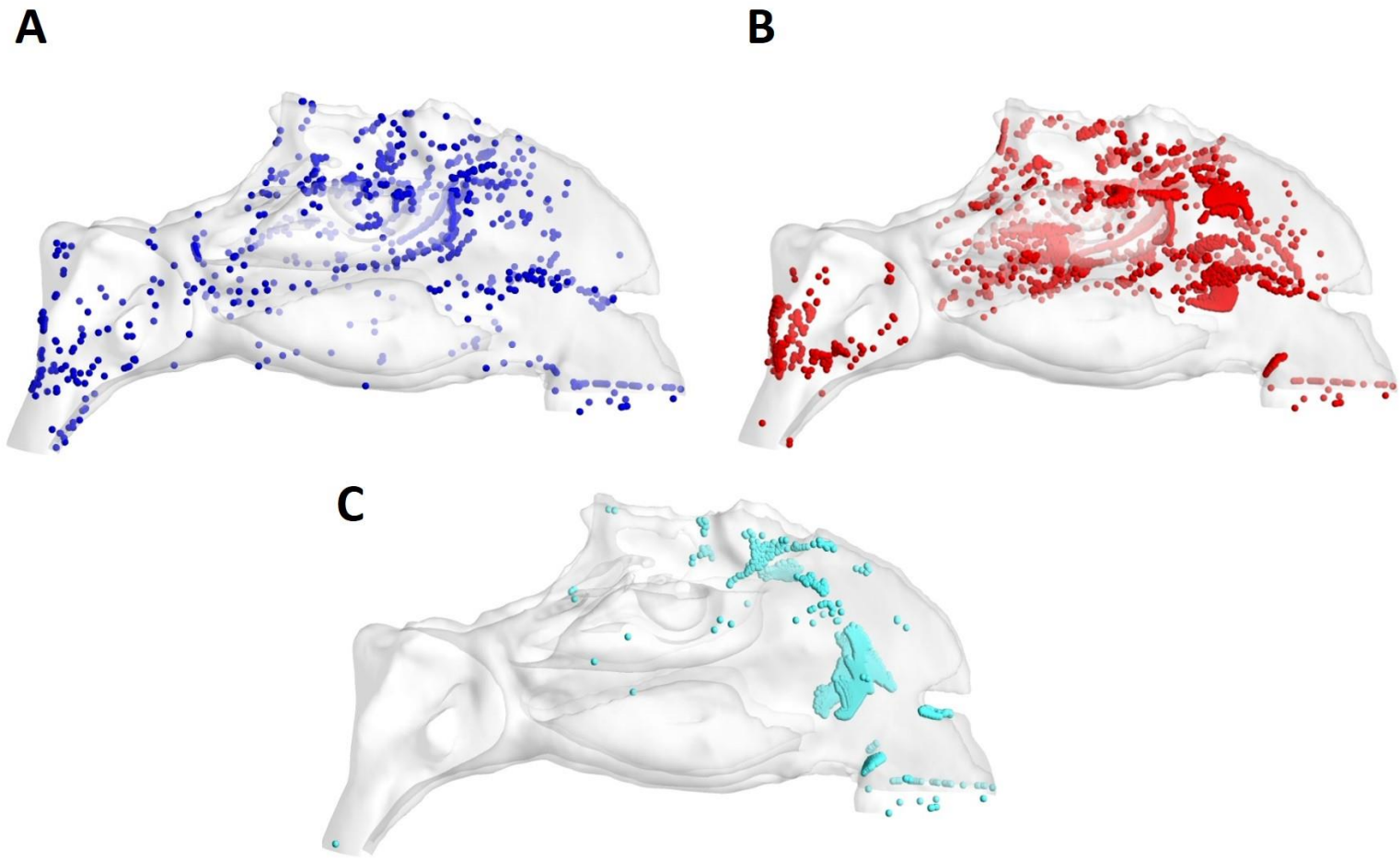

Figure 5.10 Representative deposition patterns of microparticles in the human nasal cavity. At lower particle size of 2 µm (A) the particles show low and distributed deposition, when particle size reaches 10 µm (B) the deposition of particles is increased with preferential deposition at the middle and upper regions of nasal cavity and at a particle size of 20 µm (C) all the particles released are deposited within the nasal cavity with preferential deposition in the anterior region. (At an inhalational air flow rate of 20 L min^{-1}).

5.4.2.1 Agreement with published literature

5.4.2.1.1 Results from nebulization

The region-specific particle deposition data were compared with the experimental data from Schroeter[214] to validate the computational predictions and presented in **Figure 5.11.** Results from the flow rate case of 15 L min^{-1} were used**.** The overall deposition in all the regions was in good qualitative agreement with the experimental data. For example, in 10 µm particles inhaled at 15 L min^{-1}, the olfactory deposition fraction matched closely with Subject 3.

5.4.2.2 Results from bi-directional delivery technique

The data for whole nasal deposition from Kleven *et al.*[506] was used to validate the deposition efficiency which had also used 6 L min^{-1}. The whole nose deposition data from the current simulations were in reasonable agreement with the experimental data (62 vs 73.96 ± 21 %).

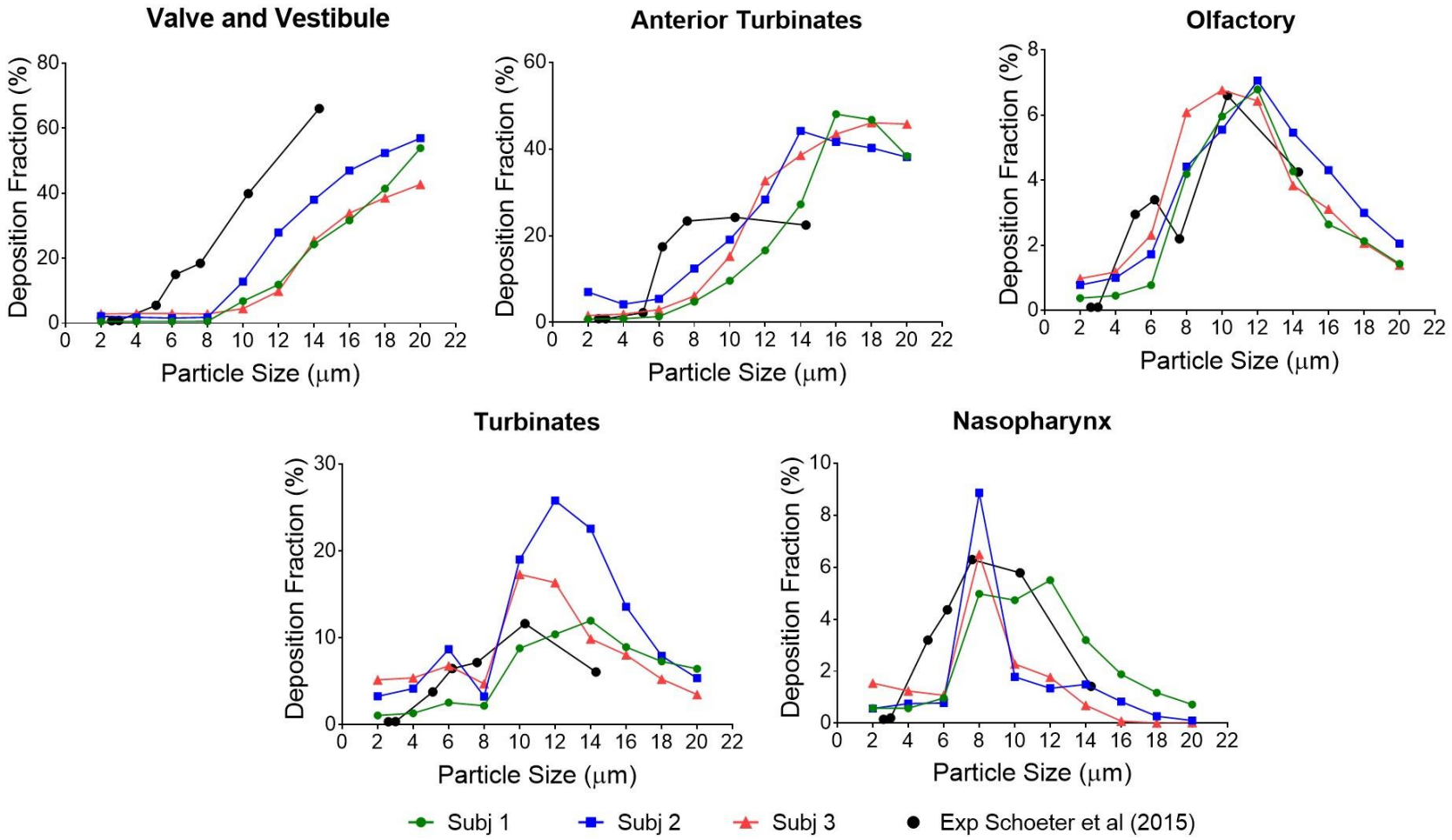

Figure 5.11 Comparision of computational predictions of microparticle deposition in three subjects (nebulization delivery technique) with the experimental data from Schroeter et al.[214] *at a steady air flow rate of 15 L min*$^{-1}$.

5.4.3 Simulation of airflow with nebulization and bi-directional delivery techniques

The representative air velocity profile in the olfactory/turbinate region for nebulization is shown in **Figure 5.12.** With nebulization, higher velocities were observed in the middle and lower portions of anterior turbinates and turbinates, while lower velocity was observed in the upper region of anterior turbinates and the olfactory region. A recirculation zone (shown with a red arrow) is observed in the upper dorsal part of the nasal valve area of Subject 1 and 2. The recirculation zone is a result of sudden area expansion in cross-sectional and effective flow areas. Airflow towards the olfactory region increased as the velocity was increased up to 20 L min^{-1} of inhalational flow rates[215,509] as seen from **Figure 5.12**.

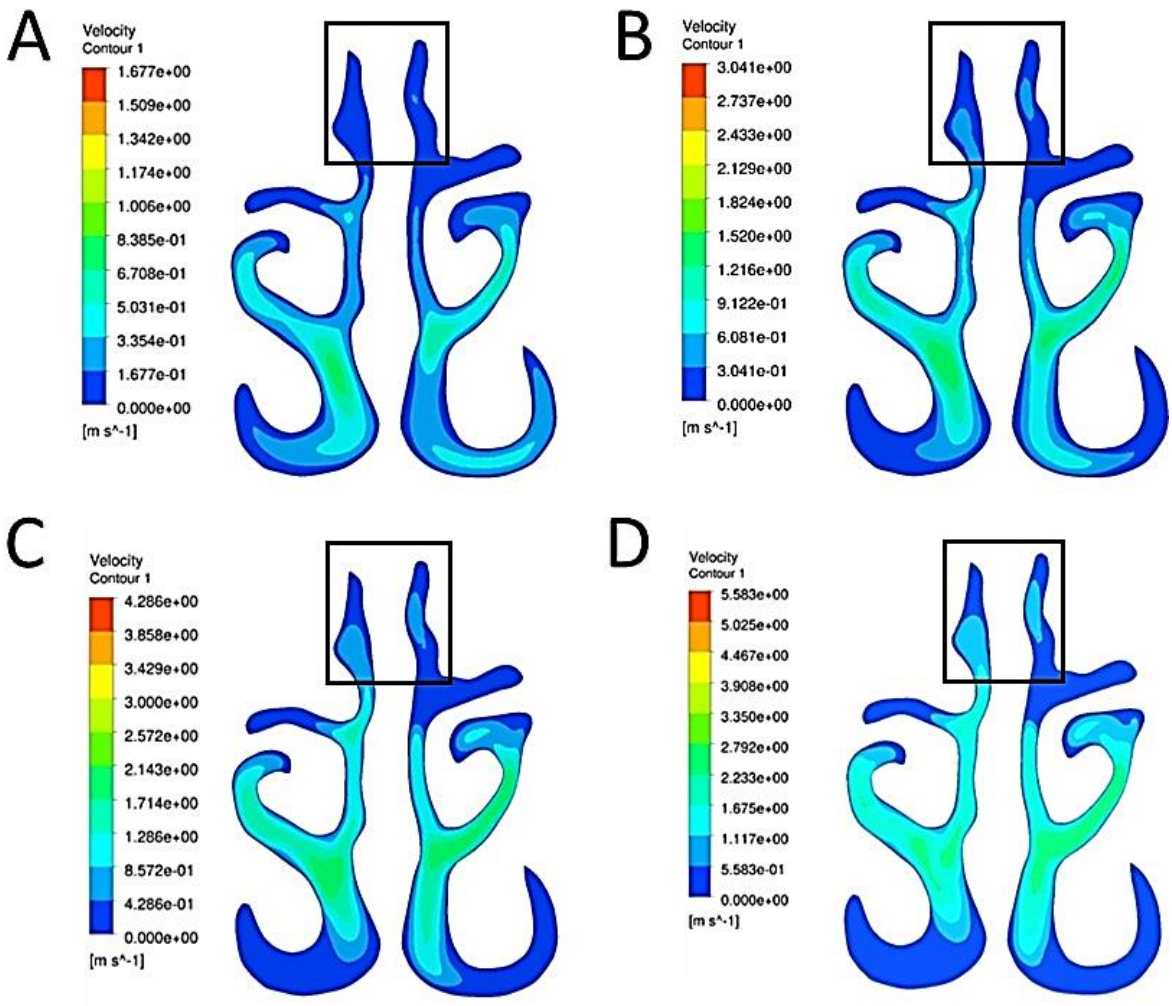

Figure 5.12 Representative velocity profile of the air in the olfactory/turbinate region with nebulization at (A) 5 L min^{-1}, (B) 10 L min^{-1}, (C) 15 L min^{-1} and (D) 20 L min^{-1} inhalational air flow rates. Increased air flow in the olfactory region (Inset) can be observed with the increase in inhalational air flow rate.

The representative air velocity profile in the olfactory/turbinate region for bi-directional delivery technique is shown in **Figure 5.13.** With the bi-directional method, the nasopharynx is closed. Hence airflow enters through one nostril and exits from another nostril. The velocity was maximum at the nasal valve region of the exit nostril. In this study, air flow was simulated at an upward angle of 60° which led to higher velocity in regions of superior turbinates and the olfactory region as shown in **Figure 5.13**.

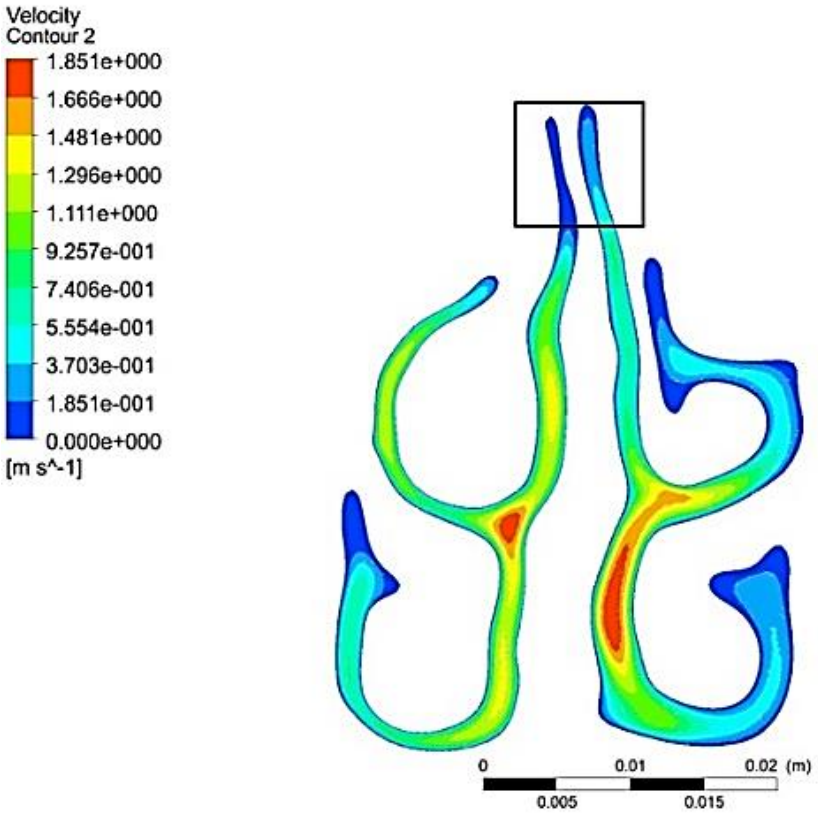

Figure 5.13 Representative velocity profile of the airflow in the olfactory/turbinate region with bi-directional delivery technique. Increased airflow in the olfactory regions (Inset) were observed.

Fluid streamlines for an inhalation air flow rate of 20 L min^{-1} and bi-directional flow rate of 6 L min^{-1} is shown in **Figure 5.14.** Airflow was at the highest speed in the nasal valve area due to the minimum cross-sectional area.

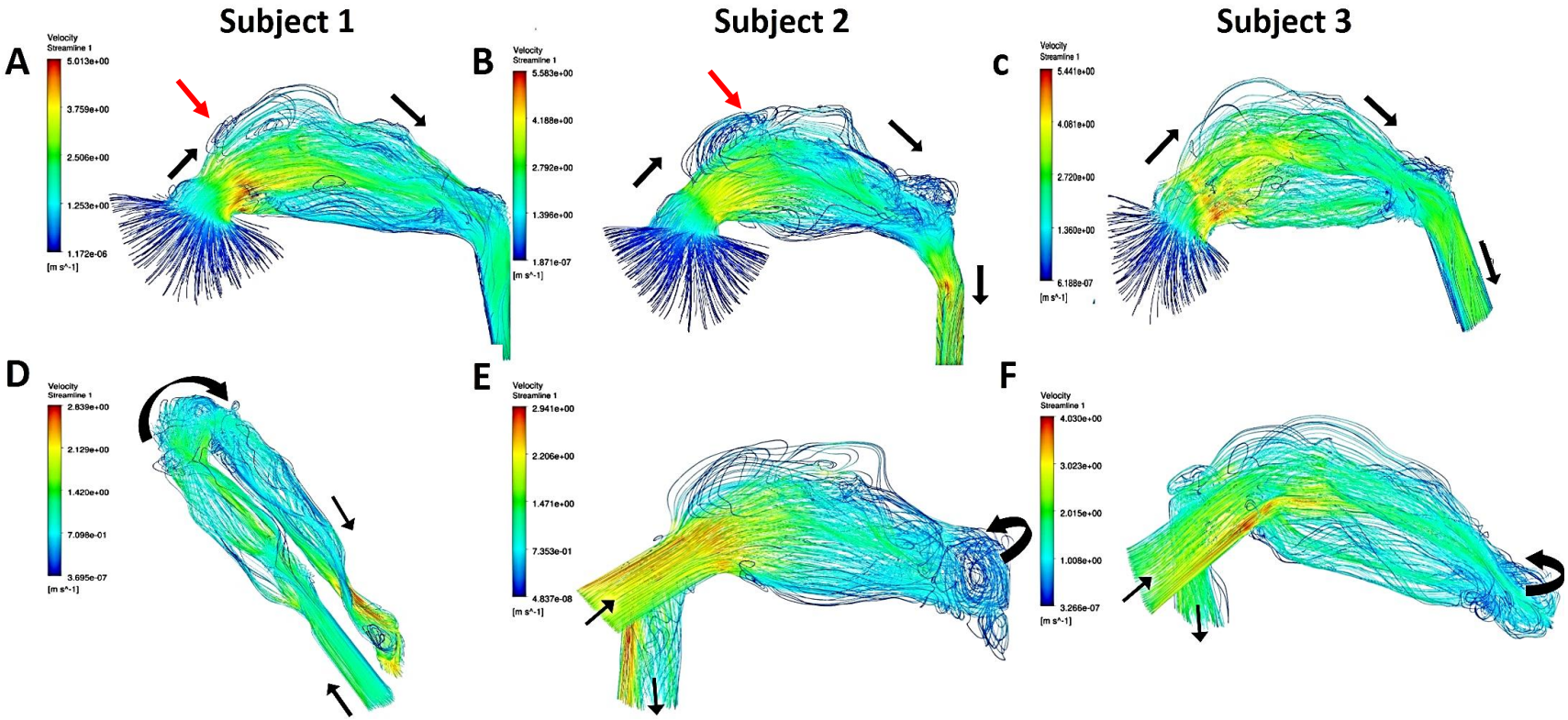

Figure 5.14 Representative airflow streamlines of nebulization and bi-directional delivery methods in three subjects. Black arrows indicate the direction of airflow. (A),(B) & (C) represent the nebulization airflow streamlines at 20 L min^{-1}. (D),(E) & (F) represent the bi-directional air flow streamlines at 6 L min^{-1}. (D) represents the top view of airflow streamlines in bi-directional simulations. (E) & (F) represent a side view of airflow streamlines in bi-directional simulations. Red arrows indicate the regions of recirculation in the nasal cavity. The colour map indicates the velocity of air flow. Streamlines for other inhalational airflow rates (5, 10 and 15 L min^{-1}) are presented in ***Appendix F.***

5.4.4 Results of particle deposition under nebulization

Regional deposition data in three subjects were analyzed and compared with an aim to identify the variability in particle deposition pattern and presented as region-specific particle deposition data at the peak inhalation flow rate of 20 L min^{-1} in **Figure 5.15.**

5.4.4.1 Nasal valve and vestibule

Deposition in the nasal valve and vestibule area increased with increase in particle size. Maximum deposition of 61 % was observed for the 20 µm particles. The higher inertia of particles and filtering effect of the nasal valve due to its minimum cross-sectional area might have been the reason for the observed trend. The deposition patterns between the subjects were comparable without any statistically significant difference (P = 0.8690).

5.4.4.2 Anterior turbinates

Deposition in anterior turbinates increased with increase in particle size up to 20 µm for Subject 1 and the maximum deposition observed was 38 %. The maximum deposition of 49 % was observed for the Subject 2 and Subject 3 at a particle size of 14 µm and then the deposition slightly decreased. The deposition of 10 µm or bigger particles in Subject 1 was about 15 % smaller than Subjects 2 and 3. However, the deposition patterns between the subjects were comparable without any statistically significant difference (P = 0.7658).

5.4.4.3 Olfactory region

All the three subjects demonstrated comparable particle deposition with particles of size 10 µm showing highest deposition in the olfactory region. Interestingly, a narrow range of particle size was found to be optimum for enhanced deposition in the olfactory region: the deposition was maximum with the particle size of 8-12 µm for all three subjects. A maximum deposition of 9 % was observed in Subject 1 for the 10 µm particle size. The deposition

patterns between the subjects were comparable without any statistically significant difference (P =0.9795).

5.4.4.4 Turbinates

The turbinate region included all parts of the nasal passage past the anterior nasal passage to the nasal choana where the two nasal airways coalesce. This region presents the largest mucosal surface for drug distribution. The deposition pattern was comparable between the three subjects. Maximum deposition in turbinates of 14 % and 22 % was observed with 14 µm particles for Subject 1 and Subject 2. For Subject 3, maximum deposition of 20 % was with 10 µm particles. For Subject 2 and 3, deposition fraction in the turbinates decreased for particles above 10 µm size. For Subject 1 the deposition fraction in the turbinates decreased for particles above 12 µm. The deposition patterns between the subjects were comparable without any statistically significant difference (P =0.1465).

5.4.4.5 Nasopharynx

Particles around 8 µm consistently showed maximum deposition in the nasopharynx region for all the subjects. The maximum deposition was 6.7 %, 16.95 % and 12.56 % with Subjects 1, 2 and 3 respectively. The deposition pattern was comparable between the three subjects without any statistically significant difference (P =0.8309).

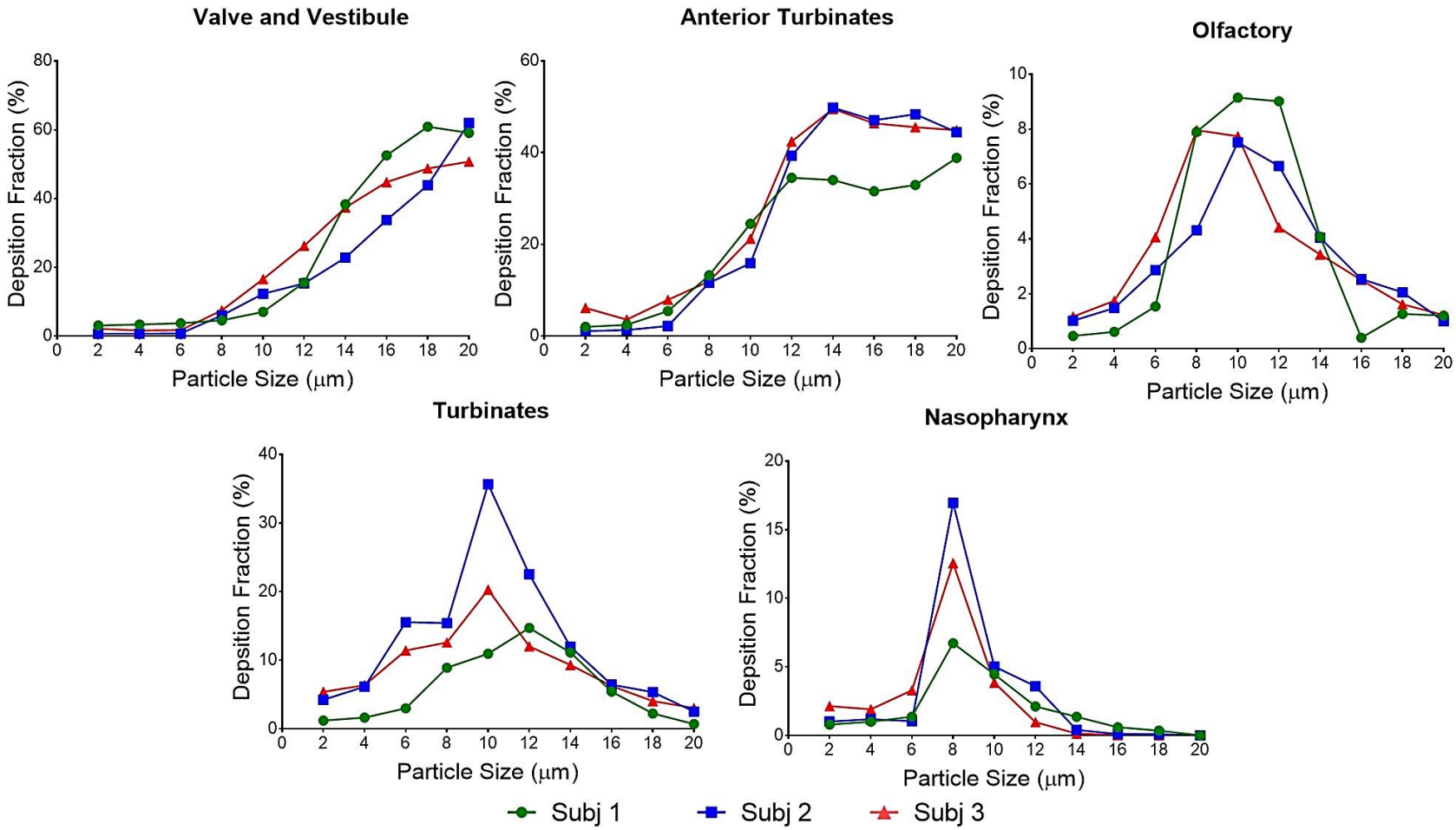

Figure 5.15 Regional specific deposition in nasal cavities of three human subjects at an inhalation rate of 20 L min^{-1}. No significant difference in deposition patterns in olfactory regions between the human subjects was observed.

5.4.4.6 Other airflow rate simulations

Results from computational simulations for lower inhalational rates of 5 L min^{-1} and 10 L min^{-1} for all three subjects are presented in **Figure 5.16**. The deposition fraction increased with increase in the particle size, and flow rate in the nasal valve and vestibule region. The maximum deposition observed in this region was 51.93 % for 20 µm particles at 10 L min^{-1} in Subject 2. The deposition pattern in the anterior turbinates region was similar and was a function of particle inertia. For air flow rates of 5 L min^{-1} and 10 L min^{-1}, the deposition increased with increase in particle size until 20 µm. For the higher flow rates, a trend of decrease in particle deposition was observed in all the subjects at a particle size of 14-18 µm. Deposition patterns were significantly different between subjects at 5 L min^{-1} ($P = 0.0080$). Turbinates received increased deposition with an increase in particle size at 5 L min^{-1} air flow rate and for other flow rates deposition was maximum with particle sizes up to 14 µm and then decreased. A significant difference of deposition pattern in turbinates between the subjects was observed at 10 L min^{-1} ($P = 0.0361$). The nasopharynx received comparatively low deposition in all the subjects despite large surface area; the deposition decreased with the increase in flow rates and a sharp increase in particle deposition was observed at 8-10 µm for all the subjects observed at all the flow rates.

5.4.4.7 Particles escaped from the nasal passages

The particles that escaped from the nasal passages were also determined. The particle size and airflow rate had a significant effect on the deposition of the particles. About 75 % to 90 % of the smaller particles (less than 6 µm) escaped the nasal cavity without depositing. The lower the airflow rate, the higher was the percentage of particles that escaped. Particles between 8 to 12 µm showed huge variations depending on the airflow rate. Around 76 % to 85 % of particles escaped at the low 5 L min^{-1} airflow rate, and the number decreased to 50 to 15 % at the high 20 L min^{-1} air flow rate. Particles greater than 14 µm in size had low escape percentage, with about 1 % of particles escaping at the higher flow rates, and between 22 to 50 % at the lower airflow rates.

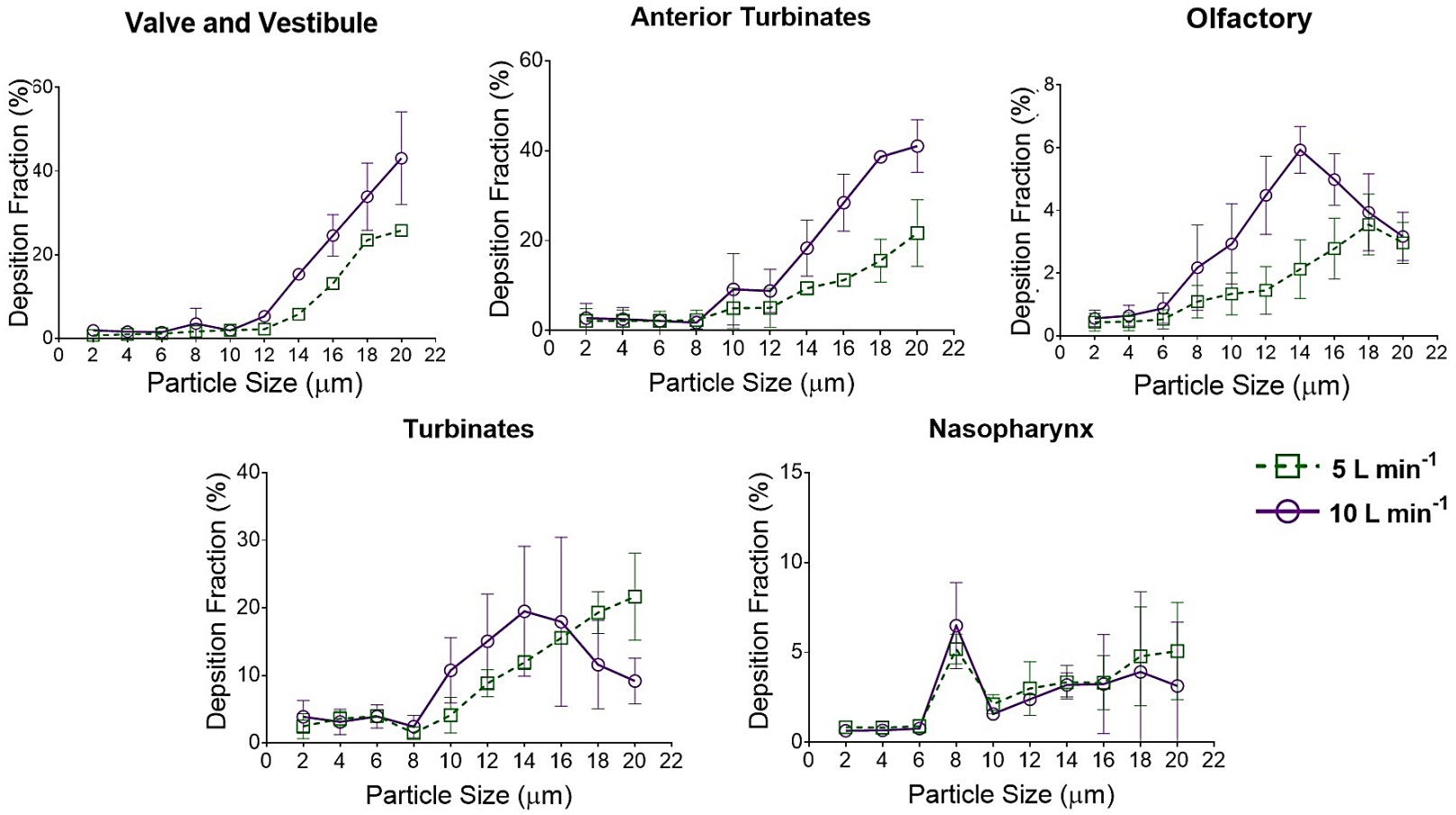

Figure 5.16 Region-specific deposition of particles with different flow rates, the data presented are means of three individual subjects.

5.4.5 Identification of suitable particle size to maximize olfactory deposition with the bi-directional delivery technique

Region-specific deposition in nasal cavities was assessed with a bi-directional delivery technique at an air flow rate of 6 L min^{-1} and presented in **Figure 5.17** and **Figure 5.18**. For each subject, two protocols of simulations were run with a different nostril serving as an outlet each time and were referred as left to right and right to left indicating the direction of airflow. Results were analyzed to identify a suitable particle size to maximize the deposition in the olfactory region. Also, the results were compared to identify any variability in the deposition data between the subjects. Due to the particle release position located near the nasal valve, deposition fractions were not calculated in the vestibule and nasal valve region.

5.4.5.1 Anterior turbinates

Particle deposition followed a similar trend to the inhalational flow with an increase in deposition observed with increase in particle size. A maximum deposition of 47 % was observed with 20 µm particles for Subject 3. The deposition pattern between the subjects and the left and right protocols was comparable ($P > 0.2$). A significant difference in deposition pattern between the subjects ($P = 0.0187$) was observed.

5.4.5.2 Olfactory region

Deposition in the olfactory region was higher than by the nebulization delivery technique in all the subjects. Deposition increased with increase in particle size up to 18 µm and then decreased about 2-4 % in all the subjects with 20 µm particles. The greatest deposition of 13.16 % was observed with the 16 µm particle in Subject 2 with the right to left protocol. The deposition pattern between the subjects and the left and right protocols was comparable ($P > 0.4$).

5.4.5.3 Turbinates

With increase in particle size, the deposition in the turbinates region increased. The maximum deposition for all the subjects was ~30 % with particle size around 16-20 µm. There was no significant difference observed between left to right and right to left protocols of all the subjects or between the individual subjects ($P > 0.2$).

5.4.5.4 Nasopharynx

Bi-directional delivery technique produced higher deposition in the nasopharynx compared to nebulization. The increase in particle deposition was observed with increase in size. The maximum deposition of ~25 % was observed with 16 µm particles in Subject 1. There was a significant difference between left to right and right to left protocols and deposition data for Subject 3 ($P = 0.0350$) and in the deposition pattern between subjects ($P = 0.0014$).

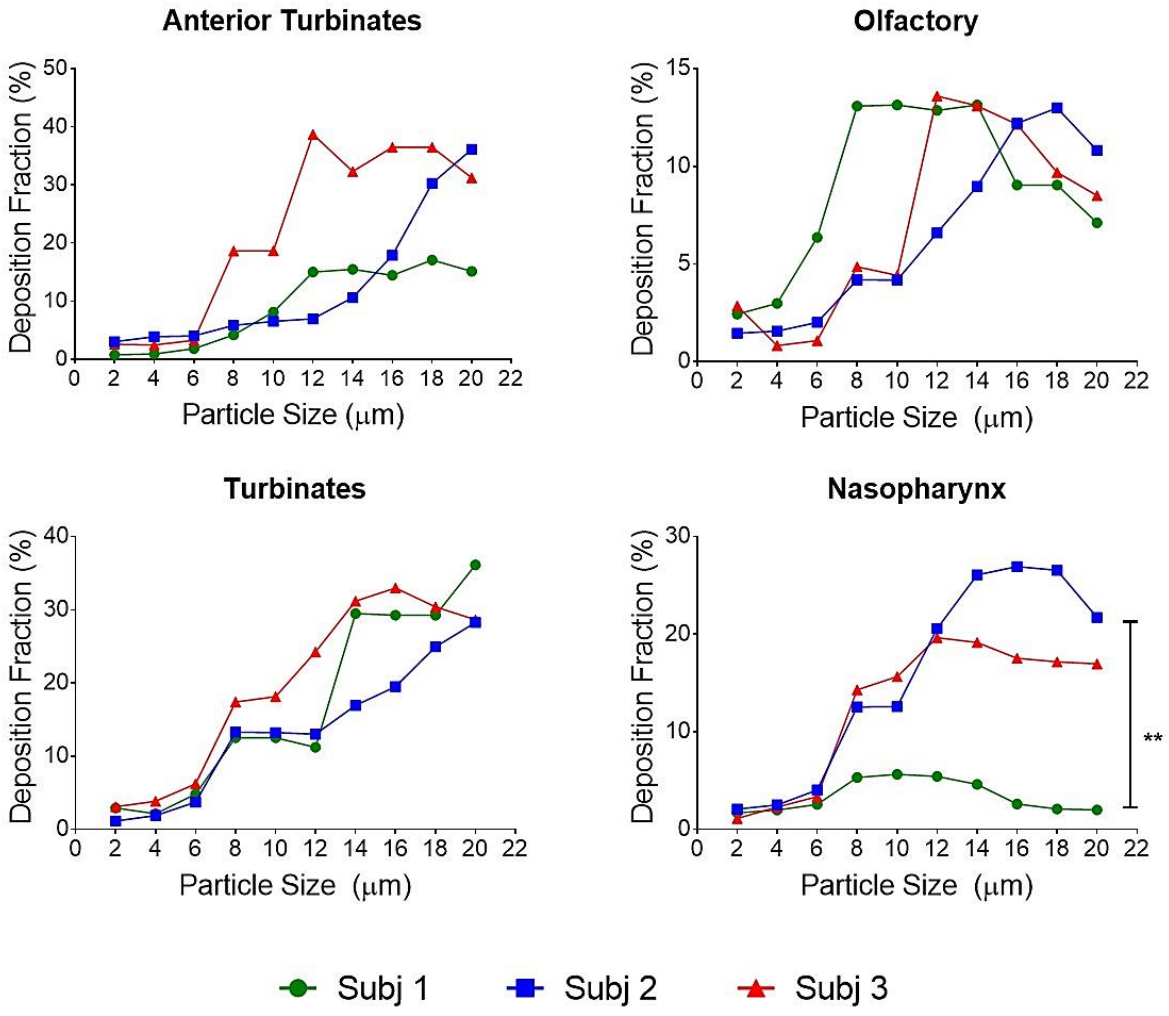

*Figure 5.17 Effect of particle size on region-specific deposition in the nasal cavities of three human subjects with bi-directional delivery technique at an air flow rate of 6 L min^{-1} when bi-directional airflow was simulated from left to right. (**P < 0.01).*

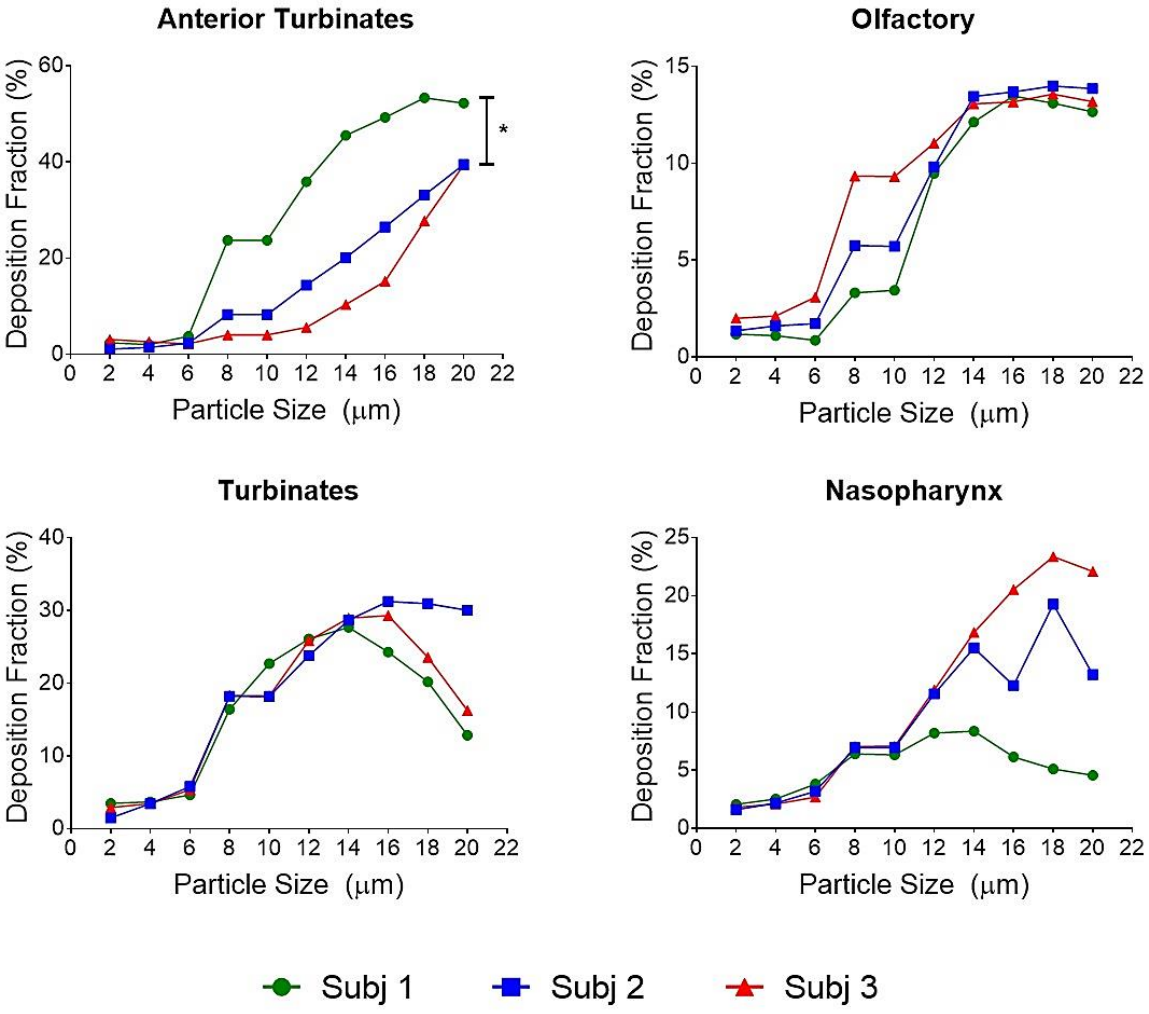

*Figure 5.18 Effect of particle size on region-specific deposition in the nasal cavities of three human subjects with bi-directional delivery technique at an air flow rate of 6 L min^{-1} when bi-directional airflow was simulated from right to left. (*P < 0.05).*

5.4.5.5 Total nasal deposition

The total nasal deposition with the bi-directional delivery technique was dependent upon the particle size. For smaller particles (less than 6 µm) the total deposition was around 11 to 26 %. For particles between 8–12 µm the total nasal deposition was around 43-91 %. Almost 99 % total nasal deposition was observed after particle size reached 14 µm or higher.

5.5 Discussion

To exploit advantages of the nasal route to improve nose-to-brain drug delivery, targeted drug delivery to the olfactory region is very important[214,215,509]. Previous **Chapters** of this thesis have experimentally demonstrated the preferential deposition of particles in the olfactory region as a function of particle size. This **Chapter** utilizes computational simulations to investigate the effect of particle size on olfactory deposition by nebulization and bi-directional delivery techniques in human subjects.

Anatomically accurate 3D-human nasal cavity models of three subjects were constructed, and steady laminar airflow was simulated at airflow rates of 5, 10, and 20 $Lmin^{-1}$ and a bi-directional airflow rate of 6 $Lmin^{-1}$. For nebulization, the flow patterns did not change very much with an increase in the inhalational airflow rates. At the lower airflow rate (5 L min^{-1}), the majority of the flow passes through the middle and lower portion of the nasal cavity resulting in low airflow towards the upper narrow olfactory region. With an increase in the inhalational airflow rate (20 L min^{-1}) airflow bypasses the meatuses due to stronger momentum increasing the airflow towards the olfactory region. Increased airflow towards the olfactory region was evident for bi-directional delivery and could have been due to the simulation of airflow at an upward angle of 60º. Although the airflow was simulated at a particular angle, the characteristic geometry of the nasal cavity might have offered some resistance for alteration of the downstream flow pattern resulting in the majority of airflow through the middle and lower regions of the nasal cavity similar to the nebulization[514].

For the nebulization technique, whole nasal deposition was a function of particle size and flow rate for all the regions in the nasal cavity. The smaller particles (less than 6 µm)

have shorter relaxation times and lack momentum to deviate from the airflow; thereby a low portion was deposited in the nasal cavity. Larger particles (> 8 μm) have high inertia, and consequently, high deposition rates; the whole nasal deposition rate increased with an increase in the particle size. The deposition rate increased with the increase in inhalational flow rate. This may have been due to the higher air momentum and increased secondary flows at the higher flow rates which contributed to the increased particle deposition rates in the nasal cavity[215]. At a particle size of 18 μm and flowrate of 20 L min^{-1} 99 % of particles were deposited.

For bi-directional delivery technique, the whole nasal deposition was a function of particle size. Although the smaller particles (less than 6 μm) escaped the nasal cavity due to lower inertia, the total deposition compared to the respective particle size by nebulization was higher with bi-directional delivery. The increased transit time of a particle in the nasal passages due to bi-directional airflow by the closed nasopharynx contributed to this improved deposition rates. Similarly, the larger particles showed higher deposition rates and when the particle size reached 14 μm 99 % percent of the particles were deposited.

The region-specific deposition of particles with nebulization was analyzed and compared with the experimental results in a nasal cast (airflow rate of 15 L min^{-1}) from Schroeter *et al.* [214]. The region-specific deposition predictions were in good agreement with the experimental data except for the valve and vestibule region. The trend of deposition was similar between the studies. The particle size resulting in maximum deposition in each region was comparable between simulation studies and the experimental data. The underprediction of the deposition in the nasal valve region and vestibule area could have been due to the geometrical complexity and narrow width of this region. Similar anatomical partitioning of the nasal cavity and the density of the particles used in both the studies were the reasons for the comparison.

One of the primary objectives of this **Chapter** was to study the effect of the particle size on region-specific deposition with nebulization delivery. For the nebulization studies, the deposition patterns were dependent on particle size and flow rate in all of the regions. Inertia played an essential role in the region-specific particle deposition. The overall deposition was comparable between all the three subjects with two exceptions. Firstly, the deposition in

anterior turbinates at the lower flow rate (5 L min^{-1}) between subjects was significantly different. This variability could have been due to the gravitational sedimentation effect of particles at lower inhalation rates coupled with the complex anterior turbinate geometry. The anterior turbinates have a very narrow width (~1 cm), and the geometry expands suddenly due to the formation of turbinates. A recirculation was observed in this region due to the geometrical complexity and might have augmented the different particle deposition patterns in this region between the subjects[214]. Secondly, a notable difference in a deposition in the turbinate area at a flow rate of 10 L min^{-1} occurred.

Olfactory deposition in the nebulization delivery method was dependent on particle size and flow rate. At lower flow rates (5 and 10 L min^{-1}) the particles sized 14-18 µm were shown to improve the olfactory deposition. The increased deposition was observed with the higher flow rate. At the higher flow rates (15 L min^{-1}) and peak inhalational flow rate (20 L min^{-1}) the optimum size of particles with enhanced olfactory deposition was found to be 10-11 µm. Shi *et al.*[215] and Liu *et al.*[487] have reported increased deposition of particles in the middle region of nasal cavity at a particle size of 10 µm. Schroeter *et al.*[214] reported preferential deposition of 10 µm particles in the olfactory region. The geometric differences between human nasal cavities can cause variation in the deposition of microparticles[481,482]. Hence, there is a need to investigate the inter-subject variability in olfactory deposition to examine if the same particle size range identified in this study is suitable for enhancing the deposition. The results from the computational studies in this chapter showed no inter-subject variability between the olfatory deposition of the microparticles and are in agreement with the reported studies, which reinforce that particles with a size around 10 µm can have enhanced deposition in the olfactory region when nebulized.

The second objective of this **Chapter** was to study the combined effect of particle size with bi-directional delivery on region-specific deposition in the nasal cavity. To the best of the authors knowledge, this was the first study to investigate region-specific deposition with bi-directional delivery. Therefore, the data from this thesis cannot be compared with any other experimental data. However, whole nasal deposition data in a human nasal cast has been reported in the literature by Kleven *et al.*[506].The inlet conditions used in this study are similar to the current simulations. The whole nasal deposition data were comparable between

the simulation and experimental studies. In this thesis, the region-specific deposition with two protocols, where a different nostril served as an outlet each time (referred as left to right and right to left, indicating the direction of airflow) has been analyzed.

For bi-directional delivery, the particle deposition in the anterior turbinates was a function of particle size. However, due to the complex nasal geometry and gravitational sedimentation, significant variations in deposition between the subjects was observed. For Subject 1 the difference was notable between the left to right and right to left protocols. The deposition in the turbinates was a function of particle size. However, a decrease in the deposition was observed after particle size reaching 14-16 µm. The filtering effect of the nasal valve with larger particles could be a reason for this decrease. Bi-directional flow enhanced the deposition in the turbinate region compared to the nebulization due to the enhanced air penetration into these regions[515].The deposition patterns between the two protocols and subjects were comparable. The deposition in the nasopharynx was dependent on the particle size. However, the deposition reached a plateau phase when the particle size was 12-14 µm and then there was a slight decrease in deposition with 20 µm particles. Also, significant differences in the deposition of particles at the nasopharynx between subjects were observed, which could have been due to the combined effect of airflow, inertia, and interception. In addition to the inertia, the interception of particles at the nasopharynx due to the change in airflow (i.e. changes of about 180° near the nasopharynx) can increase the number of particles depositing in this region. Due to the substantial change in the airflow direction, the chance of variation in particles depositing in this region can be high. Also, the notable difference observed between left to right and right to left protocols of Subject 3 can be attributed to the significant change in airflow direction and increased chances of interception. The bi-directional delivery significantly increases the deposition in the nasopharynx.

Results of this study indicate that deposition in the olfactory region is a function of particle size. A suitable size of particles for targeting the olfactory region with the bi-directional delivery was found to be 14-18 µm (**Figure 5.19**). The bi-directional delivery significantly enhanced the deposition of particles in the olfactory region compared to the nebulization delivery (*P = 0.0183). Enhanced deposition in the olfactory region can be due

to the combined effect of increased airflow to the olfactory region and the release position of the particles. The particles were released at the nasal valve in the bi-directional delivery. The release position prevented the deposition of particles in the nasal vestibule and enhanced the deposition in the olfactory region. Another reason could be the angle of air flow; the 60° upward angle increased the airflow towards the olfactory region thereby increasing the olfactory deposition.

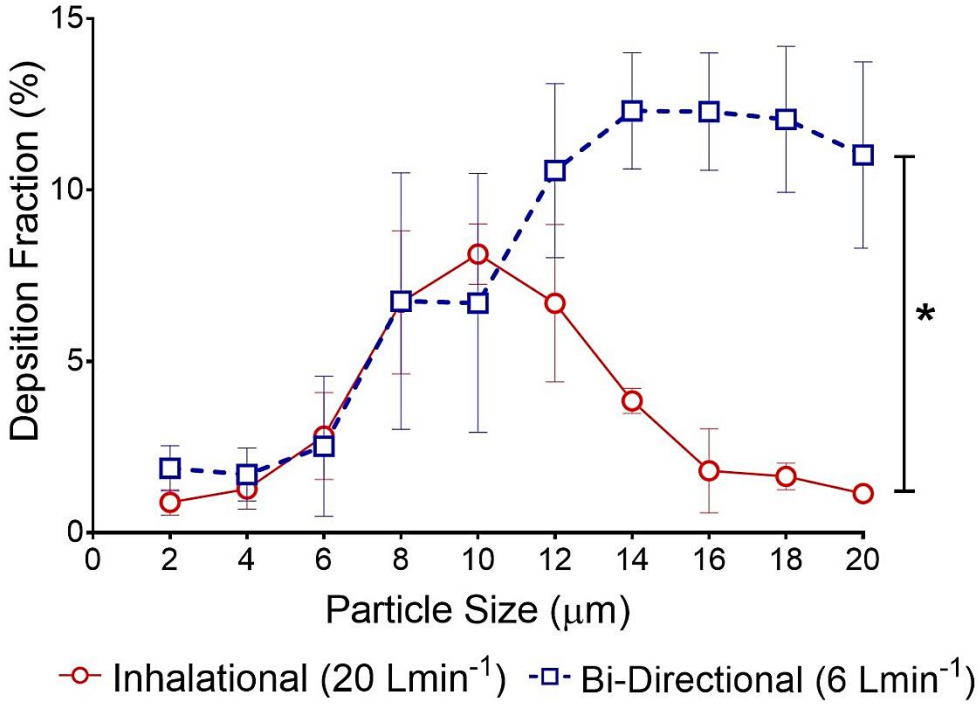

Figure 5.19 Comparison of maximum olfactory deposition by nebulization (20 L min^{-1}) vs. bi-directional delivery (6 L min^{-1}) techniques. Particles sized 14-18 µm showed the highest deposition with bi-directional delivery technique. The data presented are the means of three individual subjects ± SD.

When particle size increased to 20 µm, the olfactory deposition started to show a decreasing trend. At the higher particle size, the particle has higher inertia and is more likely to deviate from the main flow, hence, 20 µm particles were deposited more in the turbinate regions. If the simulations were to continue with higher particle size due to the increase in inertia of particles the trend of decreased olfactory deposition would continue. While particles between 14-18 µm had the right inertia to reach the olfactory region. Also, the airflow rate tested in this study was low (6 L min^{-1}), so gravity might have had an effect on

larger particles and reduced their penetration to the upper dorsal regions of nasal cavity like the olfactory region.

Results of this study corroborate with the results from by Djupesland *et al.*[214,504,516] who demonstrated higher deposition efficiency in the upper nasal cavity with the bi-directional delivery technique. The high deposition can be attributed to increased airflow velocities and penetration in the upper nasal cavity with the bi-directional delivery technique. The region-specific deposition patterns reported in this study identified the suitable particle size to maximize the deposition.The results from this study can help in optimizing the particle size of the powder formulations to target the region of interest in the nasal cavity.

The computational simulations in this chapter assessed the variability in deposition pattern of the particle s between the subjects with nebulization and bi-directional delivery techniques. Anterior turbinates have shown a significant difference in particle deposition pattern with the nebulization technique. The anterior turbinates and nasopharynx region received the various deposition patterns in three individuals with the bi-directional delivery technique. Gravitational sedimentation and the effect of geometry were speculated to cause the variability in anterior turbinate deposition, and the bi-directional air flow was speculated to be the reason for the variability in the nasopharynx.

Computational predictions of region-specific particle deposition patterns in this study can provide detailed insights into the effect of particle size and inter-individual variability which is otherwise difficult to observe experimentally. Geometry and particle size were shown to impact the region-specific deposition. Also, particle release position and airflow angle also might affect the deposition of particles in the olfactory region.

5.6 Key findings

The computational simulations in this chapter suggests particles around 10 µm size show high deposition in the olfactory region of all three subjects studied under nebulization with no significant variability observed in the deposition pattern between subjects. Microparticles with 8 µm were found to improve deposition in the nasopharynx with the nebulization delivery technique. Microparticles sized between 14-18 µm are found to be suitable for enhanced drug delivery in the olfactory region with the bi-directional delivery technique. This study identified that the bi-directional delivery technique can enhance the olfactory deposition of microparticles compared to nebulization without any inter-subject variability and might be a desirable method to enhance nose-to-brain delivery of drugs. Anterior turbinates and nasopharynx were found to have significant variation in the particle deposition of particles.

5.7 Limitations and future directions

This study assumes particles are of uniform size; future computational simulations shall consider the effect of polydisperse particles on region-specific deposition in the nasal cavity especially the olfactory region, to further exploit the probability of enhancing delivery to this region. The olfactory region in this study contains some part of the meatuses due to the geometrical definition of regions. A better resolution of the 3-D structure can provide further details of olfactory deposition. Three human subjects were used in this study, but analyzing large population data might provide more insight into the inter-individual variability. In addition, future studies need to explore the potential of bi-directional delivery by changing the parameters such as particle release position and airflow angle which might have an impact on the particle deposition in the olfactory region.

Chapter 6

Summary and future outlook

6 Summary and future outlook

The inability of most of the drugs administered orally or IV to reach the brain at therapeutic levels due to the BBB has moved the focus to using the intranasal route of delivery to deliver drugs to the brain. The olfactory pathway in the olfactory region and trigeminal neural pathway in the nasal cavity can transport drugs directly to the brain as discussed in **Chapter 1**. Therefore, targeting drugs to the olfactory region has the potential to enhance nose-to-brain delivery[517,518]. However, targeted delivery to the olfactory region is difficult due to its location in the posterior uppermost part of the nasal cavity. Convoluted and narrow air passages limit drug delivery to the olfactory region, and most of the administered drugs are either filtered by the nasal valve region or lost to the lungs[1,507]. Furthermore, retaining drugs in the nasal cavity is a challenging task due to mucociliary clearance[48]. The clinical feasibility of nose-to-brain delivery of drugs is still challenging due to a very low dose of drugs reaching the olfactory region and thereby the brain. Given the increasing number of drugs being discovered for the treatment of complex CNS disorders, developing efficient delivery systems to enhance nose-to-brain drug delivery by targeting the olfactory region has become very topical [215,493,509].

Various formulation strategies to enhance nose-to-brain drug delivery are under investigation. One promising strategy is formulating drugs as particulate delivery systems. Formulating drugs as particulate delivery systems can reduce side effects and enhance brain absorption of polar and large drug molecules which otherwise have minimal absorption into the brain[230]. Another strategy is the use of mucoadhesive polymers to improve their residence time in the nasal cavity[197]. In addition to these strategies, recent modeling studies suggest that particles around 10 µm size can target the olfactory region[214,215], which can be beneficial to the nose-to-brain delivery of drugs. Therefore, the objective of this thesis was to examine the potential of combining these formulation strategies for enhancing nose-to-brain delivery of drugs. Features of microparticles that make them an attractive nose-to-brain drug delivery system were described extensively in **Chapter 1** of this thesis and included the ability to target the olfactory region due to their size.

Chapter 3 of this thesis examined the potential of size tailored mucoadhesive microparticles to target the olfactory region *in-vitro* and the potential of TSP as a mucoadhesive carrier of drugs. Designing appropriate *in-vitro* methods to test the objectives of this thesis was in itself challenging. Mucoadhesion of TSP-microparticles in the nasal cavity is vital for facilitating nose-to-brain drug delivery. Previously reported *in-vitro* methods were modified to mimic as closely as possible the human nasal environment and respiration. In this thesis, a combination of *in-vitro* and *ex-vivo* methods were employed to evaluate the mucoadhesion. This enabled one of the key identifications of the work presented in this thesis; the mechanism of mucoadhesion and visualization of the two critical stages involved in the mucoadhesion process; contact and consolidation[221]. TSP-microparticles were found to sustain drug release compared to their solution forms. The rate-limiting step of drug release from microparticles was found to be diffusion of the drug from the polymer matrix. The release studies served as a guide to their potential kinetics *in-vivo*. However, any *in-vitro* data has to be interpreted with caution due to the artificial nature of *in-vitro* experiments compared to the *in-vivo* environment.

As discussed in **Section 3.9** use of hydrophilic drugs in this study may be a limitation for the extrapolation of the data reported to different classes of drugs. The release behaviour of model drug from TSP-microparticles changed from diffusion controlled (Higuchi) to diffusion/erosion controlled (Korsmeyer-peppas) when the molecular weight reached 40 kDa. Whether this is an effect of TSP-microparticles or the cellulose acetate membrane used for the *in-vitro* studies needs to be examined and poses the question of reliability of data extrapolation to release behaviour of large molecules (>40 kDa) from TSP-microparticles. Mucociliary clearance and effect of other stimulations such as respiration and sneezing, which cannot be simulated *in-vitro* can affect drug release *in-vivo* resulting in a different release profile.

Though selective deposition of the particles in different regions of the human nasal cavity as a function of particle size has been reported previously[491], formulating particles to a specific size to enhance the deposition in the olfactory region, however, has not been previously examined. This thesis demonstrated preferential deposition of 10 µm particles in the olfactory region of a 3D-human nasal replica at normal breathing rates. Therefore, the

results of this study are only applicable for the peak normal inhalational airflow rate and when particles are released from the nostrils. Particle density can affect the deposition of particles in human nasal cavities[519]. The microparticles used in this thesis had a density of 1.3 kg/m^3 which is similar to other published report[214] that demonstrated high deposition in the olfactory region with 10 µm particles, therefore, the effect of density on the deposition was not evaluated in this thesis. However, to translate the proposed delivery system to a clinical stage, future work will be required to examine the effect of particle density, effect of inhalational airflow rate individually and in combination with the particle size on the olfactory deposition of particles. Although this thesis provided evidence for enhanced deposition in the olfactory region, the critical question 'whether this enhancement can produce any therapeutic effect?' remains. Data correlating this enhancement with the biological relevance is the key for translation of such a microparticle system from lab to market and needs to be generated.

Data from the animal studies are essential to understand the behavior of delivery systems in the dynamic *in-vivo* environment. **Chapter 4** of this thesis examined the potential of mucoadhesive TSP-microparticles loaded with an AED phenytoin to enhance its nose-to-brain delivery *in-vivo*.

The interesting observation with TSP-microparticles when phenytoin was loaded in to them was their drug release profiles. Though the release of phenytoin was sustained when incorporated into TSP-microparticles, the release of phenytoin within the first 5 min from the microparticles was significantly higher than phenytoin released from the unformulated powder due to the change in crystallinity. The change from a crystalline into an amorphous phase can aid nose-to-brain delivery of phenytoin by increasing its solubility[520]. This change in physical form is speculated to play an essential role in the shelf life of the microparticles. Therefore, a six-month stability study of TSP-microparticles containing phenytoin was conducted according to the ICH guidelines. The transformation of amorphous phase to crystalline nature was observed by six months. Since polymers with similar functional groups may prevent the recrystallization for more prolonged periods, it would be interesting to examine the effect of chemical modifications to TSP with an aim to control the recrystallization of the phenytoin in TSP-microparticles. Also, studies to investigate the

correlation of such a change in physical state to the extent and rate of drug absorption and therapeutic efficacy are needed to further exploit the potential of TSP formulations.

The concentrations of phenytoin observed *in-vivo* in the olfactory bulb and the brain can be correlated to the burst release of phenytoin from TSP-microparticles observed *in-vitro*, and the availability of phenytoin at the site of absorption (olfactory region). While the intranasal solution failed to achieve high concentrations at the olfactory region after 30 min, TSP-microparticles were hypothesized to withstand mucociliary clearance and show high levels of phenytoin at the olfactory region over 60 min and the concentrations of phenytoin were expected to increase beyond this period. Correlating the *in-vitro* and *in-vivo* data it can be hypothesized that, 50-60 % of the dose of phenytoin administered as TSP-microparticles was sufficient to produce equivalent or higher brain concentrations of phenytoin than phenytoin administered as intranasal solution. This reduction in dose can be correlated to the decreased systemic absorption and increased direct nose-to-brain delivery. The objective of this work presented in this thesis was to examine the potential of formulation strategies to enhance nose-to-brain delivery. The time points selected for the *in-vivo* studies demonstrated the potential of TSP-microparticles to increase drug delivery to the brain. The time points chosen in this study and the olfactory bulb phenytoin concentrations measured have provided insights into the initial stages of the drug release from TSP-microparticles.

Nevertheless, to progress into a clinical trial stage, any future work will require data from more extended time periods to thoroughly understand the pharmacokinetic profile of the drug administered when formulated into TSP-microparticles. Furthermore, it will allow safety to be assessed further and the overall absolute bioavailability of the drug to be calculated. Also, future work will require the development of more sensitive assays so drug concentrations in specific regions of the brain can be quantified, which can provide valuable data for treatment of CNS disorders that are specific to an area in the brain. In addition, studies to investigate the biological efficacy in disease animal models are critical for the translation to a clinical stage and need to be included in the future work.

In-silico methods have been shown complementary results from *in-vitro* and *in-vivo* studies[521]. They can provide insight and answer to experimentally tricky observations. The recent trend in incorporating *in-silico* methods in the drug development process has

established a branch linking engineering and medical sciences. With continuous development both the fields complement each other and facilitate the complicated and tedious process of drug development.

Chapter 5 of this thesis utilized *in-silico* techniques like CFPD to examine the experimentally challenging studies like the effect of inhalational airflow and never reported studies like the effect of inter-subject variability on the deposition of particles in the nasal cavity. The *in-silico* studies in this thesis suggested that the 10 µm sized particles were able to enhance the olfactory deposition rates in all the three human subjects examined without significant inter-subject variability. The bi-directional delivery technique has demonstrated higher olfactory deposition with no inter-subject variability. However, this is a small sample size including only male subjects, and future work will be required to assess the data from a larger population including different sex, race and geographical locations. Also, further resolution of anatomical models to clearly identify the olfactory region is required in the future work. Since in-silico studies can generate data on various experimentally difficult facets like particle release position, variable air velocity, geometrical complexity, etc. a comprehensive database needs to be developed to identify, compare and comprehend the results from different subjects which might help advance the liaison of two fields for faster drug development in nose-to-brain delivery.

The formulative approach of administering size specific 10 µm particles increased deposition in the olfactory region. The observations from **Chapter 3** and **Chapter 4** posed an exciting research hypothesis that such a formulative approach used in combination with an intranasal targeting device can further augment olfactory targeting. Therefore in **Chapter 5**, a CFPD modeling technique was employed to answer this question with an aim to study the effect of particle size combined with bi-directional delivery technique on olfactory deposition. The results of this study provided an essential identification; microparticles sized between 14-18 µm showed significantly enhanced drug deposition in the olfactory region combined with the bi-directional delivery technique. The airflow direction in the bi-directional delivery technique was anticipated to be reason for increase in the particle size showing preferential deposition in the olfactory region.

Many other targeting devices are being developed to improve olfactory deposition; it would be interesting to examine the particle size effect on these targeting devices and to identify if such a combined approach can further enhance olfactory targeting. Future studies will be required to acquire deposition data from a large population to determine any differences in deposition patterns between the subjects. Effect of surface modification of size-specific particles with olfactory neuron-specific proteins like lectins on nose-to-brain delivery of drugs could be an exciting research question for the future studies. While this thesis provides evidence to support that the size controlled particles increase deposition in the olfactory region, the biological relevance of this increased deposition needs to be investigated in future studies.

In summary, the *in-vitro*, *in-vivo* and *in-silico* studies complement and refine each other and are essential to optimize a drug delivery system. This thesis utilized a formulation strategy, the development of a microparticle delivery system and integrated data from *in-vitro*, *in-vivo* and *in-silico* studies to refine and optimize the delivery system. Together, the data presented in this thesis provides evidence for the potential of a size tailored mucoadhesive microparticle delivery system to enhance nose-to-brain drug delivery.

References

7 References

1. Djupesland, P. G. Nasal drug delivery devices: Characteristics and performance in a clinical perspective-a review. *Drug Deliv. Transl. Res.* **3,** 42–62 (2013).

2. Kapoor, M., Cloyd, J. C. & Siegel, R. A. A review of intranasal formulations for the treatment of seizure emergencies. *J. Control. Release* **237,** 147–159 (2016).

3. U.S.FDA. Drugs@FDA: FDA Approved Drug Products. (2018). Available at: https://www.accessdata.fda.gov/scripts/cder/daf/. (Accessed: 10th March 2018)

4. Harkema, J. R., Carey, S. A. & Wagner, J. G. The Nose Revisited: A Brief Review of the Comparative Structure, Function, and Toxicologic Pathology of the Nasal Epithelium. *Toxicol. Pathol.* **34,** 252–269 (2006).

5. Nicolaas G.M. Schipper, J. C. V. & Merkus, F. W. H. M. The Nasal Mucociliary Clearance: Relevance to Nasal Drug Delivery. *Pharm. Res.* **8,** 807–14 (1991).

6. Chien, Y.W., Su, K.S.E., and Chang, S.-F. *Nasal systemic drug delivery*. (Marcel Dekker, Inc, 1989).

7. Tiozzo Fasiolo, L. *et al.* Opportunity and challenges of nasal powders: Drug formulation and delivery. *Eur. J. Pharm. Sci.* **113,** 2–17 (2018).

8. Gizurarson, S. The relevance of nasal physiology to the design of drug absorption studies. *Advanced Drug Delivery Reviews* **11,** 329–347 (1993).

9. Thorne, J. J. L. and R. G. Intranasal Drug Delivery to the Brain. in *Drug Delivery to the Brain: Physiological Concepts, Methodologies and Approaches* (ed. Margareta Hammarlund-Udenaes, Elizabeth C.M. de Lange, R. G. T.) 401–30 (Springer Science & Business Media, 2013).

10. Field, P. M., Li, Y. & Raisman, G. Ensheathment of the olfactory nerves in the adult rat. *J. Neurocytol.* **32,** 317–324 (2003).

11. Carmichael, S. T., Clugnet, M. -C & Price, J. L. Central olfactory connections in the macaque monkey. *J. Comp. Neurol.* **346,** 403–434 (1994).

12. Hegg, C. C., Irwin, M. & Lucero, M. T. Calcium store-mediated signaling in sustentacular cells of the mouse olfactory epithelium. *Glia* **57,** 634–644 (2009).

13. Caggiano, M., Kauer, J. S. & Hunter, D. D. Globose basal cells are neuronal progenitors in the olfactory epithelium: A lineage analysis using a replication-incompetent retrovirus. *Neuron* **13,** 339–352 (1994).

14. Iwai, N., Zhou, Z., Roop, D. R. & Behringer, R. R. Horizontal Basal Cells Are Multipotent Progenitors in Normal and Injured Adult Olfactory Epithelium. *Stem Cells* **26,** 1298–1306 (2008).

15. Elsaesser, R. & Paysan, J. The sense of smell, its signalling pathways, and the dichotomy of cilia and microvilli in olfactory sensory cells. *BMC Neuroscience* **8,** (2007).

16. Ward, A. THIEME Atlas of Anatomy general anatomy and musculoskeletal system. *Acupunct. Med.* **26,** 253–253 (2008).

17. Finger, T. E., Jeor, V. L. S., Kinnamon, J. C. & Silver, W. L. Ultrastructure of substance P- and CGRP-immunoreactive nerve fibers in the nasal epithelium of rodents. *J. Comp. Neurol.* **294,** 293–305 (1990).

18. Finger, T. E., Böttger, B., Schaefer, M. L. & Silver, W. L. Trigeminal collaterals in the nasal epithelium and olfactory bulb: A potential route for direct modulation of olfactory information by trigeminal stimuli. *J. Comp. Neurol.* **444,** 221–226 (2002).

19. Broadwell, R. D. & Balin, B. J. Endocytic and exocytic pathways of the neuronal secretory process and trans synaptic transfer of wheat germ agglutinin-horseradish peroxidase in vivo. *J. Comp. Neurol.* **242,** 632–650 (1985).

20. Deatly AM, Haase AT, Fewster PH, Lewis E, B. M. Human herpes virus infections and Alzheimer's disease. *Neuropathol Appl Neurobiol* **16,** 213–23 (1990).

21. Anton, F. & Peppel, P. Central projections of trigeminal primary afferents innervating the nasal mucosa: A horseradish peroxidase study in the rat. *Neuroscience* **41,** 617–628 (1991).

22. Doty, R. L. The olfactory vector hypothesis of neurodegenerative disease: Is it viable? *Annals of Neurology* **63,** 7–15 (2008).

23. Kristensson, K. & Olsson, Y. Uptake of exogenous proteins in mouse olfactory cells. *Acta Neuropathol.* **19,** 145–154 (1971).

24. Thorne, R. G., Emory, C. R., Ala, T. A., Frey, W. H. & Frey Ii, W. H. Quantitative analysis of the olfactory pathway for drug delivery to the brain. *Brain Res.* **692,** 278–282 (1995).

25. Baker, H. & Spencer, R. F. Transneuronal transport of peroxidase-conjugated wheat germ agglutinin (WGA-HRP) from the olfactory epithelium to the brain of the adult rat. *Exp. brain Res.* **63,** 461–73 (1986).

26. Kristensson, K. Microbes' roadmap to neurons. *Nature Reviews Neuroscience* **12,** 345–357 (2011).

27. Thorne, R. G., Pronk, G. J., Padmanabhan, V. & Frey, W. H. Delivery of insulin-like growth factor-I to the rat brain and spinal cord along olfactory and trigeminal pathways following intranasal administration. *Neuroscience* **127,** 481–496 (2004).

28. Khan, A. R., Liu, M., Khan, M. W. & Zhai, G. Progress in brain targeting drug delivery system by nasal route. *Journal of Controlled Release* **268,** 364–389 (2017).

29. Thorne, R. G., Hrabetová, S. & Nicholson, C. Diffusion of epidermal growth factor in rat brain extracellular space measured by integrative optical imaging. *J. Neurophysiol.* **92,** 3471–81 (2004).

30. Illum, L. Is nose-to-brain transport of drugs in man a reality? *J. Pharm. Pharmacol.* **56,** 3–17 (2004).

31. Dhuria, S. V., Hanson, L. R. & Frey, W. H. *Intranasal delivery to the central nervous system: Mechanisms and experimental considerations*. *Journal of Pharmaceutical Sciences* **99,** 1654–1673 (2010).

32. Lochhead, J. J. & Thorne, R. G. Intranasal delivery of biologics to the central nervous system. *Adv. Drug Deliv. Rev.* **64,** 614–628 (2012).

33. Edeling, M. A., Smith, C. & Owen, D. Life of a clathrin coat: Insights from clathrin and AP structures. *Nat. Rev. Mol. Cell Biol.* **7,** 32–44 (2006).

34. Rejman, J., Oberle, V., Zuhron, I. S. & HoekstraA, D. Size-dependent internalization of particles via the pathways of clathrin- and caveolae-mediated endocytosis. *Biochem. J.* **377,** 159–169 (2004).

35. Jones, A. T. Gateways and tools for drug delivery: Endocytic pathways and the cellular dynamics of cell penetrating peptides. *Int. J. Pharm.* **354,** 34–38 (2008).

36. Altner, H. & Altner-Kolnberger, I. Freeze-fracture and tracer experiments on the permeability of the zonulae occludentes in the olfactory mucosa of vertebrates. *Cell Tissue Res.* **154,** 51–59 (1974).

37. Miyamoto, M. *et al.* Effect of poly-L-arginine on the nasal absorption of FITC-dextran of different molecular weights and recombinant human granulocyte colony-stimulating factor (rhG-CSF) in rats. *Int. J. Pharm.* **226,** 127–138 (2001).

38. Faber, W. M. The nasal mucosa and the subarachnoid space. *Am. J. Anat.* **62,** 121–48 (1937).

39. Jansson, B. & Björk, E. Visualization of in vivo olfactory uptake and transfer using fluorescein dextran. *J. Drug Target.* **10,** 379–386 (2002).

40. Thorne, R. G. & Frey, W. H. Delivery of neurotrophic factors to the central nervous system: pharmacokinetic considerations. *Clin. Pharmacokinet.* **40,** 907–946 (2001).

41. Hadaczek, P. *et al.* The 'Perivascular Pump' Driven by Arterial Pulsation Is a Powerful Mechanism for the Distribution of Therapeutic Molecules within the Brain. *Mol. Ther.* **14,** 69–78 (2006).

42. Iliff, J. J. *et al.* A paravascular pathway facilitates CSF flow through the brain parenchyma and the clearance of interstitial solutes, including amyloid β. *Sci. Transl. Med.* **4,** (2012).

43. Rennels, M. L., Gregory, T. F., Blaumanis, O. R., Fujimoto, K. & Grady, P. A. Evidence for a 'Paravascular' fluid circulation in the mammalian central nervous system, provided by the rapid distribution of tracer protein throughout the brain from the subarachnoid space. *Brain Res.* **326,** 47–63 (1985).

44. I, Carlstedt, JK Sheehan, AP Corfield, J. G. Mucous glycoproteins: a gel of a problem. *Essays Biochem.* **20,** 10–76 (1985).

45. Sanderson, M. J. & Sleigh, M. A. Ciliary Activity of Cultured Rabbit Tracheal Epithelium: Beat Pattern and Metachrony. *J. Cell Sci* **47,** 331–347 (1981).

46. Mygind, N. & Dahl, R. Anatomy, physiology and function of the nasal cavities in health and disease. *Advanced Drug Delivery Reviews* **29,** 3–12 (1998).

47. Chien, Y. W. & Chang, S. F. Intranasal drug delivery for systemic medications. *Crit. Rev. Ther. Drug Carrier Syst.* **4,** 67–194 (1987).

48. Marttin, E., Schipper, N. G. M., Coos Verhoef, J. & Merkus, F. W. H. M. Nasal mucociliary

clearance as a factor in nasal drug delivery. *Adv. Drug Deliv. Rev.* **29,** 13–38 (1998).

49. Petruson, B., Hansson, H. A. & Karlsson, G. Structural and Functional Aspects of Cells in the Nasal Mucociliary System. *Arch. Otolaryngol.* **110,** 576–581 (1984).

50. Satir, P. & Sleigh, M. A. the Physiology of Cilia and Mucociliary Interactions. *Annu. Rev. Physiol* **52,** 137–55 (1990).

51. Lucas AM, D. L. Principles Underlying Ciliary Activity in the Respiratory Tractii. A Comparison of Nasal Clearance in Man, Monkey and Other Mammals. *Arch Otolaryngol* **20,** 518–41 (1934).

52. Andersen I, P. D. Measurement of nasal mucociliary clearance. *Eur J Respir Dis Suppl.* **127,** 37–40 (1983).

53. Duchateau, G. S., Graamans, K., Zuidema, J. & Merkus, F. W. Correlation between nasal ciliary beat frequency and mucus transport rate in volunteers. *Laryngoscope* **95,** 854–859 (1985).

54. Soane, R. J. *et al.* Evaluation of the clearance characteristics of bioadhesive systems in humans. *Int. J. Pharm.* **178,** 55–65 (1999).

55. Shipley, M. T. Transport of molecules from nose to brain: Transneuronal anterograde and retrograde labeling in the rat olfactory system by wheat germ agglutinin-horseradish peroxidase applied to the nasal epithelium. *Brain Res. Bull.* **15,** 129–142 (1985).

56. Smolnik, R., Molle, M., Fehm, H. L. & Born, J. Brain potentials and attention after acute and subchronic intranasal administration of ACTH 4-10 and desacetyl-alpha-MSH in humans. *Neuroendocrinology* **70,** 63–72 (1999).

57. Chapman, C. D. *et al.* Intranasal treatment of central nervous system dysfunction in humans. *Pharm. Res.* **30,** 2475–2484 (2013).

58. Matthias Reitz, Maria Demestre, Jan Sedlacik, Hildegard Meissner, Jens Fiehler, B. & Seung U. Kim, Manfredwestphal, N. O. S. Intranasal Delivery of Neural Stem/Progenitor Cells: A Noninvasive Passage to Target Intracerebral Glioma. *Stem Cells Transl. Med.* 866–873 (2012).

59. McGowan, J. W. D., Shao, Q., Vig, P. J. S. & Bidwell, G. L. Intranasal administration of elastin-like polypeptide for therapeutic delivery to the central nervous system. *Drug Des. Devel. Ther.* **10,** 2803–2813 (2016).

60. Rapoport, A. & Winner, P. Nasal delivery of antimigraine drugs: Clinical rationale and evidence base. *Headache* **46,** (2006).

61. Febbraro, F., Andersen, K. J., Sanchez-Guajardo, V., Tentillier, N. & Romero-Ramos, M. Chronic intranasal deferoxamine ameliorates motor defects and pathology in the α-synuclein rAAV Parkinson's model. *Exp. Neurol.* **247,** 45–58 (2013).

62. Guo, C. *et al.* Intranasal deferoxamine reverses iron-induced memory deficits and inhibits amyloidogenic APP processing in a transgenic mouse model of Alzheimer's disease. *Neurobiol. Aging* **34,** 562–575 (2013).

63. Hanson, L. R. *et al.* Intranasal deferoxamine provides increased brain exposure and significant

protection in rat ischemic stroke. *J. Pharmacol. Exp. Ther.* **330,** 679–86 (2009).

64. Danielyan, L. *et al.* Intranasal delivery of cells to the brain. *Eur. J. Cell Biol.* **88,** 315–324 (2009).

65. Charlton, S. T. *et al.* Evaluation of direct transport pathways of glycine receptor antagonists and an angiotensin antagonist from the nasal cavity to the central nervous system in the rat model. *Pharm. Res.* **25,** 1531–1543 (2008).

66. Stevens, J., Ploeger, B. A., Van Der Graaf, P. H., Danhof, M. & De Lange, E. C. M. Systemic and direct nose-to-brain transport pharmacokinetic model for remoxipride after intravenous and intranasal administration. *Drug Metab. Dispos.* **39,** 2275–2282 (2011).

67. Munjal, S. *et al.* A multicenter, open-label, long-term safety and tolerability study of DFN-02, an intranasal spray of sumatriptan 10 mg plus permeation enhancer DDM, for the acute treatment of episodic migraine. *J. Headache Pain* **18,** (2017).

68. Munjal, S. *et al.* A Randomized Trial Comparing the Pharmacokinetics, Safety, and Tolerability of DFN-02, an Intranasal Sumatriptan Spray Containing a Permeation Enhancer, With Intranasal and Subcutaneous Sumatriptan in Healthy Adults. *Headache* **56,** 1455–1465 (2016).

69. Avcu, N. *et al.* Intranasal Lidocaine in Acute Treatment of Migraine: A Randomized Controlled Trial. *Ann. Emerg. Med.* (2016). doi:10.1016/j.annemergmed.2016.09.031

70. Winner, P. *et al.* Efficacy and tolerability of zolmitriptan nasal spray for the treatment of acute migraine in adolescents: Results of a randomized, double-blind, multi-center, parallel-group study (TEENZ). *Headache* **56,** 1107–1119 (2016).

71. Mischley, L. K. *et al.* A randomized, double-blind phase I/IIa study of intranasal glutathione in Parkinson's disease. *Mov. Disord.* **30,** 1696–1701 (2015).

72. Born, J. *et al.* Sniffing neuropeptides: A transnasal approach to the human brain. *Nat. Neurosci.* **5,** 514–516 (2002).

73. Vaka, S. R. K., Sammeta, S. M., Day, L. B. & Murthy, S. N. Delivery of nerve growth factor to brain via intranasal administration and enhancement of brain uptake. *J. Pharm. Sci.* **98,** 3640–3646 (2009).

74. Lv, Q. *et al.* Intranasal delivery of nerve growth factor attenuates aquaporins-4-induced edema following traumatic brain injury in rats. *Brain Res.* **1493,** 80–89 (2013).

75. Zhao, Y. Z. *et al.* Gelatin nanostructured lipid carriers-mediated intranasal delivery of basic fibroblast growth factor enhances functional recovery in hemiparkinsonian rats. *Nanomedicine Nanotechnology, Biol. Med.* **10,** 755–764 (2014).

76. Zhao, Y. Z. *et al.* Intranasal delivery of bFGF with nanoliposomes enhances in vivo neuroprotection and neural injury recovery in a rodent stroke model. *J. Control. Release* **224,** 165–175 (2016).

77. Serova, L. I., Laukova, M., Alaluf, L. G., Pucillo, L. & Sabban, E. L. Intranasal neuropeptide Y reverses anxiety and depressive-like behavior impaired by single prolonged stress PTSD model. *Eur. Neuropsychopharmacol.* **24,** 142–147 (2014).

78. Dine, J. *et al.* Intranasally applied neuropeptide S shifts a high-anxiety electrophysiological endophenotype in the ventral hippocampus towards a 'normal'-anxiety onee0120272. *PLoS One* **10,** 1–10 (2015).

79. Vaka, S. R. K., Murthy, S. N., Balaji, A. & Repka, M. A. Delivery of brain-derived neurotrophic factor via nose-to-brain pathway. *Pharm. Res.* **29,** 441–447 (2012).

80. Alcalá-Barraza, S. R. *et al.* Intranasal delivery of neurotrophic factors BDNF, CNTF, EPO, and NT-4 to the CNS. *J. Drug Target.* **18,** 179–190 (2010).

81. Chen, H. *et al.* Focused ultrasound-enhanced intranasal brain delivery of brain-derived neurotrophic factor. *Sci. Rep.* **6,** 1–8 (2016).

82. Samaridou, E. & Alonso, M. J. Nose-to-brain peptide delivery - The potential of nanotechnology. *Bioorganic Med. Chem.* **26,** 2888–2905 (2018).

83. Francis, G. J. *et al.* Intranasal insulin prevents cognitive decline, cerebral atrophy and white matter changes in murine type I diabetic encephalopathy. *Brain* **131,** 3311–3334 (2008).

84. Craft, S. *et al.* Intranasal insulin therapy for Alzheimer disease and amnestic mild cognitive impairment: A pilot clinical trial. *Arch. Neurol.* **69,** 29–38 (2012).

85. Claxton, A. *et al.* Long-acting intranasal insulin detemir improves cognition for adults with mild cognitive impairment or early-stage Alzheimer's Disease dementia. *J. Alzheimer's Dis.* **44,** 897–906 (2015).

86. Rosenbloom, M. H. *et al.* A single-dose pilot trial of intranasal rapid-acting insulin in apolipoprotein E4 carriers with mild-moderate Alzheimer's disease. *CNS Drugs* **28,** 1185–1189 (2014).

87. Jauch-Chara, K. *et al.* Intranasal insulin suppresses food intake via enhancement of brain energy levels in humans. *Diabetes* **61,** 2261–2268 (2012).

88. Baier, P. C. *et al.* Effects of intranasal hypocretin-1 (orexin A) on sleep in narcolepsy with cataplexy. *Sleep Med.* **12,** 941–946 (2011).

89. Baier, P. C. *et al.* Olfactory dysfunction in patients with narcolepsy with cataplexy is restored by intranasal Orexin A (Hypocretin-1). *Brain* **131,** 2734–2741 (2008).

90. Deadwyler, S. A., Porrino, L., Siegel, J. M. & Hampson, R. E. Systemic and Nasal Delivery of Orexin-A (Hypocretin-1) Reduces the Effects of Sleep Deprivation on Cognitive Performance in Nonhuman Primates. *J. Neurosci.* **27,** 14239–14247 (2007).

91. Fan, X. *et al.* No effect of adjunctive, repeated dose intranasal insulin treatment on psychopathology and cognition in patients with schizophrenia. *J. Clin. Psychopharmacol.* **33,** 226–230 (2013).

92. Freiherr, J. *et al.* Intranasal insulin as a treatment for alzheimer's disease: A review of basic research and clinical evidence. *CNS Drugs* **27,** 505–514 (2013).

93. Reger, M. A. *et al.* Effects of intranasal insulin on cognition in memory-impaired older adults: Modulation by APOE genotype. *Neurobiol. Aging* **27,** 451–458 (2006).

94. Craft S, A. P. The Study of Nasal Insulin in the Fight Against Forgetfulness (SNIFF). (2014).

Available at: https://clinicaltrials.gov/ct2/show/NCT01767909.

95. Zhao, Y. *et al.* Pharmacokinetic Evaluation of Intranasally Administered Vinyl Polymer-Coated Lorazepam Microparticles in Rabbits. *AAPS J.* **14,** 218–224 (2012).

96. Hallschmid, M., Benedict, C., Born, J., Fehm, H. L. & Kern, W. Manipulating central nervous mechanisms of food intake and body weight regulation by intranasal administration of neuropeptides in man. *Physiol. Behav.* **83,** 55–64 (2004).

97. Bohringer, A., Schwabe, L., Richter, S. & Schachinger, H. Intranasal insulin attenuates the hypothalamic-pituitary-adrenal axis response to psychosocial stress. *Psychoneuroendocrinology* **33,** 1394–1400 (2008).

98. Williams, D. R. & Bürkner, P. C. Effects of intranasal oxytocin on symptoms of schizophrenia: A multivariate Bayesian meta-analysis. *Psychoneuroendocrinology* **75,** 141–151 (2017).

99. Pedersen, C. A. *et al.* Intranasal oxytocin reduces psychotic symptoms and improves Theory of Mind and social perception in schizophrenia. *Schizophr. Res.* **132,** 50–53 (2011).

100. Jarskog, L. F. *et al.* A 12-week randomized controlled trial of twice-daily intranasal oxytocin for social cognitive deficits in people with schizophrenia. *Schizophr. Res.* **185,** 88–95 (2017).

101. Tachibana, M. *et al.* Long-Term Administration of Intranasal Oxytocin Is a Safe and Promising Therapy for Early Adolescent Boys with Autism Spectrum Disorders. *J. Child Adolesc. Psychopharmacol.* **23,** 123–127 (2013).

102. Guastella, A. J. *et al.* The effects of a course of intranasal oxytocin on social behaviors in youth diagnosed with autism spectrum disorders: A randomized controlled trial. *J. Child Psychol. Psychiatry Allied Discip.* **56,** 444–452 (2015).

103. Gordon, I. *et al.* Intranasal Oxytocin Enhances Connectivity in the Neural Circuitry Supporting Social Motivation and Social Perception in Children with Autism. *Sci. Rep.* **6,** 1–14 (2016).

104. Sack, M. *et al.* Intranasal oxytocin reduces provoked symptoms in female patients with posttraumatic stress disorder despite exerting sympathomimetic and positive chronotropic effects in a randomized controlled trial. *BMC Med.* **15,** 1–11 (2017).

105. Guastella, A. J. *et al.* Intranasal Oxytocin Improves Emotion Recognition for Youth with Autism Spectrum Disorders. *Biol. Psychiatry* **67,** 692–694 (2010).

106. van Zuiden, M. *et al.* Intranasal Oxytocin to Prevent Posttraumatic Stress Disorder Symptoms: A Randomized Controlled Trial in Emergency Department Patients. *Biol. Psychiatry* **81,** 1030–1040 (2017).

107. Murgatroyd, C. A. *et al.* Effects of chronic social stress and maternal intranasal oxytocin and vasopressin on offspring interferon-γ and behavior. *Front. Endocrinol. (Lausanne).* **7,** 1–11 (2016).

108. Guastella, A. J., Kenyon, A. R., Alvares, G. A., Carson, D. S. & Hickie, I. B. Intranasal Arginine Vasopressin Enhances the Encoding of Happy and Angry Faces in Humans. *Biol. Psychiatry* **67,** 1220–1222 (2010).

109. Henkin, R. I. Intranasal insulin: From nose to brain. *Nutrition* **26,** 624–633 (2010).

110. Danielyan, L. *et al.* Therapeutic Efficacy of Intranasally Delivered Mesenchymal Stem Cells in a Rat Model of Parkinson Disease. *Rejuvenation Res.* **14,** 3–16 (2011).

111. Wei, N. *et al.* Delayed intranasal delivery of hypoxic-preconditioned bone marrow mesenchymal stem cells enhanced cell homing and therapeutic benefits after ischemic stroke in mice. *Cell Transplant.* **22,** 977–991 (2013).

112. Donega, V. *et al.* Intranasal Mesenchymal Stem Cell Treatment for Neonatal Brain Damage: Long-Term Cognitive and Sensorimotor Improvement. *PLoS One* **8,** (2013).

113. van Velthoven, C. T. J. *et al.* Mesenchymal stem cell transplantation attenuates brain injury after neonatal stroke. *Stroke.* **44,** 1426–32 (2013).

114. Fransson, M. *et al.* CAR/FoxP3-engineered T regulatory cells target the CNS and suppress EAE upon intranasal delivery. *J. Neuroinflammation* **9,** (2012).

115. Casettari, L. & Illum, L. Chitosan in nasal delivery systems for therapeutic drugs. *Journal of Controlled Release* **190,** 189–200 (2014).

116. Liu, L. B., Xue, Y. X. & Liu, Y. H. Bradykinin increases the permeability of the blood-tumor barrier by the caveolae-mediated transcellular pathway. *J. Neurooncol.* **99,** 187–194 (2010).

117. Zhang, H., Ting Gu, Y. & Xue, Y. X. Bradykinin-induced blood-brain tumor barrier permeability increase is mediated by adenosine 5'-triphosphate-sensitive potassium channel. *Brain Res.* **1144,** 33–41 (2007).

118. O'Reilly, M. A., Huang, Y. & Hynynen, K. The impact of standing wave effects on transcranial focused ultrasound disruption of the blood-brain barrier in a rat model. *Phys. Med. Biol.* **55,** 5251–5267 (2010).

119. Brem, H. *et al.* Interstitial chemotherapy with drug polymer implants for the treatment of recurrent gliomas. *J. Neurosurg.* **74,** 441–446 (1991).

120. Gallia GL, Brem S, B. H. Local treatment of malignant brain tumors using implantable chemotherapeutic polymers. *J Natl Compr Canc Netw.* **3,** 721–8 (2005).

121. Sutradhar, K. B. & Sumi, C. D. Implantable microchip: The futuristic controlled drug delivery system. *Drug Deliv.* **23,** 1–11 (2016).

122. Pavan B, D. A. Prodrugs and endogenous transporters: are they suitable tools for drug targeting into the central nervous system? *Curr Pharm Des* **17,** 3560–76 (2011).

123. Gynther, M. *et al.* Large Neutral Amino Acid Transporter Enables Brain Drug Delivery via Prodrugs Large Neutral Amino Acid Transporter Enables Brain Drug Delivery via Prodrugs. *J. Med. Chem.* **51,** 932–936 (2008).

124. Sezaki, H. Mucosal penetration enhancement. *Journal of Drug Targeting* **3,** 175–177 (1995).

125. Merkus, F. W. H. M., Schipper, N. G. M., Hermens, W. A. J. J., Romeijn, S. G. & Verhoef, J. C. Absorption enhancers in nasal drug delivery: efficacy and safety. *J. Control. Release* **24,** 201–208 (1993).

126. Pavan, B. & Dalpiaz, A. Prodrugs and Endogenous Transporters: Are They Suitable Tools for Drug Targeting into the Central Nervous System? *Curr. Pharm. Des.* **17,** 3560–3576 (2011).

127. Gynther, M. *et al.* Large neutral amino acid transporter enables brain drug delivery via prodrugs. *J. Med. Chem.* **51,** 932–936 (2008).

128. Chen, P., Bodor, N., Wu, W. M. & Prokai, L. Strategies to target kyotorphin analogues to the brain. *J. Med. Chem.* **41,** 3773–3781 (1998).

129. Singh, R. K., Prasad, D. N. & Bhardwaj, T. R. Design, synthesis, chemical and biological evaluation of brain targeted alkylating agent using reversible redox prodrug approach. *Arab. J. Chem.* **10,** 420–429 (2017).

130. Shadab, M. D. *et al.* Bromocriptine loaded chitosan nanoparticles intended for direct nose to brain delivery: Pharmacodynamic, Pharmacokinetic and Scintigraphy study in mice model. *Eur. J. Pharm. Sci.* **48,** 393–405 (2013).

131. Gavini, E. *et al.* Influence of chitosan glutamate on the in vivo intranasal absorption of rokitamycin from microspheres. *J. Pharm. Sci.* **100,** 1488–1502 (2011).

132. Nagpal, K., Singh, S. K. & Mishra, D. N. Optimization of brain targeted chitosan nanoparticles of Rivastigmine for improved efficacy and safety. *Int. J. Biol. Macromol.* **59,** 72–83 (2013).

133. Haque, S., Md, S., Sahni, J. K., Ali, J. & Baboota, S. Development and evaluation of brain targeted intranasal alginate nanoparticles for treatment of depression. *J. Psychiatr. Res.* **48,** 1–12 (2014).

134. Haque, S. *et al.* Venlafaxine loaded chitosan NPs for brain targeting: Pharmacokinetic and pharmacodynamic evaluation. *Carbohydr. Polym.* **89,** 72–79 (2012).

135. Patel, D., Naik, S. & Misra, A. Improved transnasal transport and brain uptake of tizanidine HCl-loaded thiolated chitosan nanoparticles for alleviation of pain. *J. Pharm. Sci.* **101,** 690–706 (2012).

136. Sharma, D. *et al.* Nose to Brain Delivery of Midazolam Loaded PLGA Nanoparticles: In Vitro and In Vivo Investigations. *Curr. Drug Deliv.* **13,** 557–64 (2016).

137. Jose, S. *et al.* Thermo-sensitive gels containing lorazepam microspheres for intranasal brain targeting. *Int. J. Pharm.* **441,** 516–526 (2013).

138. Wang, X., Chi, N. & Tang, X. Preparation of estradiol chitosan nanoparticles for improving nasal absorption and brain targeting. *Eur. J. Pharm. Biopharm.* **70,** 735–740 (2008).

139. Lungare, S., Hallam, K. & Badhan, R. K. S. Phytochemical-loaded mesoporous silica nanoparticles for nose-to-brain olfactory drug delivery. *Int. J. Pharm.* **513,** 280–293 (2016).

140. Abdelbary, G. A. & Tadros, M. I. Brain targeting of olanzapine via intranasal delivery of core-shell difunctional block copolymer mixed nanomicellar carriers: In vitro characterization, ex vivo estimation of nasal toxicity and in vivo biodistribution studies. *Int. J. Pharm.* **452,** 300–310 (2013).

141. Illum, L. Nasal drug delivery - Possibilities, problems and solutions. *J. Control. Release* **87,** 187–198 (2003).

142. Pires, P. C. & Santos, A. O. Nanosystems in nose-to-brain drug delivery: A review of non-clinical brain targeting studies. *J. Control. Release* **270,** 89–100 (2017).

143. Mittal, D. *et al.* Brain targeted nanoparticulate drug delivery system of rasagiline via intranasal route. *Drug Deliv.* **23,** 130–139 (2016).

144. Wen, Z. *et al.* Odorranalectin-conjugated nanoparticles: Preparation, brain delivery and pharmacodynamic study on Parkinson's disease following intranasal administration. *J. Control. Release* **151,** 131–138 (2011).

145. Veronesi, M. C., Aldouby, Y., Domb, A. J. & Kubek, M. J. Thyrotropin-releasing hormone d,l polylactide nanoparticles (TRH-NPs) protect against glutamate toxicity in vitro and kindling development in vivo. *Brain Res.* **1303,** 151–160 (2009).

146. Kubek, M. J., Domb, A. J. & Veronesi, M. C. Attenuation of Kindled Seizures by Intranasal Delivery of Neuropeptide-Loaded Nanoparticles. *Neurotherapeutics* **6,** 359–371 (2009).

147. Kumar, M. *et al.* Evaluation of neuropeptide loaded trimethyl chitosan nanoparticles for nose to brain delivery. *Int. J. Biol. Macromol.* **61,** 189–195 (2013).

148. Joachim, E. *et al.* Gelatin nanoparticles enhance the neuroprotective effects of intranasally administered osteopontin in rat ischemic stroke model. *Drug Deliv. Transl. Res.* **4,** 395–399 (2014).

149. Gao, X. *et al.* Brain delivery of vasoactive intestinal peptide enhanced with the nanoparticles conjugated with wheat germ agglutinin following intranasal administration. *J. Control. Release* **121,** 156–167 (2007).

150. Yadav, S., Gattacceca, F., Panicucci, R. & Amiji, M. M. Comparative biodistribution and pharmacokinetic analysis of cyclosporine-A in the brain upon intranasal or intravenous administration in an oil-in-water nanoemulsion formulation. *Mol. Pharm.* **12,** 1523–1533 (2015).

151. Kanazawa, T., Taki, H., Tanaka, K., Takashima, Y. & Okada, H. Cell-penetrating peptide-modified block copolymer micelles promote direct brain delivery via intranasal administration. *Pharm. Res.* **28,** 2130–2139 (2011).

152. Taki, H., Kanazawa, T., Akiyama, F., Takashima, Y. & Okada, H. Intranasal delivery of camptothecin-loaded tat-modified nanomicells for treatment of intracranial brain tumors. *Pharmaceuticals* **5,** 1092–1102 (2012).

153. Narayan, R. *et al.* Development of risperidone liposomes for brain targeting through intranasal route. *Life Sci.* **163,** 38–45 (2016).

154. Subodhkant Samudre, Avinash Tekade, Kanchan Thorve, Anup Jamodkar, Gauri Parashar, N. C. Xanthan Gum Coated Mucoadhesive Liposomes for Efficient Nose to Brain Delivery of Curcumin. *Drug Deliv. Lett.* **5,** 201–207 (2015).

155. Khan, S., Patil, K., Bobade, N., Yeole, P. & Gaikwad, R. Formulation of intranasal mucoadhesive temperature-mediated in situ gel containing ropinirole and evaluation of brain targeting efficiency in rats. *J. Drug Target.* **18,** 223–234 (2010).

156. Mistry, A., Stolnik, S. & Illum, L. Nose-to-Brain Delivery: Investigation of the Transport of Nanoparticles with Different Surface Characteristics and Sizes in Excised Porcine Olfactory

Epithelium. *Mol. Pharm.* **12,** 2755–2766 (2015).

157. Kohane, D. S. Microparticles and nanoparticles for drug delivery. *Biotechnology and Bioengineering* **96,** 203–209 (2007).

158. Varde, N. K. & Pack, D. W. Microspheres for controlled release drug delivery. *Expert Opin. Biol. Ther.* **4,** 35–51 (2004).

159. Chattaraj, S. C., Rathinavelu, A. & Das, S. K. Biodegradable microparticles of influenza viral vaccine: Comparison of the effects of routes of administration on the in vivo immune response in mice. *J. Control. Release* **58,** 223–232 (1999).

160. Verma, R. K., Kaur, J., Kumar, K., Yadav, A. B. & Misra, A. Intracellular time course, pharmacokinetics, and biodistribution of isoniazid and rifabutin following pulmonary delivery of inhalable microparticles to mice. *Antimicrob. Agents Chemother.* **52,** 3195–3201 (2008).

161. Cambronero-Rojas, A. *et al.* Capreomycin oleate microparticles for intramuscular administration: Preparation, in vitro release and preliminary in vivo evaluation. *J. Control. Release* **209,** 229–237 (2015).

162. Vasa, D. M., O'Donnell, L. A. & Wildfong, P. L. D. Influence of Dosage Form, Formulation, and Delivery Device on Olfactory Deposition and Clearance: Enhancement of Nose-to-CNS Uptake. *J. Pharm. Innov.* **10,** 200–210 (2015).

163. Soane, R. J., Hinchcliffe, M., Davis, S. S. & Illum, L. Clearance characteristics of chitosan based formulations in the sheep nasal cavity. *Int. J. Pharm.* **217,** 183–191 (2001).

164. Vasa, D. M., Buckner, I. S., Cavanaugh, J. E. & Wildfong, P. L. D. Improved Flux of Levodopa via Direct Deposition of Solid Microparticles on Nasal Tissue. *AAPS PharmSciTech* **18,** 904–912 (2016).

165. Patil, S., Babbar, A., Mathur, R., Mishra, A. & Sawant, K. Mucoadhesive chitosan microspheres of carvedilol for nasal administration. *J. Drug Target.* **18,** 321–331 (2010).

166. Elmowafy, E., Osman, R., El-Shamy, A. E. H. A. & Awad, G. A. S. Nasal polysaccharides-glucose regulator microparticles: Optimization, tolerability and antidiabetic activity in rats. *Carbohydr. Polym.* **108,** 257–265 (2014).

167. Lim, S. T., Forbes, B., Berry, D. J., Martin, G. P. & Brown, M. B. In vivo evaluation of novel hyaluronan/chitosan microparticulate delivery systems for the nasal delivery of gentamicin in rabbits. *Int. J. Pharm.* **231,** 73–82 (2002).

168. Krauland, A. H., Leitner, V. M., Grabovac, V. & Bernkop-Schnürch, A. In vivo evaluation of a nasal insulin delivery system based on thiolated chitosan. *J. Pharm. Sci.* **95,** 2463–2472 (2006).

169. Abdel Mouez, M., Zaki, N. M., Mansour, S. & Geneidi, A. S. Bioavailability enhancement of verapamil HCl via intranasal chitosan microspheres. *Eur. J. Pharm. Sci.* **51,** 59–66 (2014).

170. Kozlovskaya, L. & Stepensky, D. Quantitative analysis of the brain-targeted delivery of drugs and model compounds using nano-delivery systems. *J. Control. Release* **171,** 17–23 (2013).

171. Kozlovskaya, L., Abou-Kaoud, M. & Stepensky, D. Quantitative analysis of drug delivery to

the brain via nasal route. *Journal of Controlled Release* **189,** 133–140 (2014).

172. Sun, Y., Shi, K., Wan, F. & Cui, F. De. Methotrexate-loaded microspheres for nose to brain delivery: In vitro/in vivo evaluation. *J. Drug Deliv. Sci. Technol.* **22,** 167–174 (2012).

173. Dalpiaz, A. *et al.* Brain uptake of an anti-ischemic agent by nasal administration of microparticles. *J. Pharm. Sci.* **97,** 4889–4903 (2008).

174. Dalpiaz, A. *et al.* Brain uptake of a zidovudine prodrug after nasal administration of solid lipid microparticles. *Mol. Pharm.* **11,** 1550–1561 (2014).

175. Rassu, G. *et al.* Solid microparticles based on chitosan or methyl-??-cyclodextrin: A first formulative approach to increase the nose-to-brain transport of deferoxamine mesylate. *J. Control. Release* **201,** 68–77 (2015).

176. Khan, A. *et al.* Brain Targeting of Temozolomide via the Intranasal Route Using Lipid-Based Nanoparticles: Brain Pharmacokinetic and Scintigraphic Analyses. *Mol. Pharm.* **13,** 3773–3782 (2016).

177. Salama, H. A., Mahmoud, A. A., Kamel, A. O., Abdel Hady, M. & Awad, G. A. S. Brain delivery of olanzapine by intranasal administration of transfersomal vesicles. *J. Liposome Res.* **22,** 336–345 (2012).

178. Devkar, T. B., Tekade, A. R. & Khandelwal, K. R. Surface engineered nanostructured lipid carriers for efficient nose to brain delivery of ondansetron HCl using Delonix regia gum as a natural mucoadhesive polymer. *Colloids Surfaces B Biointerfaces* **122,** 143–150 (2014).

179. Singh, R. & Lillard, J. W. Nanoparticle-based targeted drug delivery. *Experimental and Molecular Pathology* **86,** 215–223 (2009).

180. Li, Y., Jiang, H. L., Zhu, K. J., Liu, J. H. & Hao, Y. L. Preparation, characterization and nasal delivery of α-cobrotoxin- loaded poly(lactide-co-glycolide)/polyanhydride microspheres. *J. Control. Release* **108,** 10–20 (2005).

181. Dalpiaz, A. *et al.* Nasal chitosan microparticles target a zidovudine prodrug to brain HIV sanctuaries. *Antiviral Res.* **123,** 146–157 (2015).

182. Gavini, E. *et al.* Influence of polymeric microcarriers on the in vivo intranasal uptake of an anti-migraine drug for brain targeting. *Eur. J. Pharm. Biopharm.* **83,** 174–183 (2013).

183. Tafaghodi, M., Tabassi, S. A. S., Jaafari, M. R., Zakavi, S. R. & Momen-Nejad, M. Evaluation of the clearance characteristics of various microspheres in the human nose by gamma-scintigraphy. *Int. J. Pharm.* **280,** 125–135 (2004).

184. Sharma, N., Kulkarni, G. T., Sharma, A., Bhatnagar, A. & Kumar, N. Natural mucoadhesive microspheres of Abelmoschus esculentus polysaccharide as a new carrier for nasal drug delivery. *J. Microencapsul.* **30,** 589–598 (2013).

185. Mao, S., Chen, J., Wei, Z., Liu, H. & Bi, D. Intranasal administration of melatonin starch microspheres. *Int. J. Pharm.* **272,** 37–43 (2004).

186. Belgamwar, V. S. *et al.* Design and development of nasal mucoadhesive microspheres containing tramadol HCl for CNS targeting. *Drug Deliv.* **18,** 353–360 (2011).

187. Gungor, S., Okyar, A., Erturk-Toker, S., Baktir, G. & Ozsoy, Y. Ondansetron-loaded biodegradable microspheres as a nasal sustained delivery system: In vitro/in vivo studies. *Pharm. Dev. Technol.* **15,** 258–265 (2010).

188. Gungor, S., Okyar, A., Erturk-Toker, S., Baktir, G. & Ozsoy, Y. Ondansetron-loaded chitosan microspheres for nasal antiemetic drug delivery: An alternative approach to oral and parenteral routes. *Drug Dev. Ind. Pharm.* **36,** 806–813 (2010).

189. Gavini, E. *et al.* Nasal administration of Carbamazepine using chitosan microspheres: In vitro/in vivo studies. *Int. J. Pharm.* **307,** 9–15 (2006).

190. Ikechukwu Ugwoke, M., Kaufmann, G., Verbeke, N. & Kinget, R. Intranasal bioavailability of apomorphine from carboxymethylcellulose-based drug delivery systems. *Int. J. Pharm.* **202,** 125–131 (2000).

191. Krauland, A. H., Guggi, D. & Bernkop-Schnürch, A. Thiolated chitosan microparticles: A vehicle for nasal peptide drug delivery. *Int. J. Pharm.* **307,** 270–277 (2006).

192. Sadrai, J. V. H. & Alinagari, R. Nasal delivery of insulin using chitosan microspheres. **21,** 761–774 (2004).

193. Brime B, Ballesteros MP, F. P. Preparation and in vitro characterization of gelatin microspheres containing Levodopa for nasal administration. *J Microencapsul.* **17,** 777–84 (2000).

194. Hafner, A., Filipovic-Grcic, J., Voinovich, D. & Jalsenjak, I. Development and in vitro characterization of chitosan-based microspheres for nasal delivery of promethazine. *Drug Dev. Ind. Pharm.* **33,** 427–436 (2007).

195. Gavini, E., Rassu, G., Muzzarelli, C., Cossu, M. & Giunchedi, P. Spray-dried microspheres based on methylpyrrolidinone chitosan as new carrier for nasal administration of metoclopramide. *Eur. J. Pharm. Biopharm.* **68,** 245–252 (2008).

196. Jug, M. & Becirevic-Lacan, M. Development of a cyclodextrin-based nasal delivery system for Lorazepam. *Drug Dev. Ind. Pharm.* **34,** 817–826 (2008).

197. Rassu, G., Gavini, E., Mattana, A. & Giunchedi, P. Improvement of Antiamoebic Activity of Rokitamycin Loaded in Chitosan Microspheres. *Open Drug Deliv. J.* **2,** 38–43 (2008).

198. Alhalaweh, A., Andersson, S. & Velaga, S. P. Preparation of zolmitriptan-chitosan microparticles by spray drying for nasal delivery. *Eur. J. Pharm. Sci.* **38,** 206–214 (2009).

199. Rassu, G. *et al.* New chitosan derivatives for the preparation of rokitamycin loaded microspheres designed for ocular or nasal administration. *J. Pharm. Sci.* **98,** 4852–4865 (2009).

200. Jain, S. A., Chauk, D. S., Mahajan, H. S., Tekade, A. R. & Gattani, S. G. Formulation and evaluation of nasal mucoadhesive microspheres of Sumatriptan succinate. *J. Microencapsul.* **26,** 711–721 (2009).

201. Mahajan, H. S. & Gattani, S. G. Nasal administration of ondansetron using a novel microspheres delivery system Part II: Ex vivo and in vivo studies. *Pharm. Dev. Technol.* **15,** 653–657 (2010).

202. Gavini, E. *et al.* Mucoadhesive microspheres for nasal administration of cyclodextrins. *J. Drug Target.* **17,** 168–179 (2009).

203. Sun, Y. *et al.* The effect of chitosan molecular weight on the characteristics of spray-dried methotrexate-loaded chitosan microspheres for nasal administration. *Drug Dev. Ind. Pharm.* **35,** 379–386 (2009).

204. Nagda, C. D., Chotai, N. P., Nagda, D. C., Patel, S. B. & Patel, U. L. Development and characterization of mucoadhesive microspheres for nasal delivery of ketorolac. *Pharmazie* **66,** 249–257 (2011).

205. Vetter, A. & Bernkop-Schnürch, A. Nasal delivery of antisense oligonucleotides: In vitro evaluation of a thiomer/glutathione microparticulate delivery system. *J. Drug Target.* **18,** 303–312 (2010).

206. Cho, H. J. *et al.* Characterization and in vitro evaluation of freeze-dried microparticles composed of granisetron-cyclodextrin complex and carboxymethylcellulose for intranasal delivery. *Int. J. Pharm.* **400,** 59–65 (2010).

207. Cho, H. J., Balakrishnan, P., Chung, S. J., Shim, C. K. & Kim, D. D. Evaluation of protein stability and in vitro permeation of lyophilized polysaccharides-based microparticles for intranasal protein delivery. *Int. J. Pharm.* **416,** 77–84 (2011).

208. Patil, S. B. & Sawant, K. K. Chitosan microspheres as a delivery system for nasal insufflation. *Colloids Surfaces B Biointerfaces* **84,** 384–389 (2011).

209. Gavini, E., Rassu, G., Sanna, V., Cossu, M. & Giunchedi, P. Mucoadhesive microspheres for nasal administration of an antiemetic drug, metoclopramide: in-vitro/ex-vivo studies. *J. Pharm. Pharmacol.* **57,** 287–294 (2005).

210. Karavasili, C. *et al.* PLGA/DPPC/trimethylchitosan spray-dried microparticles for the nasal delivery of ropinirole hydrochloride: In vitro, ex vivo and cytocompatibility assessment. *Mater. Sci. Eng. C* **59,** 1053–1062 (2016).

211. Mahajan, H. S. & Gattani, S. G. Gellan gum based microparticles of metoclopromide hydrochloride for intranasal delivery: development and evaluation. *Chem. Pharm. Bull. (Tokyo).* **57,** 388–392 (2009).

212. Saladini, B., Bigucci, F., Cerchiara, T., Gallucci, M. C. & Luppi, B. Microparticles based on chitosan/pectin polyelectrolyte complexes for nasal delivery of tacrine hydrochloride. *Drug Deliv. Transl. Res.* **3,** 33–41 (2013).

213. El-Sherbiny, I. M., El-baz, N. M. & Yacoub, M. H. Inhaled nano- and microparticles for drug delivery. *Glob. Cardiol. Sci. Pract.* **2,** 1–14 (2015).

214. Schroeter, J. D., Tewksbury, E. W., Wong, B. A. & Kimbell, J. S. Experimental Measurements and Computational Predictions of Regional Particle Deposition in a Sectional Nasal Model. *J. Aerosol Med. Pulm. Drug Deliv.* **28,** 20–29 (2015).

215. Shi, H., Kleinstreuer, C. & Zhang, Z. Modeling of inertial particle transport and deposition in human nasal cavities with wall roughness. *J. Aerosol Sci.* **38,** 398–419 (2007).

216. Hoekman, J. D. & Ho, R. J. Y. Enhanced analgesic responses after preferential delivery of morphine and fentanyl to the olfactory epithelium in rats. *Anesth. Analg.* **113,** 641–651

(2011).

217. KurveTechnology. A New Spin on Nasal Drug Delivery. (2014). Available at: http://www.kurvetech.com/pdf/DepositionComp_ScintigraphicStudy.pdf.

218. Quintana, D. S. *et al.* Low-dose oxytocin delivered intranasally with Breath Powered device affects social-cognitive behavior: A randomized fourway crossover trial with nasal cavity dimension assessment. *Transl. Psychiatry* **5,** (2015).

219. Brown, V. & Liu, F. Intranasal delivery of a peptide with antidepressant-like effect. *Neuropsychopharmacology* **39,** 2131–2141 (2014).

220. Hoekman, J. D. & Ho, R. J. Y. Effects of Localized Hydrophilic Mannitol and Hydrophobic Nelfinavir Administration Targeted to Olfactory Epithelium on Brain Distribution. *AAPS PharmSciTech* **12,** 534–543 (2011).

221. Smart, J. D. The basics and underlying mechanisms of mucoadhesion. *Advanced Drug Delivery Reviews* **57,** 1556–1568 (2005).

222. Leitner, V. M., Walker, G. F. & Bernkop-Schnürch, A. Thiolated polymers: Evidence for the formation of disulphide bonds with mucus glycoproteins. *Eur. J. Pharm. Biopharm.* **56,** 207–214 (2003).

223. Mortazavi, S. A. & Smart, J. D. An investigation into the role of water movement and mucus gel dehydration in mucoadhesion. *J. Control. Release* **25,** 197–203 (1993).

224. Mathiowitz, E. and Chickering, D. . Definitions, mechanisms, and theories of bioadhesion. in *Bioadhesive drug delivery systems: Fundamentals, novel approaches, and development* (ed. Mathiowitz, E., D.E. Chickering, and C. M. L.) 1–10 (Marcel Dekker, Inc, 1999).

225. Illum, L. Nasal drug delivery - recent developments and future prospects. *J Control Release* **161,** 254–263 (2012).

226. Illum, L., Jørgensen, H., Bisgaard, H., Krogsgaard, O. & Rossing, N. Bioadhesive microspheres as a potential nasal drug delivery system. *Int. J. Pharm.* **39,** 189–199 (1987).

227. Björk, E. Degradable starch microspheres as a nasal delivery system for insulin. **47,** 233–238 (1988).

228. Björk, E. & Edman, P. Characterization of degradable starch microspheres as a nasal delivery system for drugs. *Int. J. Pharm.* **62,** 187–192 (1990).

229. Wang, J., Tabata, Y. & Morimoto, K. Aminated gelatin microspheres as a nasal delivery system for peptide drugs: Evaluation of in vitro release and in vivo insulin absorption in rats. *J. Control. Release* **113,** 31–37 (2006).

230. Björk, E., Isaksson, U., Edman, P. & Artursson, P. Starch microspheres induce pulsatile delivery of drugs and peptides across the epithelial barrier by reversible separation of the tight junctions. *J. Drug Target.* **2,** 501–507 (1995).

231. Yeh, T. H. *et al.* Mechanism and consequence of chitosan-mediated reversible epithelial tight junction opening. *Biomaterials* **32,** 6164–6173 (2011).

232. Kriwet, B. Interactions between bioadhesive poly(acrylic acid) and calciumions. *Int. J.*

Pharm. **127,** 135–145 (1996).

233. Rao PS, K. S. Tamarind seed polysaccharide. *Curr Sci* **16,** 256 (1947).

234. Gidley, M. J. *et al.* Structure and solution properties of tamarind-seed polysaccharide. *Carbohydr. Res.* **214,** 299–314 (1991).

235. Picout, D. R., Ross-Murphy, S. B., Errington, N. & Harding, S. E. Pressure cell assisted solubilization of xyloglucans: tamarind seed polysaccharide and detarium gum. *Biomacromolecules* **4,** 799–807 (2003).

236. Pardeshi, C. V., Rajput, P. V., Belgamwar, V. S. & Tekade, A. R. Formulation, optimization and evaluation of spray-dried mucoadhesive microspheres as intranasal carriers for Valsartan. *J. Microencapsul.* **29,** 103–114 (2012).

237. Bhalekar, M., Madgulkar, A., Gunjal, S. & Bagal, A. Formulation and optimisation of sustained release spray-dried microspheres of glipizide using natural polysaccharide. *PDA J. Pharm. Sci. Technol.* **67,** 146–154 (2013).

238. Aslan, N. & Cebeci, Y. Application of Box-Behnken design and response surface methodology for modeling of some Turkish coals. *Fuel* **86,** 90–97 (2007).

239. Ragonese, R., Macka, M., Hughes, J. & Petocz, P. The use of the Box-Behnken experimental design in the optimisation and robustness testing of a capillary electrophoresis method for the analysis of ethambutol hydrochloride in a pharmaceutical formulation. *J. Pharm. Biomed. Anal.* **27,** 995–1007 (2002).

240. Amin, M., Hussain, M. A., Shahwar, D. & Hussain, M. Thermal Analysis and Degradation Kinetics of Dextran and Highly Substituted Dextran Acetates. *J.Chem.Soc.Pak* **37,** (2015).

241. Katsikas, L., Jeremic, K., Jovanovic, S., Velickovic, J. S. & Popovic, I. G. The thermal degradation kinetics of dextran and pullulan. *J. Therm. Anal.* **40,** 511–517 (1993).

242. Khedr, A., Moustafa, M., Abdel-Naim, A. B., Alahdal, A. & Mosli, H. High-performance liquid chromatographic method for determination of phenytoin in rabbits receiving sildenafil. *Anal. Chem. Insights* **2008,** 61–67 (2008).

243. Sears, P. R., Yin, W.-N. & Ostrowski, L. E. Continuous mucociliary transport by primary human airway epithelial cells in vitro. *Am. J. Physiol. - Lung Cell. Mol. Physiol.* **309,** L99–L108 (2015).

244. Huang, Y. *et al.* Markers of inflammation in the breath in paediatric inflammatory bowel disease. *J. Pediatr. Gastroenterol. Nutr.* **59,** 505–510 (2014).

245. Kockisch, S., Rees, G. D., Young, S. A., Tsibouklis, J. & Smart, J. D. Polymeric microspheres for drug delivery to the oral cavity: An in vitro evaluation of mucoadhesive potential. *J. Pharm. Sci.* **92,** 1614–1623 (2003).

246. Spitzlei, M. Choosing a Method for Measuring your Material's Moisture Content. *Powder and Bulk Engineering* 1–9 (2000).

247. Willits, C. O. Methods for Determination of Moisture-Oven Drying. *Anal. Chem.* **23,** 1058–1062 (1951).

248. WHO. Stability testing of active pharmaceutical ingredients and fi nished pharmaceutical products. *WHO Technical Report Series, No. 953* 87–130 (2009). Available at: http://www.ich.org/fileadmin/Public_Web_Site/ICH_Products/Guidelines/Quality/Q1F/Stability_Guideline_WHO.pdf. (Accessed: 3rd March 2018)

249. Rubino, J. T. Solubilities and solid state properties of the sodium salts of drugs. *J. Pharm. Sci.* **78,** 485–489 (1989).

250. Samson, G. *et al.* Ex vivo study of bevacizumab transport through porcine nasal mucosa. in *European Journal of Pharmaceutics and Biopharmaceutics* **80,** 465–469 (2012).

251. Leopold, D. A. *et al.* Anterior distribution of human olfactory epithelium. *Laryngoscope* **110,** 417–421 (2000).

252. Ungaro, F., De Rosa, G., Miro, A., Quaglia, F. & La Rotonda, M. I. Cyclodextrins in the production of large porous particles: Development of dry powders for the sustained release of insulin to the lungs. *Eur. J. Pharm. Sci.* **28,** 423–432 (2006).

253. Molina, R. M. *et al.* Pulmonary distribution of nanoceria: comparison of intratracheal, microspray instillation and dry powder insufflation. *Inhal. Toxicol.* **28,** 550–560 (2016).

254. Hartman, N. R., Johns, D. G. & Mitsuya, H. Pharmacokinetic analysis of dextran sulfate in rats as pertains to its clinical usefulness for therapy of HIV infection. *AIDS Res Hum Retroviruses* **6,** 805–812 (1990).

255. Gerber, N. *et al.* Study of dose-dependent metabolism of 5,5-diphenyl-hydantoin in the rat using new methodology for isolation and quantitation of metabolites in vivo and in vitro. *J. Pharmacol. Exp. Ther.* **178,** 567–79 (1971).

256. Löscher, W. The pharmacokinetics of antiepileptic drugs in rats: Consequences for maintaining effective drug levels during prolonged drug administration in rat models of epilepsy. *Epilepsia* **48,** 1245–1258 (2007).

257. Potschka, H. & Löscher, W. In vivo evidence for P-glycoprotein-mediated transport of phenytoin at the blood-brain barrier of rats. *Epilepsia* **42,** 1231–1240 (2001).

258. Walker, M. C., Alavijeh, M. S., Shorvon, S. D. & Patsalos, P. N. Microdialysis study of the neuropharmacokinetics of phenytoin in rat hippocampus and frontal cortex. *Epilepsia* **37,** 421–427 (1996).

259. Marchi, N. *et al.* Blood-brain barrier damage and brain penetration of antiepileptic drugs: Role of serum proteins and brain edema. *Epilepsia* **50,** 664–677 (2009).

260. Zhang, J., Zhu, X., Jin, Y., Shan, W. & Huang, Y. Mechanism study of cellular uptake and tight junction opening mediated by goblet cell-specific trimethyl chitosan nanoparticles. *Mol. Pharm.* **11,** 1520–1532 (2014).

261. Croisier, F. & Jérôme, C. Chitosan-based biomaterials for tissue engineering. *Eur. Polym. J.* **49,** 780–792 (2013).

262. Kulkarni, A. D. *et al.* Xyloglucan: A functional biomacromolecule for drug delivery applications. *Int. J. Biol. Macromol.* **104,** 799–812 (2017).

263. Sumathi, S. & Ray, A. R. Release behaviour of drugs from tamarind seed polysaccharide

tablets. *J. Pharm. Pharm. Sci.* **5,** 12–18 (2002).

264. Gupta, S., Jain, S., Rao, G., Gupta, V. & Puri, R. Tamarind kernel gum: An upcoming natural polysaccharide. *Syst. Rev. Pharm.* **1,** 50 (2010).

265. FDA. GRAS Notices. (2018). Available at: https://www.accessdata.fda.gov/scripts/fdcc/?set=GRASNotices&sort=GRN_No&order=DESC&startrow=1&type=basic&search=tamarind.

266. Jacobi, C., Kruse, F. E. & Cursiefen, C. Prospective, Randomized, Controlled Comparison of SYSTANE UD ® Eye Drops Versus VISINE INTENSIV 1% EDO ® Eye Drops for the Treatment of Moderate Dry Eye. *J. Ocul. Pharmacol. Ther.* **28,** 598–603 (2012).

267. Savur, G. R. & Sreenivasan, A. Isolation and characterization of tamarind seed (Tamarindus indica L.) polysaccharide. *J. Biol. Chem.* **172,** 501–509 (1948).

268. Kaur, H., Yadav, S., Ahuja, M. & Dilbaghi, N. Synthesis, characterization and evaluation of thiolated tamarind seed polysaccharide as a mucoadhesive polymer. *Carbohydr. Polym.* **90,** 1543–1549 (2012).

269. Edwards, M., Dea, I. C. M., Bulpin, P. V. & Reid, J. S. G. Purification and properties of a novel xyloglucan-specific endo-(1→4)-β-D-glucanase from germinated nasturtium seeds (Tropaeolum majus L.). *J. Biol. Chem.* **261,** 9489–9494 (1986).

270. York, W. S., van Halbeek, H., Darvill, A. G. & Albersheim, P. Structural analysis of xyloglucan oligosaccharides by1H-n.m.r. spectroscopy and fast-atom-bombardment mass spectrometry. *Carbohydr. Res.* **200,** 9–31 (1990).

271. Fry, S. C. The structure and functions of xyloglucan. *Journal of Experimental Botany* **40,** 1–11 (1989).

272. Kochumalayil, J. J. & Berglund, L. A. Water-soluble hemicelluloses for high humidity applications – enzymatic modification of xyloglucan for mechanical and oxygen barrier properties. *Green Chem.* **16,** 1904–1910 (2014).

273. Buckeridge, M. S., Rocha, D. C., Reid, J. S. G. & Dietrich, S. M. C. Xyloglucan structure and post-germinative metabolism in seeds of Copaifera langsdorfii from savanna and forest populations. *Physiol. Plant.* **86,** 145–151 (1992).

274. Morris, E. R., Cutler, A. N., Ross-Murphy, S. B., Rees, D. A. & Price, J. Concentration and shear rate dependence of viscosity in random coil polysaccharide solutions. *Carbohydr. Polym.* **1,** 5–21 (1981).

275. Kumar, A., Garg, T., Sarma, G. S., Rath, G. & Goyal, A. K. Optimization of combinational intranasal drug delivery system for the management of migraine by using statistical design. *Eur. J. Pharm. Sci.* **70,** 140–151 (2015).

276. Madgulkar, A. R., Bhalekar, M. R., Asgaonkar, K. D. & Dikpati, A. A. Synthesis and characterization of a novel mucoadhesive derivative of xyloglucan. *Carbohydr. Polym.* **135,** 356–362 (2016).

277. Ghelardi, E. *et al.* Effect of a novel mucoadhesive polysaccharide obtained from tamarind seeds on the intraocular penetration of gentamicin and ofloxacin in rabbits. *J. Antimicrob. Chemother.* **46,** 831–834 (2000).

278. Burgalassi, S., Chetoni, P., Panichi, L., Boldrini, E. & Saettone, M. F. Xyloglucan as a novel vehicle for timolol: pharmacokinetics and pressure lowering activity in rabbits. *J. Ocul. Pharmacol. Ther.* **16,** 497–509 (2000).

279. Di Colo, G., Zambito, Y., Zaino, C. & Sanso, M. Selected polysaccharides at comparison for their mucoadhesiveness and effect on precorneal residence of different drugs in the rabbit model. *Drug Dev. Ind. Pharm.* **35,** 941–949 (2009).

280. Uccello-Barretta, G. *et al.* Synergistic interaction between TS-polysaccharide and hyaluronic acid: implications in the formulation of eye drops. *Int. J. Pharm.* **395,** 122–131 (2010).

281. Ghelardi, E. *et al.* A mucoadhesive polymer extracted from tamarind seed improves the intraocular penetration and efficacy of rufloxacin in topical treatment of experimental bacterial keratitis. *Antimicrob. Agents Chemother.* **48,** 3396–3401 (2004).

282. Burgalassi, S. *et al.* Rufloxacin eyedrops: effect of different formulations on ocular pharmacokinetics in rabbits. *Eur. J. Ophthalmol.* **16,** 311–317 (2006).

283. Miyazaki, S. *et al.* Thermally reversible xyloglucan gels as vehicles for rectal drug delivery. *J. Control. Release* **56,** 75–83 (1998).

284. Miyazaki, S. *et al.* In situ gelling xyloglucan formulations for sustained release ocular delivery of pilocarpine hydrochloride. *Int. J. Pharm.* **229,** 29–36 (2001).

285. Takahashi, A. *et al.* Percutaneous absorption of non-steroidal anti-inflammatory drugs from in situ gelling xyloglucan formulations in rats. *Int. J. Pharm.* **246,** 179–186 (2002).

286. Suisha, F. *et al.* Xyloglucan gels as sustained release vehicles for the intraperitoneal administration of mitomycin C. *Int. J. Pharm.* **172,** 27–32 (1998).

287. Kawasaki, N. *et al.* Thermally reversible xyloglucan gels as vehicles for oral drug delivery. *Int. J. Pharm.* **181,** 227–234 (1999).

288. Miyazaki, S., Kawasaki, N., Kubo, W., Endo, K. & Attwood, D. Comparison of in situ gelling formulations for the oral delivery of cimetidine. *Int. J. Pharm.* **220,** 161–168 (2001).

289. Pandit, A. P., Pol, V. V & Kulkarni, V. S. Xyloglucan Based In Situ Gel of Lidocaine HCl for the Treatment of Periodontosis. *J. Pharm.* **2016,** 3054321 (2016).

290. Ghosh, S. & Pal, S. Modified tamarind kernel polysaccharide: a novel matrix for control release of aspirin. *Int. J. Biol. Macromol.* **58,** 296–300 (2013).

291. Jana, S., Sen, K. K. & Basu, S. K. In vitro aceclofenac release from IPN matrix tablets composed of chitosan-tamarind seed polysaccharide. *Int. J. Biol. Macromol.* **65,** 241–245 (2014).

292. Razavi, M., Nyamathulla, S., Karimian, H., Moghadamtousi, S. Z. & Noordin, M. I. Hydrogel polysaccharides of tamarind and xanthan to formulate hydrodynamically balanced matrix tablets of famotidine. *Molecules* **19,** 13909–13931 (2014).

293. Razavi, M. *et al.* Gamma scintigraphic study of the hydrodynamically balanced matrix tablets of Metformin HCl in rabbits. *Drug Des. Devel. Ther.* **9,** 3125–3139 (2015).

294. Bhalekar, M. R., Bargaje, R. V, Upadhaya, P. G., Madgulkar, A. R. & Kshirsagar, S. J.

Formulation of mucoadhesive gastric retentive drug delivery using thiolated xyloglucan. *Carbohydr. Polym.* **136,** 537–542 (2016).

295. Priyadarshini, R. *et al.* Gastroretentive extended release of metformin from methacrylamide-g-gellan and tamarind seed gum composite matrix. *Carbohydr. Polym.* **137,** 100–110 (2016).

296. Rajab, M., Tounsi, A., Jouma, M., Neubert, R. H. H. & Dittgen, M. Influence of tamarind seed gum derivatives on the in vitro performance of gastro-retentive tablets based on hydroxypropylmethylcellulose. *Pharmazie* **67,** 956–957 (2012).

297. Badillo, N. & Ghaly, E. S. In vitro evaluation of theophylline matrices using xyloglucan. *Pharm. Dev. Technol.* **13,** 481–486 (2008).

298. Kulkarni, G. T., Gowthamarajan, K., Dhobe, R. R., Yohanan, F. & Suresh, B. Development of controlled release spheroids using natural polysaccharide as release modifier. *Drug Deliv.* **12,** 201–206 (2005).

299. Nayak, A. K. & Pal, D. Development of pH-sensitive tamarind seed polysaccharide-alginate composite beads for controlled diclofenac sodium delivery using response surface methodology. *Int. J. Biol. Macromol.* **49,** 784–793 (2011).

300. Pal, D. & Nayak, A. K. Novel tamarind seed polysaccharide-alginate mucoadhesive microspheres for oral gliclazide delivery: in vitro-in vivo evaluation. *Drug Deliv.* **19,** 123–131 (2012).

301. Kulkarni, R. V, Mutalik, S., Mangond, B. S. & Nayak, U. Y. Novel interpenetrated polymer network microbeads of natural polysaccharides for modified release of water soluble drug: in-vitro and in-vivo evaluation. *J. Pharm. Pharmacol.* **64,** 530–540 (2012).

302. Nayak, A. K., Pal, D. & Santra, K. Development of calcium pectinate-tamarind seed polysaccharide mucoadhesive beads containing metformin HCl. *Carbohydr. Polym.* **101,** 220–230 (2014).

303. Nayak, A. K., Pal, D. & Santra, K. Swelling and drug release behavior of metformin HCl-loaded tamarind seed polysaccharide-alginate beads. *Int. J. Biol. Macromol.* **82,** 1023–1027 (2016).

304. Nayak, A. K., Pal, D. & Santra, K. Tamarind seed polysaccharide-gellan mucoadhesive beads for controlled release of metformin HCl. *Carbohydr. Polym.* **103,** 154–163 (2014).

305. Jana, S., Saha, A., Nayak, A. K., Sen, K. K. & Basu, S. K. Aceclofenac-loaded chitosan-tamarind seed polysaccharide interpenetrating polymeric network microparticles. *Colloids Surf. B. Biointerfaces* **105,** 303–309 (2013).

306. Mahajan, H. S. & Gundare, S. A. Preparation, characterization and pulmonary pharmacokinetics of xyloglucan microspheres as dry powder inhalation. *Carbohydr. Polym.* **102,** 529–536 (2014).

307. Avachat, A. M., Gujar, K. N. & Wagh, K. V. Development and evaluation of tamarind seed xyloglucan-based mucoadhesive buccal films of rizatriptan benzoate. *Carbohydr. Polym.* **91,** 537–542 (2013).

308. Bassi, P. & Kaur, G. Polymeric films as a promising carrier for bioadhesive drug delivery: Development, characterization and optimization. *Saudi Pharm. J. SPJ Off. Publ. Saudi*

Pharm. Soc. **25,** 32–43 (2017).

309. Kulkarni, G. T., Sethi, N., Awasthi, R., Pawar, V. K. & Pahuja, V. Development of Ocular Delivery System for Glaucoma Therapy Using Natural Hydrogel as Film Forming Agent and Release Modifier. *Polim. Med.* **46,** 25–33 (2016).

310. Mahajan, H. S. & Deshmukh, S. R. Development and evaluation of gel-forming ocular films based on xyloglucan. *Carbohydr. Polym.* **122,** 243–247 (2015).

311. Dilbaghi, N., Kaur, H., Ahuja, M. & Kumar, S. Evaluation of tropicamide-loaded tamarind seed xyloglucan nanoaggregates for ophthalmic delivery. *Carbohydr. Polym.* **94,** 286–291 (2013).

312. Joseph, M. M., G, A., T K, M. & T T, S. Galactoxyloglucan-doxorubicin nanoparticles exerts superior cytotoxic effects on cancer cells-A mechanistic and in silico approach. *Int. J. Biol. Macromol.* **92,** 20–29 (2016).

313. Chen, D. *et al.* Properties of xyloglucan hydrogel as the biomedical sustained-release carriers. *J. Mater. Sci. Mater. Med.* **23,** 955–962 (2012).

314. Hirun, N., Tantishaiyakul, V. & Pichayakorn, W. Effect of Eriochrome Black T on the gelatinization of xyloglucan investigated using rheological measurement and release behavior of Eriochrome Black T from xyloglucan gel matrices. *Int. J. Pharm.* **388,** 196–201 (2010).

315. Ghosh, S., Sen, G., Jha, U. & Pal, S. Novel biodegradable polymeric flocculant based on polyacrylamide-grafted tamarind kernel polysaccharide. *Bioresour. Technol.* **101,** 9638–9644 (2010).

316. Shailaja, T., Latha, K., Sasibhushan, P., Alkabab, A. M. & Uhumwangho, M. U. A novel bioadhesive polymer: Grafting of tamarind seed polysaccharide and evaluation of its use in buccal delivery of metoprolol succinate. *Der Pharm. Lett.* **4,** 487–508 (2012).

317. Mazzarino, L. *et al.* Xyloglucan-block-poly(ε-caprolactone) copolymer nanoparticles coated with chitosan as biocompatible mucoadhesive drug delivery system. *Macromol. Biosci.* **14,** 709–719 (2014).

318. Mazzarino, L. *et al.* Nanoparticles made from xyloglucan-block-polycaprolactone copolymers: Safety assessment for drug delivery. *Toxicol. Sci.* **147,** 104–115 (2015).

319. Mahajan, H. S. & Mahajan, P. R. Development of grafted xyloglucan micelles for pulmonary delivery of curcumin: In vitro and in vivo studies. *Int. J. Biol. Macromol.* **82,** 621–627 (2016).

320. Madgulkar, A., Bhalekar, M. R. & Dikpati, A. A. Improving oral bioavailability of acyclovir using nanoparticulates of thiolated xyloglucan. *Int. J. Biol. Macromol.* **89,** 689–699 (2016).

321. Kaur, H., Ahuja, M., Kumar, S. & Dilbaghi, N. Carboxymethyl tamarind kernel polysaccharide nanoparticles for ophthalmic drug delivery. *Int. J. Biol. Macromol.* **50,** 833–839 (2012).

322. PATENT, Del, P. A. & Sanso, M. Ophthalmic compositions based on tamarind seed polysaccharide and hyaluronic acid. (2011).

323. Rana, V., Sharma, R., Kamboj, S., Singh, K. & Suresh, S. A lubricant formulation of carbamoylethyl katira and a process for preparation thereof. (2017).

324. PATENT, Giori, A., Arpini, S. & Togni, S. Tamarind seed polysaccharide for use in the treatment of inflammatory diseases. (2011).

325. PATENT & Pauly, G. Use of at least one protein extract of the moringa genus plant seeds and corresponding cosmetic and/or pharmacological composition. (2002).

326. Burgalassi, S. *et al.* Effect of xyloglucan (tamarind seed polysaccharide) on conjunctival cell adhesion to laminin and on corneal epithelium wound healing. *Eur. J. Ophthalmol.* **10,** 71–76 (2000).

327. Joseph, M. M. *et al.* Antitumor activity of galactoxyloglucan-gold nanoparticles against murine ascites and solid carcinoma. *Colloids Surf. B. Biointerfaces* **116,** 219–227 (2014).

328. Joseph, M. M., Aravind, S. R., Varghese, S., Mini, S. & Sreelekha, T. T. PST-Gold nanoparticle as an effective anticancer agent with immunomodulatory properties. *Colloids Surf. B. Biointerfaces* **104,** 32–39 (2013).

329. Aravind, S. R., Joseph, M. M., Varghese, S., Balaram, P. & Sreelekha, T. T. Antitumor and immunopotentiating activity of polysaccharide PST001 isolated from the seed kernel of Tamarindus indica: an in vivo study in mice. *ScientificWorldJournal.* **2012,** 361382 (2012).

330. Lim, S. H. & Lee, J. Xyloglucan intake attenuates myocardial injury by inhibiting apoptosis and improving energy metabolism in a rat model of myocardial infarction. *Nutr. Res.* **45,** 19–29 (2017).

331. do Rosario, M. M. T., Noleto, G. R. & de Oliveira Petkowicz, C. L. Degalactosylation of xyloglucans modify their pro-inflammatory properties on murine peritoneal macrophages. *Int. J. Biol. Macromol.* **105,** 533–540 (2017).

332. PATENT, Melloni, E. & Sardina, M. Polysaccharide polymer from the seeds of the tamarind tree for use in treating dry cough. (2015).

333. Rolando, M. & Valente, C. Establishing the tolerability and performance of tamarind seed polysaccharide (TSP) in treating dry eye syndrome: results of a clinical study. *BMC Ophthalmol.* **7,** 5 (2007).

334. Mahajan, H. S., Tyagi, V., Lohiya, G. & Nerkar, P. Thermally reversible xyloglucan gels as vehicles for nasal drug delivery. *Drug Deliv.* **19,** 270–276 (2012).

335. Davis, M. & Walker, G. Recent strategies in spray drying for the enhanced bioavailability of poorly water-soluble drugs. *J. Control. Release* **269,** 110–127 (2018).

336. PATENT & Percy, S. R. Improvement in drying and concentrating liquid substances by atomizing. (1872).

337. Cal, K. & Sollohub, K. Spray drying technique. I: Hardware and process parameters. *Journal of Pharmaceutical Sciences* **99,** 575–586 (2010).

338. Schafroth, D. C. A. & Nina, D. Spray dried biodegradable polymers as target material for controlled drug deliver. *best@buchi information bulletin 46 / 2007* (2007).

339. Vehring, R. Pharmaceutical particle engineering via spray drying. *Pharmaceutical Research* **25,** 999–1022 (2008).

340. Gharsallaoui, A., Roudaut, G., Chambin, O., Voilley, A. & Saurel, R. Applications of spray-drying in microencapsulation of food ingredients : an overview . Food Res Int Applications of spray-drying in microencapsulation of food ingredients : An overview. *Food Res. Int.* **40,** 1107–1121 (2007).

341. Tewa-Tagne, P., Briançon, S. & Fessi, H. Spray-dried microparticles containing polymeric nanocapsules: Formulation aspects, liquid phase interactions and particles characteristics. *Int. J. Pharm.* **325,** 63–74 (2006).

342. Gong, P. *et al.* Injury Mechanisms of Lactic Acid Bacteria Starter Cultures During Spray Drying: A Review. *Dry. Technol.* **32,** 793–800 (2014).

343. Tshweu, L., Katata, L., Kalombo, L. & Swai, H. Nanoencapsulation of water-soluble drug, lamivudine, using a double emulsion spray-drying technique for improving HIV treatment. *J. Nanoparticle Res.* **15,** (2013).

344. Lane, M. E., Brennan, F. S. & Corrigan, O. I. Comparison of post-emulsification freeze drying or spray drying processes for the microencapsulation of plasmid DNA. *J. Pharm. Pharmacol.* **57,** 831–8 (2005).

345. Sosnik, A. & Seremeta, K. P. Advantages and challenges of the spray-drying technology for the production of pure drug particles and drug-loaded polymeric carriers. *Adv. Colloid Interface Sci.* **223,** 40–54 (2015).

346. Maury, M., Murphy, K., Kumar, S., Shi, L. & Lee, G. Effects of process variables on the powder yield of spray-dried trehalose on a laboratory spray-dryer. *Eur. J. Pharm. Biopharm.* **59,** 565–573 (2005).

347. Elmowafy, E., Osman, R., El-Shamy, A. H. ameed & Awad, G. A. s. Nanocomplexes of an insulinotropic drug: optimization, microparticle formation, and antidiabetic activity in rats. *Int. J. Nanomedicine* **9,** 4449–4465 (2014).

348. Andrade, F. *et al.* Nanotechnology and pulmonary delivery to overcome resistance in infectious diseases. *Advanced Drug Delivery Reviews* **65,** 1816–1827 (2013).

349. Ståhl, K., Claesson, M., Lilliehorn, P., Lindén, H. & Bäckström, K. The effect of process variables on the degradation and physical properties of spray dried insulin intended for inhalation. *Int. J. Pharm.* **233,** 227–237 (2002).

350. Kincl, M., Turk, S. & Vrečer, F. Application of experimental design methodology in development and optimization of drug release method. in *International Journal of Pharmaceutics* **291,** 39–49 (2005).

351. Brandl, F. *et al.* Hydrogel-based drug delivery systems: Comparison of drug diffusivity and release kinetics. *J. Control. Release* **142,** 221–228 (2010).

352. Li, J. *et al.* Self-assembled supramolecular hydrogels formed by biodegradable PEO-PHB-PEO triblock copolymers and α-cyclodextrin for controlled drug delivery. *Biomaterials* **27,** 4132–4140 (2006).

353. Junginger, H. E., Hoogstraate, J. A. & Verhoef, J. C. Recent advances in buccal drug delivery and absorption--in vitro and in vivo studies. *J. Control. Release* **62,** 149–159 (1999).

354. Dimler, R. J., Wolff, I. A., Sloan, J. W. & Rist, C. E. Interpretation of Periodate Oxidation

Data on Degraded Dextran. *J. Am. Chem. Soc.* **77,** 6568–6573 (1955).

355. Chawananorasest, K., Saengtongdee, P. & Kaemchantuek, P. Extraction and characterization of Tamarind (Tamarind indica L.) Seed Polysaccharides (TSP) from three difference sources. *Molecules* **21,** (2016).

356. Nayak, A. kumar & Pal, D. Functionalization of Tamarind Gum for Drug Delivery. in *Functional Biopolymers* (eds. Thakur, V. K. & Thakur, M. K.) 44–45 (Springer International Publishing, 2018). doi:10.1007/978-3-319-66417-0

357. Wadell, C., Björk, E. & Camber, O. Permeability of porcine nasal mucosa correlated with human nasal absorption. *Eur. J. Pharm. Sci.* **18,** 47–53 (2003).

358. Asai, K. *et al.* The effects of water-soluble cyclodextrins on the histological integrity of the rat nasal mucosa. *Int. J. Pharm.* **246,** 25–35 (2002).

359. Tas, C. *et al.* Nasal absorption of metoclopramide from different Carbopoll® 981 based formulations: In vitro, ex vivo and in vivo evaluation. *Eur. J. Pharm. Biopharm.* **64,** 246–254 (2006).

360. Ellis, P. R. & Morris, E. R. Importance of the Rate of Hydration of Pharmaceutical Preparations of Guar Gum; a New In Vitro Monitoring Method. *Diabet. Med.* **8,** 378–381 (1991).

361. Ellis, P. R., Dawoud, F. M. & Morris, E. R. Blood glucose, plasma insulin and sensory responses to guar-containing wheat breads: effects of molecular weight and particle size of guar gum. *Br. J. Nutr.* **66,** 363–379 (1991).

362. I Ré, M. Microencapsulation by spray drying. *Dry. Technol.* **16,** 1195–1236 (1998).

363. Chew, N. Y. K., Tang, P., Chan, H. K. & Raper, J. A. How much particle surface corrugation is sufficient to improve aerosol performance of powders? *Pharm. Res.* **22,** 148–152 (2005).

364. Chew, N. Y. K. & Chan, H. K. Use of solid corrugated particles to enhance powder aerosol performance. *Pharm. Res.* **18,** 1570–1577 (2001).

365. Kulkarni, A. D., Bari, D. B., Surana, S. J. & Pardeshi, C. V. In vitro, ex vivo and in vivo performance of chitosan-based spray-dried nasal mucoadhesive microspheres of diltiazem hydrochloride. *J. Drug Deliv. Sci. Technol.* **31,** 108–117 (2016).

366. Mortazavi, S. A. & Smart, J. D. An investigation of some factors influencing the in vitro assessment of mucoadhesion. *Int. J. Pharm.* **116,** 223–230 (1995).

367. Agarwal, S. & Murthy, R. S. R. Effect of Different Polymer Concentration on Drug Release Rate and Physicochemical Properties of Mucoadhesive Gastroretentive Tablets. *Indian J. Pharm. Sci.* **77,** 705–14 (2015).

368. Kim, S. W., Bae, Y. H. & Okano, T. Hydrogels: Swelling, Drug Loading, and Release. *Pharm. Res.* **9,** 283–290 (1992).

369. Chaturvedi, M., Kumar, M. & Pathak, K. A review on mucoadhesive polymer used in nasal drug delivery system. *J. Adv. Pharm. Technol. Res.* **2,** 215 (2011).

370. Matsukawa, Y., Lee, V. H., Crandall, E. D. & Kim, K. J. Size-dependent dextran transport

across rat alveolar epithelial cell monolayers. *Journal of pharmaceutical sciences* **86,** 305–309 (1997).

371. Sakane, T. *et al.* Direct Drug Transport from the Rat Nasal Cavity to the Cerebrospinal Fluid: the Relation to the Molecular Weight of Drugs. *J. Pharm. Pharmacol.* **47,** 379–381 (1995).

372. Ngugi, A. K., Bottomley, C., Kleinschmidt, I., Sander, J. W. & Newton, C. R. Estimation of the burden of active and life-time epilepsy: A meta-analytic approach. *Epilepsia* **51,** 883–890 (2010).

373. Ngugi, A. K. *et al.* Incidence of epilepsy: A systematic review and meta-analysis. *Neurology* **77,** 1005–1012 (2011).

374. Mohanraj, R. & Brodie, M. J. Early predictors of outcome in newly diagnosed epilepsy. *Seizure* **22,** 333–344 (2013).

375. Tang, F., Hartz, A. M. S. & Bauer, B. Drug-resistant epilepsy: Multiple hypotheses, few answers. *Frontiers in Neurology* **8,** (2017).

376. Sisodiya, S. M., Lin, W. R., Harding, B. N., Squier, M. V & Thom, M. Drug resistance in epilepsy: expression of drug resistance proteins in common causes of refractory epilepsy. *Brain* **125,** 22–31 (2002).

377. Aronica, E. *et al.* Expression and cellular distribution of multidrug transporter proteins in two major causes of medically intractable epilepsy: Focal cortical dysplasia and glioneuronal tumors. *Neuroscience* **118,** 417–429 (2003).

378. Van Dycke, A., Raedt, R., Vonck, K. & Boon, P. Local delivery strategies in epilepsy; A focus on adenosine. *Seizure* **20,** 376–382 (2011).

379. Kwan, P., Schachter, S. C. & Brodie, M. J. Drug-Resistant Epilepsy. *N. Engl. J. Med.* **365,** 919–926 (2011).

380. Luna-Tortós, C., Fedrowitz, M. & Löscher, W. Several major antiepileptic drugs are substrates for human P-glycoprotein. *Neuropharmacology* **55,** 1364–1375 (2008).

381. Löscher, W. & Potschka, H. Drug resistance in brain diseases and the role of drug efflux transporters. *Nat. Rev. Neurosci.* **6,** 591–602 (2005).

382. Van Vliet, E. A. *et al.* Inhibition of the multidrug transporter P-glycoprotein improves seizure control in phenytoin-treated chronic epileptic rats. *Epilepsia* **47,** 672–680 (2006).

383. Callaghan, R., Luk, F. & Bebawy, M. Inhibition of the multidrug resistance P-glycoprotein: Time for a change of strategy? *Drug Metabolism and Disposition* **42,** 623–631 (2014).

384. DiMeco, F. *et al.* Local delivery of mitoxantrone for the treatment of malignant brain tumors in rats. *J. Neurosurg.* **97,** 1173–8 (2002).

385. Lu, C.-T. *et al.* Current approaches to enhance CNS delivery of drugs across the brain barriers. *Int. J. Nanomedicine* **9,** 2241–57 (2014).

386. Bialer, M. *et al.* Progress report on new antiepileptic drugs: A summary of the Twelfth Eilat Conference (EILAT XII). *Epilepsy Res.* **111,** 85–141 (2015).

387. Klein, P. *et al.* A randomized, double-blind, placebo-controlled, multicenter, parallel-group study to evaluate the efficacy and safety of adjunctive brivaracetam in adult patients with uncontrolled partial-onset seizures. *Epilepsia* **56,** 1890–1898 (2015).

388. Thakker, A. & Shanbag, P. A randomized controlled trial of intranasal-midazolam versus intravenous-diazepam for acute childhood seizures. *J. Neurol.* **260,** 470–474 (2013).

389. Mahmoudian, T. & Mohammad, M. Z. Comparison of intranasal midazolam with intravenous diazepam for treating acute seizures in children. *Epilepsy Behav.* **5,** 253–255 (2004).

390. Serralheiro, A., Alves, G., Fortuna, A. & Falcão, A. Direct nose-to-brain delivery of lamotrigine following intranasal administration to mice. *Int. J. Pharm.* **490,** 39–46 (2015).

391. Florence, K. *et al.* Intranasal clobazam delivery in the treatment of status epilepticus. *J. Pharm. Sci.* **100,** 692–703 (2011).

392. Wermeling, D. P. H., Miller, J. L., Archer, S. M., Manaligod, J. M. & Rudy, A. C. Bioavailability and pharmacokinetics of lorazepam after intranasal, intravenous, and intramuscular administration. *J. Clin. Pharmacol.* **41,** 1225–1231 (2001).

393. Jain, A. S., Date, A. A., Pissurlenkar, R. R. S., Coutinho, E. C. & Nagarsenker, M. S. Sulfobutyl Ether7 β-Cyclodextrin (SBE7 β-CD) Carbamazepine Complex: Preparation, Characterization, Molecular Modeling, and Evaluation of In Vivo Anti-epileptic Activity. *AAPS PharmSciTech* **12,** 1163–1175 (2011).

394. Tsuruoka, M. *et al.* Enhanced bioavailability of phenytoin by beta-cyclodextrin complexation. *J. Pharm. Soc. Japan* **101,** 360–367 (1981).

395. Widanapathirana, L., Tale, S. & Reineke, T. M. Dissolution and Solubility Enhancement of the Highly Lipophilic Drug Phenytoin via Interaction with Poly(N-isopropylacrylamide-co-vinylpyrrolidone) Excipients. *Mol. Pharm.* **12,** 2537–2543 (2015).

396. Yakou, S., Yamazaki, S., Sugihara, M., Sonobe, T. & Nagai, T. Dissolution and Bioavailability of Phenytoin in Phenytoin-Polyvinylpyrrolidone-Sodium Deoxycholate Coprecipitate. *Chem. Pharm. Bull.* **34,** (1986).

397. Afifi, S. Solid dispersion approach improving dissolution rate of Stiripentol: A novel antiepileptic drug. *Iran. J. Pharm. Res.* **14,** 1001–1014 (2015).

398. Sethia, S. & Squillante, E. Solid dispersion of carbamazepine in PVP K30 by conventional solvent evaporation and supercritical methods. *Int. J. Pharm.* **272,** 1–10 (2004).

399. Sethia, S. & Squillante, E. Physicochemical characterization of solid dispersions of carbamazepine formulated by supercritical carbon dioxide and conventional solvent evaporation method. *J. Pharm. Sci.* **91,** 1948–1957 (2002).

400. Moneghini, M., Kikic, I., Voinovich, D., Perissutti, B. & Filipović-Grcić, J. Processing of carbamazepine-PEG 4000 solid dispersions with supercritical carbon dioxide: preparation, characterisation, and in vitro dissolution. *Int. J. Pharm.* **222,** 129–138 (2001).

401. Douroumis, D., Bouropoulos, N. & Fahr, A. Physicochemical characterization of solid dispersions of three antiepileptic drugs prepared by solvent evaporation method. *J. Pharm. Pharmacol.* **59,** 645–653 (2007).

402. Franco, M. *et al.* Dissolution properties and anticonvulsant activity of phenytoin-polyethylene glycol 6000 and -polyvinylpyrrolidone K-30 solid dispersions. *Int. J. Pharm.* **225,** 63–73 (2001).

403. Jabir, N. *et al.* A Synopsis of Nano-Technological Approaches Toward Anti-Epilepsy Therapy: Present and Future Research Implications. *Curr. Drug Metab.* **16,** 336–345 (2015).

404. Thakur, R. & Gupta, R. B. Formation of phenytoin nanoparticles using rapid expansion of supercritical solution with solid cosolvent (RESS-SC) process. *Int. J. Pharm.* **308,** 190–199 (2006).

405. Wilson, B., Lavanya, Y., Priyadarshini, S. R. B., Ramasamy, M. & Jenita, J. L. Albumin nanoparticles for the delivery of gabapentin: Preparation, characterization and pharmacodynamic studies. *Int. J. Pharm.* **473,** 73–79 (2014).

406. Leyva-Gõmez, G. *et al.* Nanoparticle formulation improves the anticonvulsant effect of clonazepam on the pentylenetetrazole-induced seizures: Behavior and electroencephalogram. *J. Pharm. Sci.* **103,** 2509–2519 (2014).

407. Ying, X. *et al.* Angiopep-conjugated electro-responsive hydrogel nanoparticles: Therapeutic potential for epilepsy. *Angew. Chemie - Int. Ed.* **53,** 12436–12440 (2014).

408. Wang, Y. *et al.* Electroresponsive Nanoparticles Improve Antiseizure Effect of Phenytoin in Generalized Tonic-Clonic Seizures. *Neurotherapeutics* **13,** 603–613 (2016).

409. Eskandari, S., Varshosaz, J., Minaiyan, M. & Tabbakhian, M. Brain delivery of valproic acid via intranasal administration of nanostructured lipid carriers: in vivo pharmacodynamic studies using rat electroshock model. *Int. J. Nanomedicine* **6,** 363–371 (2011).

410. Sharma, D. *et al.* Formulation and optimization of polymeric nanoparticles for intranasal delivery of lorazepam using Box-Behnken design: In vitro and in vivo evaluation. *Biomed Res. Int.* **2014,** (2014).

411. Vyas, T. K., Babbar, A. K., Sharma, R. K., Singh, S. & Misra, A. Intranasal mucoadhesive microemulsions of clonazepam: Preliminary studies on brain targeting. *J. Pharm. Sci.* **95,** 570–580 (2006).

412. Li, Z. *et al.* Formulation of spray-dried phenytoin loaded poly(ε-caprolactone) microcarrier intended for brain delivery to treat epilepsy. *J. Pharm. Sci.* **96,** 1018–1030 (2007).

413. Cekić, N. D. *et al.* Preparation and characterisation of phenytoin-loaded alginate and alginate-chitosan microparticles. *Drug Deliv.* **14,** 483–490 (2007).

414. Schmidt, D. & Löscher, W. Drug resistance in epilepsy: Putative neurobiologic and clinical mechanisms. *Epilepsia* **46,** 858–877 (2005).

415. Keppel Hesselink, J. M. & Kopsky, D. J. Phenytoin: neuroprotection or neurotoxicity? *Neurological Sciences* **38,** 1137–1141 (2017).

416. Dyląg, T. *et al.* Synthesis and evaluation of in vivo activity of diphenylhydantoin basic derivatives. *Eur. J. Med. Chem.* **39,** 1013–1027 (2004).

417. Raftopoulos, R. *et al.* Phenytoin for neuroprotection in patients with acute optic neuritis: a randomised, placebo-controlled, phase 2 trial. *Lancet Neurol.* **15,** 259–269 (2016).

418. Zeng, Z. *et al.* Effect of phenytoin on sodium conductances in rat hippocampal CA1 pyramidal neurons. *J. Neurophysiol.* **116,** 1924–1936 (2016).

419. Rogawski, M. A. & Löscher, W. The neurobiology of antiepileptic drugs. *Nat. Rev. Neurosci.* **5,** 553–564 (2004).

420. Stella, V. J. A case for prodrugs: Fosphenytoin. *Advanced Drug Delivery Reviews* **19,** 311–330 (1996).

421. Stella, V. J., Martodihardjo, S. & Rao, V. M. Aqueous solubility and dissolution rate does not adequately predict in vivo performance: A probe utilizing some N-acyloxymethyl phenytoin prodrugs. *J. Pharm. Sci.* **88,** 775–779 (1999).

422. Antunes Viegas, D. *et al.* Development and application of an ex vivo fosphenytoin nasal bioconversion/permeability evaluation method. *Eur. J. Pharm. Sci.* **89,** 61–72 (2016).

423. Chollet, D. F. Determination of antiepileptic drugs in biological material. *Journal of Chromatography B: Analytical Technology in the Biomedical and Life Sciences* **767,** 191–233 (2002).

424. Sekikawa, H., Fujiwara, J., Naganuma, T., Nakano, M. & Arita, T. Dissolution Behaviors and Gastrointestinal Absorption of Phenytoin in Phenytoin-Polyvinylpyrrolidone Coprecipitate. *Chem. Pharm. Bull. (Tokyo).* **26,** 3033–3039 (1978).

425. Elversson, J. & Millqvist-Fureby, A. Particle size and density in spray drying-effects of carbohydrate properties. *J. Pharm. Sci.* **94,** 2049–60 (2005).

426. Corbo, G. M. *et al.* Measurement of nasal mucociliary clearance. *Arch. Dis. Child.* **64,** 546–550 (1989).

427. FDA. Guidance for Industry Bioanalytical Method Validation. 1–27 (2013). Available at: https://www.fda.gov/downloads/Drugs/GuidanceComplianceRegulatoryInformation/Guidances/UCM368107.pdf. (Accessed: 3rd April 2018)

428. Reichel, A. The Role of Blood-Brain Barrier Studies in the Pharmaceutical Industry. *Curr. Drug Metab.* **7,** 183–203 (2006).

429. Feng, M. R. Assessment of blood-brain barrier penetration: in silico, in vitro and in vivo. *Curr. Drug Metab.* **3,** 647–57 (2002).

430. Dagenais, C., Rousselle, C., Pollack, G. M. & Scherrmann, J. M. Development of an in situ mouse brain perfusion model and its application to mdr1a P-glycoprotein-deficient mice. *J. Cereb. Blood Flow Metab.* **20,** 381–386 (2000).

431. Schafroth, N., Arpagaus, C., Jadhav, U. Y., Makne, S. & Douroumis, D. Nano and microparticle engineering of water insoluble drugs using a novel spray-drying process. *Colloids Surfaces B Biointerfaces* **90,** 8–15 (2012).

432. Kauppinen, A. *et al.* Efficient production of solid dispersions by spray drying solutions of high solid content using a 3-fluid nozzle. *Eur. J. Pharm. Biopharm.* **123,** 50–58 (2018).

433. Siepmann, J. & Peppas, N. A. Higuchi equation: Derivation, applications, use and misuse. *International Journal of Pharmaceutics* **418,** 6–12 (2011).

434. Michinori, S., Teruko, I., Hiroshi, O., Hidekazu, A. & Masaki, O. Effects of absorption enhancers on the transport of model compounds in Caco-2 cell monolayers: Assessment by confocal laser scanning microscopy. *J. Pharm. Sci.* **86,** 779–785 (2000).

435. Zipp, G. L. & Rodrfguez-Hornedo, N. Growth mechanism and morphology of phenytoin and their relationship with crystallographic structure. *J. Phys. D. Appl. Phys.* **26,** B48–B55 (1993).

436. Denayer, T., Stöhrn, T. & Van Roy, M. Animal models in translational medicine: Validation and prediction. *New Horizons Transl. Med.* **2,** 5–11 (2014).

437. Church, W. H. Column chromatography analysis of brain tissue: an advanced laboratory exercise for neuroscience majors. *J. Undergrad. Neurosci. Educ.* **3,** A36-41 (2005).

438. Fridén, M., Ljungqvist, H., Middleton, B., Bredberg, U. & Hammarlund-Udenaes, M. Improved measurement of drug exposure in the brain using drug-specific correction for residual blood. *J. Cereb. Blood Flow Metab.* **30,** 150–161 (2010).

439. Fenyk-Melody, J. E. *et al.* Comparison of the effects of perfusion in determining brain penetration (brain-to-plasma ratios) of small molecules in rats. *Comp. Med.* **54,** 378–381 (2004).

440. Andrews, G. P., Laverty, T. P. & Jones, D. S. Mucoadhesive polymeric platforms for controlled drug delivery. *European Journal of Pharmaceutics and Biopharmaceutics* **71,** 505–518 (2009).

441. Colburn, W. A. & Gibaldi, M. Plasma protein binding and metabolic clearance of phenytoin in the rat. *J Pharmacol Exp Ther* **203,** 500–506 (1977).

442. Gottlieb, S. How FDA Plans to Help Consumers Capitalize on Advances in Science. *https://blogs.fda.gov* Available at: https://blogs.fda.gov/fdavoice/index.php/2017/07/how-fda-plans-to-help-consumers-capitalize-on-advances-in-science/. (Accessed: 13th March 2018)

443. Lopez-Perez, A., Sebastian, R. & Ferrero, J. M. Three-dimensional cardiac computational modelling: methods, features and applications. *BioMedical Engineering Online* **14,** (2015).

444. Roberts, P. A., Gaffney, E. A., Luthert, P. J., Foss, A. J. E. & Byrne, H. M. Mathematical and computational models of the retina in health, development and disease. *Prog. Retin. Eye Res.* **53,** 48–69 (2016).

445. Raunio, H. In silico toxicology non-testing methods. *Front. Pharmacol.* **2,** (2011).

446. Natsch, A., Emter, R. & Ellis, G. Filling the concept with data: Integrating data from different in vitro and in silico assays on skin sensitizers to explore the battery approach for animal-free skin sensitization testing. *Toxicol. Sci.* **107,** 106–121 (2009).

447. Barbolosi, D., Ciccolini, J., Lacarelle, B., Barlési, F. & André, N. Computational oncology-mathematical modelling of drug regimens for precision medicine. *Nature Reviews Clinical Oncology* **13,** 242–254 (2016).

448. Sanga, S. *et al.* Predictive oncology: A review of multidisciplinary, multiscale in silico modeling linking phenotype, morphology and growth. *Neuroimage* **37,** (2007).

449. Hayashi, M. Three Rs in mutation research --From in vivo to in silico evaluation. *AATEX* **14,**

9–13 (2007).

450. Di Ventura, B., Lemerle, C., Michalodimitrakis, K. & Serrano, L. From in vivo to in silico biology and back. *Nature* **443,** 527–533 (2006).

451. Gerhard, F. A., Webster, D. J., van Lenthe, G. H. & Muller, R. In silico biology of bone modelling and remodelling: adaptation. *Philos. Trans. R. Soc. A Math. Phys. Eng. Sci.* **367,** 2011–2030 (2009).

452. An, G. In silico experiments of existing and hypothetical cytokine-directed clinical trials using agent-based modeling. *Critical Care Medicine* **32,** 2050–2060 (2004).

453. Peirce, S. M., Gabhann, F. Mac & Bautch, V. L. Integration of experimental and computational approaches to sprouting angiogenesis. *Current Opinion in Hematology* **19,** 184–191 (2012).

454. Weinhold, I. & Mlynski, G. Numerical simulation of airflow in the human nose. *Eur. Arch. Oto-Rhino-Laryngology* **261,** 452–455 (2004).

455. Hörschler, I., Meinke, M. & Schröder, W. Numerical simulation of the flow field in a model of the nasal cavity. *Comput. Fluids* **32,** 39–45 (2003).

456. Zamankhan, P. *et al.* Airflow and deposition of nano-particles in a human nasal cavity. *Aerosol Sci. Technol.* **40,** 463–476 (2006).

457. Shang, Y. D., Inthavong, K. & Tu, J. Y. Detailed micro-particle deposition patterns in the human nasal cavity influenced by the breathing zone. *Comput. Fluids* **114,** 141–150 (2015).

458. Karakosta, P., Alexopoulos, A. H. & Kiparissides, C. Computational model of particle deposition in the nasal cavity under steady and dynamic flow. *Comput. Methods Biomech. Biomed. Engin.* **18,** 514–526 (2015).

459. Tong, X., Dong, J., Shang, Y., Inthavong, K. & Tu, J. Effects of nasal drug delivery device and its orientation on sprayed particle deposition in a realistic human nasal cavity. *Comput. Biol. Med.* **77,** 40–48 (2016).

460. Bahmanzadeh, H., Abouali, O. & Ahmadi, G. Unsteady particle tracking of micro-particle deposition in the human nasal cavity under cyclic inspiratory flow. *J. Aerosol Sci.* **101,** 86–103 (2016).

461. Quadrio, M. *et al.* Review of computational fluid dynamics in the assessment of nasal air flow and analysis of its limitations. *European Archives of Oto-Rhino-Laryngology* **271,** 2349–2354 (2014).

462. Wen, J. *et al.* Airflow Patterns in Both Sides of a Realistic Human Nasal Cavity for Laminar and Turbulent Conditions. in *16th Australasian Fluid Mechanics Conference (AFMC)* (eds. Jacobs, P. et al.) 68–74 (School of Engineering, The University of Queensland, 2007).

463. Swift, D. L. & Proctor, D. F. Access of air to the respiratory tract. in *Respiratory Defence Mechanisms* (ed. Brain, J. D., Proctor, D. F. & Reid, L. M.) (Marcel Dekker, Inc, 1977).

464. Kim, S. K. & Chung, S. K. An investigation on airflow in disordered nasal cavity and its corrected models by tomographic PIV. *Meas. Sci. Technol.* **15,** 1090–1096 (2004).

465. Kelly, J. T., Prasad, a K. & Wexler, a S. Detailed flow patterns in the nasal cavity. *J. Appl. Physiol.* **89,** 323–337 (2000).

466. Churchill, S. E., Shackelford, L. L., Georgi, J. N. & Black, M. T. Morphological variation and airflow dynamics in the human nose. *Am. J. Hum. Biol.* **16,** 625–638 (2004).

467. Subramaniam, R. P., Richardson, R. B., Morgan, K. T., Kimbell, J. S. & Guilmette, R. A. Computational fluid dynamics simulations of inspiratory airflow in the human nose and nasopharynx. *Inhal. Toxicol.* **10,** 91–120 (1998).

468. Zhao, K., Scherer, P. W., Hajiloo, S. A. & Dalton, P. Effect of anatomy on human nasal air flow and odorant transport patterns: Implications for olfaction. *Chem. Senses* **29,** 365–379 (2004).

469. Chen, X. B., Lee, H. P., Chong, V. F. H. & De Wang, Y. Assessment of septal deviation effects on nasal air flow: A computational fluid dynamics model. *Laryngoscope* **119,** 1730–1736 (2009).

470. Lee, H. P., Poh, H. J., Chong, F. H. & Wang, D. Y. Changes of airflow pattern in inferior turbinate hypertrophy: A computational fluid dynamics model. *Am. J. Rhinol. Allergy* **23,** 153–158 (2009).

471. Garcia, G. J. M., Bailie, N., Martins, D. a & Kimbell, J. S. Atrophic rhinitis: a CFD study of air conditioning in the nasal cavity. *J. Appl. Physiol.* **103,** 1082–1092 (2007).

472. Hahn, I., Scherer, P. W. & Mozell, M. M. Velocity profiles measured for airflow through a large-scale model of the human nasal cavity. *J. Appl. Physiol.* **75,** 2273–2287 (1993).

473. Zhu, J. H., Lee, H. P., Lim, K. M., Lee, S. J. & Wang, D. Y. Evaluation and comparison of nasal airway flow patterns among three subjects from Caucasian, Chinese and Indian ethnic groups using computational fluid dynamics simulation. *Respir. Physiol. Neurobiol.* **175,** 62–69 (2011).

474. Cheng, K. H., Swift, D. L. & Yeh, H. C. Deposition of ultrafine aerosols and thoron progeny in replicas of nasal airways of young children. *Aerosol Sci. Technol.* **23,** 541–552 (1995).

475. Cheng, K. H., Cheng, Y. S., Yeh, H. C. & Swift, D. L. Deposition of ultrafine aerosols in the head airways during natural breathing and during simulated breath holding using replicate human upper airway casts. *Aerosol Sci. Technol.* **23,** 465–474 (1995).

476. Cheng, Y.-S., Yamada, Y., Yeh, H.-C. & Swift, D. L. Diffusional deposition of ultrafine aerosols in a human nasal cast. *J. Aerosol Sci.* **19,** 741–751 (1988).

477. Swift, D. L. Inspiratory Inertial Deposition of Aerosols in Human Nasal Airway Replicate Casts: Implication for the Proposed NCRP Lung Model. *Radiat. Prot. Dosimetry* **38,** 29–34 (1991).

478. Swift, D. L. *et al.* Inspiratory deposition of ultrafine particles in human nasal replicate cast. *J. Aerosol Sci.* **23,** 65–72 (1992).

479. Zwartz, G. J. & Guilmette, R. A. Effect of flow rate on particle deposition in a replica of a human nasal airway. *Inhal. Toxicol.* **13,** 109–127 (2001).

480. Cheng, Y. S. Aerosol deposition in the extrathoracic region. *Aerosol Sci. Technol.* **37,** 659–

671 (2003).

481. Kelly, J. T., Asgharian, B., Kimbell, J. S. & Wong, B. A. Particle deposition in human nasal airway replicas manufactured by different methods. Part I: Inertial regime particles. *Aerosol Sci. Technol.* **38,** 1063–1071 (2004).

482. Kelly, J. T., Asgharian, B., Kimbell, J. S. & Wong, B. A. Particle deposition in human nasal airway replicas manufactured by different methods. Part II: Ultrafine particles. *Aerosol Sci. Technol.* **38,** 1072–1079 (2004).

483. Li, X., Inthavong, K. & Tu, J. Particle inhalation and deposition in a human nasal cavity from the external surrounding environment. *Build. Environ.* **47,** 32–39 (2012).

484. Shang, Y., Dong, J., Inthavong, K. & Tu, J. Comparative numerical modeling of inhaled micron-sized particle deposition in human and rat nasal cavities. *Inhal. Toxicol.* **27,** 694–705 (2015).

485. Inthavong, K., Ge, Q., Se, C. M. K., Yang, W. & Tu, J. Y. Simulation of sprayed particle deposition in a human nasal cavity including a nasal spray device. *J. Aerosol Sci.* **42,** 100–113 (2011).

486. Inthavong, K. *et al.* A Numerical Study of Spray Particle Deposition in a Human Nasal Cavity. *Aerosol Sci. Technol.* **40,** 1034–1045 (2006).

487. Liu, Y., Matida, E. A., Gu, J. & Johnson, M. R. Numerical simulation of aerosol deposition in a 3-D human nasal cavity using RANS, RANS/EIM, and LES. *J. Aerosol Sci.* **38,** 683–700 (2007).

488. Inthavong, K., Tian, Z. F., Tu, J. Y., Yang, W. & Xue, C. Optimising nasal spray parameters for efficient drug delivery using computational fluid dynamics. *Comput. Biol. Med.* **38,** 713–726 (2008).

489. Keeler, J. A., Patki, A., Woodard, C. R. & Frank-Ito, D. O. A Computational Study of Nasal Spray Deposition Pattern in Four Ethnic Groups. *J. Aerosol Med. Pulm. Drug Deliv.* **28,** 1–14 (2015).

490. Shanley, K. T., Zamankhan, P., Ahmadi, G., Hopke, P. K. & Cheng, Y. S. Numerical simulations investigating the regional and overall deposition efficiency of the human nasal cavity. *Inhal. Toxicol.* **20,** 1093–1100 (2008).

491. Liu, Y., Matida, E. A. & Johnson, M. R. Experimental measurements and computational modeling of aerosol deposition in the Carleton-Civic standardized human nasal cavity. *J. Aerosol Sci.* **41,** 569–586 (2010).

492. Farhadi Ghalati, P. *et al.* Numerical analysis of micro- and nano-particle deposition in a realistic human upper airway. *Comput. Biol. Med.* **42,** 39–49 (2012).

493. Xi, J. *et al.* Visualization and Quantification of Nasal and Olfactory Deposition in a Sectional Adult Nasal Airway Cast. *Pharm. Res.* **33,** 1527–1541 (2016).

494. Tepper, S. J. *et al.* AVP-825 breath-powered intranasal delivery system containing 22 mg sumatriptan powder vs 100 mg oral sumatriptan in the acute treatment of migraines (The COMPASS Study): A comparative randomized clinical trial across multiple attacks. *Headache* **55,** 621–635 (2015).

495. Djupesland, P. G., Skretting, A., Winderen, M. & Holand, T. Bi-directional nasal delivery of aerosols can prevent lung deposition. *J. Aerosol Med.* **17,** 249–59 (2004).

496. Luthringer, R. *et al.* Rapid absorption of sumatriptan powder and effects on glyceryl trinitrate model of headache following intranasal delivery using a novel bi-directional device. *J. Pharm. Pharmacol.* **61,** 1219–1228 (2009).

497. Djupesland, P. G. & Dočekal, P. Intranasal sumatriptan powder delivered by a novel breath-actuated bi-directional device for the acute treatment of migraine: A randomised, placebo-controlled study. *Cephalalgia* **30,** 933–942 (2010).

498. Obaidi, M. *et al.* Improved pharmacokinetics of sumatriptan with breath powered™ nasal delivery of sumatriptan powder. *Headache* **53,** 1323–1333 (2013).

499. Vlckova, I. *et al.* Effective treatment of mild-to-moderate nasal polyposis with fluticasone delivered by a novel device. *Rhinology* **47,** 419–426 (2009).

500. Djupesland, P. G., Vlckova, I. & Hewson, G. Impact of baseline nasal polyp size and previous surgery on efficacy of fluticasone delivered with a novel device: A subgroup analysis. *Am. J. Rhinol. Allergy* **24,** 291–295 (2010).

501. Hansen, F. S., Djupesland, P. G. & Fokkens, W. J. Preliminary efficacy of fluticasone delivered by a novel device in recalcitrant chronic rhinosinusitis. *Rhinology* **48,** 292–299 (2010).

502. Djupesland, P. G., Messina, J. C. & Mahmoud, R. A. The nasal approach to delivering treatment for brain diseases: an anatomic, physiologic, and delivery technology overview. *Ther. Deliv.* **5,** 709–733 (2014).

503. Skretting, A. & Djupesland, P. G. A new method for scintigraphic quantification of deposition and clearance in anatomical regions of the human nose. *Nucl. Med. Commun.* **30,** (2009).

504. Djupesland, P. G., Skretting, A., Winderen, M. & Holand, T. Breath actuated device improves delivery to target sites beyond the nasal valve. *Laryngoscope* **116,** 466–72 (2006).

505. Djupesland, P. G. & Skretting, A. Nasal Deposition and Clearance in Man: Comparison of a Bidirectional Powder Device and a Traditional Liquid Spray Pump. *J. Aerosol Med. Pulm. Drug Deliv.* **25,** 280–289 (2012).

506. Kleven, M. *et al.* Using Computational Fluid Dynamics (CFD) to Improve the Bi-Directional Nasal Drug Delivery Concept. *Food Bioprod. Process.* **83,** 107–117 (2005).

507. Xi, J., Wang, Z., Nevorski, D., White, T. & Zhou, Y. Nasal and Olfactory Deposition with Normal and Bidirectional Intranasal Delivery Techniques: *In Vitro* Tests and Numerical Simulations. *J. Aerosol Med. Pulm. Drug Deliv.* **29,** jamp.2016.1295 (2016).

508. Dong, J., Shang, Y., Inthavong, K., Chan, H. K. & Tu, J. Numerical Comparison of Nasal Aerosol Administration Systems for Efficient Nose-to-Brain Drug Delivery. *Pharm. Res.* **35,** (2018).

509. Si, X. A., Xi, J., Kim, J. W., Zhou, Y. & Zhong, H. Modeling of release position and ventilation effects on olfactory aerosol drug delivery. *Respir. Physiol. Neurobiol.* **186,** 22–32 (2013).

510. Nejati, A., Kabaliuk, N., Jermy, M. C. & Cater, J. E. A deformable template method for describing and averaging the anatomical variation of the human nasal cavity. *BMC Med. Imaging* **16,** 55 (2016).

511. Terheyden, H., Maune, S., Mertens, J. & Hilberg, O. Acoustic rhinometry: validation by three-dimensionally reconstructed computer tomographic scans. *J. Appl. Physiol.* **89,** 1013–1021 (2000).

512. Corey, J. P., Gungor, A., Nelson, R., Fredberg, J. & Lai, V. A comparison of the nasal cross-sectional areas and volumes obtained with acoustic rhinometry and magnetic resonance imaging. *Otolaryngol. - Head Neck Surg.* **117,** 349–354 (1997).

513. Cheng, Y. S. *et al.* Nasal Deposition of Ultrafine Particles in Human Volunteers and Its Relationship to Airway Geometry. *Aerosol Sci. Technol.* **25,** 274–291 (1996).

514. Keyhani, K., Scherer, P. W. & Mozell, M. M. Numerical Simulation of Airflow in the Human Nasal Cavity. *J. Biomech. Eng.* **117,** 429 (1995).

515. Möller, W. *et al.* Topical drug delivery in chronic rhinosinusitis patients before and after sinus surgery using pulsating aerosols. *Pulsating Aerosols Top. Up. Airw. Ther.* **8,** e74991 (2013).

516. Djupesland, P. G., Messina, J. C. & Mahmoud, R. A. Breath powered nasal delivery: A new route to rapid headache relief. *Headache* **53,** 72–84 (2013).

517. Brasnjevic, I., Steinbusch, H. W. M., Schmitz, C. & Martinez-Martinez, P. Delivery of peptide and protein drugs over the blood-brain barrier. *Prog. Neurobiol.* **87,** 212–251 (2009).

518. Hanson, L. R. & Frey, W. H. Strategies for intranasal delivery of therapeutics for the prevention and treatment of neuroAIDS. *J. Neuroimmune Pharmacol.* **2,** 81–86 (2007).

519. Lipmann, M. & Albert, R. E. The Effect of Particle Size on the Regional Deposition of Inhaled Aerosols in the Human Respiratory Tract. *Am. Ind. Hyg. Assoc. J.* **30,** 257–275 (1969).

520. Hancock, B. C. & Parks, M. What is the true solubility advantage for amorphous pharmaceuticals? *Pharm. Res.* **17,** 397–404 (2000).

521. Brodland, G. W. How computational models can help unlock biological systems. *Seminars in Cell and Developmental Biology* **47–48,** 62–73 (2015).

Appendices

8 Appendices

A. Clinical trials on nose-to-brain drug delivery

The PubMed database (http://www.ncbi.nlm.nih.gov/pubmed/) was searched with the specific keyword string for intranasal drug delivery to the brain. Clinical trials intended for the drug delivery to the brain via nasal route were identified after reading the titles and/or abstracts. While few of the important clinical trials are references in the **Chapter 1** a full list is uploaded to the following web link.

https://files.acrobat.com/a/preview/c4afac0e-4406-492b-bd01-0897060ecef6

Search criteria: ("nose"[MeSH Terms] OR "nose"[All Fields] OR "nasal"[All Fields] OR "transnasal"[All Fields] OR "intranasal"[All Fields] OR "olfactory"[All Fields]) AND ("brain"[MeSH Terms] OR "brain"[All Fields] OR "central nervous system"[MeSH Terms] OR "central nervous system"[All Fields] OR "cerebrospinal"[All Fields]) AND (“targeting” [All Fields] OR "delivery"[All Fields] OR "transport"[All Fields]) AND (“clinical trial” (Filter)).

B. Calculation of %DTP values for microparticle formulations

The PubMed database (http://www.ncbi.nlm.nih.gov/pubmed/) was searched with following keyword string to identify the suitable literature. The %DTP values for the individual studies identified are given in **Table 21**.

Search criteria: ("nose"[MeSH Terms] OR "nose"[All Fields] OR "nasal"[All Fields] OR "transnasal"[All Fields] OR "intranasal"[All Fields] OR "olfactory"[All Fields]) AND ("brain"[MeSH Terms] OR "brain"[All Fields] OR "central nervous system"[MeSH Terms] OR "central nervous system"[All Fields] OR "cerebrospinal"[All Fields]) AND (“targeting” [All Fields] OR "delivery"[All Fields] OR "transport"[All Fields]) AND ("Microparticles [All Fields] OR Micro [All Fields] or particles [All Fields]).

Table 21 %DTP values calculated for the microparticle formulations from the reported literature.

Reference	Intravenous route		Intranasal route		F value	% DTP	Drug
	AUC blood	AUC brain	AUC blood	AUC brain			
Dilpiaz *et al.*2008	4210	0	583	3480	0	100	N6-cyclopentyladenosine
	4210	0	807	33495	6420.53	80.83	
Gavini *et al.* 2010	144	0	47	55	17.95	67.36	Rokitamycin
Sun *et al.* 2012	480.37	0	129.16	25.18	6.77	73.11	Methotrexate
Rassu *et al.* 2015	145.10	NR	8.92	198.20	12.18	93.85	deferoxamine mesylate
	145.10	NR	14.89	815.70	83.70	89.73	
Dalpiaz *et al.* 2014	NR	NR	NR	NR	NA	100 (claimed)	
	NR	NR	NR	NR	NA	100 (claimed)	Zidovudine Prodrug
Dilpiaz *et al.* 2015	NR	NR	NR	354	NA	100 (claimed)	

C. *Ex-vivo* mucoadhesion apparatus

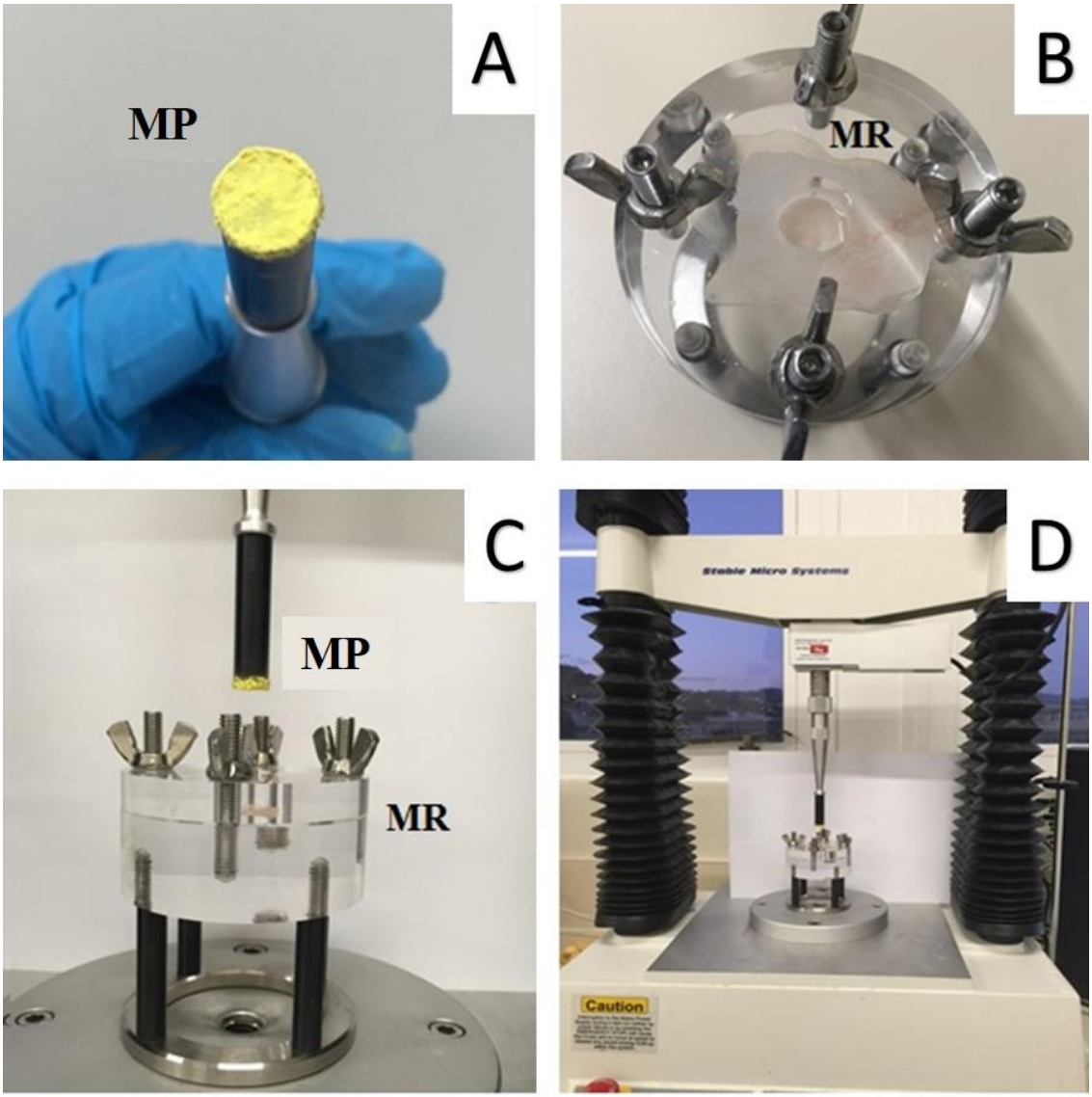

Figure 8.1 Tensile strength apparatus used to measure the ex-vivo mucoadhesion strength of the TSP-microparticles. (A) TSP-microparticles containing FITC-Dextrans attached to the moving probe (MP) (B) Special mucoadhesion rig (MR) with porcine olfactory mucosa (C &D) Assembly and pre-test positions of the MP and MR on a tensile strength apparatus.

D. Microparticle insufflation studies

Average weight of microparticles being expelled from the insufflator device was established using a series of experiments (n = 5) where a constant volume of air (10mL) was sucked into the syringe and mass of the expelled microparticles is determined using an electronic balance.

Table 22. Microparticle expulsion from insufflator device. Weight of empty insufflator (W_1), weight of insufflator loaded with microparticles (W_2) and weight of insufflator after expulsion of microparticles (W_3) were used to calculate the weight of loaded microparticles and expelled microparticles.

W_1* (g)	**W_2* (g)**	**W_3* (g)**	**Loaded microparticles [(W_2-W_1)*1000] (mg)**	**Expelled microparticles [(W_3-W_1)*1000] (mg)**	**Average ± SD (mg)**
19.4342	19.4451	19.4392	10.9000	5.9000	
19.4342	19.4454	19.4397	11.2000	5.7000	
19.4342	19.4460	19.4404	11.8000	5.6000	5.8360 ± 0.3
19.4342	19.4455	19.4400	11.3000	5.5000	
19.4342	19.4466	19.4401	12.4000	6.4800	

** Weights include mass of 10 mL of sucked air.*

E. HPLC method validation data for peripheral tissues

Table 23 Intraday and inter-day accuracy and precision of phenytoin and its metabolite in lung tissue (n = 6, mean ± SD).

	Nominal concentration (µg/mL)	**%CV**	**%bias**	**Accuracy %**
Intraday	Metabolite			
	1	6.99	-9.17	107.26
	5	5.68	-11.41	112.30
	10	5.18	-5.01	103.56
	Phenytoin			
	1	5.62	-12.01	112.99
	5	9.42	-6.81	108.58
	10	6.53	-2.41	100.86
Inter-day	Metabolite			
	1	6.44	-4.47	104.47
	5	8.05	-10.42	110.42
	10	4.28	-9.70	109.70
	Phenytoin			
	1	4.97	4.97	105.70
	5	5.06	-10.28	110.28
	10	6.94	-4.57	104.57

Table 24 Intraday and inter-day accuracy and precision of phenytoin and its metabolite in liver tissue (n = 6, mean ± SD).

	Nominal concentration (µg/mL)	**%CV**	**%bias**	**Accuracy %**
Intraday	Metabolite			
	1	6.02	-9.25	109.25
	5	6.48	-0.78	100.78
	10	2.98	4.21	95.79
	Phenytoin			
	1	3.79	-13.34	113.34
	5	4.45	-2.66	102.66
	10	2.15	5.03	94.97
Inter-day	Metabolite			
	1	6.05	-4.57	104.57
	5	6.63	-7.55	107.55
	10	3.32	-4.81	104.81
	Phenytoin			
	1	3.48	3.48	104.58
	5	5.70	-2.97	102.97
	10	3.87	-3.87	103.87

Table 25 Intraday and inter-day accuracy and precision of phenytoin and its metabolite in kidney tissue (n = 6, mean ± SD).

	Nominal concentration (µg/mL)	**%CV**	**%bias**	**Accuracy %**
Intraday	Metabolite			
	1	1.67	-10.19	110.19
	5	6.29	0.93	99.07
	10	7.49	5.61	94.39
	Phenytoin			
	1	4.49	5.03	94.97
	5	8.92	-4.82	104.82
	10	7.42	12.65	87.35
Inter-day	Metabolite			
	1	4.54	2.86	97.14
	5	8.25	-2.92	102.92
	10	8.07	-0.58	99.79
	Phenytoin			
	1	4.94	4.94	98.99
	5	6.35	3.77	96.23
	10	7.40	8.59	90.93

Table 26 Intraday and inter-day accuracy and precision of phenytoin and its metabolite in spleen tissue (n = 6, mean ± SD).

	Nominal concentration (µg/mL)	**%CV**	**%bias**	**Accuracy %**
Intraday	Metabolite			
	1	2.40	3.99	96.01
	5	0.32	6.13	-4.01
	10	9.99	4.05	95.95
	Phenytoin			
	1	5.89	-1.61	101.61
	5	7.16	4.47	95.53
	10	3.95	8.47	91.53
Inter-day	Metabolite			
	1	5.66	8.57	91.43
	5	4.69	-3.30	103.30
	10	6.36	2.83	97.17
	Phenytoin			
	1	10.71	10.71	97.75
	5	5.71	5.84	94.16
	10	5.84	10.43	89.57

Table 27 Intraday and inter-day accuracy and precision of phenytoin and its metabolite in heart tissue (n = 6, mean ± SD).

	Nominal concentration (µg/mL)	**%CV**	**%bias**	**Accuracy %**
Intraday	Metabolite			
	1	4.19	-5.61	105.61
	5	1.93	1.63	98.37
	10	5.82	8.11	91.89
	Phenytoin			
	1	7.30	-13.60	113.60
	5	1.74	6.08	93.92
	10	3.78	-0.92	100.92
Inter-day	Metabolite			
	1	9.81	6.23	93.77
	5	4.03	0.54	99.46
	10	4.56	3.57	96.01
	Phenytoin			
	1	5.30	5.30	107.94
	5	3.15	5.07	94.93
	10	5.43	7.09	92.99

F. Airflow in nasal cavities of three human subjects at different nebulization velocities

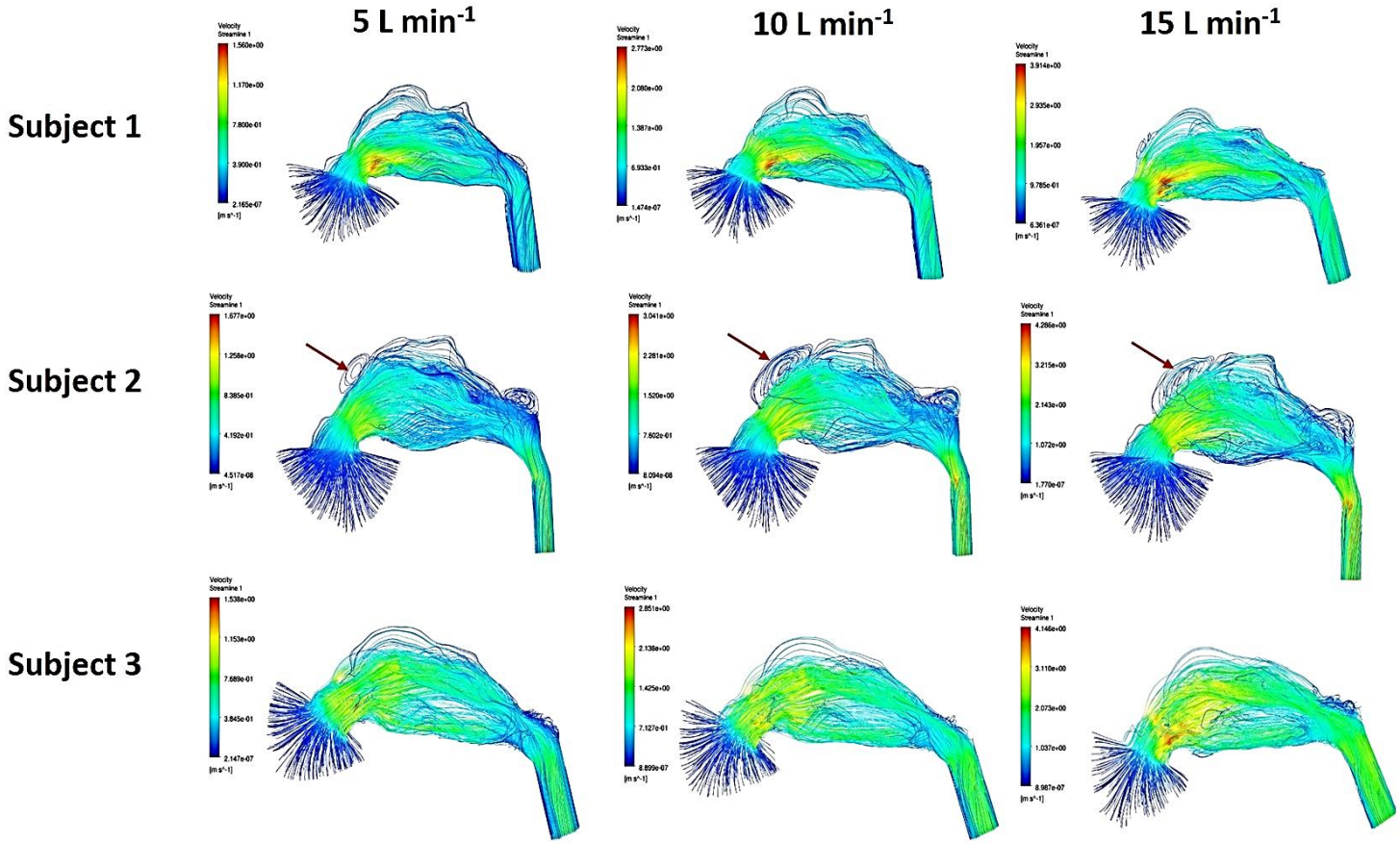

Figure 8.2 Representative airflow streamlines of nebulization and bi-directional delivery methods in three subjects at different nebulization airflow rates. Arrows indicate the region of recirculation. The color map indicates the velocity of air flow